

About Charged Excitons, Polarons, and Electron Spin Relaxation in Solids

Habilitationsschrift

zur

Erlangung des akademischen Grades

doctor rerum naturalium habilitatus (Dr. rer. nat. habil.)

an der Mathematisch–Naturwissenschaftlichen Fakultät

der

Ernst–Moritz–Arndt–Universität Greifswald

vorgelegt von

Franz Xaver Bronold

geboren am 1. August 1964

in Ingolstadt

Greifswald, Juni 2004

Dekan : Prof. Dr. J.-P. Hildebrandt

1. Gutachter : Prof. Dr. H. Fehske

2. Gutachter : Prof. Dr. L. J. Sham

3. Gutachter : Prof. Dr. R. Zimmermann

Tag der Habilitation : 24.05.2005

Abstract

Solid state physics is undoubtedly an applied science. It provides (together with chemistry) the theoretical framework for systematically manipulating the materials on which modern day technology is based. At the same time, it is continually driven by the forces this technology creates. The main driving force of solid state physics is most likely the economic pressure for miniaturization, which subsequently inspires solid state scientists to explore new materials and to identify ways to tap into microscopic processes which are not yet commercially exploited. In turn, each new generation of materials fabricated and each new attempt to utilize the microscopic fabric of materials for technological applications provide a unique laboratory for testing and eventually replenishing the general notions and concepts of solid state physics.

The author's research interests and activities, which are summarized in this report, illustrate unintentionally, but at the same time quite naturally, the various ways in which solid state physics is currently pushed forward by technology. Charged excitons, for instance, to be discussed in Chapter 1, can be most clearly observed in high-quality low-dimensional semiconductor structures (quantum wells, quantum wires, and quantum dots), grown with techniques originally developed for engineering the VLSI circuitry of modern microprocessors. These structures can be also used to study the fundamental aspects of quantum mechanics of many-body systems. Here we consider the optical properties of a doped quantum well. We are particularly interested in the consequences of the dynamical response of the interacting conduction band electrons to the sudden appearance of the photo-induced valence band hole. At low-to-intermediate conduction band electron densities this leads to the formation of charged excitons (trions), that is, in-medium bound states comprising two conduction band electrons and one valence band hole. Whereas at high densities, the dynamical response gives rise to power-law signatures in the optical susceptibility at the Fermi energy (Fermi-edge signatures). The concept of a dynamical (or transient) response to a sudden perturbation (in contrast to an adiabatic response to a stationary perturbation) is rather general. It also plays, for instance, an important role in the Kondo effect. In this sense, the quantum well can be considered as a model system in which fundamental quantum mechanical effects can be realized and studied in a controlled manner. Chapter 2, on the other hand, is devoted to polarons. The revival of polaron physics is due mainly to materials synthesized quite recently during the last couple of decades – the high-temperature superconducting perovskites and the colossal magneto-resistance manganites, both of which with a huge technological potential. At the same time, however, these materials defy a complete description within the generally accepted framework of solid state physics. Instead, they seriously challenge basic concepts, for instance, the concept of a quasi-particle or the concept of extended and localized states. One consequence of this challenge is the increasing awareness in the solid state physics community of problems which have not yet found a satisfactory solution. We focus in Chapter 2 on one of those problems, Anderson localization in an interacting system, which comes here in the guise of self-trapping (polaron formation) in an imperfect crystal with strong electron-phonon coupling. Finally, Chapter 3 addresses the electron spin dynamics in a non-magnetic semiconductor. The

application-driven desire to utilize the electron spin for data storage and processing created a tremendous world-wide activity to investigate spin-dependent effects in semiconductors. This has led to the newly emerging field of spintronics. A subclass of spintronic device concepts attempts to utilize electron spin polarizations in non-magnetic semiconductors. The device operation is thus performed by an externally induced non-equilibrium spin polarization, which decays after the external probe is removed. The characterization of the spin polarization requires therefore a kinetic theory. In Chapter 3 we specifically present a semiclassical kinetic theory for the non-equilibrium electron spin dynamics in III-V semiconductors, paying due attention to the subtle band structure effects, which cause spin relaxation, and the multiple timescales on which the spin polarization evolves. Even if spintronics may turn out to be technologically not yet feasible, it has already led to a new class of model systems for the investigation of spin dephasing in solids.

The three chapters of this report can be read independently. Each chapter starts with introductory remarks, which motivate the investigation at hand. The core parts, respectively, give a complete, self-contained description of the theoretical methods and concepts employed and the theoretical results obtained. Concluding remarks summarize the content of each chapter separately and give a short outlook for future research directions. The topics treated in the three chapters are rather different, each one is therefore separately preceded by an abstract. To assist a quick orientation, we restate the abstracts here again.

Chapter 1 discusses the calculation of the optical susceptibility of a doped quantum well. We primarily focus on the linear optical response of a weakly n-doped quantum well, where the interaction between the photo-induced neutral exciton with the excess carriers in the conduction band leads to the formation of a negatively charged exciton (trion). In this regime, we conceptualize trion formation as the lowest order dynamical response of the conduction band electrons to the sudden appearance of the photo-induced valence band hole. The cluster mean field approximation can then be applied to determine the optical response. It reduces the calculation of the optical susceptibility to the solution of two in-medium few-body problems: an in-medium two-particle problem (exciton) and an in-medium three-particle problem (trion). The medium, described in Hartree-Fock approximation, decorates the interactions within the two- and three-body clusters with phase space factors and the single particle energies with Hartree-Fock corrections. Although screening is strictly speaking beyond the cluster mean field approximation, it can be phenomenologically included replacing the bare Coulomb interaction by a statically screened one. Besides a detailed description of the cluster mean field approach, we present semi-analytical results for the extreme dilute limit, where medium corrections are negligible and excess carriers only provide a reservoir for bound state formation. Even within this crude approximation, the overall agreement with experimental results is quite good. Experimental data from highly doped quantum wells show that bound states disappear at a critical density. The optical response in the vicinity of the conduction band Fermi energy displays then a power-law dependence typical for the Fermi-edge signature. This regime is beyond the cluster mean field approximation. In the second half of the chapter we make therefore an attempt to derive a minimal set of equations for the calculation of the optical response at arbitrary conduction band electron density. Our approach is based on a systematic parquet analysis of the intra- and interband four-point functions. Since the parquet equations correspond to the crossing symmetric summation of two-line reducible diagrams, the two interband channels responsible for the Fermi-edge signature are naturally accounted for. Additional effort is however necessary to incorporate the system's propensity of trion formation at low-to-intermediate densities. For that purpose, we identify a subclass of two-line irreducible interband diagrams containing three particle correlations which, at low enough density, lead to trion formation. Including this set of diagrams in the driving term of the interband parquet equations gives then an interband vertex, which also contains at low enough densities a contribution

from trion states. The optical susceptibility obtained from this vertex extrapolates, at least in principle, between the bound state dominated low-to-intermediate density regime to the Fermi-edge dominated high density regime. The discussion in the second part of the chapter remains qualitative and should be understood as exploratory.

Chapter 2 discusses self-trapping of a single charge carrier (polaron formation) in a disordered environment, with special emphasis on Anderson localization of polaron states. In the first half of the chapter we study, at zero temperature, the dynamics of a single electron in a Holstein model augmented by site-diagonal, binary-alloy type disorder. The average over the phonon vacuum and the alloy configurations is performed within an effective single-site approximation, which maps the lattice problem on to a problem involving only a single self-consistently embedded impurity site. In particular, we employ the dynamical coherent potential approximation, which is nothing but the single particle limit of the more general dynamical mean field theory. We present numerical results for a Bethe lattice with infinite coordination number. In particular, we investigate, in the intermediate electron-phonon coupling regime, the spectral and diffusion properties in the vicinity of the high-energy edge of the lowest polaronic subband. To characterize the diffusion properties, we define a spectrally resolved delocalization time, which is, for a given energy, the characteristic time scale on which the electron leaves a given site. We find delocalization times substantially enhanced for states with a large phonon content, i.e., in the absence (presence) of alloy-type disorder at the high-energy edge(s) of the polaronic subband (mini-subbands). According to their delocalization times, we discriminate between “fast” quasi-particle-like and “sluggish” defect-like polaron states. Within the dynamical coherent potential approximation it is however impossible to determine the critical disorder needed to localize polaron states. Accordingly, mobility edges for polaron states cannot be determined. To overcome the limitations of the dynamical mean field theory, we adopted therefore the statistical dynamical mean-field theory to the disordered Holstein model. The second half of chapter 2 is a detailed discussion of this approach. The statistical dynamical mean field approximation maps the lattice problem on to an ensemble of self-consistently embedded impurity problems, in contrast to the single impurity problem obtained within the dynamical coherent potential approximation (viz. dynamical mean field approximation). It is not only capable of accounting the polaron formation process but also the spatial fluctuations giving rise to Anderson localization. The statistical dynamical mean field approximation is a probabilistic approach, focusing on the distributions instead of the average values for observables of interest. We employ a Monte-Carlo sampling technique to solve the self-consistent equations of the theory on a Bethe lattice with finite coordination number, representing distributions for random variables by random samples and discussing various ways to determine mobility edges from the random sample for the local Green function. Specifically, we give, as a function of the “polaron parameters”, such as adiabaticity and electron-phonon coupling constants, a detailed discussion of the localization properties of a single polaron, using a bare electron as a reference system.

Chapter 3 presents a semiclassical kinetic theory for the non-equilibrium electron spin dynamics in non-magnetic semiconductors. The approach accounts for elastic as well as inelastic scattering and treats Elliott-Yafet and motional-narrowing processes, such as D’yakonov-Perel’ and variable g-factor processes, on an equal footing. Focusing on small spin polarizations and small momentum transfer scattering, we derive, starting from the full quantum kinetic equations, a Fokker-Planck equation for the electron spin polarization. The dynamics of the spin polarization is thereby visualized in terms of a “test” spin polarization which scatters off “field” particles (electrons, impurities, phonons). We then construct, using a rigorous multiple time scale approach, a Bloch equation for the macroscopic (\vec{k} -averaged) spin polarization on the long time scale, where the spin polarization decays. Spin-conserving energy relaxation and diffusion, which

occur on a short time scale, after the initial spin polarization has been injected, are incorporated and shown to give rise to a weight function which defines the energy averages required for the calculation of the spin relaxation tensor of the Bloch equation. We give explicit expressions for the spin relaxation tensor, applicable to bulk and quantum wells. To illustrate our approach, we calculate for specific situations the lifetime of a photogenerated electron spin polarization in bulk GaAs and a GaAs quantum well. For bulk GaAs, we discuss the magnetic field dependence of spin relaxation times taking electron-impurity and electron-phonon scattering into account. We focus in particular on the competition between the quenching of the D'yakonov-Perel' process and the field-induced variable g-factor process. We find an optimal magnetic field for which the spin lifetimes are maximal and point out that the sign of the slope of the field dependence of the transverse spin lifetime reveals whether the Elliott-Yafet or the D'yakonov-Perel' process dominates spin relaxation at small magnetic fields. For a GaAs quantum well, we calculate spin lifetimes at temperatures and densities where electron-electron and electron-impurity scattering dominate. We find that spin lifetimes are non-monotonic functions of temperature and density. Our results show that at electron densities and temperatures, where the cross-over from the non-degenerate to the degenerate regime occurs, spin lifetimes are particularly long.

Contents

1	Charged Excitons in Weakly Doped Quantum Wells [1–3]	1
1.1	Introductory Remarks	2
1.2	Model Hamiltonian and Optical Susceptibility	4
1.3	Cluster Mean Field Approximation	5
1.3.1	General Formalism	5
1.3.2	Exciton Representation	9
1.3.3	Extreme Dilute Limit	11
1.4	Numerical Results [3]	13
1.5	Beyond the Cluster Mean Field Approximation: An Outlook	17
1.5.1	The Problem of the Fermi-Edge Signature	17
1.5.2	Parquet Analysis	19
1.5.3	Minimal Set of Equations	26
1.6	Concluding Remarks	29
	Appendix Hylleraas Variational Approach for the Trion Groundstate	31
2	Polaron Formation and Disorder [4–7]	37
2.1	Introductory Remarks	38
2.2	Dynamical Coherent Potential Approximation (DCPA) [4]	40
2.2.1	The Concept of an Effective Single Site	40
2.2.2	Calculation of the One-Resolvent	42
2.2.3	Validity of the Factorization Procedure	46
2.2.4	Calculation of the Two-Resolvent	47
2.2.5	Specification to a Bethe Lattice	50
2.3	Numerical Results I [4]	52
2.3.1	Spectral Properties	52
2.3.2	Diffusion Properties	56
2.4	Critique	61
2.5	Statistical Dynamical Mean Field Theory (statDMFT) [5–7]	62
2.5.1	Disorder and Interactions	62
2.5.2	General Formalism	64
2.5.3	Specification to a Bethe Lattice	67
2.5.4	Localization Criterion	68
2.5.5	Single Electron and T=0 Limit	69
2.6	Numerical Results II [7]	71
2.6.1	Electron States	71
2.6.2	Polaron States	77
2.7	Concluding Remarks	84

Appendix A Polaron Impurity Model	87
Appendix B DCPA Ward Identity	89
Appendix C $\Omega = 0$ Limit of the DCPA Equations	91
Appendix D StatDMFT for a Single Polaron: Multiple Scattering Approach	93
Appendix E Large Coordination Number Limit of the statDMFT	97
3 Electron Spin Dynamics in Semiconductors [9–11]	99
3.1 Introductory Remarks	99
3.2 Spin Dependence of Semiconductor Electronic Structure	102
3.3 Semiclassical Kinetic Theory	104
3.3.1 Kinetic Equations	104
3.3.2 Calculation of the Self-Energies	108
3.3.3 Diffusion Approximation	111
3.3.4 Multiple Time Scale Analysis	115
3.4 Applications	124
3.4.1 Spin Relaxation in Quantum Well Structures [9]	125
3.4.2 Spin Relaxation in Bulk Semiconductors [10,11]	133
3.5 Concluding Remarks	141
Appendix Construction of the Fokker-Planck Differential Operator	145
Bibliography	149
Acknowledgements	159
Declaration	161
Curriculum Vitae	163

List of Figures

1.1	Dynamical response of CB electrons to the photogenerated VB hole	3
1.2	Experimental absorption spectra for a 10nm CdTe quantum well at T=2K	4
1.3	Dynamical part of the exciton self-energy (not a Feynman diagram)	10
1.4	Exciton spectral function $D_X(\tilde{\omega})$ for $na_B^2 = 0.008$ and $4R\beta = 10$	13
1.5	Trion absorption bands for different temperatures and CB electron densities	14
1.6	Temperature and density dependence of the ratio of spectral weights $\frac{f_T}{f_X}$	15
1.7	Phenomenologically broadened optical absorption spectrum	16
1.8	Feynman diagrams for the CB electron and VB hole self-energy	18
1.9	Feynman diagram for a generic four point function	20
1.10	The five chaining operations used to construct reducible four-point functions	21
1.11	Lowest order diagrams generated by the five chaining operations	22
1.12	Three particle correlations burried in the two-line irreducible block	25
1.13	Complete two-line irreducible eh vertex with trion part separated off	25
1.14	The independent variables for the trion groundstate calculation	32
2.1	Illustration of the “philosophy” behind an effective single-site approximation	41
2.2	Schematic representation of a fourth order process contributing to $Q_i^{[2]}$	47
2.3	Schematic representation of the second order processes contributing to the local DCPA vertex	48
2.4	Schematic representation of the integral equation for the local DCPA vertex	49
2.5	DCPA spectral and diffusion properties of the Holstein model in the vicinity of the first polaronic subband for $\lambda = 0.98$, $\alpha = 0.25$	53
2.6	Blow-up of Fig. 2.5 in the immediate vicinity of the high-energy edge of the lowest polaronic subband	54
2.7	DCPA spectral and diffusion properties of the Holstein alloy in the vicinity of the high-energy edge of the first polaronic subband for $c = 0.5$ and $\delta = -0.01$	55
2.8	DCPA density of states $N(\omega)$ for the Holstein alloy in the vicinity of the first polaronic subband	56
2.9	Scattering strength dependence of the DCPA spectral and diffusion properties in the vicinity of the high-energy edge of the first polaronic subband	57
2.10	η -asymptotics of the spectrally resolved return probability $P(\omega, \eta)$ for the Holstein model	58
2.11	Spectrally resolved delocalization time $T_0(\omega)$ for the Holstein model in the vicinity of the high energy edge of the first polaronic subband	59
2.12	Spectrally resolved delocalization time $T_0(\omega)$ for the Holstein alloy in the vicinity of the high energy edge of the first polaronic subband for $c = 0.5$ and $\delta = -0.002$	61
2.13	Illustration of the cavity method	64

2.14	$K = 2$ Bethe lattice	67
2.15	Distribution for the LDOS of the Anderson model at $\omega = 0$ and three different degrees of disorder	72
2.16	Average and typical LDOS for the Anderson model with $\bar{\gamma} = 1.5$ and $\eta = 10^{-10}$	73
2.17	η -scaling of the distribution for the LDOS of the Anderson model below ($\omega = -0.9$) and above ($\omega = 0$) the lower mobility edge for $\bar{\gamma} = 1.5$	74
2.18	η -scaling of the typical LDOS of the Anderson model at $\omega = 0$ for $\bar{\gamma} = 1.5$	75
2.19	Mobility edge trajectory for an electron in the Anderson model	76
2.20	Evolution of the LDOS $N(\omega)$ and the imaginary part of the interaction self-energy for the Holstein model with increasing electron-phonon coupling and fixed adiabaticity	77
2.21	Typical tunnel rates $\Gamma^{\text{typ}}(\omega)$ for the lowest polaronic subband in the Anderson-Holstein model	78
2.22	Average and typical LDOS for the lowest polaronic subband in the anti-adiabatic, strong coupling regime for $\bar{\gamma}/W = 2.5$ with W the width of lowest subband of the pure Holstein model	79
2.23	η -scaling of the distribution for the LDOS for two energies within the lowest polaronic subband (anti-adiabatic strong-coupling regime)	80
2.24	Comparison of the disorder dependence of the typical LDOS in the center of the band of the pure Anderson model and the center of the lowest polaronic subband of the Anderson-Holstein model in the anti-adiabatic strong coupling regime	81
2.25	Parts of the mobility edge trajectories for the lowest polaronic subband of the Anderson-Holstein model in the anti-adiabatic strong coupling and the adiabatic intermediate-to-strong coupling regime	82
2.26	Evolution of the (low-energy) average and typical LDOS for the Anderson-Holstein model for four different degrees of disorder	83
2.27	Average and typical LDOS of the Anderson-Holstein model in the Anderson regime	84
2.28	Average LDOS for the Bethe lattice with connectivity $K = 2, 4$ and 8	98
3.1	Experimentally measured time-resolved Faraday rotation for bulk GaAs	101
3.2	Self-energies contributing to the Born approximation	108
3.3	Symbolic representation of type I and II scattering processes	112
3.4	Graphical illustration of the collision terms in the diffusion approximation	113
3.5	Schematic illustration of the time evolution of the non-equilibrium spin polarization as given by the Fokker-Planck equation	116
3.6	Friction, diffusion, and angle randomization coefficient for a modulation doped quantum well at $n = 4 \times 10^9 \text{cm}^{-2}$ and $T = 10\text{K}$	127
3.7	Friction, diffusion, and angle randomization coefficient for a modulation doped quantum well at $n = 4 \times 10^{11} \text{cm}^{-2}$ and $T = 10\text{K}$	128
3.8	Weight function $p(\epsilon)$ for a modulation doped quantum well at $T = 10\text{K}$ and three different electron densities	129
3.9	D'yakonov-Perel' spin lifetime for a 25nm modulation doped quantum well as a function of electron density and three different temperatures	130
3.10	D'yakonov-Perel' spin lifetime for a 25nm doped quantum well as a function of electron density for $T = 40\text{K}$ and for three degrees of compensation	131
3.11	D'yakonov-Perel' spin lifetime for a 25nm doped quantum well as a function of temperature at an electron density $n = 3 \times 10^{10} \text{cm}^{-2}$ and three degrees of compensation	132

3.12	D'yakonov-Perel' spin lifetime for a 10nm GaAs quantum well as a function of temperature for $n = 1.86 \times 10^{11} \text{cm}^{-2}$ and two degrees of compensation	133
3.13	Transverse spin relaxation time for bulk GaAs as a function of electron density and for $T = 0$	137
3.14	Spin relaxation time for bulk GaAs as a function of magnetic field for $T = 0$ and various electron densities	139
3.15	Transverse spin lifetime for bulk GaAs as a function of magnetic field for $T = 0$, $n = 10^{18} \text{cm}^{-3}$, and for various degrees of compensation	140
3.16	Spin relaxation time for bulk GaAs as a function of magnetic field for an electron density $n = 10^{17} \text{cm}^{-3}$ and various temperatures	141
3.17	Range of integration for the integrals defining the friction, diffusion, and angle randomization coefficients due to electron-electron scattering in a quantum well . .	147

Chapter 1

Charged Excitons in Weakly Doped Quantum Wells [1–3]

This chapter is an extended version of my invited contribution [1] to the NATO workshop *Optical Properties of 2D systems with interacting electrons*, supplemented with material from Refs. [2,3]. It discusses the calculation of the optical susceptibility of a doped quantum well. We primarily focus on the linear optical response of a weakly n-doped quantum well, where the interaction between the photo-induced neutral exciton with the excess carriers in the conduction band leads to the formation of a negatively charged exciton (trion), i.e., a bound state made out of two conduction band electrons and one valence band hole. In this regime, we conceptualize trion formation as the lowest order dynamical response of the conduction band electrons to the sudden appearance of the photo-induced valence band hole. The cluster mean field approximation can then be applied to determine the optical response. It reduces the calculation of the optical susceptibility to the solution of two in-medium few-body problems: an in-medium two-particle problem (exciton) and an in-medium three-particle problem (trion). The medium, described in Hartree-Fock approximation, decorates the interactions within the two- and three-body clusters with phase space factors and the single particle energies with Hartree-Fock corrections. Although screening is strictly speaking beyond the cluster mean field approximation, it can be phenomenologically included replacing the bare Coulomb interaction by a statically screened one. Besides a detailed description of the cluster mean field approach, we present semi-analytical results for the extreme dilute limit, where medium corrections are negligible and excess carriers only provide a reservoir for bound state formation. Even within this crude approximation, the overall agreement with experimental data is quite good. Experimental results from highly doped quantum wells show that bound states disappear at a critical density. The optical response in the vicinity of the conduction band Fermi energy displays then a power-law dependence typical for the Fermi-edge signature. This regime is beyond the cluster mean field approximation. In the second half of the chapter we make therefore an attempt to derive a minimal set of equations for the calculation of the optical response at arbitrary conduction band electron densities. Our approach is based on a systematic parquet analysis of the intra- and interband four-point functions. Special attention is devoted to the problem of incorporating screening and the system's propensity of trion formation at low-to-intermediate densities in the parquet equations for the interband interaction vertex. The optical susceptibility obtained from this vertex extrapolates then, at least in principle, from the bound state dominated low-to-intermediate density regime to the Fermi-edge dominated high density regime. The discussion in the second part of the chapter remains qualitative and should be understood as exploratory.

1.1 Introductory Remarks

The interaction of an optically generated neutral exciton with excess carriers in the conduction band has been the subject of extensive experimental and theoretical investigations. In particular the high density regime attracted much interest.

For bulk semiconductors the high density regime is well understood [12–17]: Dynamical screening and Pauli blocking prohibit the formation of bound eh states,¹ the exciton is therefore unstable and its spectral weight distributed among eh scattering states. Residual correlations between the valence band (VB) hole and conduction band (CB) electrons are still important, however. As a result, the optical response displays in the vicinity of the CB Fermi energy a power-law dependence. The optical absorption, e.g., is then given by $I(\omega) \sim (\omega - \omega_T)^\alpha$, with a threshold ω_T and an exponent α . At low enough temperatures and/or small enough CB electron to VB hole mass ratios, the exponent α can be negative and the celebrated Fermi-edge singularity develops. [14–17]

Conceptually, the Fermi-edge singularity in the optical response of a doped bulk semiconductor is analogous to the edge singularity in the X-ray spectrum of a core level in a metal. [18–20] Both result from correlations between a Fermi sea of electrons and a single hole (see below). However, in contrast to the Fermi-edge singularity in the X-ray spectra of metals, the Fermi-edge singularity in doped bulk semiconductors has not yet been observed. Doping not only provides charge carriers but also counter-ions, which act as very efficient scattering centers. As a consequence, the optical lineshapes of doped bulk semiconductors at low temperatures are dominated by disorder and not by correlation effects. The Fermi-edge singularity is buried within a disorder-broadened line.

The situation is different in modulation-doped quantum wells, where counter-ions are spatially well separated from the two-dimensional electron gas. [21] Impurity scattering is therefore substantially suppressed and correlation effects are expected to strongly influence the optical response. Considerable theoretical [17, 22–27] and experimental [28–33] work has therefore been devoted to examine the optical properties of quasi-two dimensional doped semiconductors. In some of these systems, the Fermi-edge singularity has indeed been observed in the low-temperature optical response. Qualitatively, the high-density optical response is well understood. Although, a complete, quantitative theoretical analysis is still missing.

Recently the center of interest shifted to low densities. Following the seminal experiment of Kheng and coworkers [34], which showed that in a weakly n-doped semiconductor quantum well, photogenerated eh pairs give rise to negatively charged excitons (trions), i.e., bound eeh states comprising two CB electrons and one VB hole, numerous theoretical [2, 3, 35–42] and experimental studies [43–50] have been devoted to investigate the optical properties of weakly doped quantum wells. The importance of eeh states in the low density regime is now unambiguously established and a qualitative understanding of the low density regime is starting to emerge.

Both the Fermi-edge signature and the trion are consequences of the dynamical response of the CB electrons to the sudden appearance (absorption) or disappearance (emission) of the photogenerated VB hole. A typical lowest order process is depicted in Fig. 1.1. The photogenerated VB hole scatters from one momentum state to another and simultaneously excites a virtual $e\bar{e}$ pair (recall our notation, \bar{e} denotes a CB hole) to compensate for the momentum transfer. At low densities, the Coulomb interaction is strong enough to correlate the VB hole with two CB electrons (the photoexcited CB electron and the CB electron from the $e\bar{e}$ pair) and a (negatively charged) trion appears. At higher CB electron densities, an *arbitrary* number of $e\bar{e}$ pairs is excited, giving rise to, among others, the screening of the Coulomb interaction. At some density, the Coulomb interaction is then perhaps too weak to support trions and/or excitons, but the

¹We use the following notation: e , \bar{e} , and h denote, respectively, conduction band electrons, conduction band holes, and valence band holes; a negatively charged exciton (trion), e.g., is therefore an eeh cluster.

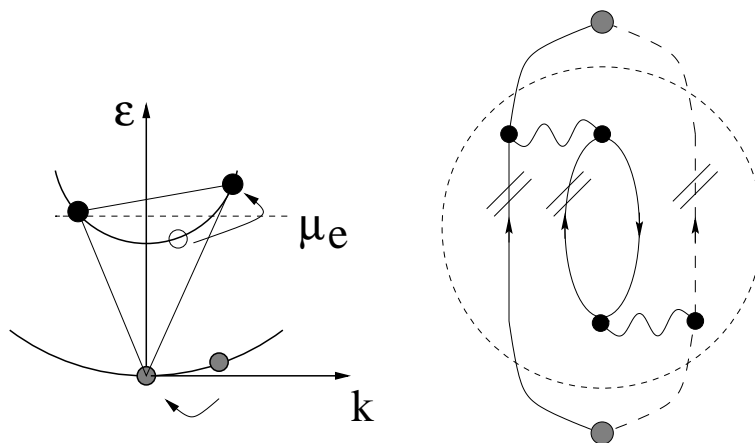


Figure 1.1: The left panel illustrates a typical dynamical response of the CB electrons to the photogenerated VB hole in an idealized n-doped semiconductor (μ_e is the chemical potential for the CB electrons). The right panel shows the corresponding Feynman diagram. The dashed upward running line denotes a VB hole, whereas the upward and downward running solid lines depict, respectively, a CB electron and CB hole. Multiple scattering, indicated by the thin stripes attached to the participating lines, correlates the intermediate eeh cluster to a trion.

residual correlations might produce the power-law dependence typical for the Fermi-edge signatures. The concept of a dynamical or transient response to a sudden perturbation, in contrast to an adiabatic response to a stationary perturbation, occurs also in other contexts. For instance, the Kondo effect [51] can be understood along those lines, although the scattering center – a localized spin – is then not structureless and possesses a memory.

Experimentally the density dependence of the optical response of a doped quantum well has been traced from the low density, trion-dominated regime all the way up to the high density regime, where bound states disappear. [32, 43, 48, 49] For the purpose of illustration we show in Fig. 1.2 the optical density, measured by transmission spectroscopy, for a doped CdTe quantum well. [48] For the nominally undoped sample (a) the exciton line is dominant, with a weak low-energy shoulder, because of unintentional doping. The doped samples show first a double peak structure, due to trion and exciton absorption, and then a broad hump at the Fermi-edge denoted by “FES”. In this sample, the Fermi-edge singularity is not particularly strong. Disorder effects due to impurities and/or interface roughness broaden the correlation driven singularity to a hump.

A unified theoretical description of the full density dependence of the optical susceptibility is still missing. To construct such a theory is a rather formidable task, which we try to address in the second part of this chapter. In the first part we focus on the low density regime, where bound states dominate. In this regime, the cluster meanfield approximation can be effectively used to calculate the optical susceptibility. [2, 3] In contrast to early theoretical studies of trion states [35–39], the cluster mean field approximation explicitly accounts for a low density of excess carriers and describes trion and exciton states simultaneously. Medium effects, such as Pauli blocking, (Hartree-Fock) corrections to the single particle energies, and (static) screening are incorporated. The high density regime, however, where the power-law dependence at the CB Fermi-edge is observed, cannot be systematically reached.

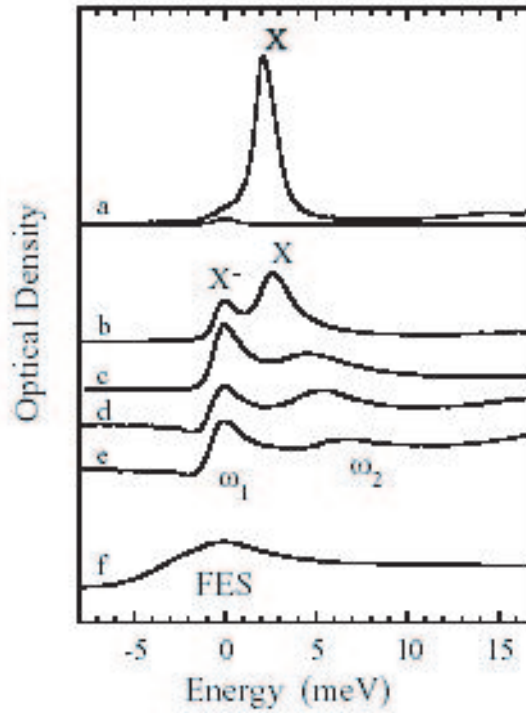


Figure 1.2: Optical absorption spectra for a 10nm CdTe quantum well at $T=2\text{K}$. The data are taken from Ref. [48]. Electron densities n are (b) 0.2, (c) 1.0, (d) 1.3, (e) 1.8, and (f) $3.0 \times 10^{11}\text{cm}^{-2}$. Sample (a) is nominally undoped. The zero of energy ($\approx 1.61\text{ eV}$) is taken at the lowest absorption peak, X^- or ω_1 , in each case. The authors normalized the integrated optical densities [$=\log(1/\text{transmission})$] since the structures have different numbers of quantum wells.

1.2 Model Hamiltonian and Optical Susceptibility

We consider for simplicity an idealized, strictly two-dimensional quantum well with two isotropic parabolic bands. With an appropriate choice of single particle states, our formalism can be of course also applied to more realistic quantum well models, which include, e.g., valence band mixing and finite band off-sets. Anticipating the application of the model to III-V semiconductors such as GaAs, the two bands correspond to the conduction band and the heavy hole valence band. Both are doubly spin degenerate. We denote both electron and hole spin by the label $\sigma = \uparrow, \downarrow$ keeping in mind however that in GaAs the spin of the electron is $s_z = \pm 1/2$ whereas the “spin” of the heavy hole is $j_z = \pm 3/2$. We assume a single hole in the valence band and a concentration n of electrons in the conduction band. The charge carriers are coupled through the Coulomb interaction and the total Hamiltonian is given by

$$\begin{aligned}
 H &= H_0 + V \\
 &= \sum_{\vec{k}\sigma} [\epsilon_c(k) a_{\vec{k}\sigma}^\dagger a_{\vec{k}\sigma} + \epsilon_v(k) b_{\vec{k}\sigma}^\dagger b_{\vec{k}\sigma}] \\
 &\quad + \frac{1}{2} \sum_{\vec{k}\vec{p}\vec{q}\sigma\tau} v(q) [a_{\vec{k}+\vec{q}\sigma}^\dagger a_{\vec{p}-\vec{q}\tau}^\dagger a_{\vec{p}\tau} a_{\vec{k}\sigma} - 2a_{\vec{k}+\vec{q}\sigma}^\dagger b_{\vec{p}-\vec{q}\tau}^\dagger b_{\vec{p}\tau} a_{\vec{k}\sigma}],
 \end{aligned} \tag{1.1}$$

where $\epsilon_c(k) = E_g + k^2/2m_e$ and $\epsilon_v(k) = k^2/2m_h$ are the conduction band and valence band dispersions ($\hbar = 1$), respectively, and $v(q) = 4\pi e^2/\epsilon_0 q$ is the Coulomb interaction in two dimensions; ϵ_0 is the background dielectric constant and e is the electron charge.

If the momentum dependence of the dipole matrix element r_γ is ignored, linear response theory gives for the optical susceptibility [52],

$$\chi(\omega) = 2|r_\gamma|^2 \sum_{12} P(12; \omega), \quad (1.2)$$

where ‘1’ stands for \vec{k}_1 and $P(12; \omega) = \langle\langle b_{-1}a_1; a_2^\dagger b_{-2}^\dagger \rangle\rangle_\omega$ denotes the Fourier transform of the retarded two-time eh pair propagator,

$$\begin{aligned} P(12; t - t') &= \langle\langle (b_{-1}a_1)(t); (a_2^\dagger b_{-2}^\dagger)(t') \rangle\rangle \\ &= -i\Theta(t - t') \langle\langle (b_{-1}a_1)(t), (a_2^\dagger b_{-2}^\dagger)(t') \rangle\rangle. \end{aligned} \quad (1.3)$$

Here, the thermodynamic average is defined by $\langle\langle \dots \rangle\rangle = Z^{-1} Tr(e^{-\beta\mathcal{H}} \dots)$, with $Z = Tr e^{-\beta\mathcal{H}}$ the partition function, and $\mathcal{H} = H - \mu_e N_e$ the grand-canonical Hamiltonian. The imaginary part of $\chi(\omega)$ determines, apart from a constant factor, the optical absorption $I_{abs}(\omega) \sim -Im\chi(\omega)$. The overall factor of two in front of the sum on the rhs of Eq. (1.2) comes from the spin (see also below).

Within the simple model (1.1) the calculation of the optical susceptibility $\chi(\omega)$ reduces therefore to a well-defined many-body problem: The calculation of the eh -pair propagator $P(12; \omega)$.

1.3 Cluster Mean Field Approximation

1.3.1 General Formalism

In this section we calculate the eh -pair propagator $P(12; \omega)$ in the low density regime, where bound states (exciton, trion) prevail. In this regime it is feasible to exclusively work with two-time correlation functions and to apply the cluster mean field approximation (CMFA).

Originally, the CMFA was developed to attack many-body problems in nuclear physics and in plasma physics. [53–55] It rearranges the equations of motion for two-time correlation functions into an hierarchy of Dyson-type equations and is closely related to the Mori memory function method, although the mathematical details are quite different. So far, the CMFA has been mostly used to calculate corrections to the random phase approximation and to investigate in-medium bound states, for which it is in fact tailor-made. For instance, it has been applied to describe deuteron-, triton, and α particle formation in expanding hot nuclear matter. [56–59]

Using CMFA techniques [53–55], we can derive a formally exact Dyson-type equation for the eh pair propagator $P(12; \omega)$. Keeping in mind that the spin configurations of the various correlation functions are fixed, because of the spin-independence of the Coulomb scattering, we suppress the spin variables and write:

$$[\omega + i\eta - \epsilon_c(1) - \epsilon_v(-1)]P(12; \omega) = N(1)\{\delta_{12} + \sum_3 [M^{st}(13) + \delta M(13; \omega)]P(32; \omega)\}, \quad (1.4)$$

with

$$M^{st}(12) = N^{-1}(1)N^{-1}(2)\langle\langle [b_{-1}a_1, V], a_2^\dagger b_{-2}^\dagger \rangle\rangle, \quad (1.5)$$

$$\delta M(12; \omega) = N^{-1}(1)N^{-1}(2)\langle\langle [b_{-1}a_1, V]; [V, a_2^\dagger b_{-2}^\dagger] \rangle\rangle_\omega, \quad (1.6)$$

$$N(1) = \langle\langle [b_{-1}a_1, a_1^\dagger b_{-1}^\dagger] \rangle\rangle, \quad (1.7)$$

where the operator V is defined in Eq. (1.1). The function $M(12; \omega) = M^{st}(12) + \delta M(12; \omega)$ has the meaning of an eh pair self-energy. Thus, Eq. (1.4) is of the Dyson-type. Applying the

CMFA technique to the correlation function $\delta M(12; \omega)$, and so on, we obtain an hierarchy of Dyson-type equations for correlation functions with an increasing number of particles. Clearly this set of equations has to be truncated and it is the truncation which restricts the CMFA to low CB electron densities.

We now describe in detail a truncation procedure which is valid in the limit of vanishing hole concentration and for not too high electron densities. [2, 3]

First, we consider the static part $M^{st}(12)$ of the eh pair self-energy. Working out the commutators and taking into account that the VB hole concentration vanishes, we find that $M^{st}(12)$ contains two terms: (i) the bare electron-hole interaction and the Hartree-Fock corrections to the single particle energies resulting from the finite density of the CB electrons. Assuming a possible jellium to compensate for the Hartree term, only Fock terms survive. In first order, the VB hole energy is then unchanged, while the correction to the CB electron energy is the usual Fock term, which we simply add to the bare dispersion: $\tilde{\epsilon}_c(1) = \epsilon_c(1) - \sum_2 v(1-2)f(2)$, with the CB electron distribution function $f(1) = \langle a_1^\dagger a_1 \rangle$.

The vanishing VB hole concentration implies $\langle b_1^\dagger b_1 \rangle = 0$, i.e., $N(1) = 1 - \langle a_1^\dagger a_1 \rangle = 1 - f(1) \equiv \bar{f}(1)$. The Dyson-type equation for $P(12; \omega)$ can therefore be written in a more familiar form:

$$[\omega + i\eta - Z(1)]P(12; \omega) = \bar{f}(1) \left\{ \delta_{12} - \sum_3 [v(1-3) - \delta M(13; \omega)]P(32; \omega) \right\}, \quad (1.8)$$

with $Z(1) = \tilde{\epsilon}_c(1) + \epsilon_v(-1)$. Note, without the dynamic part of the eh pair self-energy, i.e. for $\delta M(12; \omega) = 0$, Eq. (1.8) describes the propagation of the photo-induced eh pair in the presence of a *rigid* CB Fermi sea, which gives rise to the phase-space filling factor $\bar{f}(1)$ and the Fock correction to the CB electron energy.

The dynamical response of the CB electrons, i.e., the creation of virtual $e\bar{e}$ pairs, is encoded in the dynamical (resonating) part of the eh pair self-energy, which, for vanishing VB hole concentration, reduces to

$$\begin{aligned} \delta M(12; \omega) = & \frac{1}{\bar{f}(1)\bar{f}(2)} \sum_{4567} v(5)v(7) \left[R(1, 4, 4 + 5, 5 - 1 | 2, 6, 6 + 7, 7 - 2; \omega) \right. \\ & - R(1 - 5, 4, 4 - 5, -1 | 2, 6, 6 + 7, 7 - 2; \omega) \\ & - R(1, 4, 4 + 5, 5 - 1 | 2 - 7, 6, 6 - 7, -2; \omega) \\ & \left. + R(1 - 5, 4, 4 - 5, -1 | 2 - 7, 6, 6 - 7, -2; \omega) \right]. \end{aligned} \quad (1.9)$$

We defined an eightpoint $ee\bar{e}h$ function,

$$R(1234|5678; \omega) = \langle \langle b_4 a_3^\dagger a_2 a_1; a_5^\dagger a_6^\dagger a_7 b_8^\dagger \rangle \rangle_\omega, \quad (1.10)$$

for which, as indicated above, we again derive a Dyson-type equation, symbolically written as $R(\omega) = R^{(0)}(\omega) + R^{(0)}(\omega)[K^{st} + \delta K(\omega)]R(\omega)$. [Assuming that the spin configuration of the photogenerated eh pair is $(\uparrow\downarrow)$, the spin configuration of the $ee\bar{e}h$ cluster defining R is $(\uparrow\sigma\sigma\downarrow)$; σ is then summed over in Eq. (1.9).] In the low (CB electron) density limit, we need $\delta M(12; \omega)$ only to $o(n)$. Using an \bar{e} -line expansion² for $\delta M(12; \omega)$, we can show (i) that the term $\delta K(\omega)$ gives rise to $o(n^2)$ contributions to $\delta M(12; \omega)$ and is thus negligible at low densities, and (ii) that,

²This notation is borrowed from Brückners theory of effective interactions in nuclear matter. The \bar{e} -line expansion could be formalized, using a time-independent perturbation expansion with respect to the Hartree-Fock groundstate, and then systematically applied to construct an hierarchy of Dyson-type equations for two-time correlation functions with an increasing number of particles. We did not pursue it here because the leading equations, which are the only ones needed in the low density limit, can be obtained by inspection.

in leading order in the CB electron density, the eightpoint $ee\bar{e}h$ function appearing in Eq. (1.9) in fact factorizes into

$$R(1234 = 3 - 1 - 2|5678 = 7 - 5 - 6; \omega) = \delta_{3,7} f(3) G_3(12|56; \omega + \tilde{\epsilon}_c(3)), \quad (1.11)$$

with a sixpoint eeh function

$$G_5(12|34; \omega) = \langle\langle b_{5-1-2} a_2 a_1; a_3^\dagger a_4^\dagger b_{5-3-4}^\dagger \rangle\rangle_\omega, \quad (1.12)$$

which satisfies the Dyson-type equation

$$[\omega + i\eta - Z_5(12)] G_5(12|34; \omega) = I(12|34) + \sum_{67} \mathcal{V}_5(12|67) G_5(67|34; \omega), \quad (1.13)$$

with $\mathcal{V}_5(12|67) = [\bar{f}(1) - f(2)]v(7-2)\delta_{6,1+2-7} - \bar{f}(1)v(1-6)\delta_{7,2} - \bar{f}(2)v(2-7)\delta_{6,1}$ and $Z_5(12) = \tilde{\epsilon}_c(1) + \tilde{\epsilon}_c(2) + \epsilon_v(5-1-2)$. Note, the pair-wise interactions within the eeh cluster are independent of the cluster's center-of-mass momentum '5', as it should be.³ The groundstate of the eeh cluster has antiparallel CB electron spin. Focusing on the eeh groundstate, we fix therefore the spin configuration of the eeh cluster defining G to $(\uparrow\downarrow)$. For this spin configuration, $I(12|34) = \delta_{1,3}\delta_{2,4}\bar{f}(1)\bar{f}(2)$, and the spin eventually leads to the overall factor of two in Eq. (1.2) for the optical susceptibility.

Using the factorization (1.11) in (1.9), the dynamical part of the eh pair self-energy becomes

$$\begin{aligned} \delta M(12; \omega) = & \frac{1}{\bar{f}(1)\bar{f}(2)} \sum_{456} v(4)v(5)f(6) \left[G_6(1, 6-4|2, 6-5; \omega + \tilde{\epsilon}_c(6)) \right. \\ & - G_6(1+4, 6-4|2, 6-5; \omega + \tilde{\epsilon}_c(6)) \\ & - G_6(1, 6-4|5+2, 6-5; \omega + \tilde{\epsilon}_c(6)) \\ & \left. + G_6(1+4, 6-4|5+2, 6-5; \omega + \tilde{\epsilon}_c(6)) \right]. \end{aligned} \quad (1.14)$$

Thus, at low densities, the hierarchy of Dyson-type equations can be truncated at the level of a sixpoint eeh function and, in leading order in the CB electron density, the optically generated eh pair is only coupled to an eeh cluster. Note, similar to M^{st} , δM also contains corrections to the single particle energies. Inserting, e.g., the bare eeh six-point function $G^{(0)}$ into Eq. (1.14) generates four second order terms, two of which are vertex corrections, while the remaining two constitute the Born corrections to the VB hole and CB electron energies.

To account for the phase-space filling factors, it is convenient to define reduced Green functions,

$$P(12; \omega) = \sqrt{\bar{f}(1)\bar{f}(2)} \tilde{P}(12; \omega), \quad (1.15)$$

$$G_5(12|34; \omega) = \sqrt{\bar{f}(1)\bar{f}(2)\bar{f}(3)\bar{f}(4)} \tilde{G}_5(12|34; \omega). \quad (1.16)$$

The Dyson-type equation for the eh pair propagator can then be recast into

$$\sum_3 [(\omega + i\eta - Z(1))\delta_{1,3} - \tilde{M}^{st}(13) - \delta\tilde{M}(13; \omega)] \tilde{P}(32; \omega) = \delta_{1,2}, \quad (1.17)$$

³For the eeh six-point function $G_5(12|34)$ defined in Eq. (1.12), we adopted the convention to explicitly display the CB electron momenta as arguments, while the momentum of the VB hole is implicitly obtained by the center-of-mass momentum, given by the subscript, minus the sum of the two CB electron momenta. We use the same convention for the interaction vertex $\mathcal{V}_5(12|34)$ and thus have to keep track of the center-of-mass momentum.

with $\tilde{M}^{st}(13) = -\sqrt{\bar{f}(1)\bar{f}(3)}v(1-3)$ and $\delta\tilde{M}(13;\omega) = \sqrt{\bar{f}(1)\bar{f}(3)}\delta M(13;\omega)$. Note, the inhomogeneity contains no longer phase-space filling factors. Similarly, Eq. (1.13) leads to a Dyson-type equation for \tilde{G} , whose inhomogeneity consists only of Kronecker deltas:

$$[\omega + i\eta - Z_5(12)]\tilde{G}_5(12|34;\omega) = \delta_{1,3}\delta_{2,4} + \sum_{67} \tilde{\mathcal{V}}_5(12|67)\tilde{G}_5(67|34;\omega). \quad (1.18)$$

The interaction kernel is now given by

$$\tilde{\mathcal{V}}_5(12|34) = \sum_{\alpha} \tilde{\mathcal{V}}_5^{\alpha}(12|34), \quad (1.19)$$

where we introduced channel notation, as is customary in few-body physics. Channel $\alpha = \text{I}$ is the CB electron – CB electron channel (VB hole is free), whereas $\alpha = \text{II}, \text{III}$ denote the two VB hole – CB electron channels (one of the CB electrons is free, respectively). Explicitly, for $f^2 \ll 1$ the pair-wise interactions read

$$\tilde{\mathcal{V}}_5^{\text{I}}(12|34) = \sqrt{(\bar{f}(1) - f(2))(\bar{f}(3) - f(4))}v(1-3)\delta_{3+4,1+2} \quad (1.20)$$

$$\tilde{\mathcal{V}}_5^{\text{II}}(12|34) = -\sqrt{\bar{f}(1)\bar{f}(3)}v(1-3)\delta_{4,2}, \quad (1.21)$$

$$\tilde{\mathcal{V}}_5^{\text{III}}(12|34) = -\sqrt{\bar{f}(2)\bar{f}(4)}v(2-4)\delta_{1,3}. \quad (1.22)$$

The inhomogenous integral equation (1.18) can be formally solved using a spectral representation,

$$\tilde{G}_5(12|34;\omega) = \sum_n \frac{\Psi_{5n}(12)\Psi_{5n}^*(34)}{\omega + i\eta - \Omega_n(5)}, \quad (1.23)$$

with (ortho-normalized) *eeh* wavefunctions $\Psi_{5n}(12)$ satisfying an in-medium *eeh* Lippmann-Schwinger equation:

$$[\Omega_n(5) - Z_5(12)]\Psi_{5n}(12) - \sum_{34} \tilde{\mathcal{V}}_5(12|34)\Psi_{5n}(34) = 0. \quad (1.24)$$

The spectral representation is assumed to comprise bound and scattering states of the *eeh* cluster. Equations (1.23) and (1.16) enable us to express the dynamic part of the *eh* pair self-energy in an extremely compact form:

$$\delta\tilde{M}(34;\omega) = \sum_{5n} f(5) \frac{\Xi_{5n}(3)\Xi_{5n}^*(4)}{\omega + i\eta + \tilde{\epsilon}_c(5) - \Omega_n(5)}, \quad (1.25)$$

where we defined an vertex function $\Xi_{5n}(3)$. For low enough CB electron density, $f^2 \ll 1$ and the vertex function is given by

$$\Xi_{5n}(3) = \sum_7 v(5-7)\sqrt{\bar{f}(7)}[\Psi_{5n}(37) - \Psi_{5n}(7, 3+5-7)]. \quad (1.26)$$

All multiple-scattering events within the *eeh* cluster are now encoded in the (normalized and complete) momentum-space *eeh* wavefunction $\Psi_{5n}(37)$. Here, ‘n’ and ‘5’ depict, respectively, internal quantum numbers and the (center-of-mass) momentum of the (propagating) bound *eeh* cluster. Note again, the pair-wise interactions in Eq. (1.24) are independent of the center-of-mass momentum ‘5’ of the *eeh* cluster.

Once Equation (1.24) is solved, the dynamic part of the eh pair self-energy $\delta\tilde{M}(12;\omega)$ is fixed. For a given kernel, $[\omega + i\eta - Z(1)]\delta_{1,3} + \sqrt{\tilde{f}(1)\tilde{f}(3)}v(1-3) - \delta\tilde{M}(13;\omega)$, the Dyson-type equation (1.17) can be solved by standard means, e.g., by matrix inversion. [52] Note, the energy ω enters only as a parameter. We thus succeeded to reduce the calculation of the optical susceptibility, which in terms of the reduced eh propagator is given by $\chi(\omega) = 2|r_\gamma|^2 \sum_{12} \sqrt{\tilde{f}(1)\tilde{f}(2)}\tilde{P}(12;\omega)$, to the solution of an in-medium eeh Lippmann-Schwinger equation for an eeh wavefunction Ψ and the solution of a Dyson-type equation for the eh pair propagator \tilde{P} .

Before we specialize our approach to the extreme dilute limit, where a semi-analytical calculation of $\chi(\omega)$ is possible, a few more comments are in order. Equation (1.24) describes an eeh cluster embedded in a Hartree-Fock medium. The medium gives rise to phase-space filling factors and to corrections to the CB electron energy. The pair-wise interaction is however still mediated by the bare Coulomb potential, screening is not accounted for. This is not surprising, since the lowest order \bar{e} -line expansion allows only for one virtual $e\bar{e}$ pair, whereas screening requires an arbitrary number of $e\bar{e}$ pairs. Screening could be however phenomenologically included, without destroying the mathematical structure of the equations, by simply replacing the bare interaction $v(q)$ by the *statically* screened interaction $v_s(q) = v(q)/\epsilon(\omega = 0, q)$ with $\epsilon(\omega = 0, q)$ obtained, e.g., from Thomas-Fermi-Hückel theory. It is even conceivable to use a more sophisticated static screening model, based, e.g., on the static plasmon-pole approximation. [52] To be consistent, the single-particle energies ϵ_v and ϵ_c should then be modified by the Coulomb-hole and exchange self-energies. Thus, band-gap renormalization would be also included. A justification of this ad-hoc approach is however beyond the CMFA and has to be given by techniques based on multi-time correlation functions. In Section 1.5 a first attempt is made to address this issue from a more general point of view.

1.3.2 Exciton Representation

As a first step towards a semi-analytical calculation of the optical susceptibility $\chi(\omega)$, we rewrite in this subsection the integral equation for \tilde{P} [cf. Eq. (1.17)] into a set of linear algebraic equations. For energies ω close to the exciton groundstate energy E_X , the set of equations can be truncated and then easily solved. Medium corrections are still included. The approach is now however restricted to energies in the vicinity of the exciton resonance.

It is convenient to split the Dyson equation (1.17) into two coupled integral equations. Introducing a free eh pair propagator, $\tilde{P}^{(0)}(12;\omega) = \delta_{1,2}[\omega + i\eta - Z(1)]^{-1}$, Eq. (1.17) is equivalent to

$$\tilde{P}^{st}(12;\omega) = \tilde{P}^{(0)}(12;\omega) + \sum_{34} \tilde{P}^{(0)}(13;\omega)\tilde{M}^{st}(34)\tilde{P}^{st}(42;\omega), \quad (1.27)$$

$$\tilde{P}(12;\omega) = \tilde{P}^{st}(12;\omega) + \sum_{34} \tilde{P}^{st}(13;\omega)\delta\tilde{M}(34;\omega)\tilde{P}(42;\omega). \quad (1.28)$$

The first integral equation is readily solved using again a spectral representation,

$$\tilde{P}^{st}(12;\omega) = \sum_\nu \frac{\Phi_\nu(1)\Phi_\nu^*(2)}{\omega + i\eta - E_\nu}, \quad (1.29)$$

where the (normalized and complete) eh momentum-space wave functions $\Phi_\nu(1)$ obey an in-medium eh Lippmann-Schwinger equation (Wannier equation),

$$[E_\nu - Z(1)]\Phi_\nu(1) - \sum_2 \tilde{M}^{st}(12)\Phi_\nu(2) = 0. \quad (1.30)$$

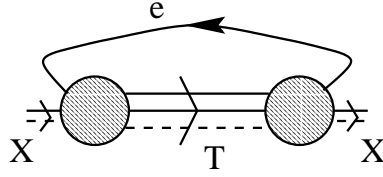


Figure 1.3: Graphical illustration (not a Feynman diagram) of the dynamical part of the exciton self-energy $\delta\tilde{M}_X(\omega)$. The full circles denote the exciton-trion coupling constants u_{5T}^X and $[u_{5T}^X]^*$.

The solutions of this equation can be obtained numerically using again, e.g., matrix inversion. [52] The lowest eigenstate is the exciton groundstate with energy E_X and wavefunction Φ_X .

To approximately solve for $\omega \approx E_X$ the second integral equation (1.28), we employ a simple approximation scheme based on the “exciton representation”, i.e., on a bilinear expansion of \tilde{P} in terms of the solutions of Eq. (1.30). Writing $\tilde{P}(12; \omega) = \sum_{\nu, \mu} \tilde{P}_{\nu\mu}(\omega) \Phi_\nu(1) \Phi_\mu(2)^*$, we transform Eq. (1.28) into an infinite set of algebraic equations for the expansion coefficients,

$$[\omega + i\eta - E_\nu] \tilde{P}_{\nu\mu}(\omega) = \delta_{\nu, \mu} + \sum_{\lambda} \delta\tilde{M}_{\nu\lambda}(\omega) \tilde{P}_{\lambda\mu}(\omega), \quad (1.31)$$

where

$$\delta\tilde{M}_{\nu\lambda}(\omega) = \sum_{5n} f(5) \frac{u_{5n}^\nu [u_{5n}^\lambda]^*}{\omega + i\eta + \tilde{\epsilon}_c(5) - \Omega_n(5)}, \quad (1.32)$$

and $u_{5n}^\nu = \sum_1 \Phi_\nu^*(1) \Xi_{5n}(1)$. For energies ω close to the exciton groundstate energy E_X , we expect the exciton and trion groundstates to be dominant. Thus, we solve Eq. (1.31) by employing *one-pole approximations*: First, we keep only the term corresponding to the exciton ground state $\nu = X$ and neglect the coupling to excited exciton states $\nu \neq X$. Next, assuming that the main modification of the exciton ground state comes from the groundstate of the eeh cluster, i.e., from the trion denoted by $n = T$, we restrict the sum in Eq. (1.32) to the term $n = T$.

Let us emphasize, the one-pole approximations are by no means mandatory and various improvements are possible. For example, if the exciton binding energy is small, i.e., if the exciton groundstate is not well separated from the first excited state, the first excited state has to be kept. This gives rise to two coupled algebraic equations (two-pole approximation). It is even conceivable to treat all eh scattering states in a similar way, introducing an “effective” excited eh state, which carries the spectral weight of the whole continuum. Excited trion states (eeh scattering states) can be also taken into account by simply extending the sum in Eq. (1.32) to the respective states or by introducing an “effective” eeh continuum state. The theoretical work by Esser and coworkers [41] indicates that eeh scattering states are indeed necessary to obtain good quantitative agreement between theory and experiment.

For the purpose of demonstration, however, we neglect here scattering states and stick to the simple one-pole approximation described above. The optical susceptibility in the vicinity of the exciton resonance is then given by

$$\chi(\omega) \simeq \frac{2|s_X|^2}{\omega + i\eta - E_X - \delta\tilde{M}_X(\omega)}, \quad (1.33)$$

with an exciton self-energy (see Fig. 1.3)

$$\delta\tilde{M}_X(\omega) = \sum_5 f(5) \frac{|u_{5T}^X|^2}{\omega + i\eta + \tilde{\epsilon}_c(5) - \Omega_T(5)}, \quad (1.34)$$

and an exciton oscillator strength $s_X = r_\gamma \sum_1 \sqrt{\bar{f}(1)} \Phi_X(1)$. Note, the one-pole approximation is conceptually close to the T-matrix model considered by Suris and coworkers in their analysis of absorption and reflection spectra of modulation-doped quantum wells. [42]

Equation (1.33) gives the optical susceptibility $\chi(\omega)$ for $\omega \approx E_X$. Lowest order medium corrections such as phase-space filling and Fock corrections to the single particle energies are included.⁴ The one-pole approximation restricts however Eq. (1.33) to low enough CB electron densities, where bound states are well separated from continuum states.

1.3.3 Extreme Dilute Limit

We expect Eq. (1.33) to be valid only for low enough CB electron densities, where the exciton groundstate is well defined and separated from the eh continuum states. In leading order, CB electrons do then neither modify the wavefunction nor the energy of bound states (i.e. exciton and trion). In the following, we ignore therefore Pauli blocking and the Fock correction to the CB electron energy, i.e., we set $\bar{f} \rightarrow 1$ and $\tilde{\epsilon}_c \rightarrow \epsilon_c$. It is then possible to obtain the groundstate of Eq. (1.30) analytically and the groundstate of Eq. (1.24) variationally. In this regime, CB electrons are moreover non-degenerate and the Fermi function in Eq. (1.34) can be replaced by a Boltzmann function parameterized by the CB electron density n . Even this simple approach is beyond most of the current theoretical investigations concerned with optical properties of weakly doped quantum wells. An exception is the work of Esser and coworkers. [40, 41]

Measuring energies in units of the 2D exciton binding energy $4R$ (R is the 3D exciton Rydberg) and length in units of the 3D Bohr radius a_B , we define $\tilde{\chi}(\tilde{\omega}) \equiv \chi(4R\tilde{\omega} + E_g)/4R$, with $\tilde{\omega} = [\omega - E_g]/4R$, and rewrite the optical susceptibility into dimensionless form⁵

$$\tilde{\chi}(\tilde{\omega}) = \frac{|s_X|^2}{8R^2} \frac{1}{\tilde{\omega} + i\tilde{\eta} + 1 - \delta\tilde{M}_X(\tilde{\omega})}. \quad (1.35)$$

Here, $\tilde{\eta} = \eta/4R$ and

$$\delta\tilde{M}_X(\tilde{\omega}) \equiv \delta M_X(4R\tilde{\omega} + E_g)/4R \quad (1.36)$$

$$= \tilde{\beta} \frac{M_T}{M_X} (na_B^2) |u_T^X|^2 I(\tilde{\omega}), \quad (1.37)$$

where $\tilde{\beta} = 4\beta R$, $M_X = m_e + m_h$, and $M_T = 2m_e + m_h$ are, respectively, the thermal energy measured in units of $4R$, the exciton mass, and the trion mass. The exponential integral,

$$I(\tilde{\omega}) = \int_0^\infty dy \frac{e^{-\tilde{\beta} \frac{M_T}{M_X} y}}{\tilde{\omega} + i\tilde{\eta} - \tilde{\epsilon}_T + y}, \quad (1.38)$$

where $\tilde{\epsilon}_T = [\Omega_T(0) - 2E_g]/4R$ is the energy of a trion at rest, i.e., the *internal* trion energy, which is the binding energy of *two* CB electrons to one VB hole. The dimensionless exciton-trion coupling constant u_T^X finally is given by an integral involving the wave function of the trion groundstate, the Coulomb interaction, and the wavefunction of the exciton groundstate (see below). For simplicity we neglected the weak dependence of u_T^X on the (center-of-mass) momentum of the trion. Note, for vanishing CB electron density n , $\delta\tilde{M}_X(\tilde{\omega}) \rightarrow 0$ and $\tilde{\chi}(\tilde{\omega})$ describes a single exciton resonance at $\tilde{\omega} = -1$.

⁴If one subscribes to the ad-hoc procedure mentioned in the previous section, static screening could be also accounted for.

⁵Notice the different usage of the tilde symbol in this subsection. Because medium corrections are now ignored, no confusion with the reduced Green functions of the previous subsection should result.

To obtain the exciton-trion coupling constant u_T^X and the internal trion energy $\tilde{\epsilon}_T$, we employ the variational technique originally used by Stébé and coworkers [35, 36] to calculate various properties of an isolated trion. For that purpose, we set $E_T = \Omega_T - 2E_g$, transform Eq. (1.24) to configuration space⁶

$$[T + V]\Psi_T(\vec{r}_{e1}\vec{r}_{e2}\vec{r}_h) = E_T\Psi_T(\vec{r}_{e1}\vec{r}_{e2}\vec{r}_h), \quad (1.39)$$

with kinetic and potential energies ($\hbar = 1$),

$$T = -\frac{1}{2m_e}(\Delta_{e1} + \Delta_{e2}) - \frac{1}{2m_h}\Delta_h,$$

$$V = -\frac{e^2}{\epsilon_0}\left(\frac{1}{|\vec{r}_{e1} - \vec{r}_h|} + \frac{1}{|\vec{r}_{e2} - \vec{r}_h|} - \frac{1}{|\vec{r}_{e1} - \vec{r}_{e2}|}\right),$$

separate away the center-of-mass motion, which is simply a plane wave, and make a variational Hylleraas Ansatz for the internal part of the trion groundstate wavefunction,

$$\Psi_T(s, t, u) = \Phi(ks, kt, ku), \quad (1.40)$$

with

$$\Phi(s, t, u) = \sum_{l,n,m} c_{lnm}|lnm\rangle, \quad (1.41)$$

where $|lnm\rangle = e^{-\frac{\sigma}{2}s}t^l u^m$ and u, s , and t are Hylleraas coordinates for the internal motion of the eeh cluster. The scale factor k can be interpreted as the VB hole's effective charge; it describes the fact that each CB electron is partially screened from the VB hole by the other CB electron. Note, since the trion groundstate is a singlet, $\Phi(s, t, u)$ has to be an even function in t , that is, m has to be even. The expansion coefficients c_{lnm} and the effective charge k are determined by the Ritz variational principle, i.e., by minimizing the energy functional $E[\Psi_T] = \langle\Psi_T|T+V|\Psi_T\rangle/\langle\Psi_T|\Psi_T\rangle$. The variation yields an eigenvalue problem (for the effective charge k) which is then iteratively solved. The largest eigenvalue can be related to the trion energy E_T ($\rightarrow \tilde{\epsilon}_T$), while the associated eigenfunction can be used to obtain the expansion coefficients c_{lnm} for the trion wavefunction. The details of the calculation are given in the Appendix. With the Hylleraas variational function Ψ_T , which we normalize to one, the exciton-trion coupling constant becomes

$$u_T^X = \sqrt{\frac{2}{N\pi}} \frac{1}{k(1+\sigma)} \int_0^\infty ds \int_0^s du \int_0^u dt \frac{2\pi(s^2 - t^2)u}{\sqrt{(u^2 - t^2)(s^2 - u^2)}} e^{-\frac{s+t}{k(1+\sigma)}} \left[\frac{2}{s-t} - \frac{1}{u}\right] \Phi(s, t, u), \quad (1.42)$$

where N is the norm of Φ and $\sigma = m_e/m_h$.

Before we turn to the discussion of numerical results, we emphasize that we could have obtained more general expressions for the optical susceptibility had we solved the full in-medium few-body problems (1.24) and (1.30). Neglecting medium effects turns the in-medium few-body problems simply into “vacuum few-body problems” which can be easily solved. The CMFA concept itself is of course more general.

⁶To solve the eeh problem, we shall use atomic units, which are, however, at the end of the calculation, translated into the excitonic units adopted in this section.

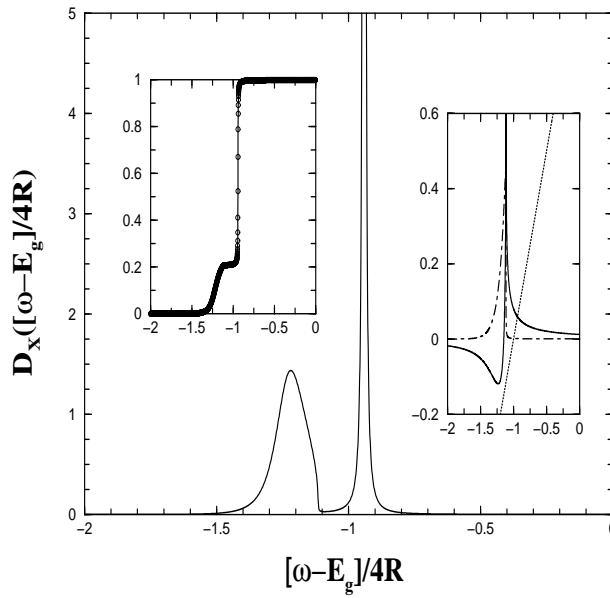


Figure 1.4: The spectral function $D_X(\tilde{\omega})$ for $na_B^2 = 0.008$ and $4R\beta = 10$. The effective mass ratio $\sigma = 0.146$, corresponding to GaAs, and $\tilde{\eta} = 0.001$. The left inset depicts the integrated spectral weight $C_X(\tilde{\omega})$, whereas the right inset displays $\tilde{\Gamma}_X(\tilde{\omega})$ (dot-dashed line) and $\tilde{\Delta}_X(\tilde{\omega})$ (solid line). The energy for which $\tilde{\Delta}_X(\tilde{\omega})$ crosses $\tilde{\omega} + 1$ (dotted line) defines the exciton line at $\tilde{\omega} = -0.94$.

1.4 Numerical Results [3]

We present numerical results obtained in the extreme dilute limit, where medium corrections are negligible and the non-degenerate CB electrons only provide a reservoir for bound state formation. The assumption of non-degeneracy seriously constrains the temperature and density range in which our theory is now applicable. Specifically, using the well-known formula, $\beta\mu_e = \log[\exp(\pi n\beta/m_e) - 1]$, which relates the chemical potential μ_e of a 2D gas of free electrons (with mass m_e) to its density n , we estimate $\tilde{\beta}(na_B^2) < 1$, i.e. depending on the density, the temperature has to be sufficiently high. We should apply Eq. (1.35) therefore only to densities and temperatures for which this inequality is satisfied.

Using a 2D 22-term Hylleraas wavefunction (see Appendix), we calculated in Ref. [2, 3] the optical absorption along the lines explained in the previous subsections. For a mass ratio $\sigma = m_e/m_h = 0.146$, corresponding to GaAs, we found $u_T^X \simeq 1.0896$ and $\tilde{\epsilon}_T = -1.1151$. The binding energy (in units of $4R$) for *one* electron is therefore $\tilde{W}_T = 0.1151$ in agreement with the binding energies obtained by other means. [38] The vertex u_T^X was obtained from Eq. (1.42) by Gaussian quadrature.

The optical absorption in the vicinity of the exciton resonance is related to the exciton spectral function

$$D_X(\tilde{\omega}) = -Im\tilde{\chi}(\tilde{\omega}), \quad (1.43)$$

shown in Fig. 1.4 for $na_B^2 = 0.008$ and $4R\beta = 10$. The overall structure is in qualitative agreement with experiments, despite the simplicity of the model and the rather crude approximations.

Below a narrow peak at $\tilde{\omega} = -0.94$, we notice a broad absorption band characterized by a sharp high energy edge at $\tilde{\omega} = -1.1151$ and a low-energy tail. To facilitate a microscopic understanding of the absorption features, we plot in the right inset of Fig. 1.4 real and imaginary

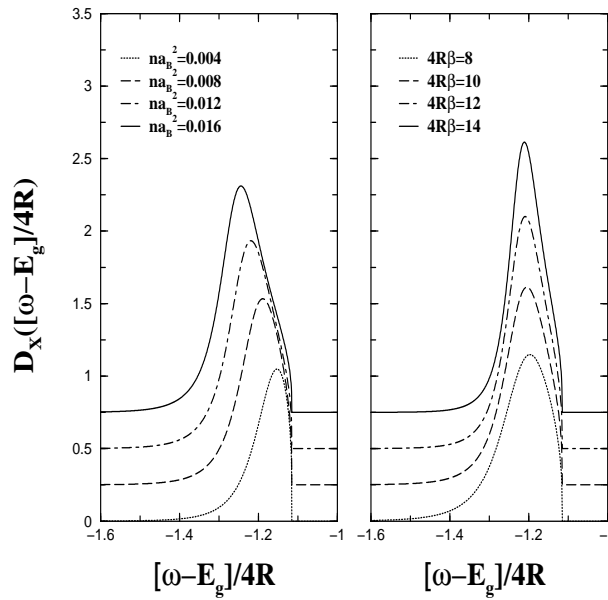


Figure 1.5: The left and right panels show, respectively, trion absorption bands as a function of CB electron density for a fixed temperature $4R\beta = 10$ and as a function of temperature for a fixed CB electron density $na_B^2 = 0.01$. The quasi-exciton line located at $\tilde{\omega} > -1$ is not shown. The effective mass ratio $\sigma = 0.146$, corresponding to GaAs, and $\tilde{\eta} = 0$. For clarity absorption bands corresponding to different parameters are artificially shifted along the vertical axis.

parts of the exciton self-energy: $\delta\tilde{M}_X(\tilde{\omega}) = \tilde{\Delta}_X(\tilde{\omega}) - i\tilde{\Gamma}_X(\tilde{\omega})$. The narrow peak is obviously a consequence of the pole of the spectral function $D_X(\tilde{\omega})$ at $\tilde{\omega} = -0.94 \equiv \tilde{\epsilon}_X$, where $\tilde{\epsilon}_X$ is the energy which simultaneously satisfies $\tilde{\Delta}_X(\tilde{\epsilon}_X) = \tilde{\epsilon}_X + 1$ and $\tilde{\Gamma}_X(\tilde{\epsilon}_X) = 0$. A pole in a spectral function is usually interpreted as a quasi-particle. [61] Accordingly, we attribute the narrow peak in Fig. 1.4 to a *quasi-exciton*. We also see, the peak has actually no width. Because of the one-pole approximation to the *eeh* problem, $\tilde{\Gamma}_X(\tilde{\epsilon}_X) = 0$. Had we included *eeh* scattering states, $\tilde{\Gamma}_X(\tilde{\epsilon}_X)$ would be finite and the exciton line would have a width.

The origin of the broad absorption band, in contrast, is the itinerant trion. The sharp high energy edge, for example, comes from a resonance of $\tilde{\Delta}_X(\tilde{\omega})$ at the trion formation energy $\tilde{\epsilon}_T = -1.1151$, i.e. the high energy edge of the band corresponds to a trion with momentum zero. The low energy tail, on the other hand, is due to trion states with finite momenta. Note, due to the large value of $\tilde{\Gamma}_X(\tilde{\omega})$ in the vicinity of the edge, trion states with small momentum are significantly damped. Accordingly, the maximum of the absorption due to the trion is inside the band, corresponding to the creation of a trion with finite momentum. The maximum coincides with the high energy edge only for very low CB electron densities, in agreement with the calculations of Ref. [37]. The spectral weight of the band, however, is then also very small (see Figs. 1.5 and 1.6).

To analyze the spectral weights associated with, respectively, the trion absorption band and the quasi-exciton line, we show in the left inset of Fig. 1.4 the integrated spectral weight up to an energy $\tilde{\omega}$ defined in terms of the cumulant $C_X(\tilde{\omega}) = \int_{-\infty}^{\tilde{\omega}} d\tilde{E} D_X(\tilde{E})$. As can be seen, the integrated spectral weight of the trion absorption band corresponds to the plateau value just below $\tilde{\omega} = -1$, i.e. $f_T = C_X(-1)$. The inset also demonstrates that the total spectral weight adds up to one. Accordingly, the spectral weight of the quasi-exciton is given by $f_X = 1 - f_T$. This “sum rule” is a consequence of the one-pole approximations which distribute the spectral

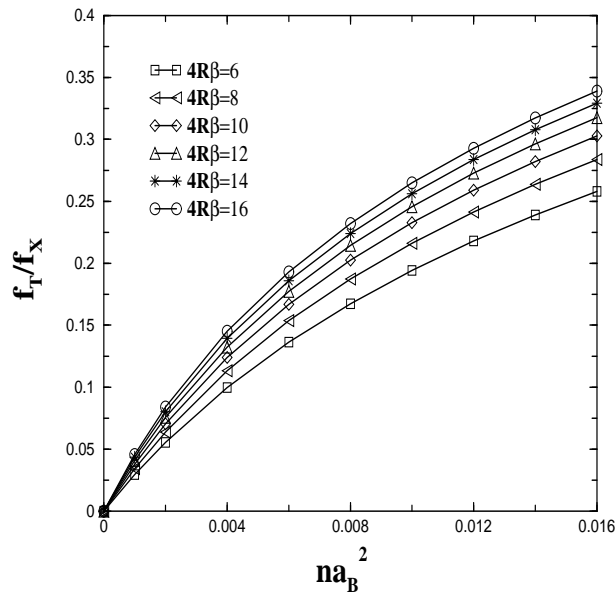


Figure 1.6: The ratio of the integrated spectral weights $\frac{f_T}{f_X}$ as a function of CB electron density and temperature. The effective mass ratio $\sigma = 0.146$, corresponding to GaAs, and $\tilde{\eta} = 0$.

weight of the original photo-induced eh pair, which is normalized to one, between the exciton line and the trion band.⁷ If scattering states had been taken into account, they would have also carried spectral weight, i.e., in a complete theory, the combined spectral weight of trion band and exciton line has to be of course less than one.

Our exploratory calculation neglected scattering states, because, at low enough CB electron densities, in particular, within the range of validity of our *numerical* results, scattering states are expected to carry almost no spectral weight. Indeed, the more refined calculations of Esser and coworkers [41] seem to verify this assessment. The spectral weight, which can be associated with scattering states, is less than 5% of the spectral weight of the exciton groundstate. As already pointed out, scattering states are however important to determine the shape and width of the exciton line. [41]

We now present a quantitative investigation of the integrated spectral weights as a function of CB electron density and temperature. To that end, we calculated for various trion absorption bands the integrated spectral weights $f_T = C_X(-1)$ and deduced from the “sum rule”, $f_X = 1 - f_T$, the corresponding spectral weights for the quasi-exciton. Figure 1.5 depicts typical trion absorption bands used to obtain the data shown in Fig. 1.6. As expected, for fixed temperature, f_T/f_X grows with CB electron density because the probability for two CB electrons to be close enough to a VB hole to form a trion increases. The density dependence is not linear, however. Instead, we observe an initial fast increase and then a pronounced slowing down indicating the subtle interplay between trion and quasi-exciton oscillator strength. At higher CB electron densities, we anticipate an even more complicated behavior. The ratio f_T/f_X should show non-trivial features especially for densities close to a critical density, where the trion is expected to break up into an exciton and a free CB electron. For fixed CB electron density, f_T/f_X increases with decreasing temperature. The increase also tends to saturate.

The numerical results are in qualitative agreement with experimental data, despite the sim-

⁷At this level of sophistication, the lineshape in the vicinity of the exciton resonance is thus a consequence of the fragmentation of the photo-induced eh pair into a quasi-exciton and a trion.

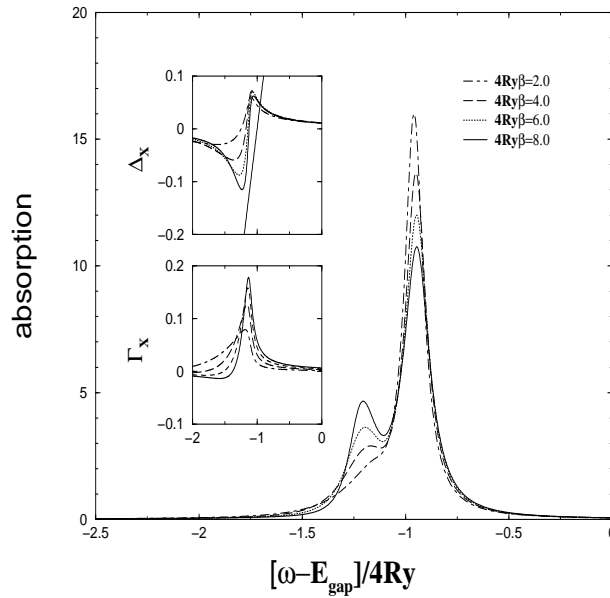


Figure 1.7: Optical absorption, i.e. the spectral function $D_X(\tilde{\omega})$ with $\tilde{\omega} = (\omega - E_g)/4Ry$, as a function of temperature for fixed electron density $na_B^2 = 0.02$. The effective mass ratio $\sigma = 0.5$, corresponding to CdTe; Ry is the CdTe Rydberg. To phenomenologically account for ignored scattering processes, we set the parameter $\tilde{\eta}$ artificially to the rather large value 0.05. The two insets show the corresponding real ($\tilde{\Delta}_X$) and imaginary ($\tilde{\Gamma}_X$) parts of the exciton self-energy δM_X . The dashed straight line in the inset for $\tilde{\Delta}_X$ is the function $\tilde{\omega} + 1$.

plicity of the quantum well model and the neglect of scattering processes due to impurities and phonons. Our theoretical approach can be brought more into accordance with observed lineshapes, if we use the parameter $\tilde{\eta}$ to simulate ignored scattering processes. The optical absorption in the vicinity of the exciton resonance acquires then a shape as shown in Fig. 1.7 for the particular case of $na_B^2 = 0.02$, $\tilde{\eta} = 0.05$, and an effective mass ratio $\sigma = 0.5$, corresponding to CdTe. Figure 1.7 should be compared with Fig. 1.2, in particular with panel (b), although the experimental conditions ($na_B^2 \approx 0.03$ and $\beta \approx 250$, $\tilde{\beta}(na_B^2) \approx 7.5$) are admittedly somewhat outside the range of applicability of what we call “extreme dilute limit”; the temperature is too low for the electrons to be non-degenerate. Nevertheless, the (qualitative) agreement is encouraging and, if nothing else, the calculation at least verifies the experimental observation that with decreasing temperature trion absorption increases on the expense of the exciton absorption.

In most cases, however, typical experimental conditions are clearly beyond the extreme dilute limit.⁸ Doping concentrations are usually too high and the effect of the medium on bound state wavefunctions and energies cannot be ignored. As long as bound states are stable, the optical susceptibility in the vicinity of the exciton resonance is given by Eq. (1.33), furnished however with the solutions of the full in-medium eh and eeh Lippmann-Schwinger equations. To obtain the correct shape of the exciton line it is moreover necessary to include in the calculation of the exciton self-energy (1.34) eeh scattering states. At least the two-body break-up into an exciton and a CB electron should be incorporated. The solution of the in-medium eeh problem is computationally challenging. The transformation to configuration space is no longer advantageous because the phase-space filling factors yield a non-local potential. Numerically manageable

⁸With respect to the experimental data shown in Fig. 1.2, the extreme dilute limit would be applicable to data between panel (a) and (b) which are unfortunately not available.

equations in momentum space are obtained by rewriting the in-medium *eeh* Lippmann-Schwinger equation (1.24) in Faddeev or Alt-Grassberger-Sandhas (AGS) form. [62] The AGS approach is moreover well suited for the calculation of *eeh* scattering amplitudes.

1.5 Beyond the Cluster Mean Field Approximation: An Outlook

1.5.1 The Problem of the Fermi-Edge Signature

In the previous section we presented a detailed description of the CMFA for the optical response of a weakly n-doped idealized semiconductor quantum well. The CMFA, tailor-made for low CB electron densities, reduces the calculation of the optical susceptibility to the solution of the Lippmann-Schwinger equations for, respectively, an *eh* and an *eeh* cluster, embedded in a Hartree-Fock medium. The medium is therefore static. This is of course an approximation. In general, the medium has its own dynamics. Screening of the interaction, e.g., is a dynamic process. Moreover, beyond the first order Hartree-Fock corrections, single-particle self-energies are also energy dependent. Thus, a complete description of the optical response has to incorporate vertex (screening) and single particle self-energy corrections.

Closely connected with vertex and single-particle self-energy corrections is the Fermi-edge signature at high densities. Physically, the particular absorption or emission lineshape depends on the interplay of two effects: (i) The final state interaction between the photo-excited VB hole and CB electron and (ii) the so called “orthogonality catastrophe” discussed by Anderson [63] and Hopfield. [64] At finite temperature the “orthogonality catastrophe” is not an issue and final state interactions dominate. We focus therefore on the final state interactions.⁹

If the Fermi sea is assumed to be rigid, the photo-generated CB electron and VB hole form a bound state: the Mahan exciton, in contrast to the atomic exciton, formed at vanishing CB electron density. The Mahan exciton gives rise to a singularity in the optical absorption at $\omega = E_g + (1 + m_e/m_h)\mu_e - \epsilon_b$, where ϵ_b is the binding energy of the Mahan exciton. If the constraint of a rigid Fermi sea is relaxed, the Mahan exciton interacts with $e\bar{e}$ excitations of the CB electron Fermi sea. As a consequence, the bound state broadens and shifts, producing a power-law dependence of the optical absorption at the Fermi-edge. [14] The broadening turns out to be particularly large for small VB hole masses and/or high temperatures. The singularity is then completely wiped out.

Similar to the theoretical modeling of core level X-ray spectra in metals [18–20], two strategies have been employed to calculate the power-law dependence of the optical absorption/emission in doped semiconductors. The first approach goes back to the seminal work by Combescot and Nozières (CN approach) [16] and maps the original many-body problem on to an effective one-body problem. Whereas the second approach due originally to Mahan [14], is a genuine many-body treatment based on the diagrammatic calculation of the *eh* propagator, taking not only parallel (rigid CB electron Fermi sea) but also anti-parallel *eh* (dynamic response of the CB electron Fermi sea) channels into account. Shortly after Mahan’s seminal work, Gavoret, Nozières, Roulet, and Combescot (GNRC approach) [15] systematized the many-body approach within a parquet analysis of the *eh* interaction vertex.

The one-body approach, in one form or another, has been extensively applied to doped quantum wells. [23–27] For the one-body approach to work, it is however necessary to either neglect the interaction between CB electrons or to treat it in a mean field approximation. The latter is generally expected to be sufficient at high doping concentrations, although the Fermi liquid

⁹Formally, the “orthogonality catastrophe” is remedied by the VB hole self-energy. A description of the final state interactions which obeys Ward identities should therefore automatically cure the “orthogonality catastrophe”.

$$\begin{aligned}
-\beta \Sigma_{e,\sigma}(\mathbf{k}) &= \text{Diagram 1} + \text{Diagram 2} + \text{Diagram 3} \quad (\text{a}) \\
-\beta \Sigma_{h,\sigma}(\mathbf{k}) &= \text{Diagram 4} \quad (\text{b})
\end{aligned}$$

Figure 1.8: CB electron (a) and VB hole (b) self-energy at vanishing VB hole density, expressed in terms of the bare (empty box) and full (dashed box) vertices. The internal lines are fully dressed CB electron (full line) and VB hole (dashed line) propagators. The vertices are direct vertices in the particle-particle channel, with the incoming lines attached to the bottom and the lower left (right) leg connected to the upper left (right) leg (see also Fig. 1.9).

arguments usually invoked might not be straightforwardly applicable to low-dimensional systems such as doped quantum wells. At low doping concentration, however, the model of non-interacting CB electrons must fail. The clear signature of charged excitons at low-to-intermediate densities demonstrates that the interaction between CB electrons cannot be neglected or treated in a mean field manner. Otherwise the trion wavefunction and energy would be completely wrong. The low-density regime is therefore beyond the one-body approach.

A theoretical examination of the optical response of a doped quantum well, which attempts to cover the whole doping concentration range, has to avoid the mapping on to an effective one-body model. In this subsection, we adopt therefore the many-body point of view and extend the GNRC approach to the two-band model (1.1). Our goal is to derive, within the framework of a two-band parquet analysis of the ee and eh interaction vertices, a minimal set of equations, which gives the Fermi-edge signatures at high densities and the double-peak structures due to charged and neutral excitons at low densities. Within the two-band parquet analysis, the two eh channels (parallel and antiparallel) as well as the screening of the Coulomb interaction are automatically included. The main task is to incorporate eeh correlations. This section should be understood as an exploration into an almost impassable terrain (“parquet plus bound states”). The proposed equations have to be further analyzed and perhaps simplified before a numerical solution can be attempted.

In contrast to the previous section we now employ multi-time correlation functions. Four-point functions depend now on three time variables, or, in energy space, on three energies. We work in Matsubara space and use a four-vector notation $k = (\vec{k}, i\omega_n)$ and define $\Sigma_k = -(1/\beta) \sum_{i\omega_n, \vec{k}}$. An exact expression for the (linear) optical susceptibility is given by (factor two comes from the spin)

$$\begin{aligned}
\chi(q) &= 2|r_\gamma|^2 \sum_k G_\uparrow(k) \mathcal{G}_\downarrow(q-k) \\
&\quad + 2|r_\gamma|^2 \sum_{k,r} G_\uparrow(k) \mathcal{G}_\downarrow(q-k) (\Gamma_{eh})_{\uparrow\downarrow}(k,r;q) G_\uparrow(r) \mathcal{G}_\downarrow(q-r), \quad (1.44)
\end{aligned}$$

where the function $(\Gamma_{eh})_{\uparrow\downarrow}$ is the connected part (viz. interaction vertex) of the (optically active) eh four-point function and $G_\sigma(r)$ and $\mathcal{G}_\sigma(r)$ are the fully dressed electron and hole propagators,

respectively. At vanishing VB hole density, the electron self-energy,

$$\Sigma_{e,\sigma}(k) = \Sigma_{e,\sigma}^d(k) + \Sigma_{e,\sigma}^x(k) , \quad (1.45)$$

contains a direct part,

$$\Sigma_{e,\sigma}^d(k) = - \sum_{r,\sigma'} (\Gamma_{ee}GG \star \Gamma_{ee}^{(0)})_{\sigma,\sigma'}(k, k; r) G_{\sigma'}(r - k) , \quad (1.46)$$

where we neglected the Hartree term, which we assume to be compensated by a positive jellium, and an exchange part,

$$\Sigma_{e,\sigma}^x(k) = \sum_r (\Gamma_{ee}^{(0)})_{\sigma,\sigma}(k, r - k; r) G_{\sigma}(r - k) \quad (1.47)$$

$$+ \sum_r (\Gamma_{ee}GG \star \Gamma_{ee}^{(0)})_{\sigma,\sigma}(k, r - k; r) G_{\sigma}(r - k) . \quad (1.48)$$

The hole self-energy contains at vanishing VB hole density only a direct term

$$\Sigma_{h,\sigma}(k) = \Sigma_{h,\sigma}^d(k) = - \sum_{r,\sigma'} (\Gamma_{eh}GG \star \Gamma_{eh}^{(0)})_{\sigma,\sigma'}(k, k; r) G_{\sigma'}(r - k) . \quad (1.49)$$

In Eqs. (1.46) – (1.49) we anticipated the channel notation introduced below. The operation \star denotes here the chaining operation which generates either electron-electron or electron-hole ladders (see Fig. 1.8). The functions $(\Gamma_{ee})_{\sigma,\tau}$ and $(\Gamma_{eh})_{\sigma,\tau}$ denote, respectively, the fully dressed ee and eh interaction. The bare interactions are given by $(\Gamma_{ee}^{(0)})_{\sigma,\tau} = (\Gamma_{eh}^{(0)})_{\sigma,\tau} = v$, with v the Coulomb potential in two dimensions. Equation (1.44) gives the optical susceptibility for complex (Matsubara) energies. The optical absorption has to be obtained via analytical continuation in the usual way. Symbolically, $I_{abs}(\omega) \sim -\text{Im}\chi(\vec{q} = 0, i\nu_m \rightarrow \omega - \mu_e + i\eta)$, but technically the analytical continuation has to be performed numerically, e.g., with a Padé approximant.

From Eqs. (1.44) – (1.49) it is clear, the fully dressed interaction vertices $(\Gamma_{eh})_{\sigma,\tau}$ and $(\Gamma_{ee})_{\sigma,\tau}$ must be the central objects of any microscopic calculation of the optical susceptibility. In this section we shall discuss various approximations for $(\Gamma_{ee})_{\sigma,\tau}$ and $(\Gamma_{eh})_{\sigma,\tau}$. We do not always write the spin index, assuming then that the approximations are implemented in accordance with the restrictions enforced by the spin. Moreover to obtain a closed set of equations, we always assume that the full interaction vertices in the single-particle self-energies are replaced by the approximate ones.¹⁰

1.5.2 Parquet Analysis

The parquet analysis is a sophisticated diagrammatic method to perform vertex renormalizations of Feynman diagrams. As a result, one obtains the *parquet equations*, which are for the interaction vertex what the Dyson equation is for the Green function. The Dyson equation determines the fully dressed, one-line reducible two-point function (Green function) in terms of a one-line irreducible two-point function (self-energy). Similarly, the parquet equations express the fully dressed, two-line reducible connected¹¹ four-point function (interaction vertex) in terms of a two-line irreducible four-point function. Approximations are then made in the two-line irreducible

¹⁰This raises deep questions about conservation laws, which, at this point, we do not address. We tacitly assume that, in principle, the approximations we are going to develop can be made conserving.

¹¹We consider only connected four-point functions and suppress the label “connected” from now on.

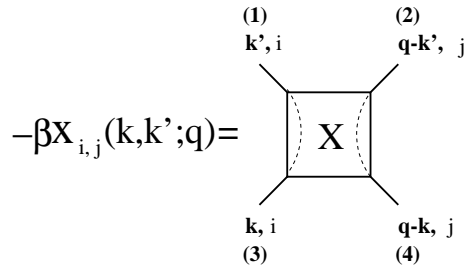


Figure 1.9: Generic four point function. By convention, we work exclusively with direct diagrams in the particle-particle channel, with incoming lines at the bottom. As indicated by the dashed lines, the left (right) lower leg is always connected to the left (right) upper leg. Since the direction of the lines is fixed, we suppress arrows giving this information. For the definition of the three channels 12, 13, and 14, respectively, it is convenient to imagine the labeling of the four external legs as shown in parentheses. The labels i and j enclose the band index (e, h) and the spin index (\uparrow, \downarrow). The four momentum q denotes the “center-of-mass” variables, whereas the four-momentum k (k') specifies the left incoming (outgoing) particle.

block. The diagrammatic method works from the start with one-line irreducible diagrams. Propagators are thus assumed to be fully dressed and to satisfy the Dyson equation. A closed set of equations is then trivially obtained, if the self-energy in the Dyson equation is expressed in terms of the interaction vertex as in Eqs. (1.45) – (1.49). If, in addition, the interaction vertices (except the zeroth order term) in the two-line irreducible block of the parquet equations are replaced by fully dressed interaction vertices, an expansion emerges, in which only dressed propagators and dressed vertices appear (skeleton expansion).

More specifically, the parquet equations are the result of the *crossing symmetric* summation of all two-line reducible diagrams, which can be generated from an arbitrary set of two-line irreducible diagrams. [65–68] The essential bookkeeping device is the classification of two-particle diagrams according to three inequivalent channels. Each channel defines a two-line reducibility, i.e., a way, how, by cutting two lines, a two-particle diagram falls apart into two disconnected pieces. We label the three channels by 12, 13, and 14. For example, an arbitrary diagram with four external legs (see Fig. 1.9) is 12 reducible (irreducible), if, by cutting two internal lines, it can (cannot) be separated into two pieces, such that one piece contains the external legs 12.¹² The definitions with respect to the 13 and 14 channels are analogous.

In this subsection we perform a *two-band* parquet analysis taking electron-electron and electron-hole interaction into account. We initially treat CB electrons and VB holes on an equal footing, taking only advantage of the vanishing VB hole concentration, which means that diagrams with closed VB hole lines are negligible. For a diagrammatic representation of the mathematical expressions, we adopt the Lande-Smith language [65,66], which exclusively works with *direct* four-point functions in the particle-particle channel (12 channel), a generic representative of which is shown in Fig. 1.9. The four-point functions are matrices in the band index (e,h) and the spin index (\uparrow, \downarrow). If not noted otherwise, the indices i and j enclose both.

With each channel attached is a certain number of chaining operations. They are shown in Fig 1.10. Any (direct) two-line reducible diagram can be constructed from them. The internal propagators are for simplicity denoted in unison by solid lines, although, depending on the external labels of the composite diagram, they can be both CB electron and VB hole propagators. The internal pair states (propagators) in each channel have to be chosen in accordance with three rules: Firstly, VB holes and CB electrons have to be conserved at each vertex. Secondly, because

¹²In the language of Ref. [67], a 12 reducible (irreducible) diagram is 12 non-simple (simple).

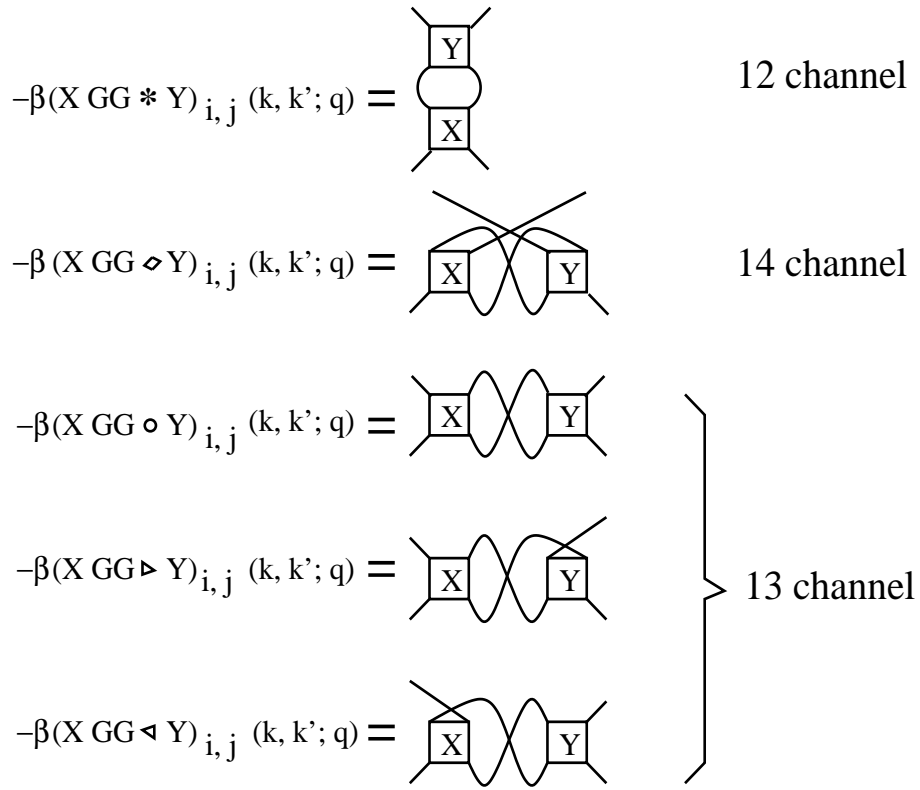


Figure 1.10: The five chaining operations (\star , \diamond , \circ , \triangleright and \triangleleft) in the three channels (12, 14, and 13). The labels i and j denote “internal quantum numbers” such as spin and band indices. The mathematical expressions are given in Eq. (1.50)–(1.54). Recall, we work with direct particle-particle vertices, with incoming lines attached to the bottom of the vertices. The direction of lines is thus fixed and arrows giving this information are not shown.

of the vanishing VB hole density, no closed VB hole lines are allowed. Thirdly, in addition to the conventions given in Fig. 1.9, VB hole lines are always attached to the right side of an electron-hole vertex, whereas CB electron lines are attached to the left.

Each chaining operation corresponds to a particular convolution of the internal variables. Mathematically, the diagrams in Fig. 1.10 read

$$(XGG \star Y)_{ij}(k, k'; q) = \sum_r X_{ij}(k, r; q) G_i(r) G_j(q - r) Y_{ij}(r, k'; q) , \quad (1.50)$$

$$(XGG \diamond Y)_{ij}(k, k'; q) = \sum_r X_{ij}(k, k + r - q; k - k' + r) G_i(k + r - q) \\ \times G_j(r - k') Y_{ij}(k + r - q, k'; r) , \quad (1.51)$$

$$(XGG \circ Y)_{ij}(k, k'; q) = - \sum_{r,l} X_{il}(k, k'; r) G_l(r - k') G_l(r - k) \\ \times Y_{lj}(r - k', r - k; q + r - k - k') , \quad (1.52)$$

$$(XGG \triangleleft Y)_{ij}(k, k'; q) = \sum_r X_{ii}(k, k - r; k + k' - r) G_i(k - r) \\ \times G_i(k' - r) Y_{ij}(k - r, k' - r; q - r) , \quad (1.53)$$

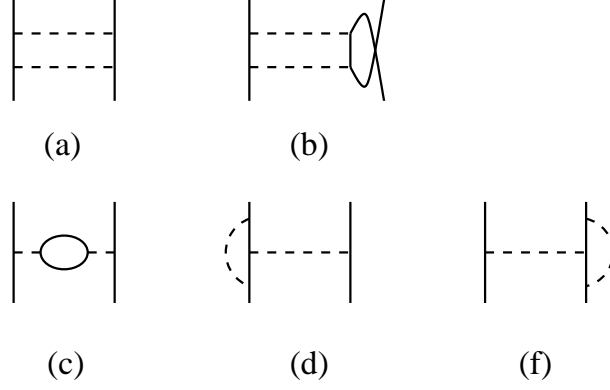


Figure 1.11: Lowest order diagrams generated by the five chaining operations: (a) particle-particle ladder (\star , channel 12), (b) particle-hole ladder (\diamond , channel 14), (c) particle-hole bubble (\circ , channel 13), (d) left vertex correction (\triangleleft , channel 13), and (e) right vertex correction (\triangleright , channel 13). Note, in the two-band model, a “particle” (“hole”) can be either a forward (backward) running CB electron line or a forward (backward) running VB hole line.

$$(XGG \triangleright Y)_{ij}(k, k'; q) = \sum_r X_{ij}(k, k'; k + k' - r) G_j(k - r) \times G_j(k' - r) Y_{ij}(k - r, q - k'; q - r) . \quad (1.54)$$

Lande and Smith have shown how the parquet summation for the interaction vertex can be performed with direct four-point functions and the five chaining operations \star , \diamond , \circ , \triangleleft , and \triangleright . [65] Their crucial observation was that the chaining operations satisfy generalized associativity relations, which ensure that each permitted diagram is generated only once. Technically, they defined particular classes of two-line reducible diagrams (in the 12, 13 and 14 channel, respectively), proved that they are disjoint, and finally showed that any diagram one might think of is included in the sum of the two-line reducible blocks which can be generated from the (complete) two-line irreducible block. With the matrix structure introduced in Fig. 1.9, we can adopt the Lande-Smith approach to a two-band semiconductor. As a result, the fully dressed direct interaction vertex is given by

$$\Gamma = \Gamma_0 + \Gamma GG \triangleleft \Gamma_0 + \Gamma_0 GG \triangleright \Gamma + \Gamma GG \triangleleft \Gamma_0 GG \triangleright \Gamma \quad (1.55)$$

$$\Gamma_0 = I + K^{12} + K^{13} + K^{14} \quad (1.56)$$

$$K^{12} = (\Gamma - K^{12}) GG \star \Gamma \quad (1.57)$$

$$K^{14} = (\Gamma - K^{14}) GG \diamond \Gamma \quad (1.58)$$

$$K^{13} = (\Gamma_0 - K^{13}) GG \bullet \Gamma_0 , \quad (1.59)$$

where $XGG \bullet Y = XGG \circ Y + XGG \circ (\Gamma GG \triangleleft Y)$ is the dressed bubble operation. The first term on the rhs of Eq. (1.56) denotes the two-line irreducible block. It contains the bare interaction $\Gamma^{(0)}$ and an infinite number of additional diagrams. Equations (1.55) – (1.59) are *exact* as long as *all* two-line irreducible diagrams are included in the block I . They become approximate only, when we replace I by a subclass of two-line irreducible diagrams, for instance, by the bare interaction $\Gamma^{(0)}$. Depending on the external labels, Eqs. (1.55) – (1.59) determine Γ_{ee} and Γ_{eh} , with the internal propagators chosen in accordance to the three rules given above.

In Fig. 1.11 we show the lowest order diagrams generated by the five chaining operations. The operations \star , \diamond , \circ create particle-particle ladders, particle-hole ladders, and particle-hole bubbles, respectively, where a particle (hole) can be both a CB electron (CB hole) and a VB hole (VB

electron). They are the “standard” partial summations. For instance, exciton formation is buried in the particle-particle channel while screening is the result of the bubble diagrams. The remaining two operations, \triangleleft and \triangleright , give rise to left and right vertex corrections, respectively. Although vertex corrections have to be included to ensure that all diagrams are accounted for, we will in the following for simplicity ignore them. It cannot be rigorously justified, has however the advantage that each channel is then uniquely defined by one explicit chaining operation.¹³ Without vertex corrections $\Gamma = \Gamma_0 = I + K^{12} + K^{13} + K^{14}$. It is then possible to define 12, 13, and 14 irreducible blocks, $\Gamma^{12} = \Gamma - K^{12}$, $\Gamma^{13} = \Gamma - K^{13}$, and $\Gamma^{14} = \Gamma - K^{14}$, and rewrite Eqs. (1.55) – (1.59) in a more familiar form:

$$\Gamma^{12} = I + \Gamma^{13}GG \circ \Gamma + \Gamma^{14}GG \diamond \Gamma, \quad (1.60)$$

$$\Gamma^{13} = I + \Gamma^{12}GG \star \Gamma + \Gamma^{14}GG \diamond \Gamma, \quad (1.61)$$

$$\Gamma^{14} = I + \Gamma^{12}GG \star \Gamma + \Gamma^{13}GG \circ \Gamma, \quad (1.62)$$

with Γ given by either one of the three (at this level equivalent) Bethe-Salpeter equations,

$$\Gamma = \Gamma^{12} + \Gamma^{12}GG \star \Gamma, \quad (1.63)$$

$$\Gamma = \Gamma^{13} + \Gamma^{13}GG \circ \Gamma, \quad (1.64)$$

$$\Gamma = \Gamma^{14} + \Gamma^{14}GG \diamond \Gamma. \quad (1.65)$$

We first consider the (simplified) parquet equations (1.60) – (1.62) for the ee vertex. Fixing the external legs as CB electrons and choosing the internal lines accordingly, we find in the limit of vanishing VB hole concentration the following set of equations:

$$(\Gamma_{ee}^{12})_{\sigma\tau} = (I_{ee})_{\sigma\tau} + (\Gamma_{ee}^{13}GG \circ \Gamma_{ee})_{\sigma\tau} + (\Gamma_{ee}^{14}GG \diamond \Gamma_{ee})_{\sigma\tau}, \quad (1.66)$$

$$(\Gamma_{ee}^{13})_{\sigma\tau} = (I_{ee})_{\sigma\tau} + (\Gamma_{ee}^{12}GG \star \Gamma_{ee})_{\sigma\tau} + (\Gamma_{ee}^{14}GG \diamond \Gamma_{ee})_{\sigma\tau}, \quad (1.67)$$

$$(\Gamma_{ee}^{14})_{\sigma\tau} = (I_{ee})_{\sigma\tau} + (\Gamma_{ee}^{12}GG \star \Gamma_{ee})_{\sigma\tau} + (\Gamma_{ee}^{13}GG \circ \Gamma_{ee})_{\sigma\tau}, \quad (1.68)$$

$$(\Gamma_{ee})_{\sigma\tau} = (\Gamma_{ee}^{13})_{\sigma\tau} + (\Gamma_{ee}^{13}GG \circ \Gamma_{ee})_{\sigma\tau}, \quad (1.69)$$

$$(I_{ee})_{\sigma\tau} = (\Gamma_{ee}^{(0)})_{\sigma\tau} + (R_{ee})_{\sigma\tau}, \quad (1.70)$$

The first three equations determine that part of the ee interaction, which is irreducible in the indicated channel. The fourth equation is the Bethe-Salpeter equation (in the 13 channel) from which the full ee vertex can be obtained. As long as the full set of equations is considered, the Bethe-Salpeter equation can be written in any one of the three channels. The last equation collects all diagrams irreducible in all three channels. The functional I_{ee} contains the bare electron-electron interaction $\Gamma_{ee}^{(0)}$ and a complicated rest (see below). Note the absence of processes with internal VB hole lines. Diagrams with antiparallel internal VB hole lines are negligible because of the vanishing VB hole concentration. Whereas diagrams with parallel internal VB hole lines or a single intermediate VB hole line do not contribute because they violate particle conservation.

The parquet equations for the eh vertex can be obtained by fixing the left (right) external legs as CB electrons (VB holes) and choosing the internal lines accordingly. They have a similar

¹³Usually, parquet equations are written in terms of symmetrized vertices (Hugenholtz representation); direct and exchange diagrams are thus treated simultaneously. [67] Vertex corrections in the sense of Lande and Smith do then not occur and each channel is specified by a single chaining operation. However, because exchange diagrams can mix channels, the danger of overcounting is then pertinent and requires properly defined symmetry factors. In the parquet context, the issue of overcounting has been only addressed by Lande and Smith. They found working with direct diagrams more suitable to ensure that every permissible diagram is counted exactly once. The drawback is that the 13 channel comes then with three chaining operations: the bubble operation and the two vertex corrections.

structure, except that the vertex Γ_{eh}^{13} is not required. This is again a consequence of the vanishing VB hole concentration. Thus, the eh vertex satisfies

$$(\Gamma_{eh}^{12})_{\sigma\tau} = (I_{eh})_{\sigma\tau} + (\Gamma_{ee}^{13}GG \circ \Gamma_{eh})_{\sigma\tau} + (\Gamma_{eh}^{14}G\mathcal{G} \diamond \Gamma_{eh})_{\sigma\tau}, \quad (1.71)$$

$$(\Gamma_{eh}^{14})_{\sigma\tau} = (I_{eh})_{\sigma\tau} + (\Gamma_{ee}^{13}GG \circ \Gamma_{eh})_{\sigma\tau} + (\Gamma_{eh}^{12}G\mathcal{G} \star \Gamma_{eh})_{\sigma\tau}, \quad (1.72)$$

$$(\Gamma_{eh})_{\sigma\tau} = (\Gamma_{eh}^{12})_{\sigma\tau} + (\Gamma_{eh}^{12}G\mathcal{G} \star \Gamma_{eh})_{\sigma\tau}, \quad (1.73)$$

$$(I_{eh})_{\sigma\tau} = (\Gamma_{eh}^{(0)})_{\sigma\tau} + (R_{eh})_{\sigma\tau}. \quad (1.74)$$

As in the ee sector, the first two equations construct, respectively, that part of the eh vertex, which is irreducible in the indicated channel. The third equation is the Bethe-Salpeter equation, from which the full eh vertex is obtained. The Bethe-Salpeter equation is written in the 12 channel. The functional I_{eh} finally denotes the class of diagrams irreducible in all three channels. As in the case of electron-electron interaction, it contains the bare interaction vertex $\Gamma_{eh}^{(0)}$ and a complicated rest R_{eh} .

The functionals R_{ij} depend on the fully dressed interaction vertices Γ_{ij} . It is impossible to give an exact expression for R_{ij} and diagrams contributing to R_{ij} have to be selected according to physical considerations. Usually R_{ij} is neglected. Equations (1.66) – (1.74) for the interaction vertices together with Eqs. (1.45) – (1.49) for the single particle self-energies are then the starting point, from which various standard *two-particle* approximations can be derived. The equations contain, e.g., parallel and anti-parallel eh channels as well as an $e\bar{e}$ channel. The eh channels yield the power-law dependencies of the optical response while the latter describes screening. Thus, suitable reduction procedures yield either the equations used by Gavoret and coworkers [15] to study the Fermi-edge singularity (GNRC approach) or the screened ladder approximation for the eh vertex [12, 13], which is the workhorse of the modern theory of semiconductor optics. [52]

Without the residual part R_{ij} , Eqs. (1.66) – (1.74) contain only two-particle correlations. For doped bulk semiconductors this is sufficient. For a doped quantum well, however, the existence of charged excitons, i.e., bound states comprising three particles, suggests that the summation of two-particle channels is not enough. Three particle correlations have to be incorporated. From the structure of the Eqs. (1.66) – (1.74) it is clear that three particle correlations can be only included in R_{ij} . Thus, any theoretical description of the optical response of (low-dimensional) doped semiconductor structures, which tries to cover the whole density range, from bound state dominated low to Fermi-edge dominated high densities, has to be on a par with a parquet theory, which, in addition to the various ee and eh channels, takes also eeh correlations into account.

To include three particle correlations, we now consider R_{eh} , the lowest order diagrams of which are shown in Fig. 1.12.¹⁴ The block R_{eh} is at least fourth order in the fully dressed interaction vertices and involves at least six internal propagators. From experiments we know that at low densities correlations between two CB electrons and one VB hole are very important, eventually giving rise to a three particle bound state. To account for this fact, we suggest to include in R_{eh} all multiple scattering processes between the intermediate two CB electrons and VB hole as symbolized by the thin stripes in Fig. 1.12. Because of the vanishing VB hole density, the VB hole propagator passes through the diagrams in Fig. 1.12 without being able to form a closed loop. Separating the processes shown in Fig. 1.12 from the rest, the complete irreducible eh interaction I_{eh} can be written as

$$I_{eh} = \Gamma_{eh}^{(0)} + R_{eh}^T[\Gamma_{ee}, \Gamma_{eh}] + \delta R_{eh}[\Gamma_{ee}, \Gamma_{eh}], \quad (1.75)$$

¹⁴For drawing purposes we attached the external lines to the vertices, which are now denoted by circles instead of boxes, freely. To obtain the mathematical expressions the diagrams have to be redrawn using the notation and conventions introduced in Fig. 1.9.

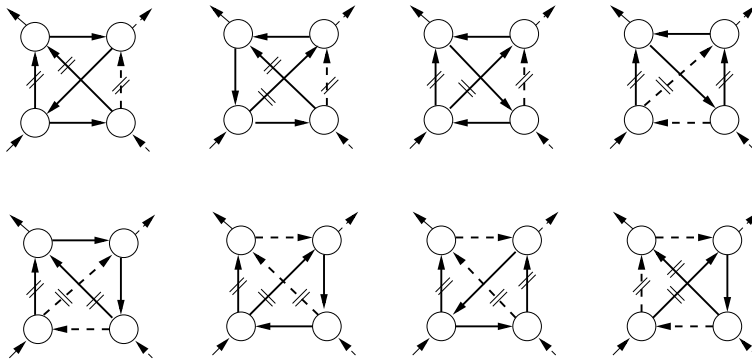
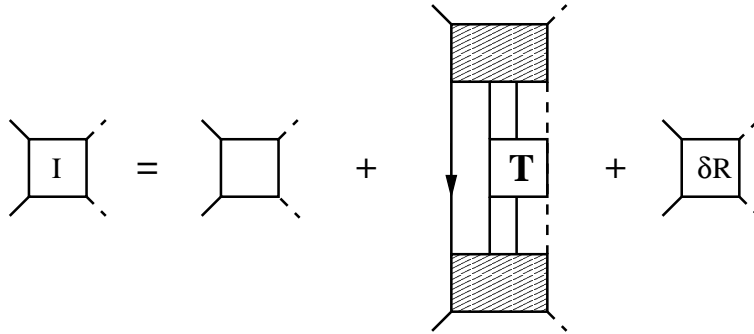
Figure 1.12: Three particle correlations considered in R_{eh} .

Figure 1.13: Complete irreducible eh vertex, I_{eh} , with eeh correlations separated off. To indicate that the leftmost internal line in the second diagram on the rhs is a backward running CB electron line, we explicitly attached an arrow to this line. The remaining lines are, in accordance with our conventions, upward running.

where we explicitly indicated the dependencies of the functionals R_{eh}^T and δR_{eh} on the full interaction vertices.

In Fig. 1.13 we give a graphical representation of Eq. (1.75). The block denoted by T contains the correlated propagation of an eeh cluster. In the simplest approximation, it sums a three-particle eeh ladder, with pair-wise interactions mediated by the full interaction vertices Γ_{ee} and Γ_{eh} , respectively. The other two blocks denote appropriately defined $eh\bar{e}eh$ interaction vertices, containing two pair interaction vertices and one internal line. The functional δR_{eh} comprises the remaining diagrams.

The topological structure of the lowest order contributions to the functional R_{ee} is the same as in Fig. 1.12, except that the external and internal lines are different because of particle conservation. VB hole propagators can now only appear in the form of closed loops, which are however negligible for vanishing VB hole density. Thus, all internal lines in R_{ee} are CB electron lines; eeh correlations cannot appear at all. Since there is moreover no experimental evidence of correlations between more than two internal electron lines, we ignore R_{ee} . Eventually, we even completely shortcut the ee parquet equations and replace the ee vertices in the eh parquet equations by the screened ee interaction.

1.5.3 Minimal Set of Equations

Obviously the full parquet equations (1.66) – (1.74) are extremely complicated. In this subsection we therefore look for simplifications, guided by well established approximations and the additional needs dictated by experimental findings. We anticipate an iterative process to solve the parquet equations, that is, a process which replaces the vertices on the rhs of the parquet equations by the vertices of the lhs.¹⁵ There are various ways to go through this procedure. Choosing a particular strategy biases the iteration in the sense that, e.g., the screening in the 13 channel of the ee sector is build up “faster” then let say the correlations in the 12 channel of the eh sector. Simplifications arise through the particular manner, in which the replacements are performed and, most importantly, through a suitable truncation of the iteration process. The “in-complete” iteration corresponding then to the summation of a selected class of diagrams.

First, we simplify the ee sector. Our goal is to extract, through an appropriate iterative procedure, an approximate expression for Γ_{ee}^{13} , which is the ee vertex needed in the eh sector [cf. Eq. (1.71)–(1.74)].¹⁶ The most important channels in the ee sector are the anti-parallel channels, because they contain the collective excitations of the CB electron Fermi sea responsible for screening. Accordingly, we ignore Eq. (1.66) and consider Eqs. (1.67) – (1.70) with $\Gamma_{ee}^{12} = 0$. The first step is to replace Γ_{ee} on rhs of Eqs. (1.67) and (1.68) by Γ_{ee}^{13} and Γ_{ee}^{14} , respectively. We then obtain two coupled equations,

$$\Gamma_{ee}^{13} = I_{ee} + \Gamma_{ee}^{14} GG \diamond \Gamma_{ee}^{13}, \quad (1.76)$$

$$\Gamma_{ee}^{14} = I_{ee} + \Gamma_{ee}^{13} GG \circ \Gamma_{ee}^{14}, \quad (1.77)$$

for the two vertices Γ_{ee}^{13} and Γ_{ee}^{14} . To decouple these two equations, we now replace on the rhs of Eqs. (1.76) and (1.77), $\Gamma_{ee}^{14} \rightarrow I_{ee} \rightarrow \Gamma_{ee}^{(0)}$ and $\Gamma_{ee}^{13} \rightarrow I_{ee} \rightarrow \Gamma_{ee}^{(0)}$, respectively. As a result, we find

$$\Gamma_{ee}^{13} = \Gamma_{ee}^{(0)} + \Gamma_{ee}^{(0)} GG \diamond \Gamma_{ee}^{13}, \quad (1.78)$$

$$\Gamma_{ee}^{14} = \Gamma_{ee}^{(0)} + \Gamma_{ee}^{(0)} GG \circ \Gamma_{ee}^{14}. \quad (1.79)$$

The integral equation for Γ_{ee}^{13} can be formally solved to yield

$$V_{ee}^S \equiv \Gamma_{ee}^{13} = [1 - \Gamma_{ee}^{(0)} GG]_{\diamond}^{-1} \Gamma_{ee}^{(0)}, \quad (1.80)$$

where we introduced V_{ee}^S to denote the screened ee interaction in the 13 channel. Note, Eq. (1.78) is an integral equation in the 14 channel. The screening of the 13 irreducible ee interaction is thus performed by $e\bar{e}$ excitations in the 14 channel, that is, by $e\bar{e}$ ladders. Although the replacements might at first sight seem arbitrary, we emphasize that they correspond to the first few steps in an appropriate iterative process to solve the full ee parquet equations.

We now turn to the parquet equations in the eh sector. First, we replace in Eqs. (1.71) – (1.74) Γ_{ee}^{13} by V_{ee}^S . Neglecting δR_{eh} in I_{eh} yields then a minimal set of equations,

$$\Gamma_{eh}^{12} = I_{eh} + V_{ee}^S GG \circ \Gamma_{eh} + \Gamma_{eh}^{14} GG \diamond \Gamma_{eh}, \quad (1.81)$$

$$\Gamma_{eh}^{14} = I_{eh} + V_{ee}^S GG \circ \Gamma_{eh} + \Gamma_{eh}^{12} GG \star \Gamma_{eh}, \quad (1.82)$$

$$\Gamma_{eh} = \Gamma_{eh}^{12} + \Gamma_{eh}^{12} GG \star \Gamma_{eh}, \quad (1.83)$$

$$I_{eh} = \Gamma_{eh}^{(0)} + R_{eh}^T [V_{ee}^S, \Gamma_{eh}], \quad (1.84)$$

¹⁵The self-energies of the internal propagators are assumed to contain the vertices of the previous iteration step.

¹⁶In principle, R_{eh} contains the full ee vertex. Thus, in a complete crossing symmetric theory, all three ee channels should be in fact considered. We anticipate however to short-cut the ee sector and to replace all ee interactions in R_{eh} by a screened 13 channel ee interaction.

which, augmented by Eqs. (1.45) – (1.49) for the single-particle self-energies (with $\Gamma_{ee} \rightarrow V_{ee}^S$), contains, at least in principle, the most important physical processes affecting the optical response of doped semiconductors. They determine the full eh vertex Γ_{eh} and the propagators G and \mathcal{G} required to calculate the optical susceptibility $\chi(q)$ from Eq. (1.44). The optical response on the real energy axis is then obtained via analytical continuation. The optical absorption, e.g., is given by $I_{abs}(\omega) \sim -\text{Im}\chi(\vec{q}=0, i\nu_m \rightarrow \omega - \mu_e + i\eta)$.

The physical content of the Eqs. (1.81) – (1.84) is particularly transparent. The first two equations determine, respectively, the irreducible eh interaction in the parallel (12) and anti-parallel (14) eh channel required to obtain the correct power-law dependence of the Fermi-edge signature, supplemented by the screening channel (13). For $V_{ee}^S = 0$ and $I_{eh} \rightarrow \Gamma_{eh}^{(0)}$, these two equations reduce to the GNRC equations. Keeping V_{ee}^S , the second term on the rhs of Eqs. (1.81) and (1.82), respectively, describes the screening of the eh interaction. Note, because of the vanishing VB hole concentration screening is due exclusively to CB electron bubbles (13 channel). The possibility of charged exciton formation is included in R_{eh}^T , where eeh correlations are explicitly taken into account. The full eh vertex, required to calculate the optical susceptibility, is finally obtained from the Bethe-Salpeter equation (1.83). The single particle propagators are fully dressed. To obtain a closed set of equations, the exact interaction vertices in the single-particle self-energies have to be replaced by the approximate ones, which provokes questions about consistency and conservation laws. Pragmatically, one would be tempted to replace the single-particle propagators by an appropriate quasi-particle approximation (static single-particle self-energies) which is consistent with the approximate eh interaction vertex used in the calculation of the optical susceptibility. Only a numerical solution can show, however, whether this strategy gives meaningful results.

To resume the discussion up to this point, we applied a systematic dynamic vertex renormalization procedure (parquet analysis) to derive a minimal set of equations (1.81–1.84) for the eh vertex needed for the calculation of the optical susceptibility of a n-doped quantum well. The goal was to obtain equations which contain screening, the two eh channels required for the correct description of the Fermi-edge signature at high densities, and the three particle correlations needed to capture trion formation at low densities. The equations have not yet been fully analyzed. We believe however that they constitute a promising starting point for the calculation of the optical response at arbitrary doping concentration. With suitable simplifications, their numerical solution should be within the reach of modern algorithms and computing power.

Let us finally consider a situation, where the Fermi-edge singularity is smeared out and is of no concern. This is the case, when the VB hole is rather mobile and/or the temperature is rather high. It is then sufficient to confine the theoretical treatment to one eh channel, e.g., the 12 channel. The resulting truncated set of equations,

$$\Gamma_{eh}^{12} = I_{eh} + V_{ee}^S GG \circ \Gamma_{eh}, \quad (1.85)$$

$$\Gamma_{eh} = \Gamma_{eh}^{12} + \Gamma_{eh}^{12} G \mathcal{G} \star \Gamma_{eh}, \quad (1.86)$$

$$V_{ee}^S = \Gamma_{ee}^{(0)} + \Gamma_{ee}^{(0)} GG \diamond V_{ee}^S, \quad (1.87)$$

$$I_{eh} = \Gamma_{eh}^{(0)} + R_{eh}^T [V_{ee}^S, \Gamma_{eh}], \quad (1.88)$$

can be used to construct a generalized CMFA.

Towards that end, we first replace, again in the spirit of a truncated iteration process, on the rhs of Eq. (1.85) the full vertex Γ_{eh} by Γ_{eh}^{12} . Using furthermore Eq. (1.88), we find for the 12 irreducible eh vertex an integral equation,

$$\Gamma_{eh}^{12} = \Gamma_{eh}^{(0)} + R_{eh}^T + V_{ee}^S GG \circ \Gamma_{eh}^{12}, \quad (1.89)$$

which can be formally solved to yield

$$\Gamma_{eh}^{12} = V_{eh}^S + \tilde{R}_{eh}^T, \quad (1.90)$$

with a screened eh interaction,

$$V_{eh}^S = [1 - V_{ee}^S GG]_{\circ}^{-1} \Gamma_{eh}^{(0)}, \quad (1.91)$$

and a residual term,

$$\tilde{R}_{eh}^T = [1 - V_{ee}^S GG]_{\circ}^{-1} R_{eh}^T [V_{ee}^S, \Gamma_{eh}], \quad (1.92)$$

which contains the eeh correlations. Note, Eq. (1.91) is an integral equation in the 13 channel. Thus, $e\bar{e}$ bubbles are responsible for the screening of the eh interaction, which is nothing but the random-phase approximation for Γ_{eh}^{12} .

We now replace in R_{eh}^T (and in the single-particle self-energies) the full eh vertex Γ_{eh} by V_{eh}^S . As a result, Eq. (1.90) specifies the 12 irreducible vertex Γ_{eh}^{12} in terms of the screened ee and the screened eh interaction. Through the Bethe-Salpeter equation (1.86), the full eh vertex Γ_{eh} is then only a functional of the screened interactions.

The 12 irreducible eh vertex Γ_{eh}^{12} is the sum of two parts: V_{eh}^S and \tilde{R}_{eh}^T . At low densities, where screening and phase-space filling are negligible, we expect \tilde{R}_{eh}^T to contain a pole due to an eeh bound state (trion). Thus, \tilde{R}_{eh}^T gives an important contribution to Γ_{eh}^{12} and hence to the full vertex Γ_{eh} . At high densities, on the other hand, screening and Pauli blocking prevents the formation of bound states and \tilde{R}_{eh}^T should have a minor effect on Γ_{eh}^{12} . As a result, the full eh vertex Γ_{eh} should be basically given by the screened ladder approximation.

To facilitate a comparison with the original CMFA approach, we define a generalized eh pair propagator (which depends on three energies). Symbolically, we write

$$\mathcal{P} = \mathcal{P}^{(0)} + \mathcal{P}^{(0)} \Gamma_{eh} \mathcal{P}^{(0)}, \quad (1.93)$$

with $\mathcal{P}^{(0)} = G\mathcal{G}$ and Γ_{eh} the full eh vertex. Using the Bethe-Salpeter equation (1.86) together with Eq. (1.90), we obtain an intergral equation for \mathcal{P} ,

$$\mathcal{P} = \mathcal{P}^{(0)} + \mathcal{P}^{(0)} [V_{eh}^S + \tilde{R}_{eh}^T] \mathcal{P}, \quad (1.94)$$

where $\Gamma_{eh}^{12} = V_{eh}^S + \tilde{R}_{eh}^T$ appears as a kernel. Although this equation has the formal structure of a Dyson-type equation, it is crucial to recall that the four point functions depend on three energy variables. Nevertheless, it is instructive to contrast Eq. (1.94) with Eq. (1.4), which we recast for that purpose into

$$P = P^{(0)} + P^{(0)} [M^{st} + \delta M] P. \quad (1.95)$$

Clearly, V_{eh}^S and \tilde{R}_{eh}^T play the roles of M^{st} and δM , respectively. We suspect therefore that suitable Shindo-type approximations [12, 13], which eliminate two of the three energy variables in Eq. (1.94), would enable us to derive a generalized CMFA for a reduced eh pair propagator, depending only on one energy variable, but still accounting for screening, single-particle self-energy corrections beyond first order, and three-particle correlations. In that way, the CMFA philosophy of “embedding few-body clusters in a medium” could be perhaps extended to arbitrary densities.

1.6 Concluding Remarks

In this chapter we discussed the optical response of a doped quantum well. We primarily focused on the optical absorption due to exciton and trion formation, conceptualizing the trion as an itinerant excitation formed in the course of the dynamical response of CB electrons to the photo-generated VB hole. Within this approach the trion enters the optical response through the eh pair self-energy. We also emphasized the close connection between trion formation at low doping and Fermi-edge signatures at high doping.

To incorporate trion formation in the optical response of a weakly doped quantum well, we adopted the CMFA. The CMFA reduces the calculation of the eh pair propagator to the solution of an in-medium eh and an in-medium eeh Lippmann-Schwinger equation. Medium corrections, such as Pauli blocking and the Fock corrections to the CB electron self-energy, are included. Screening however cannot be systematically accounted for. As a consequence, the CMFA can be only used at low enough CB electron densities. As far as the numerical results are concerned, we focused on the extreme dilute limit, where medium corrections can be ignored altogether and excess carriers only provide a reservoir for bound state formation. Even this simple approximation goes beyond earlier investigations because it enables us to treat neutral and charged excitons on an equal footing. The overall structure of the calculated absorption is consistent with experimental data. The numerical implementation does not capitalize the full potential of the CMFA. One of the future research directions is therefore the calculation of the optical susceptibility with medium corrections taken into account, that is, to find the solutions of the full in-medium bound state problems and use it in the optical susceptibility calculation.

The dynamical response of CB electrons to the appearance or disappearance of a VB hole plays an even more important role at higher densities, where it gives rise to screening and, at low enough temperatures and sufficiently high VB hole masses, to the celebrated Fermi-edge singularity. Based on a parquet analysis of the ee and eh vertices, we proposed a minimal set of equations which, in principle, is capable to describe the optical response in the high and the low density regime, capturing both the Fermi-edge singularity at high density and trion formation at low density. If the Fermi-edge singularity is of no concern, e.g., because the VB hole is too mobile, only screening and single-particle self-energy corrections have to be consistently accounted for. For this situation, we proposed a generalized CMFA. Both, the discussion of the minimal set of equations as well as the discussion of the generalized CMFA remained somewhat tentative. Thus, to demonstrate their feasibility it will be crucial to develop in the future efficient computational techniques for their manipulation and solution.

Appendix

Hylleraas Variational Approach for the Trion Groundstate

In the extreme dilute limit, where excess carriers provide only a reservoir for trion formation, the CMFA reduces in the vicinity of the exciton resonance the calculation of the optical susceptibility to the determination of the groundstate of an isolated eeh cluster [cf. Eq. (1.39)]: From the wavefunction Ψ_T we obtain the exciton-trion coupling constant u_T^X , which, together with the groundstate energy $\tilde{\epsilon}_T$, defines the exciton self-energy $\delta\tilde{M}_X$. The optical susceptibility is then given by Eq. (1.35). Because the eeh Schrödinger equation (1.39) is not separable, the trion groundstate Ψ_T cannot be obtained analytically. In this appendix we describe the variational approach we used to determine the groundstate wavefunction and energy. We closely followed Stébé and coworkers [35, 36], who adopted Hylleraas' variational method for the investigation of two-electron systems [60] to calculate the energy and wavefunction of an isolated trion in a semiconductor quantum well.

We start from Eq. (1.39), which in “atomic units”¹⁷ becomes

$$H = -\frac{1}{2}[\nabla_{e1}^2 + \nabla_{e2}^2] - \frac{\sigma}{2}\nabla_h^2 + \frac{1}{|\vec{r}_{e1} - \vec{r}_{e2}|} - \frac{1}{|\vec{r}_{e1} - \vec{r}_h|} - \frac{1}{|\vec{r}_{e2} - \vec{r}_h|}, \quad (\text{A.1})$$

with $\sigma = m_e/m_h$. The vectors \vec{r}_{e1} , \vec{r}_{e2} , and \vec{r}_h denote, respectively, the position of the first CB electron, the second CB electron and the VB hole in the quantum well plane. Because of translational invariance, the eigenfunctions of H have to be also eigenfunctions of the total momentum operator, that is, the eeh wavefunctions satisfy not only $H\Psi = E\Psi$, but also $-i\hbar[\nabla_{e1} + \nabla_{e2} + \nabla_h]\Psi = P\Psi$. The center of mass motion of the eeh complex is therefore a plane wave. To obtain the wavefunction for the internal motion we set $P = 0$. As a result, the kinetic energy of the VB hole, the second term in Eq. (A.1), can be replaced by $-(\sigma/2)\nabla_h^2 = -(\sigma/2)[\nabla_{e1} + \nabla_{e2}]^2$ when acting on internal wave functions. For the internal motion, only the relative coordinates are relevant (see Fig. 1.14). The position of the VB hole can be thus taken as the origin of the coordinate system. For the (isotropic) groundstate, the orientation of the triangle spanned by the three particles is moreover irrelevant. The groundstate wavefunction Ψ_T depends therefore only on three independent variables: $r_1 = |\vec{r}_{e1} - \vec{r}_h|$, $r_2 = |\vec{r}_{e2} - \vec{r}_h|$, and $r_{12} = |\vec{r}_{e1} - \vec{r}_{e2}|$. More suitable for the variational approach are however the elliptical coordinates introduced by Hylleraas,

$$\begin{aligned} s &= r_1 + r_2 & s &\geq 0, \\ t &= r_1 - r_2 & -s &\leq t \leq s, \\ u &= r_{12} & |t| &\leq u \leq s, \end{aligned} \quad (\text{A.2})$$

in terms of which Eq. (A.1) becomes

$$H = T_e + T_h + V \quad (\text{A.3})$$

$$T_e = -\partial_{ss}^2 - \partial_{tt}^2 - \partial_{uu}^2 - \frac{1}{u}\partial_u - \frac{2}{s^2 - t^2}[s\partial_s - t\partial_t] - \frac{2s(u^2 - t^2)}{u(s^2 - t^2)}\partial_{su}^2 - \frac{2t(s^2 - u^2)}{u(s^2 - t^2)}\partial_{tu}^2 \quad (\text{A.4})$$

$$T_h = -2\sigma\left\{\frac{s^2 - u^2}{s^2 - t^2}\partial_{ss}^2 + \frac{u^2 - t^2}{s^2 - t^2}\partial_{tt}^2 + \frac{s}{s^2 - t^2}\partial_s - \frac{t}{s^2 - t^2}\partial_t\right\} \quad (\text{A.5})$$

$$V = \frac{1}{u} - \frac{4s}{s^2 - t^2}. \quad (\text{A.6})$$

¹⁷We measure energies in units of $2R_0$ and lengths in units of a_0 , with $R_0 = e^4 m_e / 2\epsilon_0^2 \hbar^2$ the Rydberg and $a_0 = \hbar^2 \epsilon_0 / e^2 m_e$ the Bohr radius in a semiconductor with a background dielectric constant ϵ_0 and an electron mass m_e .

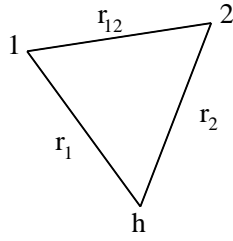


Figure 1.14: The independent variables for the trion groundstate calculation.

For the wavefunction Ψ_T , we make a Hylleraas ansatz

$$\Psi_T(s, t, u) = \Phi(ks, kt, ku), \quad (\text{A.7})$$

with

$$\Phi(s, t, u) = \sum_{l,m,n} c_{lnm} |lnm\rangle \quad (\text{A.8})$$

and

$$|lnm\rangle = e^{-\frac{s}{2}} s^l t^m u^n, \quad (\text{A.9})$$

where m is even because the trion groundstate is a singlet. The variational parameters are the expansion coefficients c_{lnm} and the effective VB hole charge k , which takes the partial screening of the charge of the VB hole seen by one of the CB electrons due to the presence of the other CB electron into account. Substituting Ψ_T into the Ritz variational principle,

$$E[\Psi_T] = \frac{\langle \Psi_T | H | \Psi_T \rangle}{\langle \Psi_T | \Psi_T \rangle}, \quad (\text{A.10})$$

and rewriting the integrals in terms of Hylleraas coordinates gives

$$E[\Psi_T] = \frac{k^2 M - kL}{N}, \quad (\text{A.11})$$

with

$$M = \langle \Phi | T_e + T_h | \Phi \rangle, \quad (\text{A.12})$$

$$L = \langle \Phi | -V | \Phi \rangle, \quad (\text{A.13})$$

$$N = \langle \Phi | \Phi \rangle, \quad (\text{A.14})$$

and

$$\langle \Phi | [\dots] | \Phi \rangle = \int_0^\infty ds \int_0^s du \int_0^u dt \frac{2\pi(s^2 - t^2)u}{\sqrt{(u^2 - t^2)(s^2 - u^2)}} \Phi^*(s, t, u) [\dots] \Phi(s, t, u). \quad (\text{A.15})$$

To proceed, we introduce a multiple index $j = (lnm)$, substitute Eq. (A.8) into Eqs. (A.12) – (A.14), and perform the integrations. The result can be compactly written as

$$M = \sum_{jj'} c_j T_{jj'} c_{j'}, \quad (\text{A.16})$$

$$L = \sum_{jj'} c_j V_{jj'} c_{j'}, \quad (\text{A.17})$$

$$N = \sum_{jj'} c_j S_{jj'} c_{j'}, \quad (\text{A.18})$$

with

$$\begin{aligned}
4\mathbf{T}_{jj'} &= \mathbf{J}_{jj'}(0, 1, 2) - \mathbf{J}_{jj'}(2, 1, 0) - 4(l' - m')(l' + m' + 2n' + 1)\mathbf{J}_{jj'}(0, 1, 0) \\
&+ 4(l' + n' + 1)\mathbf{J}_{jj'}(1, 1, 0) - 4n'(n' + 2m')\mathbf{J}_{jj'}(2, -1, 0) \\
&+ 4n'(n' + 2l')\mathbf{J}_{jj'}(0, -1, 2) - 4l'\mathbf{J}_{jj'}(-1, 1, 2) \\
&+ 4l'(l' - 1)\mathbf{J}_{jj'}(-2, 1, 2) - 4m'(m' - 1)\mathbf{J}_{jj'}(2, 1, -2) - 4n'\mathbf{J}_{jj'}(1, -1, 2) \\
&+ 2\sigma\{2(2l' + 1)\mathbf{J}_{jj'}(1, 1, 0) - 4[l'^2 - m'^2]\mathbf{J}_{jj'}(0, 1, 0) \\
&- \mathbf{J}_{jj'}(2, 1, 0) + \mathbf{J}_{jj'}(0, 3, 0) - 4l'\mathbf{J}_{jj'}(-1, 3, 0) \\
&+ 4l'(l' - 1)\mathbf{J}_{jj'}(-2, 3, 0) - 4m'(m' - 1)\mathbf{J}_{jj'}(0, 3, -2)\}, \tag{A.19}
\end{aligned}$$

$$\mathbf{V}_{jj'} = 4\mathbf{J}_{jj'}(1, 1, 0) + \mathbf{J}_{jj'}(0, 0, 2) - \mathbf{J}_{jj'}(2, 0, 0), \tag{A.20}$$

$$\mathbf{S}_{jj'} = \mathbf{J}_{jj'}(2, 1, 0) - \mathbf{J}_{jj'}(0, 1, 2), \tag{A.21}$$

and

$$\mathbf{J}_{jj'}(\lambda, \mu, \nu) = 2\pi \int_0^\infty ds e^{-s} s^{l+l'+\lambda} \int_0^s du \frac{u^{n+n'+\mu}}{\sqrt{s^2 - u^2}} \int_0^u dt \frac{t^{m+m'+\nu}}{\sqrt{u^2 - t^2}} \tag{A.22}$$

$$= 2\pi(l + l' + \lambda + n + n' + \mu + m + m' + \nu)! \mathbf{I}_{n+n'+\mu+m+m'+\nu} \mathbf{I}_{m+m'+\nu}, \tag{A.23}$$

where

$$\mathbf{I}_n = \int_0^1 dx \frac{x^n}{\sqrt{1 - x^2}}. \tag{A.24}$$

Although the integral (A.24) can be analytically obtained, we found it more convenient to calculate it numerically, in particular for large n .

The minimum conditions for the energy functional (A.11) are

$$\partial_k \mathbf{E} = 0 \quad \text{and} \quad \partial_{c_j} \mathbf{E} = 0 \quad \forall j. \tag{A.25}$$

The first condition yields

$$k = \frac{\mathbf{L}}{2\mathbf{M}}, \tag{A.26}$$

from which

$$\mathbf{E} = -\frac{\mathbf{L}^2}{4\mathbf{M}\mathbf{N}} \tag{A.27}$$

follows. Equation (A.27) is a nonlinear functional of the expansion coefficients c_j . From its minimum condition we could actually find the coefficients c_j . A better strategy is however to start with a guess for k which is then iteratively updated. For a fixed k , the minimum conditions (A.25) lead to a linear set of equations,

$$(k^2 \tilde{\mathbf{T}} - k\mathbf{V} - \mathbf{E}\mathbf{S})\vec{c} = 0, \tag{A.28}$$

with $\tilde{\mathbf{T}} = (1/2)(\mathbf{T} + \mathbf{T}^T)$, where \mathbf{T}^T is the transpose of the matrix \mathbf{T} . To determine the vector \vec{c} , which contains the expansion coefficients c_j , we follow Stébé and Ainane [35] and rewrite Eq. (A.28), which is a generalized eigenvalue problem for the trion energy \mathbf{E} , into a generalized eigenvalue problem for the effective VB hole charge k :

$$\mathbf{V}\vec{c} = k\mathbf{B}\vec{c}, \tag{A.29}$$

with a symmetric matrix

$$\mathbf{B} = \tilde{\mathbf{T}} + \Phi \mathbf{S} \quad (\text{A.30})$$

and an auxiliary quantity $\Phi = -\frac{E}{k^2}$, which contains the (unknown) effective VB hole charge k as well as the (unknown) energy E . To set up an iterative procedure, we prefer to eliminate these two quantities in favor of the (also unknown) coefficients c_j . With Eqs. (A.26) and (A.27) we find

$$\Phi = \frac{M}{N}, \quad (\text{A.31})$$

which depends only on the coefficients c_j . We now convert the generalized eigenvalue problem (A.29) to an ordinary eigenvalue problem. For that purpose, we perform a Cholesky decomposition of the (symmetric, positive definite) matrix \mathbf{B} . With

$$\mathbf{B} = \mathbf{L}\mathbf{L}^T \quad (\text{A.32})$$

and the definitions

$$\mathbf{K} = \mathbf{L}^{-1}\mathbf{V}\left(\mathbf{L}^{-1}\right)^T, \quad (\text{A.33})$$

$$\vec{d} = \mathbf{L}^T\vec{c}, \quad (\text{A.34})$$

Eq. (A.29) is equivalent to the symmetric eigenvalue problem

$$\mathbf{K}\vec{d} = k\vec{d}, \quad (\text{A.35})$$

which we solve by standard numerical recipes routines. [69] The rank of the eigenvalue problem is given by the number of expansion coefficients c_j . The more terms are taken into account, the higher is the accuracy of the groundstate energy and groundstate wavefunction. For our purpose it is sufficient to work with a 22-term Hylleraas variational function, which consists of polynomials up to order $l+m+n=4$ (with m even). The mapping of the indices l, m, n to the multiple-index j , which we use to organize the linear algebra involved, is shown in Table A.1.

For the trion groundstate, we need only the largest eigenvalue of Eq. (A.35) and the corresponding eigenvector: k_{\max} and \vec{d}_{\max} . Since the matrix \mathbf{K} depends on the expansion coefficients \vec{c} , through the quantity Φ , we have to adopt an iterative procedure: We start with an initial guess for \vec{c} and calculate the matrix \mathbf{K} from Eq. (A.33). Then, we calculate the largest eigenvalue of Eq. (A.35) and determine the corresponding eigenvector, k_{\max} and \vec{d}_{\max} , respectively, from which we first determine a new vector \vec{c} [viz. inverse of Eq. (A.34)] and then a new matrix \mathbf{K} , with which we repeat the iteration cycle until convergence is reached. If the vector \vec{c} found in this manner is substituted in Eqs. (A.27) and (A.8), we obtain the trion energy and the trion wavefunction in “atomic units”, which we then translate into the excitonic units used in the expressions for the optical susceptibility. The numerical procedure is rather robust and converges extremely fast.

The Ritz variational principle could be also used to construct excited states for the trion. It is then however necessary to chose the trial wavefunctions to be orthogonal to all (approximate) wavefunctions with lower energies. This by itself becomes very quickly an unwieldy procedure. For the trion, which is closely related to the H^- , it is moreover expected that the groundstate is the only bound state. Excited states belong thus to a continuum, in which at least one of the electrons is free. Variational principles for particular scattering states exists, for instance, states which describe the break-up of the trion into an exciton and an electron. If, however, the complete trion spectrum is required, the brute force numerical solution of the time-dependent eeh Schrödinger equation is most probably the method of choice. [40,41] Faddeev techniques [62] could be also used. These techniques, which are usually applied in momentum space, are moreover not restricted to the extreme dilute limit.

Table A.1: Mapping of the Hylleraas indices n, l, m for the 22-term Hylleraas variational function to the multiple index j which we use to label the rows and columns of the matrices defining the eigenvalue problem (A.35). The order of the Hylleraas function is given by $n + l + m$.

j	n	l	m	$n + l + m$	j	n	l	m	$n + l + m$
1	0	0	0	0	12	3	0	0	3
2	1	0	0	1	13	0	3	0	3
3	0	1	0	1	14	2	2	0	4
4	1	1	0	2	15	1	3	0	4
5	2	0	0	2	16	3	1	0	4
6	0	2	0	2	17	1	1	2	4
7	0	0	2	2	18	2	0	2	4
8	1	2	0	3	19	0	2	2	4
9	2	1	0	3	20	4	0	0	4
10	1	0	2	3	21	0	4	0	4
11	0	1	2	3	22	0	0	4	4

Chapter 2

Polaron Formation and Disorder [4–7]

This chapter discusses self-trapping of charge carriers (polaron formation) in a disordered environment. In the first half of the chapter, which is largely based on Ref. [4], we study, at zero temperature, the dynamics of a single electron in a Holstein model augmented by site-diagonal, binary-alloy type disorder. The average over the phonon vacuum and the alloy configurations is performed within an effective single-site approximation, which maps the lattice problem on to a problem involving only a single self-consistently embedded impurity site. In particular, we employ the dynamical coherent potential approximation, which is nothing but the single particle limit of the more general dynamical mean field theory. We present numerical results for a Bethe lattice with infinite coordination number. In particular, we investigate, in the intermediate electron-phonon coupling regime, the spectral and diffusion properties in the vicinity of the high-energy edge of the lowest polaronic subband. To characterize the diffusion properties, we define a spectrally resolved delocalization time, which is, for a given energy, the characteristic time scale on which the electron leaves a given site. We find delocalization times substantially enhanced for states with a large phonon content, i.e., in the absence (presence) of alloy-type disorder at the high-energy edge(s) of the polaronic subband (mini-subbands). According to their delocalization times, we discriminate between “fast” quasi-particle-like and “sluggish” defect-like polaron states. Within the dynamical coherent potential approximation it is however impossible to determine the critical disorder needed to localize polaron states. Accordingly, mobility edges for polaron states cannot be determined. To overcome the limitations of the dynamical mean field theory, we adopted therefore the statistical dynamical mean-field theory to the disordered Holstein model. The second half of the chapter is a detailed discussion of this approach. It is largely based on Ref. [7], supplemented with materials from Refs. [5, 6]. The statistical dynamical mean field approximation maps the lattice problem on to an ensemble of self-consistently embedded impurity problems, in contrast to the single impurity problem obtained within the dynamical coherent potential approximation (viz. dynamical mean field approximation). It is not only capable of accounting the polaron formation process but also the spatial fluctuations giving rise to Anderson localization. The statistical dynamical mean field approximation is a probabilistic approach, focusing on the distributions instead of the average values for observables of interest. We employ a Monte-Carlo sampling technique to solve the self-consistent equations of the theory on a Bethe lattice with finite coordination number, representing distributions for random variables by random samples and discussing various ways to determine mobility edges from the random sample for the local Green function. Specifically, we give, as a function of the

“polaron parameters”, such as adiabaticity and electron-phonon coupling constants, a detailed discussion of the localization properties of a single polaron, using a bare electron as a reference system.

2.1 Introductory Remarks

There is a large variety of materials in which due to strong electron-phonon coupling electrons and phonons lose their identity and form new composite entities: polarons. Examples of current interest are, among others, the high-temperature superconducting perovskites [70, 71], the non-metallic nickelates and bismuthates [72, 73], the colossal magneto-resistance manganites [74], and semiconducting molecular crystals. [75] In all these materials, electronic properties, for instance, the electronic spectral function or the optical conductivity, show substantial polaronic effects. The most important signature in this respect is thermally activated transport (along at least one of the crystallographic axes).

The polaron concept has been introduced by Landau [76] and ever since it played a central role in the analysis of strongly coupled electron-phonon systems. In a deformable lattice, the coupling between an electron and the lattice leads to a lattice deformation whose potential tends to bind the electron. This process is called self-trapping, because the potential depends on the state of the electron. [77, 78] Translational symmetry is not broken in this process, transport at low enough temperatures is still coherent and band-like, with a much larger mass, however, because of the lattice distortion the electrons have to carry along. The self-trapping process, i.e. the formation of polarons, is therefore only the crossover from a weakly dressed electronic quasi-particle to a heavily dressed polaronic quasi-particle. Even the small polaron, although much less mobile than the bare electron, is still itinerant and not localized. [79]

Details of the actual materials notwithstanding, the Holstein model [80], which describes electrons locally coupled to dispersionless phonons, captures the essence of the self-trapping process. Most of the theoretical work is therefore directly based on the Holstein model. [81–86] Extensions to long-range electron-phonon couplings on a discrete lattice were discussed in Refs. [87]. Despite the extensive numerical simulations, the properties of the Holstein model are not yet fully understood, especially at finite densities, where the situation changes because of the interaction between polarons. But even in the extreme dilute limit, where polarons in first approximation do not interact, many questions remain. For instance, little is quantitatively known about polaron formation in a disordered environment. On the other hand, polaronic materials are complex materials, where chemical as well as crystallographic imperfections can be quite substantial. Accordingly, the self-trapping process, producing a heavy quasi-particle, occurs in an environment where, strictly speaking, translational symmetry is broken, and where defects most probably act as nucleation sites for the formation of polarons. Therefore, a complete theory of polaron formation has to take the disordered environment into account. In particular, the notoriously difficult question of whether polaron states are band states or localized defect states can be only meaningfully addressed in a context which takes the most important effect due to disorder, the possibility of Anderson localization, explicitly into account.

In his seminal work Anderson [88] has shown that disorder, if sufficiently strong, dramatically changes the properties of the electronic states in a solid. Whereas for small disorder the electronic states are extended Bloch waves, for large disorder electronic states are localized defect states. Anderson localization, i.e., the transition from extended to localized states, is well understood for noninteracting electrons (see, for instance, the review articles [89, 90]). It depends strongly on dimensionality. In one dimension (and arguably in two dimensions [91]) localized and extended states cannot coexist, because infinitesimally small disorder suffices to localize all states at once,

whereas in three dimensions mobility edges separate localized from extended states. Since the mobility edge is of utmost importance for the transport properties [92], an enormous amount of experimental and theoretical effort has been directed towards a precise determination of its position.

That Anderson localization might affect polaron formation, and vice versa, has been emphasized several times, starting with Anderson [93] himself, who pointed out that the mobility edge might be surrounded by self-trapped states. Not much quantitative work exists however to determine, for instance, the position of the mobility edge and its consequences for the conductivity [94, 95], or the character of the states near the mobility edge [96] taking electron-phonon coupling explicitly into account. Despite some occasionally fruitful adaptations of techniques from nonlinear dynamics [97], where polaron formation is considered as an intrinsic interaction-driven nonlinearity, the precise mechanisms of the interplay of Anderson localization and polaron formation are essentially unknown.

As a first step to address this problem we applied the dynamical coherent potential approximation (DCPA) to study a single electron in the Holstein model with binary disorder, focusing especially on polaron states at the high energy edge of the lowest polaronic subband. [4] These states are extremely sensitive to disorder, with a return probability which, due to the phonon admixture, is several orders of magnitude larger than for the states at the bottom of the subband. Within the DCPA it was however impossible to determine the critical disorder needed to localize polaron states. Accordingly, mobility edges for polaron states could not be determined. To overcome the limitations of the DCPA, we adopted therefore the statistical dynamical mean-field theory (statDMFT) [98], to the Holstein model with uniformly distributed on-site energies. [5–7] The statDMFT is not only capable of accounting the polaron formation process but also the spatial fluctuations giving rise to Anderson localization. Within the statDMFT we could clearly distinguish between itinerant and localized polaron states.

As a generic model for a disordered polaronic material, we use the Anderson-Holstein model

$$H = \sum_{i\sigma} \epsilon_i n_{i\sigma} - \sum_{i,j,\sigma} J_{ij} c_{i\sigma}^\dagger c_{j\sigma} + \Omega \sum_i b_i^\dagger b_i - \sqrt{E_p \Omega} \sum_{i\sigma} (b_i + b_i^\dagger) n_{i\sigma}, \quad (2.1)$$

where $n_{i\sigma} = c_{i\sigma}^\dagger c_{i\sigma}$ is the electron density on site i , the electron transfer integral $J_{ij} = J$ for (i, j) next neighbor sites and zero otherwise, Ω is the bare phonon energy ($\hbar = 1$), and E_p is the polaron shift. The on-site energies $\{\epsilon_i\}$ are assumed to be independent, identically distributed random variables. We consider two cases: A bi-modal distribution $p(\epsilon_i) = (1 - c)\delta(\epsilon_i - \epsilon_A) + c\delta(\epsilon_i - \epsilon_B)$, with c the concentration of the B sites (“Holstein alloy”) and a uniform distribution $p(\epsilon_i) = (1/\gamma)\theta(\gamma/2 - |\epsilon_i|)$.

The strength of disorder is either specified by $|\epsilon_A - \epsilon_B|$ or by the width γ of the distribution. The structure of the Anderson-Holstein model suggests to distinguish two regimes: The weakly disordered Holstein regime, where disorder is small on the scale of the bare bandwidth, and the strongly disordered Anderson regime, where disorder is large on the scale of the width of the polaronic subbands. The “polaron properties” of the Anderson-Holstein model are governed by two parameter ratios: the adiabaticity $\alpha = \Omega/J$, indicating whether the polaron is light $\alpha \ll 1$ or heavy $\alpha \gg 1$ [78], and a dimensionless electron-phonon coupling constant, $\lambda = E_p/2J$ or $g^2 = E_p/\Omega$. Polaron formation sets in if both $\lambda > 1$ and $g^2 > 1$. The internal structure depends on α , in particular the momentum dependent phonon admixture of the polaronic quasiparticle. It is quite different in the adiabatic ($\alpha \ll 1$), non-adiabatic ($\alpha \sim 1$), and anti-adiabatic ($\alpha \gg 1$) regimes. Another important effect occurs in the intermediate coupling regime, where electron-phonon coupling initiates long-range tunneling processes. [99] Evidently, how disorder

affects polaron states strongly depends on the polaron parameters. As a result, the ‘localization properties’ are expected to be quite different in the various polaronic regimes.

The plan of the remaining part of the chapter is as follows. Section 2.2 contains a general description of the DCPA for the Anderson-Holstein model. Representative numerical DCPA results for the “Holstein alloy” are discussed in Section 2.3. Section 2.4 summarizes the DCPA investigation, including its shortcomings, and motivates the statDMFT study of the Anderson-Holstein model. A detailed description of the statDMFT is given in Section 2.5. Numerical statDMFT results for the Anderson model and the Anderson-Holstein model, both with a uniform distribution of the on-site energies, are presented in Section 2.6.

2.2 Dynamical Coherent Potential Approximation (DCPA) [4]

In this section we adopt the dynamical coherent potential approximation (DCPA) and map the Anderson-Holstein model on to a single self-consistently embedded impurity site. This was the first approach we used to investigate the interplay between polaron formation and disorder. Although the DCPA does not enable us to distinguish between itinerant and localized polaron states, an asymptotic analysis of the spectrally resolved return probability already gives valuable insights into the diffusion properties of polaron states. [4] In Section 2.5 we then adopt a generalization of the effective single-site approximation – the statistical dynamical mean field theory (statDMFT) [98] – and map the Anderson-Holstein model on to an ensemble of self-consistently embedded impurity sites. Within the statDMFT we are then able to clearly distinguish between localized and itinerant states. [5–7]

2.2.1 The Concept of an Effective Single Site

In contrast to the Anderson model, where an electron experiences only elastic impurity scattering, the electron in the Anderson-Holstein model is subject to elastic impurity and inelastic phonon scattering. It is therefore necessary to treat them simultaneously. In particular, averages over the phonon vacuum and quenched disorder need to be performed on an equal footing.

A powerful tool to approximately perform these two averages is the effective single-site approximation, where one embeds an individual scatterer into an effective medium to be determined self-consistently by enforcing the scattering from a single scatterer to vanish on the average. This scheme maps the lattice problem on to a single impurity problem in such way that local correlations are treated non-perturbatively (see Fig. 2.1). This is particularly important for polaron formation, which is a non-perturbative effect. Inter-site correlations, on the other hand, which are for instance crucial for Anderson localization, are only treated in mean field approximation. As a result, within an effective single-site approximation, itinerant and localized polaron states cannot be distinguished.

In the case of elastic impurity scattering the effective single-site approximation yields the well-known coherent potential approximation (CPA). [100–103] The DCPA, originally developed by Sumi [104], is a direct extension of the CPA to problems involving *inelastic* scattering. It has been primarily used to investigate linear [104,105] and nonlinear [106–108] optical properties of polaron-excitons in molecular crystals. However, it can be applied to any on-site inelastic scattering process. Paquet and Leroux-Hugon [109] employed the DCPA, e.g., to investigate a single quantum particle subject to an on-site potential which fluctuates in time according to discrete or continuous Markov processes.

The CPA as well as the DCPA are effective single-site approximations for a single electron subject to impurity or phonon scattering, respectively. The most general effective single-site ap-

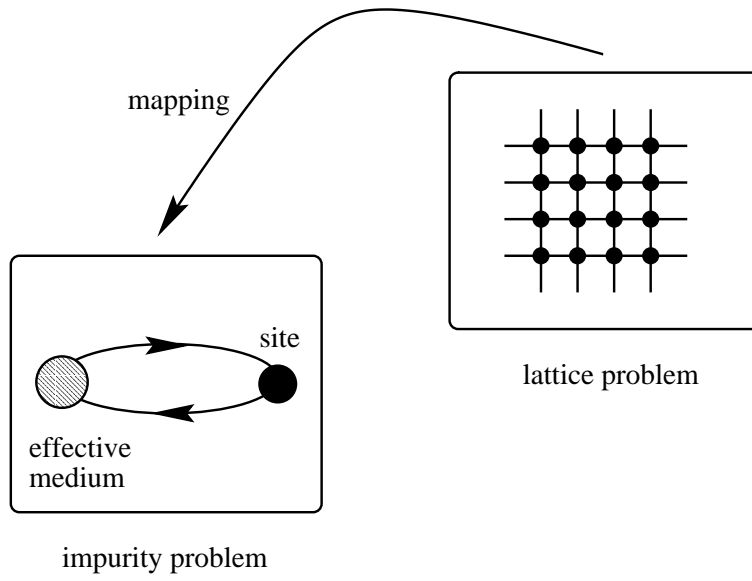


Figure 2.1: Illustration of the “philosophy” behind an effective single-site approximation. The lattice problem is mapped on to a single impurity problem, that is, a single self-consistently embedded site. The effective medium has to be determined self-consistently. The coherent potential approximation (CPA), the dynamical coherent potential approximation (DCPA), as well as the dynamical mean field theory (DMFT) belong to this group of approximations.

proximation, applicable also to dense quantum systems with mutual inelastic scattering between its constituents, is the dynamical mean field theory (DMFT). [110–112] [Naturally, in the limit of a single electron, interacting with a bath (of phonons or random scatterers), the DMFT reduces to the (D)CPA.] It can be shown, assuming that the nearest-neighbor hopping integral is scaled by a factor $1/\sqrt{Z}$, where Z denotes the coordination number of the lattice¹, that the DMFT provides an exact solution of the original model in the limit of $Z \rightarrow \infty$. Accordingly, the DMFT [i.e., in the respective limits, the (D)CPA] can be either considered as an exact theory for lattices with $Z = \infty$ or as an approximate theory for lattices with finite Z . The DMFT has been employed by Ciuchi and coworkers [113] to study, in various electron-phonon coupling regimes, the groundstate and the spectral properties of a single electron in the Holstein model. As indicated above, for a single electron, the DMFT reduces to the DCPA. The investigations of Sumi and Ciuchi et al. are therefore closely related.

Because we are interested in spectral and diffusion properties of a *single* electron, we mostly use the notation of the (D)CPA, avoiding the field-theoretical language of the DMFT. In the single-electron sector, the spin is irrelevant and the Anderson-Holstein model (2.1) becomes

$$\begin{aligned}
 H = & \sum_i \epsilon_i |i\rangle\langle i| - \sum_{i,j} J_{ij} |i\rangle\langle j| + \Omega \sum_i b_i^\dagger b_i \\
 & - \sqrt{E_p \Omega} \sum_i (b_i + b_i^\dagger) |i\rangle\langle i|,
 \end{aligned} \tag{2.2}$$

where $|i\rangle$ denotes the Wannier state on site i . Spectral properties of the model (2.2), such as the density of states, the self-energy, and the spectral function, can be deduced from the electronic

¹The coordination number Z of a lattice is the number of nearest neighbors. Sometimes the connectivity $K = Z - 1$ is used instead to characterize a lattice.

two-point function, which at temperature $T = 0$ and in Wannier representation reads

$$\mathcal{G}_{ij}(z) = \langle i | G^{\text{ave}}(z) | j \rangle, \quad (2.3)$$

with an averaged one-resolvent

$$G^{\text{ave}}(z) = \langle\langle (0 | G(z) | 0) \rangle\rangle. \quad (2.4)$$

Here, $G(z) = 1/(z - H)$ denotes the one-resolvent and $\langle\langle \dots \rangle\rangle$ and $(0 | \dots | 0)$ stand, respectively, for averages over the quenched disorder and the phonon vacuum. Henceforth, the term ‘‘averaged’’ implies, if not otherwise specified, averaged over both quenched disorder and the phonon vacuum.

From the spectral properties alone it is, in general, not possible to decide whether the states involved are itinerant or localized. A more reliable method to discriminate between the two kinds of states is to investigate the return probability P , i.e., the probability to find (in the long time limit) the electron on the same site at which it was initially injected. [114] At $T = 0$ and in Wannier representation, the correlation function, whose long time limit is the return probability, reads

$$P(t) = \langle\langle (0 | \langle i | e^{iHt} | i \rangle \langle i | e^{-iHt} | i \rangle | 0) \rangle\rangle. \quad (2.5)$$

Using Abel’s theorem, P can be conveniently expressed in terms of $p(2\eta)$, the Laplace transform of $1/2P(t/2)$. [114] Explicitly,

$$\begin{aligned} P &= \lim_{t \rightarrow \infty} P(t) \\ &= \lim_{\eta \rightarrow 0} 2\eta p(2\eta) \\ &= \lim_{\eta \rightarrow 0} 2\eta \int_{-\infty}^{\infty} \frac{d\omega}{2\pi} f(\omega - i\eta, \omega + i\eta), \end{aligned} \quad (2.6)$$

where we have defined a four-point function

$$f(z_1, z_2) = \langle i | K^{\text{ave}}(z_1, |i\rangle \langle i|, z_2) | i \rangle, \quad (2.7)$$

given in terms of an averaged two-resolvent, which (for an arbitrary electronic operator O_e) reads

$$K^{\text{ave}}(z_1, O_e, z_2) = \langle\langle (0 | G(z_1) O_e G(z_2) | 0) \rangle\rangle. \quad (2.8)$$

The behavior of the spectrally resolved return probability,

$$P(\omega, \eta) = 2\eta f(\omega - i\eta, \omega + i\eta), \quad (2.9)$$

in the limit $\eta \rightarrow 0$ allows one to distinguish localized from itinerant states. In particular, for a localized polaronic defect state, $\lim_{\eta \rightarrow 0} P(\omega, \eta)$ is finite, whereas for an itinerant polaronic quasi-particle state $\lim_{\eta \rightarrow 0} P(\omega, \eta)$ vanishes.

In the following we calculate the averaged one- and two resolvents within the DCPA.

2.2.2 Calculation of the One-Resolvent

In the spirit of the CPA we introduce an effective medium described by an effective one-resolvent

$$\bar{G}(z) = \frac{1}{z - \bar{H}(z)}, \quad (2.10)$$

with

$$\bar{H}(z) = H_0 + \Sigma(z), \quad (2.11)$$

and

$$H_0 = - \sum_{i,j} J_{ij} |i\rangle\langle j| + \Omega \sum_i b_i^\dagger b_i. \quad (2.12)$$

The unknown energy-dependent coherent potential (self-energy) operator $\Sigma(z)$ defined with respect to the reference Hamiltonian H_0 will be specified by enforcing a self-consistency condition, namely the averaged one-resolvent is forced to be equal to the averaged effective one-resolvent, i.e.,

$$G^{\text{ave}}(z) = \langle 0 | \bar{G}(z) | 0 \rangle, \quad (2.13)$$

where we have used the configuration independence of $\bar{G}(z)$.

In the above equations, the energy variable z denotes the *total* energy of the coupled electron-phonon system and not just the electron energy. The coherent potential seen by the electron, on the other hand, depends of course only on the electron energy. Therefore, the energy argument of the coherent potential is the total energy z minus the lattice energy, which is, neglecting the zero point motion of the phonons, just the total number of phonons in the system times the phonon energy. A convenient way to ensure that the coherent potential is only a function of the electron energy is to define, following Ref. [109], a set of projection operators P_q , which project onto the phonon subspace with a total number of q phonons, and to write for the coherent potential operator

$$\begin{aligned} \Sigma(z) &= \sum_q \sum_i P_q \Sigma_i^{(q)}(z) \\ &= \sum_q \sum_i P_q v^{(q)}(z) |i\rangle\langle i|, \end{aligned} \quad (2.14)$$

with $v^{(q)}(z) = v(z - q\Omega)$. From now on we shall adopt the convention that any operator or function with a superscript (q) has to be taken at the energy $z - q\Omega$. Note, in accordance with the spirit of the CPA, that the coherent potential $v(z)$ does not contain any spatial information: It neither depends on the site nor on the spatial distribution of the excited phonons.

Combining this ansatz for $\Sigma(z)$ with Eq. (2.10), we obtain for the effective one-resolvent

$$\bar{G}(z) = \sum_q P_q g^{(q)}(z), \quad (2.15)$$

with auxiliary (electronic) operators

$$g^{(q)}(z) = \frac{1}{z - q\Omega - \sum_{\vec{k}} [\epsilon_{\vec{k}} + v^{(q)}(z)] |\vec{k}\rangle\langle \vec{k}|}, \quad (2.16)$$

with $\epsilon_{\vec{k}}$ the band structure of the lattice as specified by transfer matrix elements J_{ij} .

Apparently, in contrast to the full one-resolvent $G(z)$, the effective one-resolvent $\bar{G}(z)$ is a simple operator in the phonon Hilbert space. For an arbitrary phonon state $|\{n_l\}\rangle$,

$$\bar{G}(z) |\{n_l\}\rangle = g^{(\sum_l n_l)}(z) |\{n_l\}\rangle \quad (2.17)$$

holds, i.e., (phonon) subspaces with different total phonon number are decoupled and, as a consequence, the self-consistency condition Eq. (2.13) becomes

$$G^{\text{ave}}(z) = g^{(0)}(z). \quad (2.18)$$

In order to derive a functional equation for the unknown function $v(z)$, which in turn specifies $G^{\text{ave}}(z)$, we perform a multiple-scattering analysis in the product Hilbert space of the coupled electron-phonon system. Except for the underlying Hilbert space, the mathematical manipulations parallel the CPA multiple-scattering analysis of Ref. [101]. The basic relation between the full and effective one-resolvents,

$$G(z) = \bar{G}(z) + \bar{G}(z)T(z)\bar{G}(z), \quad (2.19)$$

involves the total T-matrix,

$$T(z) = \sum_i Q_i(z), \quad (2.20)$$

which, according to Ref. [101], can be expressed in terms of individual single-site contributions

$$Q_i(z) = t_i(z) \left[1 + \bar{G}(z) \sum_{j \neq i} Q_j(z) \right], \quad (2.21)$$

with the atomic T-matrix given by

$$t_i(z) = [1 - \Delta H_i(z)\bar{G}(z)]^{-1} \Delta H_i(z). \quad (2.22)$$

From Eq. (2.21) we see that $Q_i(z)$ is a product of the atomic T-matrices $t_i(z)$ and an effective wave factor $[1 + \bar{G}(z) \sum_{j \neq i} Q_j(z)]$ describing an effective wave incident on site i modified by multiple-scattering events. The single-site perturbation

$$\Delta H_i(z) = \left[\epsilon_i - \sqrt{E_p \Omega} (b_i^\dagger + b_i) - \sum_q P_q v^{(q)}(z) \right] |i\rangle \langle i|, \quad (2.23)$$

comprises on-site energy fluctuations due to material imperfections and coupling to localized phonons on site i .

Combining Eq. (2.19) with Eq.(2.20) and taking Eq. (2.17) into account, the self-consistency condition Eq. (2.18) is satisfied if we enforce

$$\langle\langle 0|Q_i(z)|0\rangle\rangle = 0. \quad (2.24)$$

Iteration of Eq. (2.24) gives rise to an intractable infinite series involving *all* sites of the lattice. The standard procedure to obtain a numerically feasible description is to factorize the average in Eq. (2.24) into a product of averages, i.e., to average atomic T-matrices and effective wave factors separately. Relegating a discussion of the factorization procedure to the next subsection, we approximate Eq. (2.24) by

$$\begin{aligned} \langle\langle 0|Q_i(z)|0\rangle\rangle &\approx \langle\langle 0|t_i(z)|0\rangle\rangle \\ &\times \langle\langle 0|1 + \bar{G}(z) \sum_{j \neq i} Q_j(z)|0\rangle\rangle, \end{aligned} \quad (2.25)$$

reducing thereby the self-consistency condition to $\langle\langle(0|t_i(z)|0)\rangle\rangle = 0$. Because phonons on sites $j \neq i$ are not affected by scattering events encoded in $t_i(z)$ (they are “frozen” and act only as “spectators”), the single-site self-consistency condition can be formulated more generally as

$$\begin{aligned} \langle\langle(N, 0_i|t_i(z)|0_i, N)\rangle\rangle &= \langle\langle(0, 0_i|t_i^{(N)}(z)|0_i, 0)\rangle\rangle \\ &= 0 \quad \forall N, \end{aligned} \quad (2.26)$$

where $|n_i, N\rangle$ denotes an arbitrary phonon state with n phonons on site i and a total number of N phonons on all the other sites. Note the usage of the superscript notation defined above. The physical interpretation of Eq. (2.26) is the following: The electron “remembers” how many virtual phonons it has excited in previous scattering events (and, accordingly, how much energy is stored in the lattice); it does not “remember”, however, at which sites these events took place.

Instead of working directly with Eq. (2.26), it is more convenient to introduce an equivalent polaron-impurity model (PIM) [107], which describes a single perturbation $\Delta H_i(z)$ self-consistently embedded into an effective medium. Mathematically, the PIM is formulated by

$$D_i(z) = \bar{G}(z) + \bar{G}(z)t_i(z)\bar{G}(z) \quad (2.27)$$

$$= \bar{G}(z) + \bar{G}(z)\Delta H_i(z)D_i(z). \quad (2.28)$$

The self-consistency equation (2.26) is then transformed into

$$\langle\langle(0, 0_i|D_i^{(N)}(z)|0_i, 0)\rangle\rangle = g^{(N)}(z), \quad (2.29)$$

which in turn yields for the averaged one-resolvent

$$G^{\text{ave}}(z) = g^{(0)}(z) = \langle\langle(0, 0_i|D_i(z)|0_i, 0)\rangle\rangle. \quad (2.30)$$

As shown in Appendix A, it is straightforward to derive from the PIM a non-linear functional equation for the local two-point function. We get

$$\mathcal{G}_{ii}(z) = \int d\epsilon_i \frac{p(\epsilon_i)}{[F^{(0)}(z; \epsilon_i)]^{-1} - \frac{E_p\Omega}{[F^{(1)}(z; \epsilon_i)]^{-1} - \frac{2E_p\Omega}{[F^{(2)}(z; \epsilon_i)]^{-1} - \frac{3E_p\Omega}{\dots}}}, \quad (2.31)$$

with

$$F^{(n)}(z; \epsilon_i) = \frac{1}{z - n\Omega - \epsilon_i + \mathcal{G}_{ii}^{-1}(z - n\Omega) - \mathcal{R}[\mathcal{G}_{ii}(z - n\Omega)]}, \quad (2.32)$$

where $\mathcal{R}[\xi]$ denotes the inverse Hilbert transform (see below).

For $p(\epsilon_i) = \delta(\epsilon_i)$ Eqs. (2.31)–(2.32) have been given by Sumi [104] and independently by Ciuchi and coworkers. [113] Various limits of the “clean equations”, e.g., weak, intermediate, and strong electron-phonon coupling limits, have been discussed in these references. The non-linear functional couples local two-point functions with energies shifted by any *negative* integer multiple of Ω . This accounts for the fact that at zero temperature only phonon emission is possible. At finite temperature, in contrast, absorption of thermally excited phonons is also allowed. In that case, local two-point functions with energies shifted by *any* integer multiple of Ω , negative as well as positive, would be coupled. [104, 113]

The coherent potential $v(z)$ can be directly obtained from Eq. (2.30). Specifically, introducing the Hilbert transform $\tilde{N}_0[\xi]$ corresponding to the bare density of states $N_0(E) = (1/N) \sum_{\vec{k}} \delta(E - \epsilon_{\vec{k}})$, the local two-point function can be written as

$$\begin{aligned} \mathcal{G}_{ii}(z) &= \int dE \frac{N_0(E)}{z - v^{(0)}(z) - E} \\ &= \tilde{N}_0[z - v^{(0)}(z)]. \end{aligned} \quad (2.33)$$

Employing the inverse Hilbert transform, defined by $\mathcal{R} * \tilde{N}_0[\xi] = \xi$, finally leads to

$$v^{(0)}(z) = z - \mathcal{R}[\mathcal{G}_{ii}(z)]. \quad (2.34)$$

The local two-point function $\mathcal{G}_{ii}(z)$ uniquely determines the coherent potential $v^{(0)}(z)$. Once $v^{(0)}(z)$ is known any matrix element of the averaged one-resolvent can be obtained.

2.2.3 Validity of the Factorization Procedure

So far, we employed a factorization procedure to reduce the multi-site self-consistency condition to a single-site condition. Clearly, the mathematically exact average of the operator Q_i contains many terms which are not zero, even if the atomic T-matrix vanishes. The single-site self-consistency condition can be only approximate. We now analyze the validity of the factorization procedure taking advantage of the connection between the DCPA and the DMFT. As a by-product, we shall find an efficient way to derive the DCPA equations for the averaged two-resolvent.

To that end, we follow Ref. [115] and rearrange the multiple-scattering series into clusters containing a fixed number p of lattice sites. We write (suppressing the energy variable z)

$$Q_i = \sum_p Q_i^{[p]}, \quad (2.35)$$

with $Q_i^{[1]} = t_i$ and

$$\begin{aligned} Q_i^{[p]} &= t_i \sum_{j_1 \neq i} \bar{G} t_{j_1}^{[2]}(i) \sum_{j_2 \neq i, j_1} \bar{G} t_{j_2}^{[3]}(i, j_1) \\ &\dots \sum_{j_{p-1} \neq i, j_1, \dots, j_{p-2}} \bar{G} t_{j_{p-1}}^{[p]}(i, j_1, \dots, j_{p-2}) \end{aligned} \quad (2.36)$$

for $p \geq 2$. The cluster T-matrices $t_{j_{p-1}}^{[p]}(i, j_1, \dots, j_{p-2})$ are defined as the sum of all scattering processes involving at most p *different* sites i, j_1, \dots, j_{p-1} with the constraint that the entrance site has to be j_{p-1} . This constraint ensures that all p sites contributing to $Q_i^{[p]}$ are connected. The exit site, on the other hand, can be any site of the p -cluster. Notice that, in contrast to the original multiple-scattering series given in Eq. (2.21), where only successive summation indices had to be different, *all* summation indices in Eq. (2.36) are different.

We are now in a position to evaluate the importance of each individual multiple-scattering term contributing to Q_i . Keeping in mind that all processes where a site j is visited only once vanish due to the single-site self-consistency condition Eq. (2.26), only processes where *all* sites are *at least* visited twice require further analysis. Figure 2.2 schematically depicts the first non-vanishing $p = 2$ process (i.e., a fourth order process in which each of the two sites is visited twice). Writing

$$t_{nm}^{(r)} = \langle i | (0, n_i | t_i^{(r)} | m_i, 0) | i \rangle \quad (2.37)$$

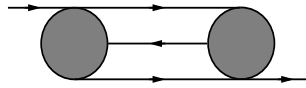


Figure 2.2: Schematic representation of a fourth order process contributing to $Q_i^{[2]}$. Atomic T-matrices and effective one-resolvents are, respectively, depicted by solid circles and solid lines. The arrows indicate the order in which the diagram has to be read. The energy arguments are clear from the context.

for the (configuration dependent) matrix elements of the atomic T-matrix, this process is analytically given by

$$Q_i^{[2],4^{th}} = \sum_{j \neq i, qr} t_{0r}^{(0)} \mathcal{G}_{ij}^{(r)} t_{0q}^{(r)} \mathcal{G}_{ji}^{(r+q)} t_{r0}^{(q)} \mathcal{G}_{ij}^{(q)} t_{q0}^{(0)} |i \rangle \langle j|. \quad (2.38)$$

To proceed further, we now imagine at this point that the hopping matrix element is scaled by $1/\sqrt{Z}$ (as in the case of the DMFT). Then, we immediately see that for large Z Eq. (2.38) is at least $\sim 1/\sqrt{Z}$ because it contains three off-diagonal two-point functions and only one free summation over sites j , i.e., for $Z \rightarrow \infty$ this process does not contribute to Q_i at all. In fact, it can be shown that all p -cluster processes in which *all* p sites are at least visited twice are suppressed by a factor containing the inverse of the coordination number Z . As a consequence, for $Z \rightarrow \infty$ these processes vanish and need not be explicitly considered in the averaging procedure.

The implication of the above discussion is three-fold. First, it corroborates, using multiple-scattering theory, the conventional CPA technique, previous work by Vlaming and Vollhardt [116], who showed, acknowledging earlier work by Schwartz and Siggia [117], that for a lattice with infinite coordination number any CPA-type theory becomes exact, i.e., for infinite coordination number, the single-site self-consistency condition is indeed sufficient to ensure that the average of Q_i as a whole vanishes.

Second, it indicates that even for a finite coordination number, processes which do not vanish due to the single-site self-consistency condition are at least suppressed.

Third, from a formal point of view, the DCPA is equivalent to the replacement of the full operator Q_i by a reduced operator Q_i^{SAP} containing only *self-avoiding paths* (SAP); Q_i^{SAP} can be obtained from Eq. (2.36) by setting $t_{j_{p-1}}^{[p]}(i, j_1, \dots, j_{p-2}) = t_{j_{p-1}} \forall p$. The coherent potential $v(z)$ is then adjusted in such a way that the averaged Q_i^{SAP} vanishes. This procedure can be envisaged, in physical terms, as a *loss of spatial memory*, because the electron “assumes” that each site it encounters is visited the first time, i.e., the electron does not “remember” whether it has visited the site before. Naturally, for a lattice with infinite coordination number, this is exact, because the probability that the electron returns to the same lattice site is vanishingly small.

The replacement $Q_i \rightarrow Q_i^{SAP}$, i.e., the erasure of the spatial memory of the electron, is of course consistent with the ansatz for the (local) self-energy operator. On the other hand, this replacement leads to an insufficient treatment of inter-site processes in the calculation of the averaged two-resolvent and, eventually, prevents a rigorous calculation of the diffusion and localization properties within the DCPA.

Keeping this shortcoming in mind, we shall nevertheless employ this formal replacement from the outset in the next subsection to simplify the calculation of the four-point function.

2.2.4 Calculation of the Two-Resolvent

The discussion of the previous subsection suggests that the single-site self-consistency condition is, from a formal point of view, equivalent to the replacement $Q_i \rightarrow Q_i^{SAP}$, i.e., only SAPs need

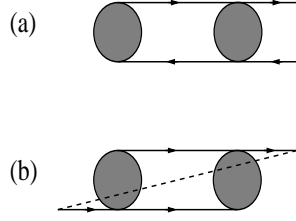


Figure 2.3: Schematic representation of the second order (ladder) process contributing to the local DCPA vertex (a) and of the second order (maximally crossed) process neglected within the DCPA (b). The dashed line depicts the operator O_e and solid circles and lines stand, respectively, for atomic T-matrices and effective one-resolvents. The arrows indicate the order in which the diagrams have to be read. The energy arguments are clear from the context.

to be explicitly considered in the averaging procedure. We now show that this replacement allows a rather straightforward derivation of the averaged two-resolvent.

For that purpose, we first recast Eq. (2.8), using Eqs. (2.17) and (2.19) together with the self-consistency condition, Eq. (2.26), into

$$K^{\text{ave}}(z_1, O_e, z_2) = g^{(0)}(z_1) [O_e + \Gamma^{\text{ave}}(z_1, O_e, z_2)] g^{(0)}(z_2). \quad (2.39)$$

Keeping only site-diagonal terms, the electronic vertex operator is given by

$$\Gamma^{\text{ave}}(z_1, O_e, z_2) = \sum_i \langle \langle 0 | \Gamma_i(z_1, O_e, z_2) | 0 \rangle \rangle, \quad (2.40)$$

with a local vertex operator

$$\Gamma_i(z_1, O_e, z_2) = Q_i^{\text{SAP}}(z_1) \bar{G}(z_1) O_e \bar{G}(z_2) \tilde{Q}_i^{\text{SAP}}(z_2). \quad (2.41)$$

In the above equations we have kept only retraceable SAP's where the second leg of the path, encoded in \tilde{Q}_i^{SAP} , retraces in *reversed* order the first leg of the path, encoded in Q_i^{SAP} and neglected retraceable SAP's where the second leg retraces the first leg in the *same* order. In more familiar terms (see Fig. 2.3), we have kept the ladder diagrams and neglected (maximally) crossed diagrams. This choice is consistent with the coherent potential determined in the previous subsection. In particular, as shown in Appendix B, the local vertex defined in the ladder approximation and the local self-energy obey the Ward identity corresponding to particle conservation. [102]

In analogy to the localization problem in the Anderson model, which contains only quenched disorder, we expect the maximally crossed diagrams to yield a significant (for certain model parameters possibly diverging) contribution to the local vertex function. As a consequence, a consistent treatment of these processes might render the potential to force $\lim_{\eta \rightarrow 0} P(\omega, \eta)$ to be finite for some energies ω and for certain model parameters. Accordingly, itinerant and localized polaron states could be rigorously distinguished. We did not, however, succeed in taking these diagrams into account. In Refs. [5–7], we adopted therefore an alternative approach, which is not based on a diagrammatic expansion of the one- or two-resolvents in terms of atomic T-matrices. Instead, it is based on the construction of random samples for local observables. From a probabilistic analysis of the random samples for the imaginary part of the local two-point function it is then possible to develop a criterion which allows to distinguish between itinerant and localized polaron states. This approach will be described in Section 2.5.

To derive an explicit equation for the local vertex function (in the ladder approximation), we have to perform the average of Eq. (2.41). To that end, it is advantageous to derive a formal

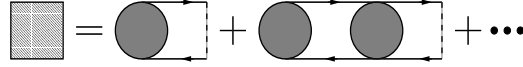


Figure 2.4: Schematic representation of Eq. (2.41). The box on the left hand side denotes the local vertex operator Γ_i , the dashed line depicts the operator O_e , and solid circles and lines stand, respectively, for atomic T-matrices and effective one-resolvents. The arrows indicate the order in which the diagram has to be read. The energy arguments are clear from the context.

operator equation for the local vertex operator Γ_i . For simplicity, we shall from now on suppress the arguments of the various operators. The implied arguments should be clear from the context. If we visualize Eq. (2.41) in terms of diagrams (see Fig. 2.4), we readily obtain

$$\Gamma_i = t_i \bar{G} \left[O_e + \sum_{j \neq i} \Gamma_j^{(i)} \right] \bar{G} t_i, \quad (2.42)$$

where $\Gamma_j^{(i)}$ stands for the vertex operator on site j given by summing up all “ladder-type paths” not visiting site i . Consequently, as far as the configuration average is concerned, the atomic T-matrices t_i and the term between the brackets are statistically independent and the configuration average factorizes, i.e.,

$$\langle\langle \Gamma_i \rangle\rangle = \langle\langle t_i \bar{G} \langle\langle O_e + \sum_{j \neq i} \Gamma_j^{(i)} \rangle\rangle \bar{G} t_i \rangle\rangle. \quad (2.43)$$

For a macroscopic solid we expect $\langle\langle \Gamma_j^{(i)} \rangle\rangle$ essentially to be the same operator as $\langle\langle \Gamma_j \rangle\rangle$. Hence, if we dealt only with quenched disorder, Eq. (2.43) would be the result given by Velický. [102] To cope with inelastic scattering, we have to keep in mind, however, that the vertex function (similar to the coherent potential) depends only on the electron energy, i.e., we have to keep track of the energy stored in the lattice (given by the total number of virtual phonons). Consistent with the ansatz for the local self-energy operator, we therefore write

$$\begin{aligned} \langle\langle \Gamma_i \rangle\rangle &= \sum_q P_q \Gamma_i^{(q)} \\ &= \sum_q P_q \gamma_i^{(q)} |i\rangle \langle i|, \end{aligned} \quad (2.44)$$

with $\gamma_i^{(q)} = \gamma_i(z_1 - q\Omega, O_e, z_2 - q\Omega)$. Thus, the phonon vacuum expectation value of Eq. (2.43) becomes

$$\gamma_i^{(0)} = \langle\langle \sum_q t_{0q}^{(0)} \left[K_i^{(q)} - \mathcal{G}_{ii}^{(q)} \gamma_i^{(q)} \mathcal{G}_{ii}^{(q)} \right] t_{q0}^{(0)} \rangle\rangle, \quad (2.45)$$

with

$$K_i^{(q)} = \langle i | g^{(q)} O_e g^{(q)} | i \rangle + \sum_l \mathcal{G}_{il}^{(q)} \gamma_l^{(q)} \mathcal{G}_{li}^{(q)}. \quad (2.46)$$

Note, the only configuration dependent quantities are now the matrix elements of the atomic T-matrix.

The linear functional for the vertex function is not “local” in the energy variables z_1 and z_2 . Instead, due to the possibility of phonon emission, Eq. (2.45) couples all vertex functions with energies shifted by any *negative* integer multiple of Ω .

Employing spatial Fourier transforms,

$$K_{\vec{Q}}^{(r)} = \sum_i e^{-i\vec{Q}\cdot\vec{R}_i} K_i^{(r)}, \quad (2.47)$$

$$a_{\vec{Q}}^{(r)} = \sum_i e^{-i\vec{Q}\cdot\vec{R}_i} \langle i | g^{(r)} O_e g^{(r)} | i \rangle, \quad (2.48)$$

$$\mathcal{A}_{\vec{Q}}^{(r)} = \sum_{\vec{R}_i - \vec{R}_j} e^{-i\vec{Q}\cdot[\vec{R}_i - \vec{R}_j]} \mathcal{G}_{ij}^{(r)} \mathcal{G}_{ji}^{(r)}, \quad (2.49)$$

$$\gamma_{\vec{Q}}^{(r)} = \sum_i e^{-i\vec{Q}\cdot\vec{R}_i} \gamma_i^{(r)}, \quad (2.50)$$

it is straightforward to combine Eqs. (2.45) and (2.46) and to derive, after some rearrangements, a single equation for the Fourier-transformed local vertex function:

$$\gamma_{\vec{Q}}^{(0)} = \sum_q \langle \langle t_{0q}^{(0)} t_{q0}^{(0)} \rangle \rangle a_{\vec{Q}}^{(q)} + \sum_q \langle \langle t_{0q}^{(0)} t_{q0}^{(0)} \rangle \rangle \{ \mathcal{A}_{\vec{Q}}^{(q)} - \mathcal{G}_{ii}^{(q)} \mathcal{G}_{ii}^{(q)} \} \gamma_{\vec{Q}}^{(q)}. \quad (2.51)$$

This equation reduces in the limit $\Omega \rightarrow 0$ and $E_p \Omega = \text{const}$ to Velický's vertex equation [102] for a model with a Gaussian distribution of on-site energies on top of a bi-modal distribution of on-site energies. This is shown in Appendix C. Note, moreover, that $\gamma_{\vec{Q}}^{(0)}$ may be used to calculate *any* matrix element of the averaged two-resolvent of interest, i.e., the averaged two-resolvent is completely determined by $\gamma_{\vec{Q}}^{(0)}$.

2.2.5 Specification to a Bethe Lattice

So far, we neither specified the coordination number Z nor the structure of the underlying lattice. The DCPA equations for the one- and two-resolvents can be used for arbitrary lattices. On the other hand, we have shown in Subsection 2.2.3 that the single-site factorization procedure essentially ignores processes, where the electron returns to the same lattice site. It is therefore consistent with the DCPA to use a lattice, which, by construction, completely prohibits this type of processes, that is, a lattice which is loop-free. A particularly simple case is the $Z = \infty$ Bethe lattice. (It should be emphasized, however, that, within the DCPA, the numerical results, in particular for the spectrally resolved return probability, are not affected much by the chosen lattice.)

The main simplification, as far as the calculation of the local two-point function is concerned, arises from the fact that the inverse Hilbert transform for a $Z = \infty$ Bethe lattice is an algebraic relation, namely $\mathcal{R}[\xi] = (1/4)\xi + 1/\xi$, which makes the self-consistent solution of Eqs. (2.31)–(2.32) particularly easy.

The calculation of the local vertex function simplifies even more, because, for a $Z = \infty$ lattice, Eq. (2.49) reduces (for almost all \vec{Q}) to $\mathcal{A}_{\vec{Q}}^{(r)}(z_1, z_2) \approx \mathcal{G}_{ii}^{(r)}(z_1) \mathcal{G}_{ii}^{(r)}(z_2)$. [112] Therefore, the second term on the rhs of Eq. (2.51) vanishes and the local vertex function becomes

$$\gamma_{\vec{Q}}^{(0)} = \sum_q \langle \langle t_{0q}^{(0)} t_{q0}^{(0)} \rangle \rangle a_{\vec{Q}}^{(q)}, \quad (2.52)$$

which yields for the Fourier transform of Eq. (2.46):

$$K_{\vec{Q}}^{(0)} = a_{\vec{Q}}^{(0)} + \mathcal{G}_{ii}^{(0)} \mathcal{G}_{ii}^{(0)} \sum_q \langle \langle t_{0q}^{(0)} t_{q0}^{(0)} \rangle \rangle a_{\vec{Q}}^{(q)}. \quad (2.53)$$

To investigate the localization properties of the polaron states, we need the four-point function $f(z_1, z_2)$ defined in Eq. (2.7). To that end, we set $O_e = |i\rangle\langle i|$ in the above equation and obtain after Fourier transformation

$$f(z_1, z_2) = \mathcal{G}_{ii}(z_1)\mathcal{G}_{ii}(z_2) + \mathcal{G}_{ii}(z_1)\mathcal{G}_{ii}(z_2) \sum_q \langle\langle t_{0q}^{(0)}(z_1)t_{q0}^{(0)}(z_2) \rangle\rangle \mathcal{G}_{ii}^{(q)}(z_1)\mathcal{G}_{ii}^{(q)}(z_2). \quad (2.54)$$

This equation holds for any lattice with $Z = \infty$. The structure of the lattice, i.e., in our case, the structure of the Bethe lattice, enters only through the local two-point function $\mathcal{G}_{ii}(z)$.

In Appendix A we show that Eq. (2.54) can be brought into a numerically more convenient form,

$$f(\omega - i\eta, \omega + i\eta) = \sum_{r=0}^{\infty} \int d\epsilon_i p(\epsilon_i) |\mathcal{D}_{r0}^{(0)}(\omega + i\eta; \epsilon_i)|^2, \quad (2.55)$$

with amplitudes $\mathcal{D}_{r0}^{(0)}(\omega + i\eta; \epsilon_i)$ satisfying the recursion relation (A.10). Thus, the calculation of the four-point function $f(\omega - i\eta, \omega + i\eta)$ requires the same (moderate) numerical effort as the calculation of the local two-point function $\mathcal{G}_{ii}(\omega + i\eta)$.

The numerical strategy is now as follows. First, we truncate the continued fraction expansions in Eq. (2.31) and find the fixed point $\mathcal{G}_{ii}^{(fix)}(\omega + i\eta)$ by iteration. The density of states then follows directly from

$$N(\omega) = -\frac{1}{\pi} \text{Im} \mathcal{G}_{ii}^{(fix)}(\omega + i\eta). \quad (2.56)$$

For the Holstein alloy, that is, for on-site energies with a bi-modal distribution $p(\epsilon_i) = (1 - c)\delta(\epsilon_i - \epsilon_A) + c\delta(\epsilon_i - \epsilon_B)$, it is interesting to study the individual contributions of the A and B sites. We calculate therefore also the two component density of states in the Holstein alloy,

$$N_\lambda(\omega) = -\frac{1}{\pi} \text{Im} \mathcal{D}_{00}^{(0)}(\omega + i\eta; \epsilon_\lambda), \quad (2.57)$$

where $\lambda = A, B$. The two amplitudes $\mathcal{D}_{00}^{(0)}(\omega + i\eta; \epsilon_A)$ and $\mathcal{D}_{00}^{(0)}(\omega + i\eta; \epsilon_B)$, which are also needed in the calculation of the spectrally resolved return probability in the Holstein alloy (see below), are given by the integrand of Eq. (2.31) without the factor $p(\epsilon_i)$ and with $\epsilon_i = \epsilon_\lambda$ and $\mathcal{G}_{ii}(z) = \mathcal{G}_{ii}^{(fix)}(z)$.

Second, we insert $\mathcal{G}_{ii}^{(fix)}(\omega + i\eta)$ in Eq. (2.34) and obtain the coherent potential $v^{(0)}(\omega + i\eta)$, which yields, using Eqs. (2.16) and (2.18), the spectral function

$$A(\omega, \epsilon_{\vec{k}}) = -\frac{1}{\pi} \text{Im} \frac{1}{\omega + i\eta - \epsilon_{\vec{k}} - v^{(0)}(\omega + i\eta)}. \quad (2.58)$$

Third, to calculate the spectrally resolved return probability $P(\omega, \eta)$ defined in Eq. (2.9), we truncate the sums in Eq. (2.55) and successively construct the amplitudes $\mathcal{D}_{r0}^{(0)}(\omega + i\eta; \epsilon_i)$ from the recursion relation, Eq. (A.10), starting from $\mathcal{D}_{00}^{(0)}(\omega + i\eta; \epsilon_i)$. For the Holstein alloy, we only need two amplitudes: $\mathcal{D}_{r0}^{(0)}(\omega + i\eta; \epsilon_A)$ and $\mathcal{D}_{r0}^{(0)}(\omega + i\eta; \epsilon_B)$. The truncation procedures and the subsequent numerical solution of the truncated equations for small $\eta > 0$ converge very well.

Table 2.1: Polaron model parameters (in units of $2J$)

J	Ω	g	$\lambda = E_p/2J$	$\alpha = \Omega/J$
0.5	0.125	0.35	0.98	0.25

2.3 Numerical Results I [4]

In this section we present DCPA results for the Holstein model ($\gamma = 0$) and the Holstein alloy, where the on-site energies obey a bi-model distribution, $p(\epsilon_i) = (1 - c)\delta(\epsilon_i - \epsilon_A) + c\delta(\epsilon_i - \epsilon_B)$. We focus on the spectral and diffusion properties of that part of the spectrum, where we expect more rigorous theories, such as the statDMFT, to predict localized states. In particular, we investigate, in the intermediate electron-phonon coupling regime, the states comprising the high-energy edge of the lowest polaronic subband (minisubband) in the Holstein model (Holstein alloy). The dispersion is extremely flat in this part of the spectrum, indicating, perhaps, already the tendency towards localization. Indeed, the statDMFT will show that very small amounts of disorder suffice to drive these states into the localized regime.

2.3.1 Spectral Properties

We discuss the spectral properties of a subclass of polaron states, which we expect to be very susceptible to an extrinsic localization transition. However, as mentioned in subsection 2.2.1, spectral properties alone cannot be used, even within a rigorous theory, to decide whether states are itinerant or localized.

We start with the Holstein model [model (2.2) with $\delta = 0$], which we characterize by two parameters, $\lambda = E_p/2J$ and $\alpha = \Omega/J$.² These parameters are conventionally used to define strong, intermediate, and weak electron-phonon coupling regimes. [118] The overall DCPA spectral features of which have been thoroughly investigated by Ciuchi et al. [113] and by Sumi. [104] The most intriguing of these regimes is, perhaps, the intermediate electron-phonon coupling regime, approximately defined by $\lambda \geq 1$, where a finite number of polaronic subbands starts to develop on the low energy side of the bare density of states. The formation of these polaronic subbands, in particular as a function of λ and α , has been intensively studied in above mentioned references. For our purpose, it is sufficient to focus, for a fixed λ and α , on the *lowest* polaronic subband.

Generic numerical results for the Holstein model in the intermediate electron-phonon coupling regime are summarized in Fig. 2.5. The polaron parameters are given in Table 2.1. We first focus on panels (a) and (b), which depict the density of states $N(\omega)$, the imaginary part of the coherent potential $\text{Im}v(\omega)$, and the spectral function $A(\omega, \epsilon_{\vec{k}})$, respectively. The spectrally resolved return probability $P(\omega, \eta)$ shown in panel (c) will be discussed in the next subsection.

The main spectral characteristics in the intermediate electron-phonon coupling regime is the formation of a well-established lowest polaronic subband with an asymmetric, steep-like density of states, separated from the rest of the spectrum by a hard gap. Below the phonon emission threshold, which is inside the second polaronic subband, no residual scattering takes place, i.e., $\text{Im}v(\omega) = 0$. That is, within the lowest polaronic subband, the electron and the phonons arrange themselves into a new (composite) entity – a polaronic quasi-particle. [113] [The pole of $\text{Im}v(\omega)$ slightly above the high-energy edge of the lowest polaronic subband does not imply a diverging scattering rate; it merely signals the presence of the gap.] That the *quasi-particle concept* indeed

²In Ref. [4] λ and α were defined differently.

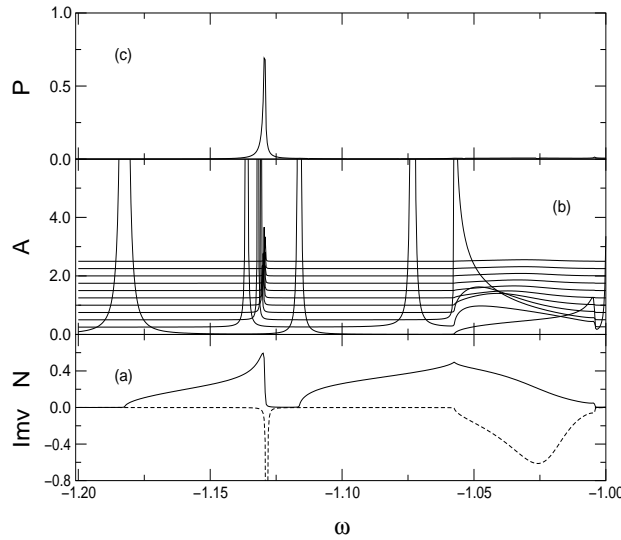


Figure 2.5: Spectral and diffusion properties of the Holstein model in the vicinity of the first polaronic subband for $\lambda = 0.98$, $\alpha = 0.25$ (see Table 2.1), and $\eta = 10^{-4}$. (a) Density of states $N(\omega)$ (solid line) and imaginary part of the coherent potential $\text{Im}v(\omega)$ (dashed line). (b) Spectral function $A(\omega, \epsilon_{\vec{k}})$ with $\epsilon_{\vec{k}}$ ranging from $\epsilon_{\vec{k}} = -1$ to $\epsilon_{\vec{k}} = 1$ (bottom to top) in steps of $\Delta\epsilon_{\vec{k}} = 0.2$. For clarity the spectral functions corresponding to different $\epsilon_{\vec{k}}$ are artificially shifted along the vertical axis. (c) Spectrally resolved return probability $P(\omega, \eta)$.

applies can be also seen from the spectral function, which features a (dispersive) quasi-particle peak in the energy range of the lowest polaronic subband. Notice the pronounced band flattening and the vanishing quasi-particle weight in the flat part of the dispersion. The band flattening is the reason for the steep-like density of states. At higher energies a second quasi-particle peak corresponding to the second polaronic subband is visible until the point where it merges with the one-phonon scattering continuum.

Both the steep-like shape of the density of states and the band flattening at the high-energy edge of the lowest polaronic subband are an *indirect* consequence of the pole in the imaginary part of the coherent potential. As can be seen in Figs. 2.6a and 2.6b, the pole in the imaginary part is accompanied by a divergence in the real part. (Both are broadened due to the finite value of η ; the pole becomes a Lorentzian and the divergence becomes a pronounced kink.) The divergence, in turn, induces a pronounced energy dependence of $\text{Re}v(\omega)$ just below the high-energy edge and it is this strong energy dependence which, as we shall show below, eventually yields the steep-like density of states and the band flattening. Physically, the energy dependence of the real part of the coherent potential reflects the increasing phonon admixture in the states as the high-energy edge of the subband is approached.

The discussion of the steep-like subband density of states is facilitated by considering

$$N_{1st}(\omega) = \frac{2}{\pi} \text{Re} \sqrt{1 - [\omega - \text{Re}v(\omega)]^2}, \quad (2.59)$$

an exact analytical expression for the lowest subband density of states, which follows from Eqs. (2.56) and (2.33) in the limit $\eta \rightarrow 0$ and the fact that for the lowest subband $\text{Im}v(\omega) = 0$. Two conclusions can be drawn from Eq. (2.59). First, the position ω_m of the maximum of the subband density of states does not coincide with the high-energy edge ω_h , because they are respectively given by $\omega_m - \text{Re}v(\omega_m) = 0$ (thin solid line in Fig. 2.6a) and $\omega_h - \text{Re}v(\omega_h) = 1$ (thin dashed line in Fig. 2.6a). Hence, the density of states at the high-energy edge is, albeit very step-like, not

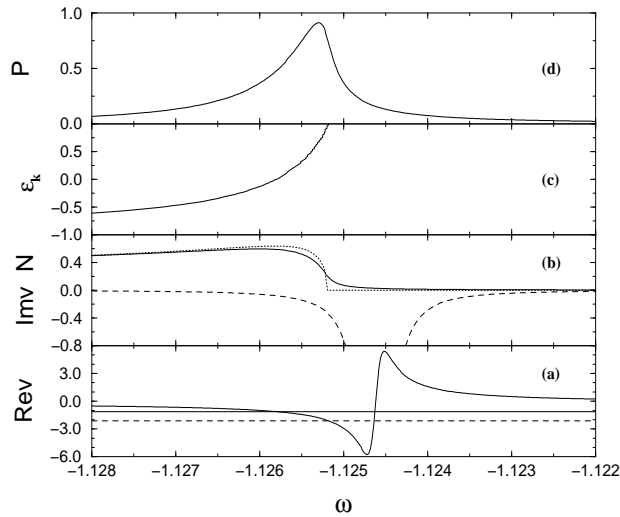


Figure 2.6: Blow-up of Fig. 2.5 in the immediate vicinity of the high-energy edge of the lowest polaronic subband. (a) Real part of the coherent potential $\text{Rev}(\omega)$ for $\eta = 10^{-4}$ (thick solid line). The interceptions with the thin and dashed solid lines determine, respectively, the maximum of the subband density of states and the position of the high-energy edge. (b) Density of states for $\eta = 10^{-4}$ (solid line) and $\eta = 10^{-8}$ (dotted line). The dashed line depicts the imaginary part of the coherent potential $\text{Im}v(\omega)$ for $\eta = 10^{-4}$. (c) The poles of the spectral function $\omega(\epsilon_{\vec{k}})$. Here we plot $\epsilon_{\vec{k}}$ vs. ω . (d) Spectrally resolved return probability $P(\omega, \eta)$ for $\eta = 10^{-4}$.

discontinuous, even for $\eta \rightarrow 0$. Second, Eq. (2.59) together with Figs. 2.6a and 2.6b reveal that the rapid change of $\text{Rev}(\omega)$ between ω_m and ω_h , caused by the divergence *above* ω_h , produces the rapidly dropping density of states in this particular energy range, and hence, the steep-like shape.

Figures 2.6a and 2.6c suggest, moreover, that the rapidly changing $\text{Rev}(\omega)$ is also responsible for the band flattening. To be more specific, we recall that the dispersion $\omega(\epsilon_{\vec{k}})$ is given by the poles of the spectral function defined in Eq. (2.58). Therefore, the change of the dispersion with $\epsilon_{\vec{k}}$ becomes

$$\frac{d\omega(\epsilon_{\vec{k}})}{d\epsilon_{\vec{k}}} = \left(1 - \frac{d\text{Rev}(\omega)}{d\omega}\bigg|_{\omega=\omega(\epsilon_{\vec{k}})}\right)^{-1}, \quad (2.60)$$

which is, of course, particularly small for $\omega_m \leq \omega \leq \omega_h$, since the divergence yields a large derivative of $\text{Rev}(\omega)$. It is, therefore, the *divergence-induced* strong ω -dependence of the real part of the coherent potential which not only causes the steep-like subband density of states but also the pronounced flattening of the subband dispersion.

The DCPA results for the lowest polaronic subband corroborate data obtained by direct numerical simulation of a finite Holstein model in the single-electron sector. [83,86,99] Specifically, the band flattening and the vanishing quasi-particle weight in the flat part of the dispersion are in good qualitative agreement. Both effects, characteristic of the intermediate electron-phonon coupling regime, are manifestations of the strong on-site electron-phonon correlations, which yield an increasing phonon admixture in the states comprising the high-energy edge of the lowest polaronic subband. [99]

Clearly, the phonon admixture in the states must significantly affect the diffusion properties. In particular, because the dispersion becomes extremely flat in the vicinity of the high-energy

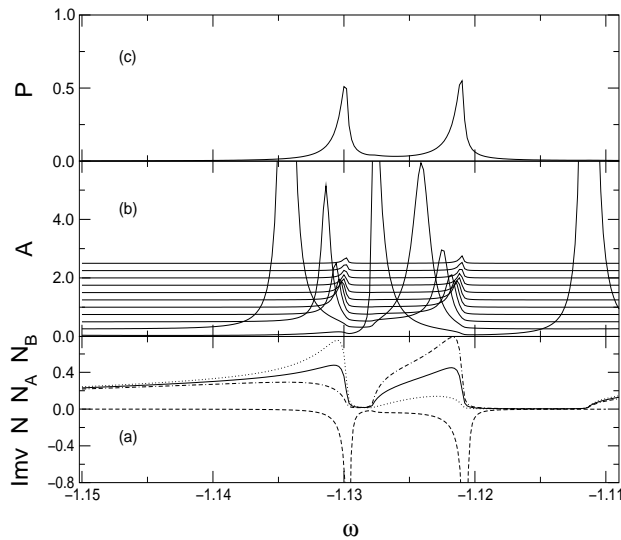


Figure 2.7: Spectral and diffusion properties of the Holstein alloy in the vicinity of the high-energy edge of the first polaronic subband for $c = 0.5$ and $\delta = -0.01$. The polaron parameters are $\lambda = 0.98$ and $\alpha = 0.25$ (see Table 2.1) and $\eta = 10^{-4}$. (a) Density of states $N(\omega)$ (solid line), component density of states $N_A(\omega)$ (dotted line) and $N_B(\omega)$ (dot-dashed line), and imaginary part of the coherent potential $\text{Im}v(\omega)$ (dashed line). (b) Spectral function $A(\omega, \epsilon_{\vec{k}})$ with $\epsilon_{\vec{k}}$ ranging from $\epsilon_{\vec{k}} = -1$ to $\epsilon_{\vec{k}} = 1$ (bottom to top) in steps of $\Delta\epsilon_{\vec{k}} = 0.2$. For clarity the spectral functions corresponding to different $\epsilon_{\vec{k}}$ are artificially shifted along the vertical axis. (c) Spectrally resolved return probability $P(\omega, \eta)$.

edge of the lowest polaronic subband, these states might be *temporarily* localized. In the next subsection, we will present an analysis of the spectrally resolved return probability $P(\omega, \eta)$, which indeed shows that the high-energy edge states are extremely “sluggish”.

However, first we illustrate the modifications of the lowest polaronic subband due to alloying. We expect disorder on the scale of the subband width to show the most dramatic effects and therefore restrict $\delta = \epsilon_A - \epsilon_B$ [in Eq. (2.2)] to small values. Further, to be specific, we chose the B atoms to be energetically close to the high-energy edge of the subbands, i.e., we consider $\delta < 0$.

Figure 2.7 shows representative numerical results for the Holstein alloy. The polaron parameters are the same as in Fig. 2.5 (see Table 2.1) and the alloy parameters are $c = 0.5$ and $\delta = -0.01$. First, we focus again on panels (a) and (b), which summarize the spectral properties in the vicinity of the lowest polaronic subband. The spectrally resolved return probability shown in panel (c) will be discussed in the next subsection.

The main effect of alloying is the formation of two mini-subbands. For the chosen parameters both mini-subband density of states exhibit a pronounced asymmetric, steeple-like shape (see Fig. 2.7a). From the strong asymmetry of the component density of states, which are also depicted in Fig. 2.7a, we find, moreover, that, although both A- and B-sites contribute to both mini-subbands, the steeple-like shape of the mini-subband density of states comes entirely either from the A-sites (lower mini-subband) or from the B-sites (upper mini-subband). As in the case without disorder, the steeple-like shape is due to strong on-site electron-phonon correlations, which yield a large phonon admixture in the states at the high-energy edges of the respective mini-subbands, and, as a consequence, to rather flat dispersions in these parts of the spectrum. The band flattening can be clearly seen from the spectral function shown in Fig. 2.7b.

The detailed appearance of the mini-subbands depends on the concentration c and the scattering strength δ . To indicate the concentration dependence, for example, we show in Fig. 2.8 the density of states $N(\omega)$ for a fixed scattering strength $\delta = -0.004$ and concentrations varying

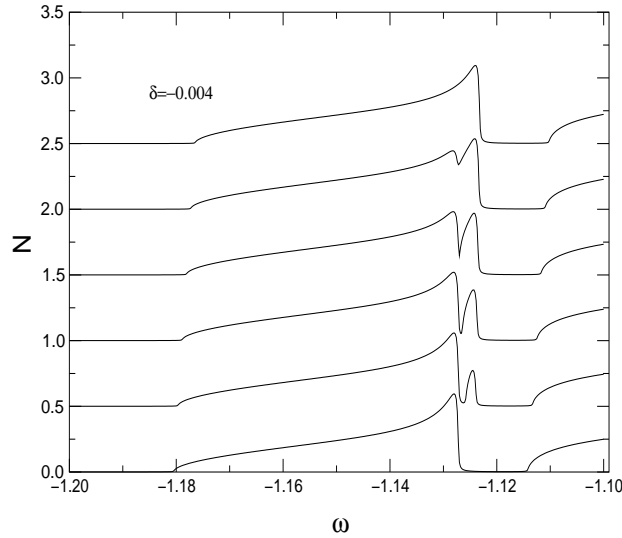


Figure 2.8: Density of states $N(\omega)$ for the Holstein alloy in the vicinity of the first polaronic subband. The polaron parameters are $\lambda = 0.98$ and $\alpha = 0.25$ (see Table 2.1) and $\eta = 10^{-4}$. The scattering strength $\delta = -0.004$ and the concentration of the B atoms varies from $c = 0.0$ (bottom) to $c = 1.0$ (top) in steps of $\Delta c = 0.2$. For clarity the density of states corresponding to different concentrations are artificially shifted along the vertical axis.

from the pure A crystal ($c = 0$) to the pure B crystal limit ($c = 1$). Note, first, the noticeable distortions of the density of states (at the high-energy edge) despite the fact that δ is much smaller than the polaronic subband width and, second, the lack of $c \leftrightarrow 1 - c$ symmetry. That rather small amounts of disorder suffice to restructure the high-energy edge can be also seen in Fig. 2.9, where the lower panel shows the density of states and the imaginary part of the coherent potential for $c = 0.5$ and three different scattering strengths δ .

It is not necessary to present an exhaustive investigation of the alloying-induced spectral changes in the whole $c - \delta$ parameter plane. The data presented suffice already to show that the modifications of the lowest polaronic subband are very similar to the ones found in an AB alloy with an *artificial* steple-like bare density of states. [119] Indeed, the broken $c \leftrightarrow 1 - c$ symmetry, the appearance of a B mini-subband at scattering strengths much smaller than the polaronic subband width, and the asymmetry between the component density of states have their counterparts in this artificial steple alloy.

In the artificial steple alloy, as well as in the Holstein alloy, states comprising the steple-like structure in the density of states are very susceptible to impurity scattering. For the Holstein alloy this is intuitively clear, because the steple in the density of states contains the states corresponding to the flat part of the dispersion. As indicated above, due to the large phonon admixture, these states might be temporarily localized, which suggests that they feel the on-site, alloy-type disorder much more strongly than the other states. The discussion of the diffusion properties in the next subsection will substantiate this intuitive picture.

2.3.2 Diffusion Properties

The spectral properties in the vicinity of the high-energy edge of the lowest polaronic subband suggest that this part of the spectrum is very susceptible to a localization transition. In subsection 2.2.1, we emphasized that the problem of localization of a polaron should be methodologically

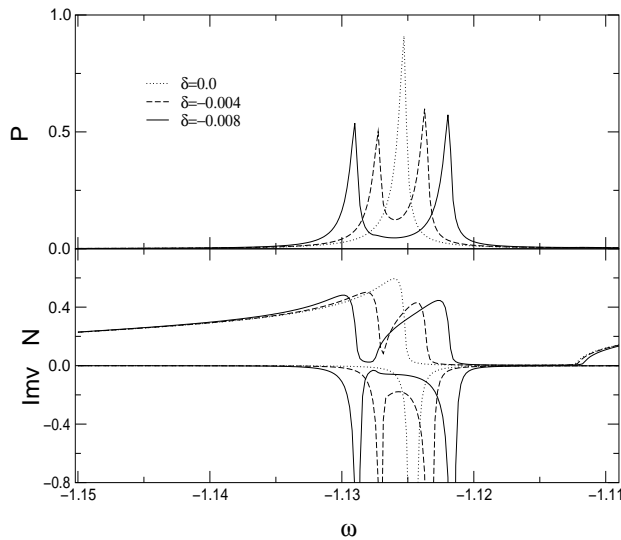


Figure 2.9: The lower panel shows the density of states $N(\omega)$ and the imaginary part of the coherent potential $\text{Im}v(\omega)$ for the Holstein alloy in the vicinity of the high-energy edge of the first polaronic subband for $c = 0.5$ and three different values of the scattering strength δ . The polaron parameters are $\lambda = 0.98$ and $\alpha = 0.25$ (see Table 2.1) and $\eta = 10^{-4}$. The corresponding spectrally resolved return probabilities $P(\omega, \eta)$ are given in the upper panel.

addressed with the same techniques used to investigate the problem of localization of an electron in a random potential. In particular, we stressed that $\lim_{\eta \rightarrow 0} P(\omega, \eta)$ would be a rigorous criterion to distinguish itinerant polaronic quasi-particle states from (any) localized polaronic defect states. We also pointed out, that a rigorous investigation of the localization issue is unfortunately beyond the DCPA because, within the DCPA, $\lim_{\eta \rightarrow 0} P(\omega, \eta)$ vanishes for all energies ω . Although localized states cannot be unambiguously identified, it is possible to identify *temporarily* localized states through the η -asymptotics of $P(\omega, \eta)$.

To motivate the investigation of the η -asymptotics of $P(\omega, \eta)$, we first emphasize that the spectrally resolved return probability $P(\omega, \eta)$ contains valuable information about the diffusion properties not only in the limit $\eta = 0$ (which is usually considered [114]) but also for a finite $\eta > 0$. For a correct interpretation of the data, we have to keep in mind, however, that a finite η broadens all spectral features. In particular, the pole [divergence] in $\text{Im}v(\omega)$ [$\text{Re}v(\omega)$] becomes, as mentioned in the previous subsection, a Lorentzian [pronounced kink], smearing out the high-energy edges of the respective bands. A finite η yields therefore small artificial tails extending into the gap regions. These tails have no direct physical meaning. In the following we analyze, therefore, the η -asymptotics of $P(\omega, \eta)$ only for energies ω below the respective sharp high-energy edges obtained for $\eta \rightarrow 0$ (see Fig. 2.6b and the insets of Figs. 2.10–2.12).

The physical content of $P(\omega, \eta)$ can be extracted from Figs. 2.5c, 2.6d, 2.7c, and the upper panel of Fig. 2.9, where we plot, for the model parameters given in the respective captions, $P(\omega, \eta)$ for $\eta = 10^{-4}$. All the data show that $P(\omega, \eta)$ does not uniformly (in ω) approach zero as $\eta \rightarrow 0$. Instead, $P(\omega, \eta)$ is substantially enhanced for certain energies ω . Close inspection of the data shows, moreover, that the maximum of $P(\omega, \eta)$ always occurs slightly below the high-energy edges of the respective (mini-)subbands, i.e., in the spectral regions where the dispersions become extremely flat. (This can be most clearly seen in Fig. 2.6.) The enhancement of $P(\omega, \eta)$ is caused by the band flattening and is therefore a direct measure of the sluggishness of the corresponding states due to their large phonon admixture. More precisely, because $1/\eta$ can be interpreted as a

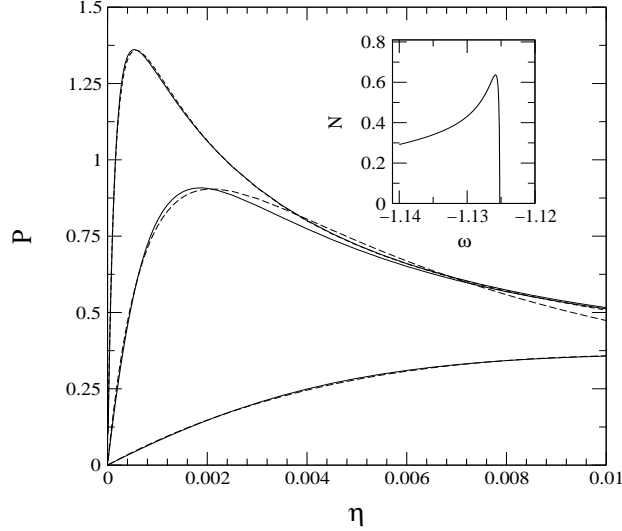


Figure 2.10: η -asymptotics of the spectrally resolved return probability $P(\omega, \eta)$ for the Holstein model. The polaron parameters are $\lambda = 0.98$ and $\alpha = 0.25$ (see Table 2.1). The three sets of curves correspond to three energies: $\omega = -1.135, -1.127$, and -1.12549 (from bottom to top). Solid [dashes] lines depict the numerical data [asymptotic expansion given in Eq. (2.61)]. The corresponding density of states for $\eta = 10^{-8}$ is shown in the inset.

characteristic time scale, a large value of $P(\omega, \eta)$ implies that the electron in the state at energy ω is not yet delocalized on the time scale $1/\eta$. Thus, the η -asymptotics of $P(\omega, \eta)$, i.e., the way $P(\omega, \eta)$ approaches zero for $\eta \rightarrow 0$, reveals the time scale on which the state at energy ω is *temporarily* localized. [Note, once more, we study the η -asymptotics of $P(\omega, \eta)$ only for ω below the $\eta \rightarrow 0$ high-energy edge and not for energies belonging to the artificial tail which is present for a finite η .]

In what follows we put these qualitative considerations on a mathematical basis. To that end, we first note that Eq. (2.6) suggests to interpret $f(\omega - i\eta, \omega + i\eta)$ as a “spectral density” corresponding to $p(2\eta)$, the Laplace image of $1/2P(t/2)$. That is, $f(\omega - i\eta, \omega + i\eta)$ gives the *spectrally resolved* diffusion behavior of the electron in the η domain. Accordingly, the counterpart of $f(\omega - i\eta, \omega + i\eta)$ in the time domain, which we denote by $F(\omega, t)$, is the “spectral density” corresponding to $1/2P(t/2)$. That is, it gives the *spectrally resolved* diffusion behavior of the electron in the time domain.

That the η -asymptotics of $P(\omega, \eta)$ indeed contain the spectrally resolved diffusion behavior of the electron can be clearly seen in Fig. 2.10, where, for the Holstein model with the polaron parameters given in Table 2.1, $P(\omega, \eta)$ is plotted as a function of η for three representative energies ω within the lowest polaronic subband, i.e., for energies below the $\eta \rightarrow 0$ high-energy edge. For the Holstein alloy, the overall behavior of $P(\omega, \eta)$ is the same. All three curves feature a hump whose shape and position strongly depend on ω . For ω in the immediate vicinity to the high-energy edge of the polaronic subband, the hump appears at a very small η and is very sharp. Far inside the subband, in contrast, the maximum appears at a larger η and is less pronounced. The distinct ω dependence of the hump indicates different characteristic time scales for the diffusion behavior of the respective states.

To explicitly extract this time scale, we perform an asymptotic expansion of $P(\omega, \eta)$ for small

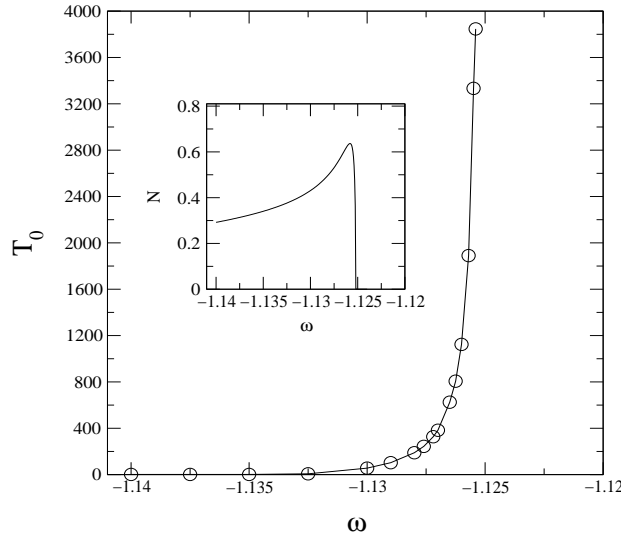


Figure 2.11: Spectrally resolved delocalization time $T_0(\omega)$ for the Holstein model in the vicinity of the high energy edge of the first polaronic subband. The polaron parameters are $\lambda = 0.98$ and $\alpha = 0.25$ (see Table 2.1). The inset shows the density of states for $\eta = 10^{-8}$. Note, the data for $T_0(\omega)$ are for energies below the $\eta \rightarrow 0$ high-energy edge.

η . The data shown in Fig. 2.10 suggest making the following ansatz

$$P(\omega, \eta) \approx K(\omega) \frac{\frac{\eta}{\eta_0(\omega)}}{\left(1 + \frac{\eta}{\eta_0(\omega)}\right)^{1+\nu(\omega)}}, \quad (2.61)$$

and determining the parameters $K(\omega)$, $\eta_0(\omega)$, and $\nu(\omega)$ through a least-square fit. The dashed lines in Fig. 2.10 show that this approach works reasonably well. Using the definition of $P(\omega, \eta)$ given in Eq. (2.9) and employing a general mathematical theorem about Laplace transforms [120], we obtain the asymptotic behavior of $F(\omega, t)$ for large t [note, since we measure energy in units of $2J$, time is measured in units of $(2J)^{-1}$]:

$$F(\omega, t) \approx K(\omega) \frac{(t\eta_0(\omega))^{\nu(\omega)}}{2\Gamma(1 + \nu(\omega))} e^{-t\eta_0(\omega)}, \quad (2.62)$$

where $\Gamma(x)$ denotes the Gamma function.

From this equation we infer that the parameter $\eta_0(\omega)$ gives rise to a characteristic time scale. Defining $T_0(\omega) = 1/\eta_0(\omega)$, we see, in particular, that for $t \gg T_0(\omega)$ the function $F(\omega, t)$ decays exponentially to zero. For $t \ll T_0(\omega)$, however, $F(\omega, t)$ is finite, implying that the state at energy ω is not yet delocalized. It is therefore natural to interpret $T_0(\omega)$ as a (spectrally resolved) *delocalization time* characterizing *temporary* localization, i.e., $T_0(\omega)$ quantifies the “sluggishness” of the state at energy ω .

In Fig. 2.11 we plot $T_0(\omega)$ for the Holstein model in the vicinity of the high-energy edge of the lowest polaronic subband. The polaron parameters are the same as in Fig. 2.5 (see Table 2.1). In the immediate vicinity of the high-energy edge, where the dispersion becomes extremely flat due to the high phonon admixture in the states, the delocalization times increase roughly three orders of magnitude (but do not diverge). That is, the states in the flat part of the polaronic subband appear to be temporarily localized on the time scales where the rest of the states are already

delocalized. Clearly, the band flattening and the enhanced delocalization times are correlated and have, moreover, the same microscopic origin, namely the increased phonon admixture in the states at the high-energy edge of the subband. More formally, it is the *divergence-induced* strong ω -dependence of $\text{Re}v(\omega)$ for $\omega_m \leq \omega \leq \omega_h$ that causes the large delocalization times at the high-energy edge of the lowest polaronic subband.

At this point it is appropriate to comment on the work of Hotta and Takada [121] who suggested that for energies where the self-energy (or, in our case, the coherent potential) diverges, states would be localized because of the infinitely strong electron-phonon coupling. They studied the half-filled (ordered) Holstein-Hubbard model, but their conclusion is quite general and should, if valid, hold for any model which produces divergences in the self-energy. Such divergences are, however, always inside a gap. In fact, they signal the presence of a gap, as can be seen, e.g., in Figs. 2.5 and 2.6, that is, there are no states at the divergence energy which could be localized. In contrast, our investigation suggests that, it is the effect the divergence has on states *within* the spectrum, namely, the band flattening it causes below the high-energy edge of the lowest polaronic subband, which could perhaps induce localization in that particular energy range. Within the DCPA, however, the effect is too weak, giving rise only to large but finite delocalization times and, hence, only to temporary localization.

It has been also suggested [113] that, if, due to some mechanism, a finite density of states appears at the divergence energy, the corresponding states would be localized. A finite η simulates such a mechanism. However, as can be seen in Fig. 2.6, the maximum of $P(\omega, \eta)$ does not occur in the tail but roughly at the maximum of the subband density of states. Therefore, at least within the DCPA, it is the band flattening and *not* the tail which is responsible for large delocalization times.

The concept of the delocalization time provides an appealing explanation of the spectral changes induced by alloying. In the previous subsection we have seen that the high-energy edge of the polaronic subband responds much more strongly to alloying than the bottom of the subband. From the perspective of the delocalization time this is now clear, because the high-energy edge contains “sluggish” defect-like states, whose large delocalization times make them feel the randomness of the on-site potential particularly strongly.

The delocalization times are also modified due to alloying. This is shown in Fig. 2.12 for a particular set of alloy parameters, $c = 0.5$ and $\delta = -0.002$. The polaron parameters are the same as before (see Table 2.1). In the previous subsection we have seen that the main effect of alloying is the formation of two mini-subbands with, due to the large phonon admixture in the states, rather flat dispersions at the two high-energy edges. As a consequence, the delocalization times are now enhanced in two narrow energy regions: At the high-energy edge of the A mini-subband and at the high-energy edge of the B mini-subband. Note, as in the case without disorder, the enhancement of the delocalization times is due to the band flattening effect, i.e., it is driven by strong on-site electron-phonon correlations. Even with the assistance of electron-impurity scattering, the on-site correlations are however not strong enough to produce divergent delocalization times.

The numerical results for the delocalization times suggest that we may tentatively distinguish two types of states: “Fast” *quasi-particle-like* states and “sluggish” *defect-like* states. In the Holstein model, defect-like states appear at the high-energy edge of the polaronic subband. Whereas in the Holstein alloy, defect-like states occur at the high-energy edges of the two mini-subbands. With and without disorder, strong on-site electron-phonon correlations are responsible for the formation of defect-like states. Because the delocalization times of the defect-like states are *several orders* of magnitude larger than the delocalization times of the quasi-particle-like states, it is moreover conceivable that the sluggishness of the defect-like states may anticipate the onset of localization.

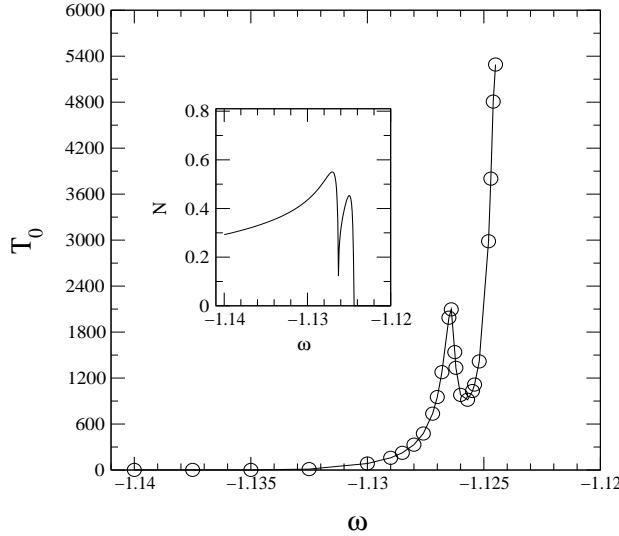


Figure 2.12: Spectrally resolved delocalization time $T_0(\omega)$ for the Holstein alloy in the vicinity of the high energy edge of the first polaronic subband for $c = 0.5$ and $\delta = -0.002$. The polaron parameters are $\lambda = 0.98$ and $\alpha = 0.25$ (see Table 2.1). The inset shows the density of states for $\eta = 10^{-8}$. Note, the data for $T_0(\omega)$ are for energies below the $\eta \rightarrow 0$ high-energy edge.

2.4 Critique

Up to this point, we have provided a self-contained description of the DCPA and employed it to investigate the dynamics of a single electron in the Holstein model augmented by site-diagonal, binary-alloy type disorder (Holstein alloy). Using multiple-scattering theory, the conventional CPA technique, we derived the DCPA equations for the averaged two- and four-point functions and emphasized the main approximation involved: namely, after each hop from one lattice site to another the electron's spatial memory is erased. We visualized the lack of spatial memory in terms of self-avoiding paths and employed this picture to give an intuitive explanation why the DCPA becomes exact for a system with infinite coordination number. We also mentioned that for a single electron the DCPA is identical to the dynamical mean field theory.

Our numerical results focused on the intermediate electron-phonon coupling regime, where polaronic subbands start to emerge. We investigated, for representative parameter sets, the effect of alloying on the high-energy edge of the lowest polaronic subband. These states are very susceptible to impurity scattering because of their large phonon admixture, which leads to a flat dispersion in this part of the spectrum, and, as a consequence, to a steeple-like density of states. The observed modifications of the spectral properties are therefore reminiscent of typical CPA results obtained for a model with a steeple-like density of states: A lack of $c \leftrightarrow 1 - c$ symmetry, an appearance of mini-subbands in the vicinity of the steeple (i.e., high-energy edge) of the subband for scattering strengths much smaller than the subband width, and an asymmetry in the component density of states.

The most notable result is, however, the large enhancement of the spectrally resolved return probability $P(\omega, \eta)$ for small but finite η in the narrow energy regions where the dispersion of the polaron states becomes extremely flat. This occurs in the absence (presence) of alloy-type disorder at the high-energy edge(s) of the polaronic subband (mini-subbands). To elucidate the physical meaning of this strong enhancement, we analyzed the η -asymptotics of $P(\omega, \eta)$ and

introduced the concept of a spectrally resolved delocalization time which is the characteristic time scale on which, at a given energy, the electron leaves a given site. The strong enhancement of $P(\omega, \eta)$ in the flat part(s) of the subband (mini-subbands) signals large delocalization times. According to their delocalization times we could thus classify, within the limitations of the DCPA, “fast” quasi-particle-like polaron states at the bottom and “sluggish” defect-like polaron states at the top of the subband (mini-subbands).

Within the DCPA, we cannot decide, however, whether “defect-like”, i.e., temporarily localized states are in fact “defect”, i.e., localized states. At this point it is important to recall that the DCPA is based on the embedding of a single impurity site into an homogenous effective medium. Spatial fluctuations, the main driving forces for Anderson localization, are wiped out. In particular, the single-site approximation implies for the calculation of the spectrally resolved return probability to ignore maximally crossed diagrams. They are however expected to yield particularly large contributions to the return probability. It is therefore conceivable that the DCPA results for the delocalization times of polaron states are only lower bounds and temporarily localized states may in fact be localized states. Clearly to further elucidate the interplay between polaron formation and Anderson localization more sophisticated methods, capable of accounting spatial fluctuations, are required. In the second half of this chapter, we present such an approach. It is based on the statistical dynamical mean field approximation, which, in contrast to the DCPA, maps the lattice problem not on to a single self-consistently embedded impurity site but on to an ensemble of self-consistently embedded impurity sites, which is then characterized in terms of probability.

2.5 Statistical Dynamical Mean Field Theory (statDMFT) [5–7]

This section gives a general description of the statistical dynamical mean field approximation (statDMFT). In contrast to the DMFT (DCPA), the statDMFT maps the lattice problem not on to a *single* self-consistently embedded impurity site but on to an *ensemble* of self-consistently embedded impurity sites. Spatial fluctuations due to quenched disorder are explicitly incorporated. As a result, the statDMFT enables us to distinguish itinerant polaronic quasi-particle states from localized polaronic defect states. Spatial fluctuations due to dynamic disorder, induced by electron-phonon scattering, are however beyond the statDMFT.

2.5.1 Disorder and Interactions

Polaron formation (self-trapping) in a disordered environment is one example of physical problems where interaction and disorder effects interfere with each other. The most prominent example is electron transport in the impurity band of doped semiconductors. Especially near the metal-insulator transition, Coulomb interaction and disorder effects cannot be separated, and it is suspected that it is precisely the interplay of both, which leads to new physical phenomena, for instance, to the formation of local moments [122] or to a new emerging magnetic phase. [123]

There is no method which could be mechanically used to investigate disordered interacting systems beyond perturbation theory. In particular, the strongly disordered regime, where Anderson localization takes place, is beyond the applicability of most theoretical techniques. Nevertheless, there have been various attempts to generalize methods, which have been successfully employed to investigate Anderson localization of noninteracting electrons, in such a way that they can be also utilized in situations where interactions are important. Most efforts have been directed towards electrons interacting via short- and/or (bare) long-range Coulomb potentials, with a few exceptions dealing with electrons coupled to phonons. [4, 5, 93–97]

After Anderson’s original work [88] and Mott’s suggestion [92] of its connection to transport properties in amorphous semiconductors, three principal techniques have been cultivated to study Anderson localization quantitatively in further detail: (i) direct numerical simulations [124], (ii) diagrammatic techniques, [125] and (iii) field-theoretical approaches. [126] Subsequently, all three techniques have been applied to interacting systems as well. Direct numerical simulations are conceptually the simplest approach. However, they are restricted to small system sizes and usually to a truncated configuration type treatment of the Coulomb interaction. To this category belong, for instance, all attempts to study the localization of two interacting electrons in the background of a frozen Fermi sea. [127] In the case of electron-phonon interaction, the size of the phonon Hilbert space is the limiting factor. Diagrammatic methods work usually only for weak interactions. [128] In principle, strong interactions can be also treated with diagrammatic techniques, if they are based on renormalized expansions, but the proliferation of diagrams makes the practical implementation very often rather complicated if not impossible. Field-theoretical techniques, in contrast, for instance based on the construction of an effective field theory for the low-energy, long-wavelength excitations [129, 130], albeit very promising, operate in abstract spaces, with order parameter functions whose physical content is sometimes hard to grasp.

Anderson [88], on the other hand, used a completely different approach. Instead of focusing on the calculation of averaged correlation functions, he emphasized that, in general, average values are not representative, especially in the strongly disordered regime. All variables of the theory, in particular, observables, should be characterized by distributions. Specifically, he examined, in probabilistic terms, the convergence properties of the renormalized perturbation series for the local hybridization function appearing in a locator expansion of the local Green function. Towards that end, he gave asymptotic estimates for the higher order terms of the series. The mathematical arguments are quite involved and have been further clarified later, most notably, by Thouless [89, 131] and Economou and Cohen. [114] A simplified probabilistic approach, based on the self-consistent solution of the second order renormalized perturbation series, started with Abou-Chacra, Anderson and Thouless. [132] It proved to be a very powerful tool, applicable not only to substitutionally [133, 134] but also to topologically disordered materials. [135, 136]

The flexibility of the simplified probabilistic analysis of the renormalized perturbation series has been recently utilized by Dobrosavljević and Kotliar [98] to analyse various physical properties of disordered electrons with strong local electron-electron correlations. [137, 138] They successfully combined the dynamical mean field approximation for the description of (local) correlations with Abou-Chacra, Anderson, and Thouless’s probabilistic treatment of the spatial fluctuations due to randomness. The statDMFT maps the original lattice problem on to an ensemble of impurity problems, which is then analysed in terms of probability. In contrast to the field-theoretical approaches, the method is very intuitive and conceptually simple. Moreover, it captures local interaction processes nonperturbatively. It is therefore capable of addressing issues beyond standard diagrammatic perturbation theories. Numerically it is somewhat involved, but not restricted to small system sizes as direct numerical simulations. The main drawback of the method is its restriction to local, short-range interactions. In principle, long-range interaction processes could be incorporated, but only at the level of static molecular fields (for instance, in the case of Coulomb interaction a Hartree term would appear), which is probably not sufficient for a complete investigation of the interplay between long-range interactions and disorder. For the Anderson-Holstein model, however, where the (electron-phonon) coupling is local, the statDMFT’s problem to deal with long-range interactions does not occur and the statDMFT is expected to capture the essential physics of the interplay between Anderson localization and self-trapping.

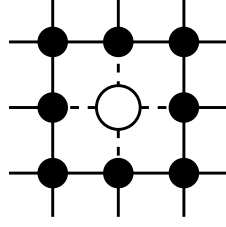


Figure 2.13: In the cavity method all sites but one are integrated out. For that purpose the lattice action is divided into three parts: $S = S_i + S^{(i)} + \Delta S(i)$, where S_i is the action on the isolated site i (denoted by an open circle), $S^{(i)}$ is the lattice action with site i excluded (full circles), and $\Delta S(i)$ is that part of the action, which connects site i with the rest of the lattice (dashed lines).

2.5.2 General Formalism

The derivation of the statDMFT for a generic model of interacting electrons has been given by Dobrosavljević and Kotliar. [98] It is based on the cavity method and applies to arbitrary lattices, temperatures, and densities. To make our presentation self-contained and to fix our notation, we outline in this subsection the cavity method, carefully paying attention to the probabilistic interpretation of the statDMFT and to specifics due to electron-phonon coupling. In Appendix D we provide, for a single electron on a Bethe lattice at zero temperature, an alternative, less general derivation based on the multiple-scattering techniques, which we used to obtain in Section 2.2 the DCPA equations for a single electron in the Anderson-Holstein model.

The starting point is the partition function

$$Z = \int \prod_{i,\sigma} \mathcal{D}c_{i\sigma}^\dagger \mathcal{D}c_{i\sigma} \mathcal{D}b_i^\dagger \mathcal{D}b_i e^{-S[c^\dagger, c, b^\dagger, b]}, \quad (2.63)$$

where the action, for a fixed realization of the on-site energies, is given by

$$\begin{aligned} S[c, c^\dagger, b, b^\dagger] &= \int_0^\beta d\tau \sum_{j,\sigma} \left\{ c_{j\sigma}^\dagger(\tau) [\partial_\tau - \mu] c_{j\sigma}(\tau) + b_j^\dagger(\tau) \partial_\tau b_j(\tau) \right. \\ &\quad \left. + H[c, c^\dagger, b, b^\dagger](\tau) \right\}. \end{aligned} \quad (2.64)$$

All sites but one are now integrated out, yielding an effective single-site action. For that purpose, the action is split into three parts: $S = S_i + S^{(i)} + \Delta S(i)$, where S_i is the action of the isolated site i , $S^{(i)}$ is the action for the system with site i excluded, and

$$\Delta S(i) = - \int_0^\beta d\tau \sum_{l,\sigma} \left\{ c_{l\sigma}^\dagger(\tau) \eta_{l\sigma}(\tau) + \eta_{l\sigma}^\dagger(\tau) c_{l\sigma}(\tau) \right\}, \quad (2.65)$$

with $\eta_{l\sigma} = J_{li} c_{i\sigma}$, is the part of the action which connects site i to its neighbors (see Fig. 2.13).

Identifying $\Delta S(i)$ as a source term to generate cavity Green functions, i.e. Green functions for the lattice with site i removed, the effective single-site action $S(i)$, defined by

$$e^{-S(i)} = \frac{1}{Z} \int \prod_{j \neq i, \sigma} \mathcal{D}c_{j\sigma}^\dagger \mathcal{D}c_{j\sigma} \mathcal{D}b_j^\dagger \mathcal{D}b_j e^{-[S_i + S^{(i)} + \Delta S(i)]}, \quad (2.66)$$

can be written as

$$S(i) = S_0 + S_i[c_{i\sigma}^\dagger, c_{i\sigma}, b_i^\dagger, b_i] - W^{(i)}[\eta^\dagger, \eta], \quad (2.67)$$

where we explicitly indicated the fields on which the various terms depend. The first term S_0 is a constant. While the second term, the action for the isolated site i , contains only the fields on site i , the third term,

$$W^{(i)}[\eta^\dagger, \eta] = 1 + \sum_n \int_0^\beta d\tau_1 \dots \int_0^\beta d\tau_n \int_0^\beta d\tau'_1 \dots \int_0^\beta d\tau'_n A^{[2n]}(\tau_1, \dots, \tau'_n), \quad (2.68)$$

with

$$\begin{aligned} A^{[2n]}(\tau_1, \dots, \tau'_n) &= (-)^n \sum_{l_1, \sigma_1} \dots \sum_{l'_n, \sigma'_n} \eta_{l_1 \sigma_1}^\dagger(\tau_1) \dots \eta_{l'_n \sigma'_n}^\dagger(\tau_n) G_{l_1 \sigma_1 \dots l'_n \sigma'_n}^{(i)}(\tau_1, \dots, \tau'_n) \\ &\times \eta_{l'_1 \sigma'_1}(\tau'_1) \dots \eta_{l_n \sigma_n}(\tau_n), \end{aligned} \quad (2.69)$$

involves fields from all sites.

The effective single-site action $S(i)$ contains the full information of the original lattice action. Integrating out all sites but one introduces a $2n$ -point cavity Green function $G_{l_1 \sigma_1 \dots l'_n \sigma'_n}^{(i)}(\tau_1, \dots, \tau'_n)$. This function is extremely involved and approximations are required to obtain feasible equations. A crucial simplification can be made by truncating Eq. (2.68) after the $n = 1$ term. This leads to a quadratic effective single-site action, similar to the DMFT [112], where it was further shown that the truncation becomes exact for lattices with infinite coordination number. As a consequence, although the cavity construction is performed for lattices with a finite coordination number, interaction processes, here due to the electron-phonon coupling, are treated as if the lattice had infinite coordination number. As a result of the truncation, the statDMFT becomes a mean field theory.

Keeping only the $n = 1$ term, Eq. (2.68) depends only on the electronic fields on site i and reduces to

$$W^{(i)}[c_i^\dagger, c_i] = 1 - \int_0^\beta d\tau \int_0^\beta d\tau' \sum_\sigma c_{i\sigma}^\dagger(\tau) H_{i\sigma i\sigma}(\tau - \tau') c_{i\sigma}(\tau'), \quad (2.70)$$

with the hybridization function

$$H_{i\sigma i\sigma}(\tau - \tau') = J^2 \sum_{lm} G_{l\sigma m\sigma}^{(i)}(\tau - \tau'). \quad (2.71)$$

The information of the lattice is now contained in the two-point cavity Green function $G_{l\sigma m\sigma}^{(i)}(\tau - \tau')$, describing all paths from site l to site m without passing through site i (note that due to the definition of J_{lm} , both sites l and m are neighboring sites to i).

Absorbing irrelevant constants, which do not affect the electron dynamics, into Z_0 , the effective single-site action reads

$$\begin{aligned} S(i) &= \int_0^\beta d\tau d\tau' \sum_\sigma c_{i\sigma}^\dagger(\tau) \left\{ [\partial_\tau + \epsilon_i - \mu] \delta(\tau - \tau') + H_{i\sigma i\sigma}(\tau - \tau') \right\} c_{i\sigma}(\tau') \\ &+ S_{ph}(i) + S_{int}(i), \end{aligned} \quad (2.72)$$

with

$$S_{ph}(i) = \int_0^\beta d\tau b_i^\dagger(\tau) [\partial_\tau + \Omega] b_i(\tau) \quad (2.73)$$

and

$$S_{int}(i) = - \int_0^\beta d\tau \sqrt{E_p \Omega} [b_i(\tau) + b_i^\dagger(\tau)] n_{i\sigma}(\tau). \quad (2.74)$$

According to Eq. (2.72), the interaction between electrons and phonons takes place only on site i , which, due to the hybridization function $H_{i\sigma i\sigma}(\tau)$, is however embedded into the full lattice.

Although, for a given $H_{i\sigma i\sigma}(\tau)$, any local Green function could be obtained from $S(i)$, the set of equations is not closed. This can be most clearly seen from the identity [98]

$$\int_0^\beta d\tau' G_{l\sigma i\sigma}(\tau - \tau') G_{i\sigma m\sigma}(\tau') = \int_0^\beta d\tau' \left\{ G_{l\sigma m\sigma}(\tau - \tau') - G_{l\sigma m\sigma}^{(i)}(\tau - \tau') \right\} G_{i\sigma i\sigma}(\tau'), \quad (2.75)$$

which connects the cavity Green function $G_{l\sigma m\sigma}^{(i)}(\tau)$ with the lattice Green function $G_{l\sigma m\sigma}(\tau)$. Therefore, the hybridization function $H_{i\sigma i\sigma}(\tau)$ defined in Eq. (2.71) is a functional of the full, nonlocal lattice Green function, which of course cannot be obtained from the effective single-site action $S(i)$.

To close the set of equations, Dobrosavljević and Kotliar [98] suggested to approximate in Eqs. (2.71) and (2.75), for a given realization of disorder, the full lattice Green function $G_{l\sigma m\sigma}(\tau)$ by the bare lattice Green function $G_{l\sigma m\sigma}^0$, with on-site energies shifted by the local self-energy. In Matsubara space the substitution reads

$$G_{i\sigma j\sigma}(i\omega_n) \rightarrow G_{i\sigma j\sigma}^0(i\omega_n) \Big|_{\epsilon_i \rightarrow \epsilon_i + \Sigma_{i\sigma}(i\omega_n)}, \quad (2.76)$$

with $\Sigma_{i\sigma}(i\omega)$ defined by

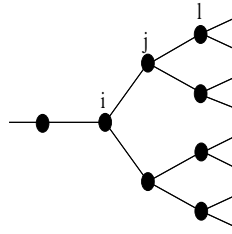
$$G_{i\sigma i\sigma}(i\omega_n) = \frac{1}{i\omega_n - \epsilon_i + \mu - H_{i\sigma i\sigma}(i\omega_n) - \Sigma_{i\sigma}(i\omega_n)}, \quad (2.77)$$

which is the Fourier transformed Dyson equation for the local Green function $G_{i\sigma i\sigma}(\tau) = -\langle T_\tau c_{i\sigma}(\tau) c_{i\sigma}^\dagger(0) \rangle_{S(i)}$ as obtained from the effective single-site action $S(i)$. Note, the substitution Eq. (2.76) is not exact, because in general the interaction self-energy is nonlocal. Besides the truncation of the effective single-site action, this is the second major approximation invoked by the statDMFT.

Now the set of Eqs. (2.71)–(2.77) is closed and constitutes the basic statDMFT equations, applicable to arbitrary temperatures, densities, and lattices. A self-consistent solution yields the local Green function $G_{i\sigma i\sigma}(i\omega_n)$.

It is crucial to realize that, due to the randomness of the on-site energies ϵ_i , the local Green function $G_{i\sigma i\sigma}(i\omega_n)$, the local self-energy $\Sigma_{i\sigma}(i\omega_n)$, and the local hybridization function $H_{i\sigma i\sigma}(i\omega_n)$ are random variables. More specifically, interpreting the site indices as labels enumerating the elements of random samples, $G_{i\sigma i\sigma}(i\omega_n)$, $\Sigma_{i\sigma}(i\omega_n)$, and $H_{i\sigma i\sigma}(i\omega_n)$ can be understood as particular realizations of the random variables $G_\sigma^{loc}(i\omega_n)$, $\Sigma_\sigma^{loc}(i\omega_n)$, and $H_\sigma^{loc}(i\omega_n)$, respectively. Thus, equations (2.71)–(2.77) are in fact stochastic recursion relations, from which random samples for the random variables $G_\sigma^{loc}(i\omega_n)$, $\Sigma_\sigma^{loc}(i\omega_n)$, and $H_\sigma^{loc}(i\omega_n)$ can be constructed. The iterative solution of Eqs. (2.71)–(2.77) is therefore equivalent to the calculation of the distribution for the random variables $G_\sigma^{loc}(i\omega_n)$, $\Sigma_\sigma^{loc}(i\omega_n)$, and $H_\sigma^{loc}(i\omega_n)$.

Starting from an initial sample $\{H_{i\sigma i\sigma}(i\omega_n)\}$ for the local hybridization function $H_\sigma^{loc}(i\omega_n)$, a sample $\{G_{i\sigma i\sigma}(i\omega_n)\}$ for the local Green function $G_\sigma^{loc}(i\omega_n)$ is obtained by solving the quantum mechanical (many-body) problem defined by $S(i)$ [cf. Eqs. (2.72)–(2.74)]. The Dyson equation (2.77) for the local Green function yields then a sample $\{\Sigma_{i\sigma}(i\omega_n)\}$ for the local self-energy

Figure 2.14: $K = 2$ Bethe lattice.

$\Sigma_{\sigma}^{loc}(i\omega_n)$, from which a new sample for the hybridization function is calculated from Eqs. (2.76), (2.75), and (2.71). Going through this loop iteratively, the random samples are successively updated until a fix point is reached.

The iteration is numerically very involved for Bravais lattices (even for a simple cubic lattice), in particular the construction of the lattice Green function through Eq. (2.76). In practice, the statDMFT is therefore formulated on a Bethe lattice, which is an infinite, loop-free graph with connectivity K (where $K + 1$ is the number of next neighbors, i.e. the coordination number Z). Besides the reduced numerical complexity, the Bethe lattice has the additional advantage that the statistical dependence of the random variables can be analysed in detail.

Finally, we mention that the statDMFT reduces to the DMFT for lattices with large coordination number. For the particular case of a Bethe lattice, this is shown in Appendix E.

2.5.3 Specification to a Bethe Lattice

Due to the absence of closed loops, the hybridization function on the Bethe lattice depends only on the *local* cavity Green function, which can be again obtained from an appropriate effective single-site action. As a result, the statDMFT simplifies enormously on a Bethe lattice.

Specifically for the $K = 2$ Bethe lattice with nearest neighbor coupling shown in Fig. 2.14, the hybridization function becomes

$$H_{i\sigma i\sigma}(i\omega_n) = J^2 \sum_{j \text{ NN } i} G_{j\sigma j\sigma}^{(i)}(i\omega_n), \quad (2.78)$$

where now only local cavity Green functions appear. This is the crucial simplification because $G_{j\sigma j\sigma}^{(i)}(i\omega_n)$ can be obtained from the effective single-site action $S^{(i)}(j)$, which has the same structure as $S(j)$, except that the hybridization function is now given by

$$H_{j\sigma j\sigma}^{(i)}(i\omega_n) = J^2 \sum_{l \neq i \text{ NN } j} G_{l\sigma l\sigma}^{(j)}(i\omega_n). \quad (2.79)$$

In addition, on a Bethe lattice, because of the absence of closed loops, the exclusion of site j already ensures that site i is not visited, i.e., $G_{l\sigma l\sigma}^{(j)}(i\omega_n) = G_{l\sigma l\sigma}^{(j)}(i\omega_n)$. Accordingly, except for the ‘base’ site i , the hybridization function for all other sides is simply given by the sum over the ‘forward’ cavity Green function. For the base site, in contrast, all the neighboring cavity Green functions contribute [see Eq. (2.78)].

As a consequence, taking i as the base site, from which the cavity construction starts, gives for the Dyson equation for the local base site Green function

$$G_{i\sigma i\sigma}(i\omega_n) = \left[i\omega_n + \mu - \epsilon_i - J^2 \sum_{j \text{ NN } i} G_{j\sigma j\sigma}^{(i)}(i\omega_n) - \Sigma_{i\sigma}(i\omega_n) \right]^{-1}, \quad (2.80)$$

whereas the Dyson equation for the local Green function at all other sites reads

$$G_{j\sigma j\sigma}^{(i)}(i\omega_n) = \left[i\omega_n + \mu - \epsilon_j - J^2 \sum_{l \neq i} \sum_{\text{NN } j} G_{l\sigma l\sigma}^{(j)}(i\omega_n) - \Sigma_{j\sigma}^{(i)}(i\omega_n) \right]^{-1}. \quad (2.81)$$

Note, all cavity Green functions $G_{j\sigma j\sigma}^{(i)}(i\omega_n)$ obey Eq. (2.81); hence they are identically distributed. Moreover, because the cavity self-energy $\Sigma_{j\sigma}^{(i)}(j\omega_n)$ is obtained from $S^{(i)}(j)$, containing only ‘forward’ sites with respect to site j , the cavity Green function are also statistically independent and $G_{j\sigma j\sigma}^{(i)}(i\omega_n)$ can be interpreted as a particular realization of the random variable $G_{\sigma}^{cav}(i\omega_n)$. The statistical dependence between cavity Green functions at different energies is another issue. Naturally, it depends on the interaction processes and the particular approximation employed to calculate the local self-energy (see below).

In principle the base site self-energy $\Sigma_{i\sigma}(i\omega_n)$ and the cavity self-energy $\Sigma_{j\sigma}^{(i)}(i\omega_n)$ are different. If, in the spirit of the DMFT, we neglect however this difference and identify $\Sigma_{i\sigma}(i\omega_n)$ with $\Sigma_{j\sigma}^{(i)}(i\omega_n)$, Eq. (2.80) reduces for i and j next neighbor sites to

$$G_{i\sigma i\sigma}(i\omega_n) = \frac{1}{[G_{i\sigma i\sigma}^{(j)}(i\omega_n)]^{-1} - J^2 G_{j\sigma j\sigma}^{(i)}(i\omega_n)}. \quad (2.82)$$

Within this approximation, the local Green function $G_{i\sigma i\sigma}(i\omega_n)$ is expressed in terms of two statistically independent random variables, $G_{i\sigma i\sigma}^{(j)}(i\omega_n)$ and $G_{j\sigma j\sigma}^{(i)}(i\omega_n)$. The identification of $\Sigma_{j\sigma}(i\omega_n)$ with $\Sigma_{j\sigma}^{(i)}(i\omega_n)$ is on the Bethe lattice analogous to the substitution Eq. (2.76) for Bravais lattices. Even on the Bethe lattice, the statDMFT involves therefore two approximations: the truncation of the effective single-site action and the conflation of the interaction self-energies [reminiscent of the substitution Eq. (2.76) for Bravais lattices].

2.5.4 Localization Criterion

In subsection 2.2.1 we introduced the spectrally resolved return probability $\lim_{\eta \rightarrow 0} P(\omega, \eta)$ as a criterion to distinguish between itinerant and localized states. In principle, the spectrally resolved return probability, which is an averaged four-point function, could be also calculated within the statDMFT. An alternative localization criterion, based on the probability distribution of two-point functions, is however more suitable from a calculational point of view.

A natural measure of the itinerancy suggested by the effective single-site action $S(i)$ is the total tunneling rate from a given site i defined by the imaginary part of the hybridization function,

$$\Gamma_{i\sigma}(\omega) = J^2 \sum_{j \text{ NN } i} N_{j\sigma}^{(i)}(\omega), \quad (2.83)$$

where $N_{j\sigma}^{(i)}(\omega)$ is the local cavity density of states (LCDOS), i.e., the imaginary part of the cavity Green function $G_{j\sigma j\sigma}^{(i)}(\omega)$. Obviously, a finite tunneling rate $\Gamma_{i\sigma}(\omega)$ implies an extended state at energy ω . Localized states, in contrast, lead to a vanishing tunneling rate. The tunneling rate vanishes if the LCDOS $N_{j\sigma}^{(i)}(\omega)$ vanishes, which, in this sense, is a transport quantity, and could by itself be used as a kind of ‘order parameter’ for localization. The tunneling rate $\Gamma_{i\sigma}(\omega)$ as well as the LCDOS $N_{j\sigma}^{(i)}(\omega)$ are random variables and whether they vanish or not depends on their distribution. The shape of the distributions has to change therefore dramatically at the localization transition.

To understand why the shape of the distribution has to change, it is convenient to look at the distribution of a related quantity, the local density of states (LDOS), defined by

$$N_{i\sigma}(\omega) = -\frac{1}{\pi} \text{Im} G_{i\sigma i\sigma}(\omega), \quad (2.84)$$

because it directly reflects the spatial dependence of the wave function: For an extended state at energy ω , where the weight of the wave function is more or less the same on every site, the distribution of the LDOS at energy ω is symmetric and the most probable value coincides with the arithmetic mean value (average value). Localized states with energy ω , on the other hand, have substantial weight only on a few sites. The distribution is therefore extremely asymmetric, with a most probable value much smaller than the arithmetic mean value, which is therefore not representative anymore. Since the LDOS $N_{j\sigma}(\omega)$ is closely related to the LCDOS $N_{j\sigma}^{(i)}(\omega)$, the distributions for the LCDOS and the tunneling rate undergo the same characteristic change at the localization transition as the distribution for the LDOS.

A priori it is not clear by what moment (or moments) the asymmetric distributions should be characterized. At this point it is useful to anticipate that distributions, in particular the distribution for the local hybridization function, can be used to calculate averaged transport quantities, such as the dc conductivity or the return probability (see below). The most probable value, i.e., the maximum of the distribution, is then expected to play a crucial role. [Note, averaged four-point functions (transport quantities) capture the localization effect, in contrast to averaged two-point functions.] It would be therefore natural to focus on the most probable values. The drawback is, however, that they cannot be directly obtained from the random samples; they require the explicit construction of histograms. More convenient quantities seem to be the so-called typical values [98], which are simply the geometric mean values of the random samples and yet capture the asymmetry of the distributions reasonably well. Therefore, we focus on the typical values.

In particular, we consider the distribution of the LDOS and distinguish localized from extended states by a detailed investigation of the average LDOS,

$$N_{\sigma}^{\text{ave}}(\omega) = \frac{1}{N_s} \sum_i N_{i\sigma}(\omega), \quad (2.85)$$

and the typical LDOS

$$N_{\sigma}^{\text{typ}}(\omega) = \exp \left[\frac{1}{N_s} \sum_i \log N_{i\sigma}(\omega) \right]. \quad (2.86)$$

Specifically, we classify states at energy ω with $N_{\sigma}^{\text{ave}}(\omega) \neq 0$ as localized if $N_{\sigma}^{\text{typ}}(\omega) \rightarrow 0$ and as extended if $N_{\sigma}^{\text{typ}}(\omega) \neq 0$. Note, the LDOS is defined for $\eta \rightarrow 0$. The numerical solution has to take this into account (see below). It should be stressed, Mirlin and Fyodorov [139] also used the LDOS as an order parameter for the Anderson transition.

2.5.5 Single Electron and T=0 Limit

The easiest way to obtain the zero temperature, single-particle limit of the statDMFT equations [Eqs. (2.71)–(2.77)] is to work with an effective single-site Hamiltonian, instead of an effective single-site action. Neglecting the spin, which for a single electron is irrelevant, the effective Hamiltonian reads

$$H(j)^{(i)} = \epsilon_j c_j^{\dagger} c_j + \Omega b_j^{\dagger} b_j - \sqrt{E_p \Omega} (b_j^{\dagger} + b_j) c_j^{\dagger} c_j + \sum_{\nu} E_{\nu} a_{\nu}^{\dagger} a_{\nu} + \sum_{\nu} [T_{\nu j} a_{\nu}^{\dagger} c_j + H.c.], \quad (2.87)$$

where the notation indicates that the Hamiltonian models the dynamics encoded in the cavity effective single-site action $S(j)^{(i)}$.

The Hamiltonian representation of $S(j)^{(i)}$ is not unique. In Eq. (2.87) the embedding is given by the hybridization with an auxiliary field a_ν . The auxiliary parameters E_ν and $T_{\nu j}$ have no physical meaning, they just parameterize the hybridization function in terms of a spectral representation:

$$H_{jj}^{(i)}(i\omega_n) = \sum_{\nu} \frac{|T_{\nu}|^2}{i\omega_n - \mu - \epsilon_j - E_{\nu}}. \quad (2.88)$$

For a given set of parameters $\{E_\nu, T_{\nu j}\}$, i.e. hybridization function $H_{jj}(i\omega_n)$, the local self-energy due to electron-phonon coupling $\Sigma_i(i\omega_n)$ can be deduced from Eq. (2.87). For finite densities, this can be done only by some approximation, introducing further uncertainties into the approach. For a single electron, however, the interaction self-energy can be obtained exactly in the form of a continued fraction [104, 113], valid over the whole range of parameters (see Section 2.2). Thus, for a single electron, no further approximations are required.

To be more specific, we calculate from Eq.(2.87) the single-electron Green function for $T = 0$, using the continued fraction expansion for the electron-phonon self-energy, identify then this Green function with the zero temperature, single-electron limit of the cavity Green function in Eq. (2.81) to obtain ($z = \omega + i\eta$)

$$G_{ii}^{(j)}(z) = \frac{1}{[F_{ii}(z)]^{-1} - \frac{\Omega E_p}{[F_{ii}(z - 1\Omega)]^{-1} - \frac{2\Omega E_p}{[F_{ii}(z - 2\Omega)]^{-1} - \frac{3\Omega E_p}{\dots}}}}, \quad (2.89)$$

with

$$F_{ii}(z) = \left[z - \epsilon_i - J^2 \sum_j G_{jj}^{(i)}(z) \right]^{-1}. \quad (2.90)$$

The local Green function follows from Eq. (2.82), setting again $i\omega_n + \mu \rightarrow z = \omega + i\eta$,

$$G_{ii}(z) = \frac{1}{[G_{ii}^{(j)}(z)]^{-1} - J^2 G_{jj}^{(i)}(z)}. \quad (2.91)$$

According to the interpretation given in the previous subsection, Equations (2.89)–(2.91) constitute stochastic recursion relations for a random sample for the local Green function $G_{\sigma}^{loc}(z)$. Note, Green functions with shifted energy appear in the continued fraction. They satisfy the same recursion relations, with energy shifted to $z - q\Omega$. In Appendix D we show how the (single electron, $T = 0$) Eqs. (2.89)–(2.91) can be directly obtained with the multiple-scattering techniques, which we employed to derive the DCPA equations for a single electron in the Anderson-Holstein model.

For a fixed energy $z - q\Omega$, the local Green functions $G_{ii}(z - q\Omega)$ are identically distributed. They are however not independent. As a consequence, for each energy $z - q\Omega$, we have to construct a separate random sample $\{G_{jj}^{(i)}(z - q\Omega)\}$ (with $j = 1, \dots, N_s$ and $q = 0, 1, \dots, M$), starting from an initial sample, which we successively update via a Monte Carlo algorithm, similar to the schemes described by other authors [94, 132], drawing the random variables on the rhs of Eq. (2.89) from the corresponding random samples created by the iteration step before. Iterating this process a sufficient number of times yields, as a fixed point of the stochastic recursion relations, a self-consistent random sample for the cavity Green function at energy $z - q\Omega$. The self-consistent random samples are then used to directly determine average and typical values of the respective random variables, or, in the form of histograms, the distributions associated with them.

2.6 Numerical Results II [7]

This subsection presents statDMFT results for a single electron in the Anderson-Holstein model at zero temperature. We solve the statDMFT equations on a Bethe lattice where, as mentioned previously, the numerical effort is manageable. As in other areas of statistical physics, the Bethe lattice calculation has the status of a mean field calculation for Bravais lattices. We expect therefore our results to be qualitatively valid for any Bravais lattice with $d \geq 3$.

For reasonable numerical accuracy, the sample size N_s , which should not be confused with the actual size of the Bethe lattice, but instead gives the precision with which we construct the random sample (cf. distributions), has to be sufficiently large. Typical sample sizes are $N_s \approx 50\,000$. The maximum depth M of the continued fraction, which describes the maximum number of virtual phonons in the lattice, has to be large enough in order to capture polaron formation. As a rough estimate we use $M \approx 5g^2$, where $g^2 = E_p/\Omega$ is approximately the average number of virtual phonons comprising the phonon cloud of the polaron.

To distinguish localized from extended states, it is crucial to investigate the stochastic recursion relations in the limit $\eta \rightarrow 0$. [132] Numerically this seems delicate. However, initializing the iteration loop with a finite imaginary part of the cavity Green functions, the stochastic recursion relations can be iterated without problems for $\eta = 0$. [140] The correct, self-consistent value of the imaginary part of the cavity Green function is then realized during the iteration.

Tracking random samples as a function of the iteration index provides therefore information about the character of the states at the energy for which the sample is constructed. Random samples corresponding to extended states converge rapidly to its fixed point, whereas random samples corresponding to localized states do not converge. Hence, extended and localized states can be detected by the differences they give rise to in the mathematical properties of the recursion relations.

Sometimes it is advantageous to keep η finite. But then it is necessary to monitor the flow of the random samples, or of its associated average and typical values, as η gets smaller and smaller. The part of the spectrum corresponding to extended states is insensitive to the η -scaling, after η is small enough to see the correct LDOS nothing changes anymore. Localized states on the other hand are strongly affected. In fact, it can be numerically verified, that the typical LDOS indeed scales to zero with $\eta \rightarrow 0$. [134, 140]

To investigate the localization properties of electron and polaron states, we specifically focused on the typical LDOS, tracking this quantity, for given energy and model parameters, as a function of η and the number of iterations. Introducing a rescaled transfer amplitude $J = \bar{J}/\sqrt{K}$, we measure energies in units of the bare bandwidth $W_0 = 4\bar{J} = 1$ and define $\bar{\lambda} = E_p/\bar{J}$, $\bar{\alpha} = \Omega/\bar{J}$, and $\bar{\gamma} = \gamma/4\bar{J}$. All calculations are carried out for the $K = 2$ Bethe lattice.

2.6.1 Electron States

To demonstrate the feasibility of the statDMFT and the associated localization criterion, we first discuss the localization properties of a single electron without coupling to phonons. In the next subsection, we will then contrast this well understood situation with the results for the coupled electron-phonon system. Some of the results of this subsection are taken from Alvermann. [140]

We begin with a qualitative discussion of the distribution for the LDOS at $\omega = 0$, shown in Fig. 2.15 for $\bar{\gamma} = 0.2, 0.5, 1.0$, and 1.5 (inset). The shape of the distribution changes dramatically with increasing disorder: For small disorder ($\bar{\gamma} < 1$), the distribution is approximately a Gaussian. The most probable value and the average value almost coincide and change little with disorder (see Table 2.2). Thus, the main effect of small disorder is to broaden the distribution. For

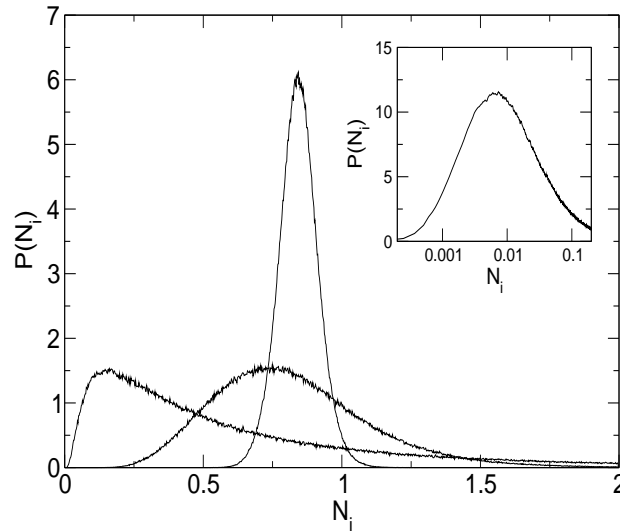


Figure 2.15: Distribution for the LDOS at $\omega = 0$ for $\bar{\gamma} = 0.2, 0.5$, and 1.0 . The inset shows the distribution for $\bar{\gamma} = 1.5$ on a logarithmic scale. In all cases $\eta = 10^{-10}$.

Table 2.2: Average, most probable, and typical LDOS at $\omega = 0$ corresponding to the distributions shown in Fig. 2.15.

$\bar{\gamma}$	N^{ave}	N^{mpv}	N^{typ}
0.2	0.844	0.843	0.841
0.5	0.822	0.749	0.773
1.0	0.710	0.162	0.445
1.5	0.568	0.006	0.106

larger disorder ($\bar{\gamma} \geq 1$), on the other hand, the distribution develops a long tail, where the most probable value is now significantly smaller than the average value (see again Table 2.2). For even larger disorder, close to the localization transition (for instance, for $\bar{\gamma} = 1.5$ shown in the inset of Fig. 2.15), the distribution becomes almost log-normal. [141] The average LDOS is now completely meaningless. Obviously, disorder does not only broaden the distribution but induces, if sufficiently strong, a change in the nature of the distribution.

From physical considerations, it is clear, that the distribution of the LDOS for a fixed energy depends strongly on whether the states at that energy are extended or localized. The amplitude of an extended state is uniformly distributed over the whole system. Thus, the LDOS does not fluctuate much from site to site, i.e., the distribution of the LDOS at a given energy has to be centered around an average LDOS. On the other hand, the amplitude of a localized state is essentially zero everywhere, except in a small range around a central site. For a given energy there is a certain number of degenerate localized states, each centered at a different site. The LDOS fluctuates therefore strongly throughout the lattice. Accordingly, the distribution of the LDOS, for a given energy, has to be very broad, with a long tail, due to the few sites where localized states have a large weight. Naturally, a complete characterization of the LDOS has to take the changes in the distribution into account, especially near the localization transition.

Within the statDMFT, distributions are represented by random samples. Any moment of the distribution, as well as the most probable value can be obtained from the histogram associated

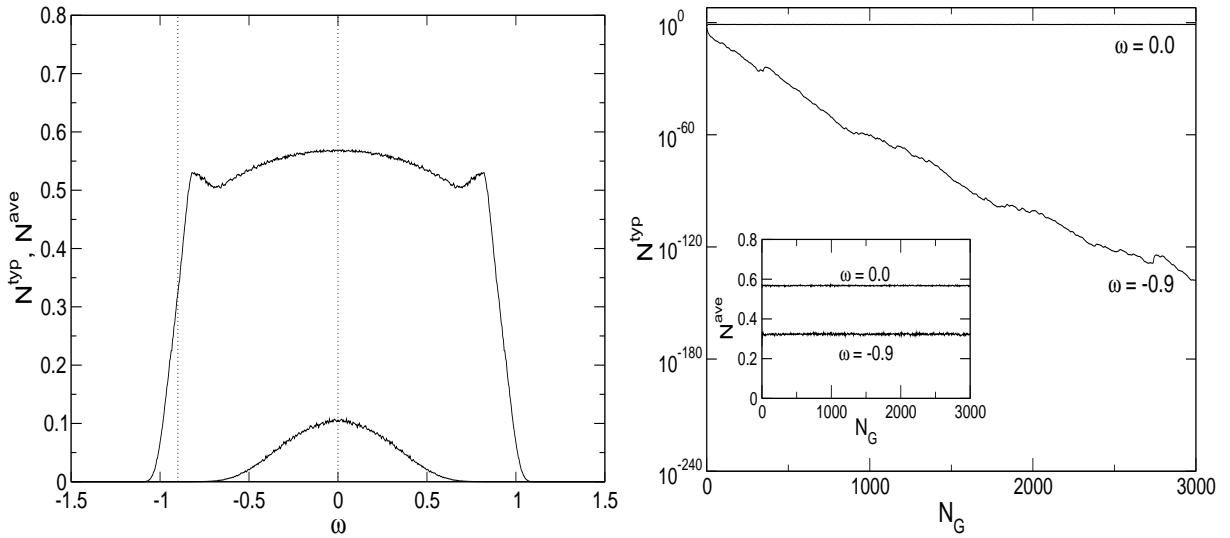


Figure 2.16: The left panel shows the average (upper curve) and typical LDOS (lower curve) for $\bar{\gamma} = 1.5$ and $\eta = 10^{-10}$. The vertical dotted lines indicate two energies, one below and one above the lower mobility edge, for which in the right panel the evolution of the average and typical LDOS is shown as a function of sample generation.

with the random sample. As indicated in subsection 2.5.4, in practice it is often better to avoid the construction of the histogram and to characterize, instead, physical quantities by their typical values, which are simply the geometric averages of the random samples. From Table 2.2 we see that the typical values capture the characteristic asymmetry of the distribution in the localized regime reasonably well ($N^{typ} \ll N^{ave}$ for $\bar{\gamma} > 1$). It is therefore indeed meaningful to use the typical LDOS as a kind of order parameter.

Let us now turn to a quantitative analysis of our results. In the left panel of Fig. 2.16 we depict, for $\bar{\gamma} = 1.5$, the typical and average LDOS over the whole spectral range of the pure Anderson model. The two main effects of disorder, the appearance of Lifshitz tails below $\omega = \pm 1.0$ and the existence of mobility edges around $\omega \sim \pm 0.8$, characterized by a vanishing of the typical LDOS (recall subsection 2.5.4), can be clearly seen. The data have been obtained for $\eta = 10^{-10}$, which is sufficiently small to reveal the intrinsic spectrum and to allow for a first estimate of the mobility edge.

A precise quantitative determination of the position of the mobility edge, requires a calculation of the typical LDOS for $\eta \rightarrow 0$. We specifically consider the lower mobility edge. With the obvious modifications all statements also hold for the upper mobility edge.

To perform the $\eta \rightarrow 0$ limit numerically, we initialize the sample with a finite LDOS and then iterate the stochastic recursion relations for $\eta = 0$ until convergence. The iteration process yields the correct, self-consistent LDOS. This procedure works extremely well, as can be seen in the right panel of Fig. 2.16, where we plot the typical and average LDOS as a function of the iteration step (in other words, the sample generation) for two energies, one below the lower mobility edge ($\omega = -0.9$) and one above ($\omega = 0$). As expected, below the lower mobility edge, the self-consistent value of the typical LDOS continues to decrease with sample generation, whereas above the mobility edge, the typical LDOS remains finite. Note, in both cases, the average LDOS stays finite and is essentially independent of the sample generation. This is the key observation, below (above) the lower mobility edge, the typical LDOS vanishes (stays finite), whereas the average LDOS remains finite in both cases.

At this point we should mention that the stable calculation of the average LDOS is subtle,

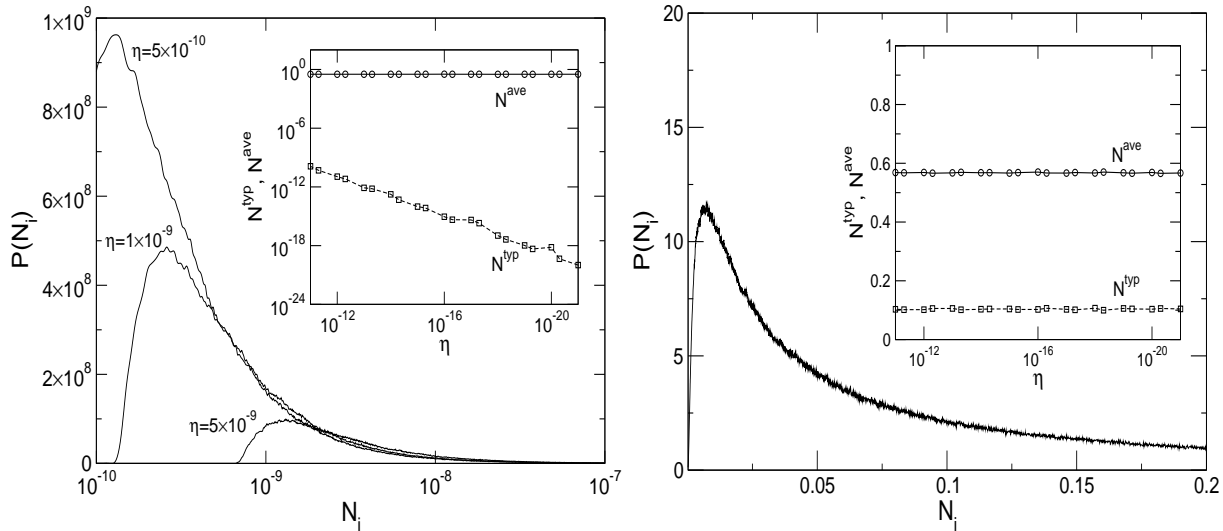


Figure 2.17: The left and right panels show, respectively, the η -scaling of the distribution for the LDOS below ($\omega = -0.9$) and above ($\omega = 0$) the lower mobility edge for $\bar{\gamma} = 1.5$. In the insets we display the corresponding average and typical LDOS as a function of η .

because of the pure statistics associated with the long tail, which, on the other hand, determines the average value. To overcome this problem, we calculated the average LDOS after each iteration step and then performed an arithmetic average over the obtained values of the average LDOS. Since the typical number of iterations $N_G \approx 1000$, we thereby effectively enlarged the sample size by three orders of magnitude, which was sufficient to obtain smooth data for the average LDOS. [140]

Thus, the tracking of the typical LDOS as a function of the sample generation can be utilized to decide whether states for a given energy are localized or not. In practice one would screen all energies comprising the spectrum and set a small threshold for the typical LDOS, for instance 10^{-30} , below which the typical LDOS is assumed to be de facto zero. According to our localization criterion, states at that energy are then classified as localized. Since this procedure can be performed arbitrarily close to the mobility edge, the position of the mobility edge can be determined very precisely. It should be also mentioned that values for the typical LDOS of the order of 10^{-200} are not numerical artifacts. The small values are correctly captured by the floating point representation of the typical LDOS.

An alternative is to use finite values of η and to track the typical LDOS with decreasing η . Below the lower mobility edge, the typical LDOS converges after a sufficient number of iterations to a value whose scale is set by the chosen η value, whereas above the lower mobility edge, the typical LDOS reaches an intrinsic value, completely unrelated to η . The average LDOS is in both cases again finite. For this procedure to work, η has to be of course small enough to resolve the intrinsic spectrum. For instance, η should not mimic Lifshitz tails.

That the procedure based on the η -dependence works excellently, can be verified in Fig. 2.17. To clarify the origin of the differences in the η -scaling of the typical and average LDOS below and above the lower mobility edge, we first look at the distributions. Below the lower mobility edge at $\omega = -0.9$, shown in left panel of Fig. 2.17, the distribution changes radically with decreasing η (note the logarithmic scale). The maximum of the distribution, i.e. the most probable value, shifts to very small values. In fact, η sets the scale for the most probable value. Accordingly, the typical value shown in the inset, decreases with η . Note, however, the average value stays at a

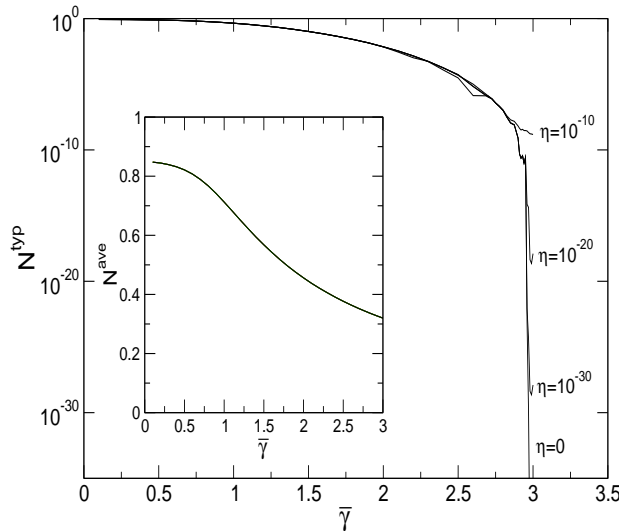


Figure 2.18: η -scaling of the typical and average (inset) LDOS at $\omega = 0$ for $\bar{\gamma} = 1.5$. Note, for the chosen η values, the average LDOS is independent of η .

constant value, independent of η . Clearly, the average value is determined by the long tail, i.e., the few sites, where the localized wave functions have appreciable weight. The average LDOS is therefore extremely less probable and indeed not a representative value. In contrast, above the lower mobility edge at $\omega = 0$, shown in the right panel of Fig. 2.17, the distribution is essentially independent of η . Accordingly, the typical as well as the average LDOS do not change with η .

Below the mobility edge, the distributions for the LDOS, the LCDOS, and the tunneling rate $\Gamma^{loc}(\omega)$ become singular for $\eta \rightarrow 0$. This behavior is closely connected with the configuration averaged, spectrally resolved return probability³

$$f_{ii}(\omega) = \lim_{\eta \rightarrow 0} (\eta/\pi) \langle |G_{ii}(\omega + i\eta)|^2 \rangle_{\{\epsilon_i\}}, \quad (2.92)$$

which is finite for localized states and zero for extended states. To reveal this relationship, we follow Logan and Wolynes [136] and introduce a joint distribution for the real and imaginary parts of the local hybridization function, $P(R(\omega), \Gamma(\omega))$, with $R(\omega) = \text{Re}H^{loc}(\omega)$ and $\Gamma(\omega) = \text{Im}H^{loc}(\omega)$, in terms of which we obtain

$$f_{ii}(\omega) = \lim_{\eta \rightarrow 0} \int_0^\infty d\Gamma(\omega) \frac{D(\omega, \Gamma(\omega))}{1 + \eta^{-1}\Gamma(\omega)}, \quad (2.93)$$

$$D(\omega, \Gamma(\omega)) = \frac{1}{\pi} \int_{-\infty}^\infty d\epsilon \int_{-\infty}^\infty dR(\omega) \frac{(\eta + \Gamma(\omega))p(\epsilon)P(R(\omega), \Gamma(\omega))}{[\omega - \epsilon - R(\omega)]^2 + [\eta + \Gamma(\omega)]^2}. \quad (2.94)$$

If the state at energy ω is localized, the (marginal) distribution for $\Gamma(\omega)$, i.e. $P(\Gamma(\omega)) = \int_{-\infty}^\infty dR(\omega)P(R(\omega), \Gamma(\omega))$, is strongly peaked around $\Gamma^{mpv}(\omega) \rightarrow 0$ (cf. the left panel of Fig. 2.17). In that regime, $D(\omega, \Gamma(\omega)) \approx \delta(\Gamma(\omega) - \Gamma^{mpv}(\omega))N^{cav}(\omega)$, with $N^{cav}(\omega) = -(1/\pi)\text{Im}G_{jj}^{(i)}(\omega)$ denoting the LCDOS. [136] Accordingly, Eq. (2.93) reduces to

$$f_{ii}(\omega) = \lim_{\eta \rightarrow 0} \frac{N^{cav}(\omega)}{1 + \eta^{-1}\Gamma^{mpv}(\omega)}, \quad (2.95)$$

³In Section 2.2 we defined the spectrally resolved return probability slightly differently as $\lim_{\eta \rightarrow 0} 2\eta \langle |G_{ii}(\omega + i\eta)|^2 \rangle_{\{\epsilon_i\}}$.

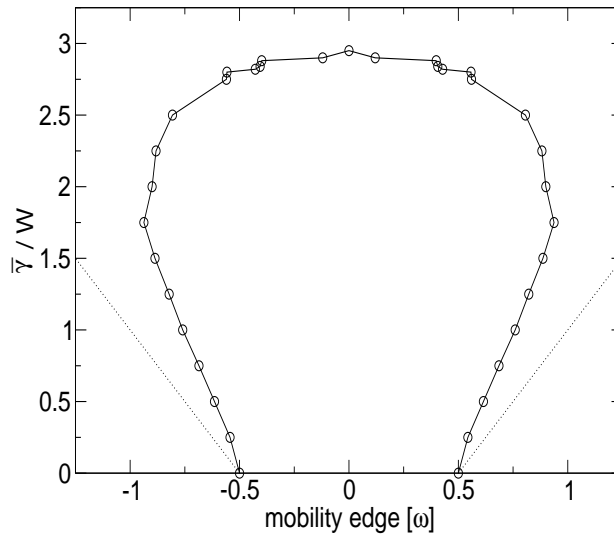


Figure 2.19: Mobility edge trajectory for an electron in the pure Anderson model. The dotted lines indicate the position of the band edges defined by $\pm(W/2 + \gamma/2)$.

which, provided $N^{cav}(\omega) \neq 0$, is finite, because $1 + \eta^{-1}\Gamma^{mpv}(\omega) \rightarrow 2$ for $\eta \rightarrow 0$. In other words, the singular behavior of the distribution for $\Gamma^{loc}(\omega)$ gives rise to a pole in $\langle |G_{ii}(\omega + i\eta)|^2 \rangle_{\{\epsilon_i\}}$ which in turn makes $f_{ii}(\omega)$ finite. From diagrammatic approaches it is known that maximally crossed diagrams, responsible for destructive interference, produce a pole in $\langle |G_{ii}(\omega + i\eta)|^2 \rangle_{\{\epsilon_i\}}$. Equation (2.93) provides therefore a link between the interference-based description of Anderson localization and the probabilistic approach adopted by the statDMFT.

The η -scaling discussed in Fig. 2.17 can be followed all the way down to $\eta = 0$, suggesting a precise procedure for the determination of mobility edges. In practice, however, we cut off the scaling at a certain threshold, for instance 10^{-30} . If the typical LDOS for a given energy ω is below the threshold, and if for that energy the average LDOS is finite, we classify the state at energy ω as localized. For $\omega = 0$ this is shown in Fig. 2.18. Clearly, for $\omega = 0$ the typical LDOS tends to zero for $\bar{\gamma} \sim 2.9$. The average LDOS on the other hand is independent of η and remains finite. Thus, according to our localization criterion, the state at energy $\omega = 0$ is localized for $\bar{\gamma} \geq 2.9$, in accordance with results obtained by Girvin and Jonson [94] and by Miller and Derrida. [134]

Performing the analysis for all energies comprising the spectrum, we can systematically map out the mobility edge trajectory. The result is shown in Fig. 2.19. Note that the statDMFT is accurate enough to detect the two transitions associated with the characteristic reentrance behavior of the mobility edge trajectory near the band edge: The delocalization transition at small disorder and the localization transition at large disorder. Even in the strongly disordered regime, where the mobility edges move to the centre of the band and all states are localized, the statDMFT works reliably well. We did not attempt to estimate the statistical error, but it should be of the order of the fluctuations visible in the plot.

Our results are in excellent agreement with results obtained by Miller and Derrida [134], suggesting that within the statDMFT mobility edges for noninteracting electrons can be indeed determined. In the next subsection, we shall demonstrate, that the statDMFT is flexible and powerful enough, to determine mobility edges in interacting systems as well.

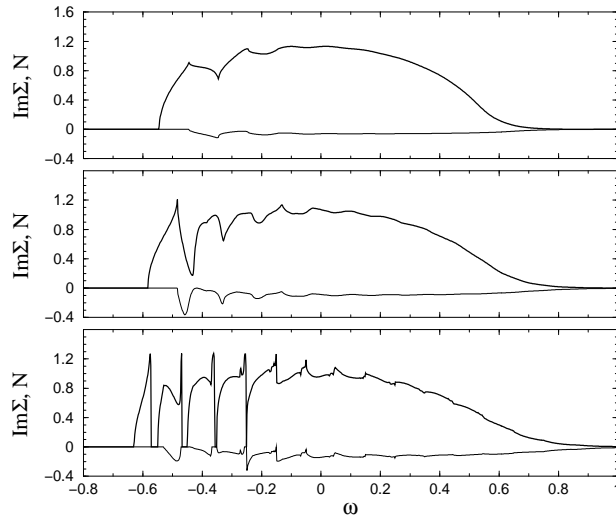


Figure 2.20: Evolution of the LDOS $N(\omega)$ (thick line) and the imaginary part of the interaction self-energy $\text{Im}\Sigma(\omega)$ (thin line) for the pure Holstein model ($\bar{\gamma} = 0$) with increasing electron-phonon coupling $\bar{\lambda} = 0.4, 0.7$, and 1.0 (from top to bottom). Results are given for $\bar{\alpha} = 0.4$ and $W_0 = 1.0$.

2.6.2 Polaron States

We now turn our attention to the consequences of the electron-phonon coupling. If the electron-phonon coupling is weak, the main effect is that the electron states above the phonon emission threshold, i.e., states whose kinetic energy is at least the phonon energy Ω , acquire a finite lifetime due to inelastic scattering, which gives rise to $\text{Im}\Sigma_i(\omega) \neq 0$. As a result, the critical disorder needed to localize these states will be larger than without electron-phonon coupling. For the states below the phonon emission threshold, we have $\text{Im}\Sigma_i(\omega) = 0$, and the critical disorder is the same as for the respective states in the pure Anderson model. [5]

Increasing the electron-phonon coupling to the point where $\bar{\lambda} > 1/\sqrt{K}$ and $g^2 > 1$, polaron formation starts and the LDOS fragments into an increasing number of polaronic subbands. [104, 113] Figure 2.20 illustrates, for the pure Holstein model ($\gamma = 0$), the evolution of the LDOS with increasing electron-phonon coupling for fixed $\bar{\alpha}$ and W_0 . The lowest subbands are either completely or partly coherent, i.e. $\text{Im}\Sigma_i(\omega) = 0$, whereas the higher order subbands are strongly damped because $\text{Im}\Sigma_i(\omega) \neq 0$. Thus, in the polaron regime, we have two energy scales: the bare bandwidth and the much smaller width of the polaronic subbands. Obviously, the width of the distribution of the on-site energies ϵ_i can be small on the scale of the bare bandwidth but large on the scale of the subband. We distinguish therefore between two regimes: The Holstein regime, where disorder is small on the scale of the bare bandwidth and the Anderson regime, where it is large on the scale of the width of the subband.

Holstein regime

For our purpose the lowest polaronic subband is of particular interest, because it is always completely coherent, i.e. $\text{Im}\Sigma_i(\omega) = 0$ throughout the subband, and no inelastic polaron-phonon scattering interferes with the localization properties of the polaron (see Fig. 2.20). Numerical studies of the ordered Holstein model demonstrated that the band dispersion of the lowest subband depends on both $\bar{\lambda}$ and $\bar{\alpha}$, and may differ significantly from the rescaled bare band. We expect therefore pronounced differences in the localization behavior depending on whether the

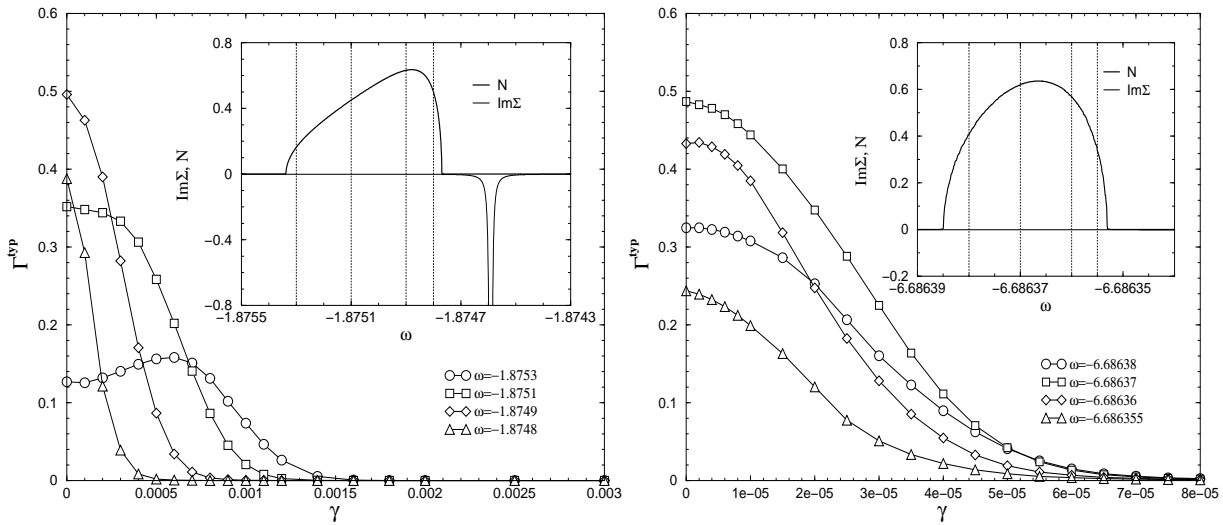


Figure 2.21: The left and right panels show, respectively, typical tunneling rates $\Gamma^{\text{typ}}(\omega)$ in the adiabatic intermediate-to-strong coupling ($\bar{\alpha} = 0.4$, $\bar{\lambda} = 1.8$) and anti-adiabatic strong coupling ($\bar{\alpha} = 1.2$ and $\bar{\lambda} = 6.66$) regime, using $W_0 = 2.0$ and $\eta = 10^{-8}$. The insets display the subband LCDOS $N(\omega)$ and the imaginary part of the interaction self-energy $\text{Im}\Sigma(\omega)$ for $\bar{\gamma} = 0$ (vertical dotted lines indicate the energies ω for which $\Gamma^{\text{typ}}(\omega)$ is plotted).

system is in the anti-adiabatic (small $\bar{\alpha}$) or adiabatic (large $\bar{\alpha}$) strong-coupling regime.

For a first orientation we present in Fig. 2.21 typical tunneling rates $\Gamma^{\text{typ}}(\omega)$ as a function of disorder strength $\bar{\gamma}$ for the lowest polaronic subband in the adiabatic intermediate-to-strong coupling (left panel) and non-to-anti-adiabatic strong coupling regime (right panel). [5] In the insets the subband LCDOS are also shown. Note, the bare bandwidth used in Fig. 2.21 is $W_0 = 2$. The data were obtained for $\eta = 10^{-8}$, which is not enough to quantitatively determine mobility edges, but the qualitative localization behavior of the states, in particular the difference between the adiabatic and anti-adiabatic regime, is already clearly revealed. In the adiabatic regime (left panel), the LCDOS is rather asymmetric because of the “hybridization” with the (optical) phonon branch, leading to a band flattening at the Brillouin-zone boundary (cf. Section 2.3). As a result, states at the zone boundary are very susceptible to disorder and the critical disorder strength for which $\Gamma^{\text{typ}}(\omega)$ vanishes at the top of the subband is substantially smaller than at the bottom of the subband. Clearly, in contrast to the Anderson model, there is a pronounced asymmetry of the localization behavior of the states within the subband. Not surprisingly, the absolute scale of disorder affecting the subband is on the order of the subband width \bar{W} , which is strongly renormalized in comparison with the bare bandwidth W_0 . In the anti-adiabatic strong coupling regime (right panel) the phonon admixture of the polaron states is nearly energy independent. Concomitantly, long-range tunneling as well as band flattening are negligible and the LDOS is rather symmetric (see inset). In fact, the dispersion of the subband is in that regime identical to the rescaled bare dispersion. [83,99] Accordingly, we expect in the anti-adiabatic strong-coupling regime disorder to affect the polaronic subband in the same way as it affects the band of the pure Anderson model. Most notably, the mobility edges should simultaneously appear on both sides of the subband. Furthermore, the mobility edge trajectories should show the characteristic reentrance behavior at the band edges and the critical disorder needed to localize all states of the subband should be determined by the states in the centre of the subband. In fact, with an appropriate scaling, the mobility edge trajectories for the lowest polaronic subband and the pure Anderson model should coincide. Below, we demonstrate that this is indeed the case.

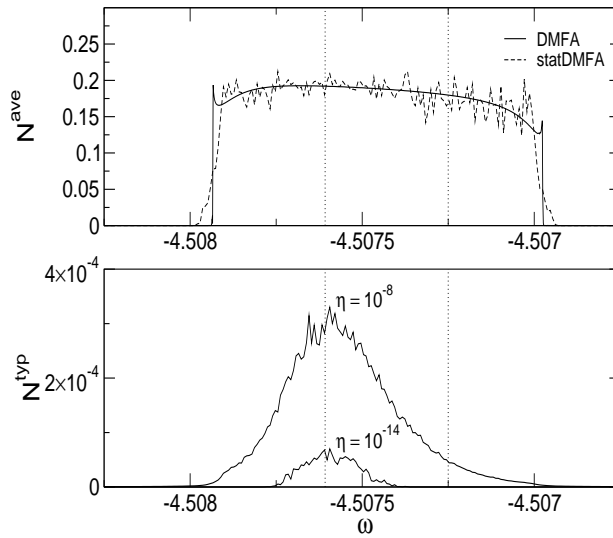


Figure 2.22: Average and typical LDOS for the lowest polaronic subband in the anti-adiabatic, strong coupling regime for $\bar{\gamma} = 2.5 \times W$; $W = 3.45 \times 10^{-4}$ is the width of the lowest subband of the pure Holstein model in units of $W_0 = 4\bar{J} = 1$. The polaron parameters are $\bar{\alpha} = 2.25$ and $\bar{\lambda} = 9$. The vertical dotted lines indicate two energies, one above ($\omega = -4.50725$) and one below ($\omega = -4.50759$) the upper mobility edge for the subband.

As for electron states in the Anderson model, a quantitative analysis of the localization behavior of polaron states in the Anderson-Holstein model requires a calculation of the typical LDOS for $\eta \rightarrow 0$. First, we consider in detail the *anti-adiabatic strong coupling* regime, where the phonon admixture of the states comprising the lowest polaronic subband is almost energy independent, and we in fact expect to recover the localization physics of a rescaled Anderson model.

We start with Fig. 2.22, which shows, for $\bar{\alpha} = 2.25$ and $\bar{\lambda} = 9$, the average and typical LDOS for the lowest subband; $\bar{\gamma} = 2.5 \times W$ with $W = 3.45 \times 10^{-4}$ the width of the subband in units of $W_0 = 4\bar{J}$. For comparison, we also show the DMFT result for the LDOS. As expected, the average LDOS is rather symmetric, the small asymmetry reflecting the fact that we are not yet in the extreme anti-adiabatic regime. As far as the effect of disorder is concerned, we see the same overall features as in the pure Anderson model (cf. Fig. 2.16): the appearance of Lifshitz tails and of mobility edges. The typical LDOS, shown in Fig. 2.22 for $\eta = 10^{-8}$ and $\eta = 10^{-14}$, vanishes on the both sides of the subband, clearly indicating the existence of mobility edges on both sides of the subband. As discussed before, a precise determination of the position of the mobility edges requires either to calculate the typical LDOS for $\eta = 0$ and to track the iteration flow with sample generation, or to follow the η -scaling of the LDOS.

For a quantitative calculation of the mobility edges, we adopted here the η -scaling approach. In Fig. 2.23 we show, for the two representative energies indicated in Fig. 2.22, the η -scaling of the distribution for the typical LDOS, the typical LDOS, and the average LDOS. Above the upper mobility edge at $\omega = -4.50725$, the distribution shows the characteristic properties associated with localized states: An extremely small most probable value and a long tail resulting in an average value much larger than the most probable value. The typical LDOS again scales to the fixed η value, while the average LDOS is independent of η . For the extended states at $\omega = -4.50759$, on the other hand, we again see that the distribution is insensitive to η and both average and typical LDOS converge to finite values independent of η .

As for the pure Anderson model, tracking the η -scaling of the LDOS for all energies comprising

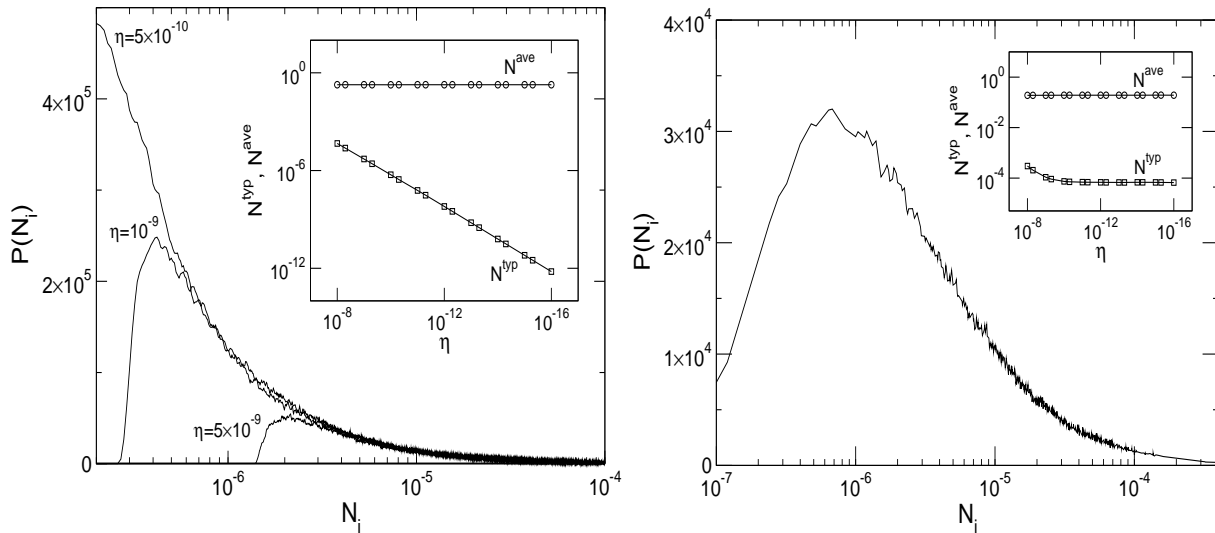


Figure 2.23: The left and right panels show, respectively, the η -scaling of the distribution for the LDOS at the two energies indicated in Fig. 2.22. The polaron parameters are the same as in Fig. 2.22. In the left panel $\omega = -4.50725$ (above the upper mobility edge), while in the right panel $\omega = -4.50759$ (below the upper mobility edge). The insets show the corresponding average and typical LDOS as a function of η .

the subband, enables us to map out the mobility edge trajectory for the subband. From physical considerations, we know that the trajectory should be the same as for the pure Anderson model. Instead of calculating the whole mobility edge trajectory, it is therefore sufficient to verify, for representative energies, that the two mobility edge trajectories indeed coincide.

As a first demonstration of this assertion, we plot in Fig. 2.24 the typical LDOS for $\omega = -4.50759$ (roughly the centre of the subband) scaled to its value at $\bar{\gamma} = 0$ as a function of disorder in units of the width of the subband and compare it with the scaled typical LDOS at $\omega = 0$ for the pure Anderson model, again as a function of $\bar{\gamma}$ scaled to the bandwidth. As anticipated, the two plots coincide. As in the pure Anderson model, the state at the centre of the (sub)band is localized for $\bar{\gamma}/W \geq 2.9$.

To provide further evidence for our assertion that the localization properties of the lowest subband in the anti-adiabatic strong coupling regime are the ones of a rescaled Anderson model, we explicitly calculated for a few selected energies the critical disorder needed to localize the states at these energies and, thereby, constructed parts of the mobility edge trajectory for the lowest subband. Note the extremely high precision of our approach, which enables us to determine the mobility edge trajectory of a subband whose width without disorder is 3.45×10^{-4} in units of $W_0 = 4\bar{J} = 1$. The results are shown in Fig. 2.25 (cf. circles). Obviously, the data points for the subband follow exactly the trajectory of the pure Anderson model, even at very strong disorder, where all states of the subband are localized (see data point at $\bar{\gamma}/W \sim 2.9$). In the anti-adiabatic strong coupling regime, the localization behavior of the states of the lowest subband is therefore identical to the behavior of the states in a rescaled Anderson model. The polaron effect, in particular the band collapse, only changes the energy scale on which localization takes place, the internal structure of the polaron states does not affect the localization properties. Thus, in the anti-adiabatic strong coupling regime, disorder can be sufficiently strong to localize all states of the lowest subband and yet too small to interfere with the internal structure of the polaron.

This is not the case in the *adiabatic intermediate-to-strong coupling* regime, where we find substantial differences between the localization properties of the lowest polaronic subband and the band of the pure Anderson model. The differences originate in the changing composite

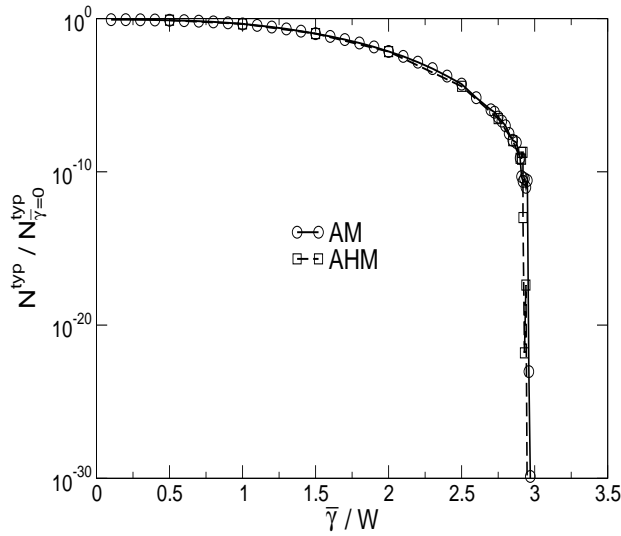


Figure 2.24: The typical LDOS at $\omega = -4.50759$ (roughly the centre of the subband) scaled to its value for $\bar{\gamma} = 0$ as a function of disorder measured in units of the width of the subband W ; $\bar{\alpha} = 2.25$ and $\bar{\lambda} = 9$. For comparison, we also plot the scaled typical LDOS for the pure Anderson model as a function of scaled disorder.

structure of the polaron states within the lowest subband. In particular at the top of the subband, where the band flattening due to the hybridization with the optical phonon branch significantly modifies the LDOS, the localization properties deviate strongly from a rescaled pure Anderson model. But also at the bottom of the subband significant deviations can be observed because of the phonon-induced long-range tunneling processes.

In the upper panel of Fig. 2.26 we show, for $\bar{\alpha} = 0.2$, $\bar{\lambda} = 1$, and $\bar{\gamma} = 0.25 \times W$, the average and typical LDOS for the lowest subband. Here, $W = 8.123 \times 10^{-3}$ is the width of the subband for the pure Holstein model (in units of $W_0 = 4\bar{J} = 1$). In contrast to the anti-adiabatic strong coupling case, the LDOS is strongly asymmetric, a direct result of the band flattening which yields a steeple at the top of the LDOS. States in the steeple, belonging to the flat part of the dispersion, are already sluggish and therefore very susceptible to disorder (recall the discussion of the DCPA delocalization time in Section 2.3). The typical LDOS vanishes therefore rapidly at the top of the subband. At the bottom, however, where states are rather mobile due to phonon-induced long-range tunneling, and hence less affected by disorder, the typical LDOS is finite.

To determine the position of the mobility edges we again employ the η -scaling approach. In Fig. 2.25 we show for $\bar{\alpha} = 0.2$ and $\bar{\lambda} = 1$ parts of the mobility edge trajectory for the lowest subband in the adiabatic strong coupling regime (cf. diamonds). As expected, the states at the bottom of the subband are almost insensitive to small amounts of disorder, resulting in a lower mobility edge which is pinned at the lower band edge, which in fact does also not change. States at the top of the subband, in contrast, are immediately affected by disorder. Small amounts of disorder (small even on the scale of the subband) are sufficient to shift the upper band edge to higher energies and to localize the states at the top of the subband. The upper mobility edge moves very fast away from the upper band edge. As a result, the mobility edge trajectory for the lowest subband in the adiabatic strong coupling regime is very asymmetric (for small disorder).

For large disorder (not shown in Fig. 2.25), of the order of the width of the subband, the upper band edge of the disorder-broadened lowest subband moves into a spectral range with significant inelastic scattering. The reason is the following: Without disorder, subbands are separated

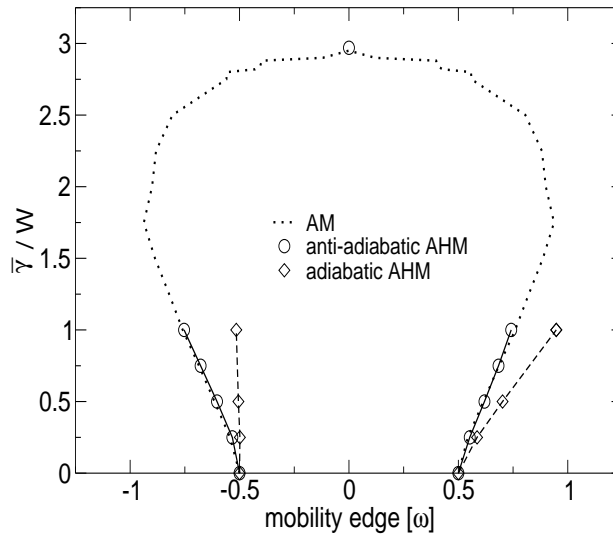


Figure 2.25: Parts of the mobility edge trajectories for the lowest polaronic subband of the Anderson-Holstein model in the anti-adiabatic strong coupling ($\bar{\alpha} = 2.25$ and $\bar{\lambda} = 9$, \circ) and the adiabatic intermediate-to-strong coupling regime ($\bar{\alpha} = 0.2$ and $\bar{\lambda} = 1$, \diamond). Disorder is measured in units of the respective width of the subbands, which, for the plot, are scaled to $W_0 = 4\bar{J} = 1$. For comparison the mobility edge trajectory for the pure Anderson model is also given (dashed line).

by singularities in the imaginary part of the electron-phonon self-energy. Increasing disorder redistributes states. In particular, it moves states into the gap region, which separated the first from the second subband, thereby giving rise to a shrinking gap. Concomitantly, the singularity in the electron-phonon self-energy broadens, its state repelling character weakens, resulting in an enhanced inelastic scattering rate for the states at the top of the lowest subband, which strongly suppresses localization in this spectral range. Both effects, the merging of the subbands and the increased inelastic scattering, occur before a reentrance behavior of the mobility edge trajectories can be observed.

To support the scenario just described we depict in the three lower panels of Fig. 2.26, for polaron parameters $\bar{\alpha} = 0.2$ and $\bar{\lambda} = 1$, the typical and average LDOS for $\bar{\gamma} = 1 \times W$, $2 \times W$, and $3 \times W$. Again, $W = 8.123 \times 10^{-3}$ is the width of the subband for the pure Holstein model (in units of $W_0 = 4\bar{J} = 1$). In all three panels, all states of the lowest subband are now delocalized, the typical LDOS is finite for all energies comprising the lowest subband. For the upper panel, where a small gap still separates the two lowest subbands, the asymmetric localization behavior of the states at the bottom and the top of the lowest subband is still visible. Nevertheless, inelastic scattering is so strong as to make the typical LDOS finite even at the top of the subband. With increasing disorder, shown in the three lower panels, the gap vanishes. More importantly, however, the typical LDOS increases with increasing disorder. Thus, in this regime, disorder delocalizes states. Eventually, of course, with disorder on the scale of the bare bandwidth, all states would be localized. However, the critical disorder strength is larger than in the case of the pure Anderson model, because the inelastic scattering has to be overcome.

The merging of the subbands signals that the internal structure of the polaron states and disorder start to strongly interfere with each other. With the vanishing subband structure, the concept of a subband mobility edge trajectory breaks down and a reentrance behavior of the mobility edge trajectory cannot be established.

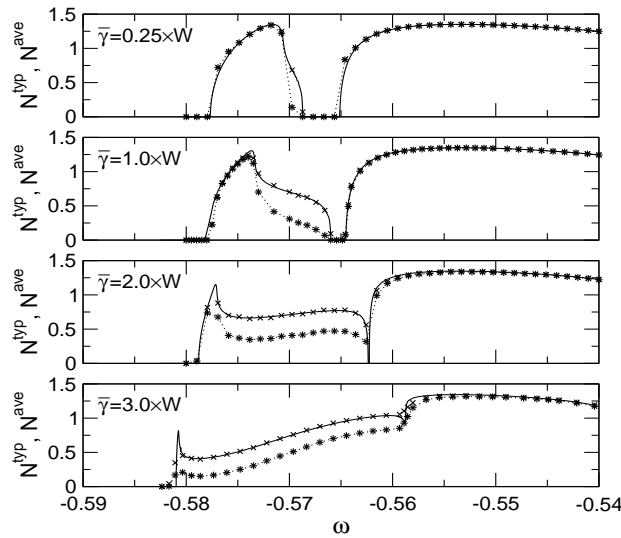


Figure 2.26: Average (crosses) and typical (stars) LDOS for $\bar{\alpha} = 0.2$, $\bar{\lambda} = 1$ and four different values for the disorder strength: $\bar{\gamma} = 0.25 \times W$, $\bar{\gamma} = 1 \times W$, $\bar{\gamma} = 2 \times W$, and $\bar{\gamma} = 3 \times W$ (from top to bottom), with $W = 8.123 \times 10^{-3}$ the width of the lowest polaron subband of the pure Holstein model (in units $W_0 = 4\bar{J} = 1$). The solid line is the DMFT result for the LCDOS.

Anderson regime

The vanishing subband structure characterizes a transition regime, between the Holstein and the Anderson regime, where disorder is on the scale of the energy gap between the subbands. The localization properties in the transition region are rather complicated. The situation becomes more transparent in what we call the Anderson regime, where disorder is large compared to the width of the polaronic subbands.

In Fig. 2.27 we show the typical and average LDOS for $\bar{\alpha} = 0.2$, $\bar{\lambda} = 0.75$, and $\bar{\gamma} = 2$. Without electron-phonon coupling, there would be mobility edges at $\omega \approx \pm 0.9$. In the presence of electron-phonon coupling, we first note that the symmetry between the lower and upper mobility edges is broken. The lower mobility edge seems to be located at $\omega \approx -0.8$, which is above the mobility edge of the noninteracting system. (Here, we did not perform the η -scaling necessary for a precise determination of the mobility edge.) Thus, at the low energy edge, electron-phonon coupling enhances the tendency towards localization. The upper mobility edge, in contrast, is shifted to higher energies ($\omega \approx 1.2$), i.e., at the upper band edge electron-phonon coupling delocalizes states and works against localization. If we mapped out a mobility edge trajectory, we would find a pronounced asymmetry between the lower and the upper part of the trajectory.

The asymmetry can be explained, if we recall that our calculation is for $T = 0$. Therefore, states at energy ω can, due to electron-phonon interaction, only couple to states at energies less than ω . This leads at the high energy side of the LDOS to a phonon-induced coupling of localized states above the mobility edge of the noninteracting system to delocalized states below. As a consequence, the localized states become delocalized. On the low energy side, the situation is different. States below the lower mobility edge of the noninteracting system remain localized, because they can only couple to states which are already localized. Above the lower mobility edge of the noninteracting system, electron-phonon interaction attempts however to transform electronic band states into polaronic (sub)band states, as suggested by Anderson. [93] Hence, these states become heavier and more susceptible to disorder. As a consequence, the lower mobility edge of the interacting system shifts above the lower mobility edge of the noninteracting one.

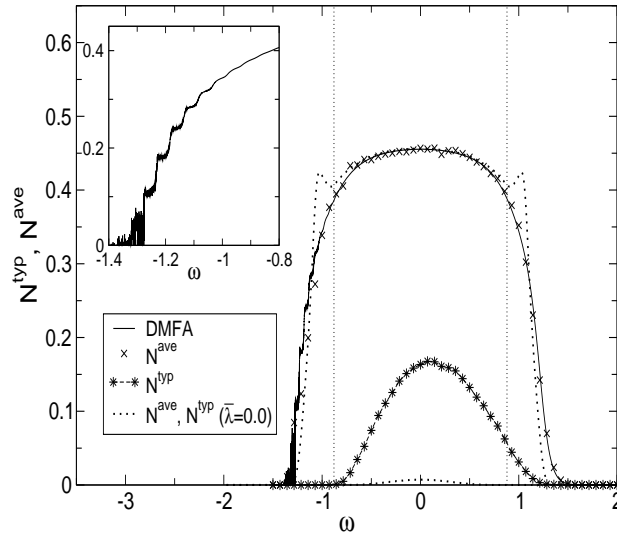


Figure 2.27: Average (crosses) and typical LDOS (stars) in the Anderson regime for $\bar{\alpha} = 0.2$, $\bar{\lambda} = 0.75$, and $\bar{\gamma} = 2$. The solid line is the LCDOS obtained from DMFT (a blow-up of the low-energy part is shown in the inset). Dashed lines depict the average and typical LDOS for $\bar{\lambda} = 0$, respectively, and the vertical dotted lines indicate the mobility edges of the noninteracting system.

Further insight about the nature of the states can be gained from the LCDOS obtained within the DMFT (cf. solid line in Fig. 2.27 and inset). Due to electron-phonon coupling, the DMFT results for the LCDOS show at the low energy side pronounced plateaus with a width given by the phonon energy. (The spikes are numerical artifacts.) The step-like increase of the DMFT LCDOS, together with the vanishing of the typical LDOS, is a clear signature for *localized polaron states*. The character of the states is here revealed by the DMFT LCDOS: It arises from polaronic defects [cf. independent boson model], which are centered around different on-site energies, because of the disorder. Since they are decoupled, the DMFT LCDOS (with a higher resolution we would see the same in the average LDOS) does not change with energy as long as the fluctuations of the on-site energies are smaller than the phonon energy. If the difference in on-site energy is equal to the phonon energy, a step arises because states with one additional phonon contribute. The step heights reflect therefore the phonon distribution of the polaronic defect states.

Whereas in the adiabatic intermediate-to-strong coupling regime *disorder* affects states differently at the bottom and the top of the polaronic subband, in the Anderson regime, *electron-phonon coupling* affects states in the vicinity of the lower and upper mobility edges of the noninteracting system differently. Only in the vicinity of the lower mobility edge of the noninteracting system, electron-phonon coupling and localization work in the same direction. At the upper mobility edge, electron-phonon coupling in fact delocalizes states.

2.7 Concluding Remarks

In the second half of this chapter we presented a detailed description of the statDMFT and applied it to the Anderson-Holstein model. Our main goal was to develop a self-consistent theory of localization in a generic disordered electron-phonon system. In particular, we investigated the localization properties of a single electron over a wide range of polaron parameters (adiabaticity and electron-phonon coupling strength).

Our approach is non-perturbative in the electron-phonon coupling and accounts for the spa-

tial fluctuations of the environment by promoting all variables of the theory to random variables. The objective of the theory is to calculate distributions (random samples). Of particular importance are the distributions for the LDOS, LCDOS, and the tunneling rate. Whereas information about the spatial dependence of the wave function Ψ_i can be extracted from the distribution for the LDOS, i.e. $\Psi_i \leftrightarrow P(N_i)$, the configuration averaged, spectrally resolved return probability is closely related to the distributions for the LCDOS and the tunneling rate, i.e. $f_{ii} \leftrightarrow P(N_i^{(j)}), P(\Gamma_i)$ [cf. Eq. 2.93].

We focused on the distribution for the LDOS. Since it is a measure of the spatial distribution of the wave function, it contains direct information about the localization properties: States are localized if the distribution of the LDOS is very asymmetric with an extremely long tail. Although the tail, which is due to the few sites on which (localized) wave functions are finite, makes the average LDOS finite, the more representative typical LDOS vanishes. Delocalized states, on the other hand, are characterized by a symmetric distribution of the LDOS for which the typical and average LDOS are of the same order of magnitude.

Using the typical LDOS to distinguish localized from extended states, we investigated in detail the localization properties of a single electron in the Anderson-Holstein model. We distinguished two parameter regimes: (i) weakly disordered Holstein regime, where disorder is small on the scale of the bare bandwidth and the polaronic subband structure is well developed, and (ii) the strongly disordered Anderson regime, with disorder large on the scale of the width of the subband, strong enough to interfere with the internal structure of the polaron states.

In the weakly disordered Holstein regime, we focused on a comparison of the mobility edge trajectories for the lowest polaronic subband and the bare band of the Anderson model. We found significant deviations, most notably in the adiabatic, intermediate-to-strong coupling regime. Two main conclusions can be drawn from our studies: (i) In the strong coupling, anti-adiabatic regime, the internal structure of the polaron is irrelevant and the localization properties of the lowest polaronic subband are essentially the ones of a rescaled Anderson model. The overall scale of the disorder is of course much smaller in the polaron case, suggesting that small polarons are most probably always localized at $T = 0$. (ii) The internal structure of the phonon dressing contributes the most in the adiabatic intermediate-to-strong coupling regime. Initially, for small disorder $\bar{\gamma} < W$ (W the width of the lowest subband in the clean system), states at the high-energy edge of the lowest polaronic subband are extremely sensitive to disorder and rather easy to localize, whereas states at the bottom are almost insensitive to disorder. In contrast to the pure Anderson model, the mobility edge trajectory (in the disorder range where it can be defined) is not symmetric with respect to the band centre. Whereas the lower mobility edge is pinned to the lower band edge, the upper mobility edge moves quickly away from the upper band edge. A reentrance of the upper mobility edge towards the centre of the subband cannot be observed, because at larger disorder strength subbands vanish and the concept of a subband mobility edge trajectory obviously breaks down.

The merging of polaron subbands is characteristic for a complicated transition regime where disorder is of the order of the energy gap and strongly interferes with the internal structure of the polaron states. In the Anderson regime, where disorder is much larger than the width of the subbands, disorder and electron-phonon coupling work in the same direction at the bottom of the band, where electron-phonon coupling even enhances the tendency towards localization, and against each other at the top, where electron-phonon coupling delocalizes states above the upper mobility edge of the noninteracting system. The mobility edge trajectory acquires therefore in the Anderson regime a pronounced asymmetry.

Several issues must be however clarified before real materials with polaronic excitations can be analysed along the lines presented in this paper. In most polaronic materials electron densities

are finite. The most pressing issue is therefore the consideration of the polaron-polaron interaction, mediated either due to phonons or due to the Coulomb potential of the electron charge. In principle, the statDMFT is capable of tackling this challenging problem. The main obstacle here is the controlled calculation of the interaction self-energy for the ensemble of impurity models. The exact continued fraction expansion works only for a single electron and cannot be adopted to finite densities. For finite densities, the interaction self-energy could be calculated perturbatively. However, self-trapping is a non-perturbative effect. To overcome the limitations of naive perturbation theory, it is at least necessary to adopt, for a given realization of disorder, a fully vertex-renormalized skeleton expansion. Formally, as long as the electron-phonon coupling is linear, the coupled electron-phonon system can be always mapped on to a purely electronic system with a retarded interaction. The parquet approach⁴, for instance, could be then used to set up such an expansion. It is also conceivable to use direct numerical simulations of the ensemble of the local Green function, based, for instance, on Quantum-Monte-Carlo or Exact Diagonalization techniques. The localization properties per se can again be simply extracted from an analysis of the distribution for the LDOS.

⁴A detailed description of the parquet approach is given in Section 1.5.

Appendix A

Polaron Impurity Model

In this appendix, we show how the local DCPA two-point function $\mathcal{G}_{ii}(z)$ [cp. Eq. (2.31)] can be calculated from the polaron impurity model (PIM). Towards that end, we apply the operation $\langle i|(N, n_i|\dots|m_i, N)|i \rangle$ on both sides of Eq. (2.28) and obtain in compact matrix notation

$$\mathcal{D}^{(N)}(z; \epsilon_i) = \tilde{G}^{(N)}(z) + \tilde{G}^{(N)}(z) \left[\sigma_{imp}^{(N)}(z; \epsilon_i) + \sigma_{ph}^{(N)}(\sqrt{E_p\Omega}) \right] \mathcal{D}^{(N)}(z; \epsilon_i), \quad (\text{A.1})$$

with matrices

$$\mathcal{D}_{nm}^{(N)}(z; \epsilon_i) = \langle i|(0, n_i|D_i^{(N)}(z)|m_i, 0)|i \rangle, \quad (\text{A.2})$$

$$\left[\sigma_{imp}^{(N)}(z; \epsilon_i) \right]_{nm} = \left[\epsilon_i - v^{(N+n)}(z) \right] \delta_{n,m}, \quad (\text{A.3})$$

$$\left[\sigma_{ph}^{(N)}(\sqrt{E_p\Omega}) \right]_{nm} = -\sqrt{E_p\Omega}\sqrt{n+1}\delta_{m,n+1} - \sqrt{E_p\Omega}\sqrt{n}\delta_{m,n-1}, \quad (\text{A.4})$$

$$\left[\tilde{G}^{(N)}(z) \right]_{nm} = \mathcal{G}_{ii}^{(N+n)}(z)\delta_{n,m}. \quad (\text{A.5})$$

To derive Eq. (A.1) we employed $\Delta H_i(z) \sim |i \rangle \langle i|$ together with $\mathcal{G}_{ii}^{(q)}(z) = \langle i|g^{(q)}(z)|i \rangle$, which follows from the definition of $\tilde{G}(z)$.

If we now introduce an auxiliary matrix

$$\tilde{H}^{(N)}(z) = \left[1 - \tilde{G}^{(N)}(z)\sigma_{ph}^{(N)}(\sqrt{E_p\Omega}) \right]^{-1} \tilde{G}^{(N)}(z), \quad (\text{A.6})$$

which sums all electron-phonon scattering processes, Eq. (A.1) can be rearranged into

$$\mathcal{D}^{(N)}(z; \epsilon_i) = \left[1 - \tilde{H}^{(N)}(z)\sigma_{imp}^{(N)}(z; \epsilon_i) \right]^{-1} \tilde{H}^{(N)}(z). \quad (\text{A.7})$$

The configuration average of Eq. (A.7) is straightforwardly performed since randomness enters only through $\sigma_{imp}^{(N)}(z; \epsilon_i)$. As a result, $\langle \langle \dots \rangle \rangle$ reduces to a site average over ϵ_i , $\langle \langle \dots \rangle \rangle_{\epsilon_i}$, and we find,

$$\langle \langle \mathcal{D}^{(N)}(z) \rangle \rangle = \langle \langle \mathcal{D}^{(N)}(z) \rangle \rangle_{\epsilon_i} = \int d\epsilon_i p(\epsilon_i) \mathcal{D}^{(N)}(z; \epsilon_i) \quad (\text{A.8})$$

or, explicitly in terms of matrix elements,

$$\langle \langle \mathcal{D}_{nm}^{(N)}(z) \rangle \rangle = \langle \langle \mathcal{D}_{nm}^{(N)}(z) \rangle \rangle_{\epsilon_i} = \int d\epsilon_i p(\epsilon_i) \mathcal{D}_{nm}^{(N)}(z; \epsilon_i), \quad (\text{A.9})$$

where the amplitudes $\mathcal{D}_{nm}^{(N)}(z; \epsilon_i)$ satisfy a recursion relation

$$\begin{aligned} \mathcal{D}_{nm}^{(N)}(z; \epsilon_i) &= F^{(N+n)}(z; \epsilon_i)\delta_{n,m} - \sqrt{E_p\Omega}F^{(N+n)}(z; \epsilon_i) \\ &\quad \times \left[\sqrt{n+1}\mathcal{D}_{n+1m}^{(N)}(z; \epsilon_i) + \sqrt{n}\mathcal{D}_{n-1m}^{(N)}(z; \epsilon_i) \right], \end{aligned} \quad (\text{A.10})$$

with

$$F^{(n)}(z; \epsilon_i) = \frac{1}{z - n\Omega - \epsilon_i + \mathcal{G}_{ii}^{-1}(z - n\Omega) - \mathcal{R}[\mathcal{G}_{ii}(z - n\Omega)]}. \quad (\text{A.11})$$

The recursion relation (A.10) can be solved by standard techniques [142], which give for the amplitude $\mathcal{D}_{00}^{(0)}(z; \epsilon_i)$ a continued fraction:

$$\mathcal{D}_{00}^{(0)}(z; \epsilon_i) = \frac{1}{[F^{(0)}(z; \epsilon_i)]^{-1} - \frac{\Omega E_p}{[F^{(1)}(z; \epsilon_i)]^{-1} - \frac{2\Omega E_p}{[F^{(2)}(z; \epsilon_i)]^{-1} - \frac{3\Omega E_p}{\dots}}}}. \quad (\text{A.12})$$

From the self-consistency condition, Eq. (2.30), finally follows

$$\mathcal{G}_{ii}(z) = \langle \langle \mathcal{D}_{00}^{(0)}(z) \rangle \rangle = \langle \langle \mathcal{D}_{00}^{(0)}(z) \rangle \rangle_{\epsilon_i} = \int d\epsilon_i p(\epsilon_i) \mathcal{D}_{00}^{(0)}(z; \epsilon_i), \quad (\text{A.13})$$

which directly yields Eq. (2.31).

At the end of this appendix, we bring the four-point function $f(\omega - i\eta, \omega + i\eta)$ [cp. Eq. (2.54)] into the numerically more convenient form of Eq. (2.55). As a preparatory step we notice, using the definition of the PIM, Eq. (2.27), together with $\mathcal{G}_{ii}^{(q)}(z) = \langle i | g^{(q)}(z) | i \rangle$, that the matrix elements of the atomic T-matrix defined in Eq. (2.37) can be written as

$$t_{0q}^{(0)}(z; \epsilon_i) = \frac{\mathcal{D}_{0q}^{(0)}(z; \epsilon_i) - \delta_{0q} \mathcal{G}_{ii}(z)}{\mathcal{G}_{ii}(z) \mathcal{G}_{ii}^{(q)}(z)}, \quad (\text{A.14})$$

with $\mathcal{D}_{0q}^{(0)}(z; \epsilon_i)$ defined in Eq. (A.2). If we now insert Eq. (A.14) into Eq. (2.54) and take into account that $\langle \langle \mathcal{D}_{00}^{(0)}(z; \epsilon_i) \rangle \rangle = \mathcal{G}_{ii}(z)$, Eq. (2.54) reduces to

$$f(z_1, z_2) = \sum_{q=0}^{\infty} \langle \langle \mathcal{D}_{0q}^{(0)}(z_1; \epsilon_i) \mathcal{D}_{q0}^{(0)}(z_2; \epsilon_i) \rangle \rangle. \quad (\text{A.15})$$

For $z_1 = z_2^* = z^*$, we may use $v^{(0)}(z) = [v^{(0)}(z^*)]^*$ and slightly rearrange the above equation into

$$f(z^*, z) = \sum_{q=0}^{\infty} \langle \langle |\mathcal{D}_{q0}^{(0)}(z; \epsilon_i)|^2 \rangle \rangle = \int d\epsilon_i p(\epsilon_i) |\mathcal{D}_{q0}^{(0)}(z; \epsilon_i)|^2, \quad (\text{A.16})$$

where we again used the fact that the configuration average reduces to a site average over ϵ_i . The amplitudes $\mathcal{D}_{q0}^{(0)}(z; \epsilon_i)$ satisfy the recursion relations (A.10). Setting $z = \omega + i\eta$ we finally obtain Eq. (2.55).

Appendix B

DCPA Ward Identity

Here we demonstrate that the (ladder) approximation employed to calculate the averaged two-resolvent is consistent with the single-site self-consistency condition used to obtain the averaged one-resolvent. In particular, we prove that for $O_e = 1_e$ the vertex operator $\Gamma_i^{(0)}(z_1, O_e, z_2)$ and the self-energy operator $\Sigma_i^{(0)}(z)$ fulfill a Ward identity, which corresponds to particle conservation. [102]

For the proof it is appropriate to work with vertex and self-energy operators instead of functions. We start with Eq.(2.39) written for $O_e = 1_e$,

$$K^{\text{ave}}(z_1, 1_e, z_2) = g^{(0)}(z_1) \left\{ 1_e + \sum_i \Gamma_i^{(0)}(z_1, 1_e, z_2) \right\} g^{(0)}(z_2), \quad (\text{B.1})$$

where we used $\Gamma^{\text{ave}} = \sum_i \Gamma_i^{(0)}$.

Alternatively, employing the resolvent identity $G(z_2) - G(z_1) = (z_1 - z_2)G(z_1)G(z_2)$ in the definition of the averaged two-resolvent, Eq. (2.8), we obtain an equivalent expression

$$K^{\text{ave}}(z_1, 1_e, z_2) = (z_1 - z_2) \{ g^{(0)}(z_2) - g^{(0)}(z_1) \}. \quad (\text{B.2})$$

Combining now Eq. (B.1) with (B.2) and using the definition of $g^{(q)}(z)$, Eq. (2.16), together with the definition of $\Sigma_i^{(q)}(z)$ in Eq. (2.14), we find that the local self-energy operator and the local vertex operator must satisfy the Ward identity

$$\Gamma_i^{(0)}(z_1, 1_e, z_2) = -(z_1 - z_2)^{-1} \{ \Sigma_i^{(0)}(z_1) - \Sigma_i^{(0)}(z_2) \}. \quad (\text{B.3})$$

We have to show that $\Gamma_i^{(0)}(z_1, 1_e, z_2)$ defined in Eq. (2.44), and $\Sigma_i^{(0)}(z)$ defined in Eq. (2.14), satisfy Eq. (B.3). The proof consists of two main steps. First, we rewrite Eq. (2.45) for $O_e = 1_e$ in operator form

$$\begin{aligned} \Gamma_i^{(0)}(z_1, 1_e, z_2) &= \sum_q \langle \langle (0, 0_i | t_i(z_1) | q_i, 0) g^{(q)}(z_1) \\ &\quad \times \{ 1_e - \sum_{j \neq i} \Gamma_j^{(q)}(z_1, 1_e, z_2) \} g^{(q)}(z_2) (0, q_i | t_i(z_2) | 0_i, 0) \rangle \rangle. \end{aligned} \quad (\text{B.4})$$

In a second step we insert Eq. (B.3), written for $z_i \rightarrow z_i - q\Omega, i = 1, 2$, into the rhs of Eq. (B.4) and recover after a lengthy but straightforward calculation an identity.

It is in order to provide a few calculational details. Instead of using Eq. (2.22) for the atomic T-matrix, it is convenient to recast Eq. (2.22) into two equivalent integral equations

$$t_i(z) = \Delta H_i(z) [1 + \bar{G}(z)t_i(z)] = [1 + t_i(z)\bar{G}(z)] \Delta H_i(z), \quad (\text{B.5})$$

and to deduce two useful identities

$$t_i(z)\bar{G}(z)U_i = t_i(z) - U_i + \sum_q P_q \Sigma_i^{(q)}(z) + t_i(z)\bar{G}(z) \sum_q P_q \Sigma_i^{(q)}(z), \quad (\text{B.6})$$

$$U_i \bar{G}(z) t_i(z) = t_i(z) - U_i + \sum_q P_q \Sigma_i^{(q)}(z) + \sum_q P_q \Sigma_i^{(q)}(z) \bar{G}(z) t_i(z), \quad (\text{B.7})$$

with $U_i = \{ \epsilon_i - \sqrt{E_p \Omega} (b_i + b_i^\dagger) | i \rangle \langle i |$. Eqs. (B.6) and (B.7) are employed at various stages of the calculation together with Eq. (2.17) and the single-site self-consistency condition Eq. (2.26).

Second, since the atomic T-matrix $t_i(z)$ keeps phonons on sites $j \neq i$ frozen, $(0, 0_i | t_i(z) Q = 0$ for any projection operator Q projecting onto a subspace with at least one phonon on a site $j \neq i$. Keeping these comments in mind, it is possible to derive the following intermediate result

$$\Gamma_i^{(0)}(z_1, 1_e, z_2) = -(z_1 - z_2)^{-1} \langle \langle (0, 0_i | t_i(z_1) \bar{G}(z_1) U_i - U_i \bar{G}(z_2) t_i(z_2) | 0_i, 0) \rangle \rangle, \quad (\text{B.8})$$

which, using Eqs. (B.6) and (B.7), reduces to

$$\Gamma_i^{(0)}(z_1, 1_e, z_2) = -(z_1 - z_2)^{-1} \left[\Sigma_i^{(0)}(z_1) - \Sigma_i^{(0)}(z_2) \right]. \quad (\text{B.9})$$

Appendix C

$\Omega = 0$ Limit of the DCPA Equations

In the limit $\Omega \rightarrow 0$ and $E_p\Omega = \text{const}$, electron-phonon coupling produces for the electron only an additional source of site-diagonal quenched disorder, on top of the site-diagonal alloy-type disorder due to ϵ_i . In this appendix we show, that in that case the DCPA formalism reduces to the CPA formalism. Thereby, we provide additional support for the consistency of the single-site decoupling scheme.

For $\Omega \rightarrow 0$ and $E_p\Omega = \text{const}$, we first notice, that the upper indices of *all* quantities appearing in the DCPA formalism can be set to zero [recall, e.g., $v^{(q)}(z) = v^{(0)}(z - q\Omega)$ and similarly for all the other quantities]. In particular, Eq. (2.32) becomes q -independent. As a result, the continued fraction in Eq. (2.31) can be summed analytically. Indeed, setting $g = \sqrt{E_p\Omega}$ and taking advantage of the continued fraction expansion of the error function [150],

$$\frac{1}{\sqrt{\pi}} \int_{-\infty}^{\infty} dt \frac{e^{-t^2}}{z - t} = \frac{1}{1 - \frac{1 \cdot \frac{1}{2}}{1 - \frac{2 \cdot \frac{1}{2}}{1 - \frac{3 \cdot \frac{1}{2}}{\dots}}}}, \quad (\text{C.1})$$

we find

$$\mathcal{G}_{ii}(\omega) = \int d\epsilon_i \int_{-\infty}^{\infty} dt \frac{e^{-\frac{t^2}{2g^2}}}{\sqrt{2\pi}g} \frac{p(\epsilon_i)}{\omega + i\eta - \epsilon_i + \mathcal{G}_{ii}(\omega) - R[\mathcal{G}_{ii}(\omega)] - t}, \quad (\text{C.2})$$

which is nothing but the CPA result for $\mathcal{G}_{ii}(\omega)$ in a model with site-diagonal Gaussian disorder ($\rightarrow t$) on top of site-diagonal alloy-type disorder ($\rightarrow \epsilon_i$).

Now we show that we also obtain the standard result for the Fourier transformation of the local matrix element of the averaged two-resolvent. With $\Omega \rightarrow 0$ and $E_p\Omega = \text{const}$, Eq. (2.51) yields for the vertex function

$$\gamma_{\vec{Q}}^{(0)} = \sum_q \langle \langle t_{0q}^{(0)} t_{q0}^{(0)} \rangle \rangle a_{\vec{Q}}^{(0)} + \sum_q \langle \langle t_{0q}^{(0)} t_{q0}^{(0)} \rangle \rangle \{ \mathcal{A}_{\vec{Q}}^{(0)} - \mathcal{G}_{ii}^{(0)} \mathcal{G}_{ii}^{(0)} \} \gamma_{\vec{Q}}^{(0)}, \quad (\text{C.3})$$

which we slightly rearrange to

$$\gamma_{\vec{Q}}^{(0)} = \frac{\Lambda a_{\vec{Q}}^{(0)}}{1 - \Lambda \{ \mathcal{A}_{\vec{Q}}^{(0)} - \mathcal{G}_{ii}^{(0)} \mathcal{G}_{ii}^{(0)} \}}, \quad (\text{C.4})$$

with

$$\Lambda = \sum_q \langle \langle t_{0q}^{(0)} t_{q0}^{(0)} \rangle \rangle. \quad (\text{C.5})$$

Note, the average over the site-diagonal Gaussian disorder is given in Eq. (C.5) by the sum over q ; this corresponds to an augmented space representation of the Gaussian disorder field. [151] Finally, employing Eq. (2.46) we find

$$\begin{aligned} K_{\vec{Q}}^{(0)} &= a_{\vec{Q}}^{(0)} + \mathcal{A}_{\vec{Q}}^{(0)} \gamma_{\vec{Q}}^{(0)} \\ &= \frac{a_{\vec{Q}}^{(0)}}{1 - \mathcal{L} \mathcal{A}_{\vec{Q}}^{(0)}}, \end{aligned} \quad (\text{C.6})$$

with

$$\mathcal{L} = \frac{\Lambda}{1 + \Lambda \mathcal{G}_{ii}^{(0)} \mathcal{G}_{ii}^{(0)}}, \quad (\text{C.7})$$

which is precisely the CPA result for $\sum_i e^{-i\vec{Q}\cdot\vec{R}_i} \langle i | K^{\text{ave}} | i \rangle$. [102]

Appendix D

StatDMFT for a Single Polaron: Multiple Scattering Approach

For a single electron at zero temperature, the statDMFT can be alternatively derived by suitably modified multiple-scattering techniques. Although this derivation is not as general as the cavity construction, it has the benefit to clarify the relationship between the statDMFT on the one hand and the (dynamical) coherent potential approximation [(D)CPA] [103, 104] on the other.

The derivation, applicable to any model with local electron-phonon coupling and local disorder, proceeds in two steps: First, for a fixed realization of disorder, multiple-scattering techniques are used to find the best single-site decoupling for the inelastic electron-phonon scattering. Technically, this results in the construction of an effective electron Hamiltonian from which all two-point functions can be obtained. In a second step, to capture the spatial fluctuations due to disorder, the local two-point function is expanded up to the second order term of the renormalized perturbation series. On a Bethe lattice, this step leads directly to the stochastic recursion relations given in the the main text. For Bravais lattices Eq. (2.76) should be additionally invoked to obtain a closed set of equations.

In the spirit of the multiple-scattering formalism introduced in Section 2.2, we define, in the Wannier representation, an effective Hamiltonian

$$\bar{H}(z) = \sum_i \epsilon_i |i\rangle\langle i| - \sum_{i,j} J_{ij} |i\rangle\langle j| + \sum_q q\Omega P_q + \Sigma(z), \quad (\text{D.1})$$

with an interaction self-energy operator

$$\Sigma(z) = \sum_i \sum_q P_q v_i(z - q\Omega) |i\rangle\langle i|. \quad (\text{D.2})$$

Here, we again introduced projection operators P_q [109], which project onto the phonon subspace with a total number of q phonons in terms of which, neglecting the zero-point motion, the lattice energy $\Omega \sum_i b_i^\dagger b_i = \sum_q q\Omega P_q$. The function $v_i(z)$ is the coherent potential, which is now site-dependent in contrast to the DCPA ansatz (2.14).

Because we now treat only inelastic electron-phonon scattering within an effective single-site approximation, the effective Hamiltonian (D.1) contains the term with the random on-site energies. This is in stark contrast to the effective Hamiltonian introduced in connection with the DCPA. The DCPA treats both the average over phonons and the average over random on-site energies within an effective single-site approximation. As a result, the DCPA effective Hamiltonian (2.11) does not contain the random on-site energies. The effective Hamiltonian (D.1) enables us to perform, for a fixed realization of on-site energies, the phonon average in a ‘‘DCPA manner’’.

By construction, the interaction self-energy is local and independent of the spatial distribution of the phonons. It only depends on the electron energy $z - q\Omega$, i.e. the total energy z minus the energy of the lattice $q\Omega$. Due to the randomness of the on-site energies, the self-energy is different for each lattice site. In contrast to a CPA treatment of the disorder, we explicitly keep therefore the site index i . It is only the spatial information due electron-phonon coupling which is lost in the particular ansatz Eq. (D.2); disorder induced fluctuations are kept and manifest themselves in the site dependence of the coherent potential $v_i(z)$.

For a fixed realization of on-site energies, the self-energy is determined by forcing the phonon vacuum averages of the full resolvent $G(z) = 1/(z - H)$ and the effective resolvent $\bar{G}(z) = 1/(z - \bar{H}(z))$ to be equal

$$\langle 0|G(z)|0\rangle = \langle 0|\bar{G}(z)|0\rangle. \quad (\text{D.3})$$

The phonon vacuum averaged resolvents are still operators in the electronic Hilbert space and all two-point functions can be obtained from $\langle 0|\bar{G}(z)|0\rangle$. (Note, for a single electron it is sufficient to work with resolvent operators. Time-ordered Green functions are not required.)

We now rewrite the Anderson-Holstein model in terms of the effective Hamiltonian

$$H = \bar{H}(z) + \sum_i \Delta H_i(z), \quad (\text{D.4})$$

with

$$\Delta H_i(z) = -\sqrt{E_p\Omega}(b_i + b_i^\dagger)|i\rangle\langle i| - \sum_q P_q v_i(z - q\Omega)|i\rangle\langle i|, \quad (\text{D.5})$$

and define a total T-matrix

$$G(z) = \bar{G}(z) + \bar{G}(z)T(z)\bar{G}(z), \quad (\text{D.6})$$

connecting the full and the effective resolvents. The total T-matrix is a sum of single-site contributions

$$T(z) = \sum_i Q_i(z), \quad (\text{D.7})$$

with

$$Q_i(z) = t_i(z) \left[1 + \bar{G}(z) \sum_{j \neq i} Q_j(z) \right], \quad (\text{D.8})$$

and the single-site T-matrix

$$t_i(z) = [1 - \Delta H_i(z)\bar{G}(z)]^{-1} \Delta H_i(z). \quad (\text{D.9})$$

Using

$$\bar{G}(z) = \sum_q \left[z - q\Omega - \sum_i [\epsilon_i + v_i(z - q\Omega)]|i\rangle\langle i| - \sum_{ij} (-J)_{ij}|i\rangle\langle j| \right]^{-1}, \quad (\text{D.10})$$

which follows from the fact that $\bar{H}(z)$ does not couple phonon subspaces with different numbers of phonons, the self-consistency equation Eq. (D.3) first reduces to $\langle 0|Q_i(z)|0\rangle = 0$ and then, within a single-site (D)CPA-type decoupling [4], eventually to

$$\langle 0|t_i(z)|0\rangle = 0. \quad (\text{D.11})$$

Of course, the single-site T-matrix $t_i(z)$ affects only phonons on site i , phonons on other sites are frozen and act only as spectators.

In Section 2.2 we have shown that the single-site self-consistency equation $\langle 0|t_i(z)|0\rangle = 0$ is equivalent to allowing only self-avoiding paths in the iterated form of $\langle 0|Q_i(z)|0\rangle = 0$. In the limit of infinite coordination number, the single-site decoupling is exact. The single-site decoupling treats electron-phonon scattering therefore as if the lattice had infinite coordination number. Accordingly, the (D)CPA-type decoupling corresponds, within the framework of the multiple-scattering formalism, to the truncation of the generating functional $W^{(i)}[\eta^\dagger, \eta]$ in Eq.

(2.68). Both give rise to an effective single-site model where the only interaction is the original local interaction of the lattice model.

Instead of working directly with the atomic T-matrix, it is advantageous to consider an ensemble of polaron impurity models specified by

$$D_i(z) = \bar{G}(z) + \bar{G}(z)t_i(z)\bar{G}(z), \quad (\text{D.12})$$

in terms of which the self-consistency equation becomes

$$\langle 0|D_i(z)|0\rangle = \langle 0|\bar{G}(z)|0\rangle = \langle 0|G(z)|0\rangle, \quad (\text{D.13})$$

i.e. the electron operator $\langle 0|G(z)|0\rangle$ is approximated by $\langle 0|D_i(z)|0\rangle$.

Note, due to the randomness of the on-site energies ϵ_i , the resolvents and its matrix elements (the two-point functions) are random variables. Hence, Eq. (D.13) is a relation between random variables. The site index on the lhs is not an inconsistency but merely indicates that the random variable $\langle 0|D_i(z)|0\rangle$ has the same distribution as the random variables displayed on the rhs. It is absolutely crucial to realize that the electronic operator $\langle 0|G(z)|0\rangle$ is in fact represented by an ensemble of resolvents, corresponding to an ensemble of polaron impurity models, similar to the ensemble of effective single-site actions appearing in the cavity method.

To determine the interaction self-energy, we use an operator identity and rewrite Eq. (D.12) into

$$D_i(z) = F_i(z) + F_i(z)\Delta H_i(z)D_i(z), \quad (\text{D.14})$$

with

$$F_i(z) = \bar{G}(z) - \bar{G}(z)\Sigma_i(z)F_i(z), \quad (\text{D.15})$$

which describes the effective medium with the interaction self-energy on site i ,

$$\Sigma_i(z) = \sum_q P_q v_i(z - q\Omega)|i\rangle\langle i|, \quad (\text{D.16})$$

subtracted. Equation (D.14) corresponds directly to the Hamiltonian representation of the effective single-site action given in the main text.

Applying $\langle i|(p_i|\dots|q_i)|i\rangle$ on both sides of Eq. (D.14), with $|i\rangle$ and $|p_i\rangle$ a Wannier state and a phonon state on site i , we obtain [cf. Eq. (A.10)]

$$\mathcal{D}_{nm}(z) = F_{ii}(z - n\Omega)\delta_{n,m} - \sqrt{\Omega E_p} F_{ii}(z - n\Omega) \left[\sqrt{n+1} \mathcal{D}_{n+1m}(z) + \sqrt{n} \mathcal{D}_{n-1m}(z) \right], \quad (\text{D.17})$$

with $D_{pq} = \langle i|(p_i|D_i(z)|q_i)|i\rangle$ and

$$F_{ii}(z) = \frac{1}{z - \epsilon_i + \mathcal{G}_{ii}^{-1}(z) - \mathcal{R}[\mathcal{G}_{ii}(z)]}. \quad (\text{D.18})$$

From Eq. (D.17) we find D_{00} in the form of a continued fraction [cf. (A.12)], which finally yields for the local two-point function

$$G_{ii}(z) = \frac{1}{[F_{ii}(z)]^{-1} - \frac{\Omega E_p}{[F_{ii}(z - 1\Omega)]^{-1} - \frac{2\Omega E_p}{[F_{ii}(z - 2\Omega)]^{-1} - \frac{3\Omega E_p}{\dots}}}}. \quad (\text{D.19})$$

By inspection, the coherent potential then becomes

$$v_i(z) = \frac{\Omega E_p}{[F_{ii}(z - 1\Omega)]^{-1} - \frac{2\Omega E_p}{[F_{ii}(z - 2\Omega)]^{-1} - \frac{3\Omega E_p}{[F_{ii}(z - 3\Omega)]^{-1} - \frac{4\Omega E_p}{\dots}}}}. \quad (\text{D.20})$$

The construction of the polaron impurity models has been performed for a fixed realization of on-site disorder. No configurational average has been performed, in contrast to the DCPA. Operators as well as functions are still random variables. To treat the spatial fluctuations, we now apply the renormalized perturbation series to each phonon subspace. Towards that end, we recall $\bar{H} = \sum_q P_q h_q(z)$ and rewrite $h_q(z)$ as

$$h_q(z) = h_q^{(i)}(z) + \xi_i(z; q)|i\rangle\langle i| + \Gamma, \quad (\text{D.21})$$

where the first term on the rhs $h_q^{(i)}(z)$ is $h_q(z)$ with site i removed, the second term $\xi_i(z; q) = \epsilon_i + v_i(z - q\Omega) + q\Omega$ ⁵, and the third term $\Gamma = -J \sum_j \text{NN } i \{ |i\rangle\langle j| + |j\rangle\langle i| \}$. [140]

As usual, the renormalized perturbation series works with a resolvent. Hence, we introduce $g_q(z) = 1/(z - h_q(z))$ and apply the operator identity

$$\begin{aligned} g_q(z) &= \frac{1}{z - h_q(z)} \\ &= \Xi_q(z) + \Xi_q(z)\Gamma g_q(z), \end{aligned} \quad (\text{D.22})$$

with $\Xi_q(z) = (z - h_q^{(i)}(z) - \xi_i(z; q))^{-1}$. From $\langle i|h_q^{(i)}(z)|j\rangle = \langle j|h_q^{(i)}(z)|i\rangle = 0$ for all j follows that $\langle i|\Xi_q(z)|i\rangle = (z - \xi_i(z; q))^{-1}$, $\langle i|\Xi_q(z)|j\rangle = \langle j|\Xi_q(z)|i\rangle = 0$ for $i \neq j$, and $\langle j|\Xi_q(z)|l\rangle = \langle j|g_q(z)|l\rangle^{(i)}$ for $j, l \neq i$. Thus, taking matrix elements with respect to Wannier states $\langle i|\dots|j\rangle$, Eq. (D.22) yields, for $i = j$,

$$\langle i|g_q(z)|i\rangle = \frac{1}{z - \xi_i(z; q)} - \frac{J}{z - \xi_i(z; q)} \sum_j \text{NN } i \langle j|g_q(z)|i\rangle, \quad (\text{D.23})$$

and, for i and j next neighbors,

$$\langle j|g_q(z)|i\rangle = -J \sum_m \text{NN } i \langle j|g_q(z)|m\rangle^{(i)} \langle i|g_q(z)|i\rangle. \quad (\text{D.24})$$

Combining Eq. (D.23) with Eq. (D.24) and specializing to a Bethe lattice yields

$$\langle i|g_q(z)|i\rangle = \left[z - \xi_i(z; q) - J^2 \sum_j \text{NN } i \langle j|g_q(z)|j\rangle^{(i)} \right]^{-1}, \quad (\text{D.25})$$

with

$$\langle j|g_q(z)|j\rangle^{(i)} = \left[z - \xi_j(z; q) - J^2 \sum_{l \neq i} \text{NN } j \langle l|g_q(z)|l\rangle^{(j)} \right]^{-1}. \quad (\text{D.26})$$

Note, although the renormalized perturbation series is separately applied to each phonon subspace, the subspaces are coupled through the coherent potential, which contains $\langle j|g_q(z)|j\rangle^{(i)}$ with $q = 0, 1, \dots, M$.

Employing the self-consistency condition, $\langle i|g_q(z)|i\rangle = G_{ii}(z - q\Omega)$ and $\langle j|g_q(z)|j\rangle^{(i)} = G_{jj}^{(i)}(z - q\Omega)$, and putting $q = 0$, Eqs. (D.25) and (D.26) are identical with the single particle limit of the stochastic recursion relations Eqs. (2.80) and (2.81).

⁵To obtain the $q\Omega$ term we used the (one-particle) completeness relation $\sum_i |i\rangle\langle i| = 1$.

Appendix E

Large Coordination Number Limit of the statDMFT

For a lattice with infinite coordination number, the statDMFT reduces to the DMFT. To demonstrate this point, it is convenient to scale the transfer amplitude $J \rightarrow \bar{J}/\sqrt{K}$. [5]

Restricting for simplicity the discussion to the Bethe lattice, Eq. (2.82) shows that for $K \rightarrow \infty$ cavity and local Green function are identical and Eq. (2.80) becomes

$$G_{i\sigma i\sigma}(i\omega_n) = \frac{1}{i\omega_n + \mu - \epsilon_i - \bar{J}^2 G_\sigma^{\text{ave}}(i\omega_n) - \Sigma_\sigma(i\omega_n)}, \quad (\text{E.1})$$

where we have used the central limit theorem to replace the hybridization function on the rhs by the average of the local Green function. At this point the scaling of J is most convenient.

The self-energy is calculated from the effective single-site action $S(i)$ where, again due to the central limit theorem, the hybridization function is replaced by $\bar{J}G_\sigma^{\text{ave}}$. The self-energy is therefore a functional of $G_\sigma^{\text{ave}}(i\omega_n)$, i.e., on the rhs of Eq. (E.1) the only random variable is ϵ_i . The sample average $(1/K) \sum_{j=1}^K (\dots)$ of Eq. (E.1) is therefore identical to the site average over ϵ_i . Denoting the site average by $\langle \dots \rangle_{\epsilon_i}$, we get

$$G_\sigma^{\text{ave}}(i\omega_n) = \left\langle \left[i\omega_n + \mu - \epsilon_i - \bar{J}^2 G_\sigma^{\text{ave}}(i\omega_n) - \Sigma_\sigma[\epsilon_i, G_\sigma^{\text{ave}}] \right]^{-1} \right\rangle_{\epsilon_i}, \quad (\text{E.2})$$

which, together with

$$\begin{aligned} S(i) \Big|_{K \rightarrow \infty} &= \int_0^\beta d\tau d\tau' \sum_\sigma c_{i\sigma}^\dagger(\tau) \left\{ [\partial_\tau + \epsilon_i - \mu] \delta(\tau - \tau') \right. \\ &\quad \left. + \bar{J}^2 G_\sigma^{\text{ave}}(\tau - \tau') \right\} c_{i\sigma}(\tau') + S_{\text{int}}(i) \end{aligned} \quad (\text{E.3})$$

constitutes the DMFT equations for the average local Green function $G_\sigma^{\text{ave}}(i\omega)$. For a single electron, Eqs. (E.2) and (E.3) reduce, for the case without disorder, to the dynamical coherent potential approximation (DCPA) equations [104] and, for the case without electron-phonon coupling, to the coherent potential approximation (CPA) equations. [103]

For the pure Anderson model this is illustrated in Fig. 2.28 for $\bar{\gamma} = 0.5$. With increasing lattice coordination number K we observe two effects. First, the difference between cavity and local Green function indeed disappears, as can be seen from the vanishing of the bumps due to the van-Hove singularities; second, the local density of states converges to the CPA density of states. Note also, Lifshitz tails, which are present within the statDMFT, also vanish, as expected, with increasing K .

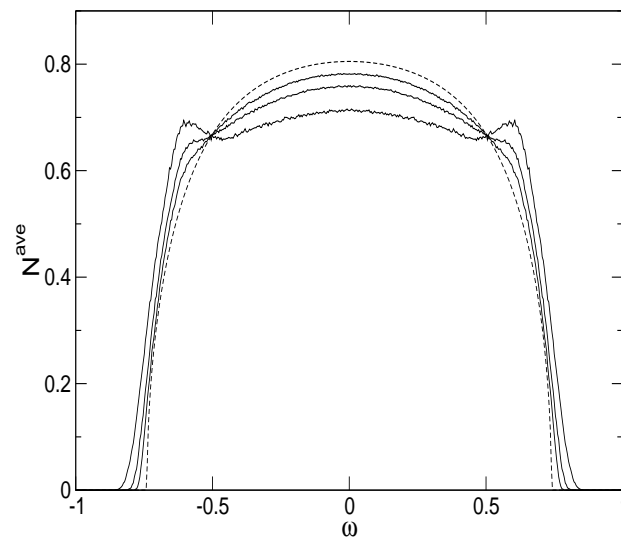


Figure 2.28: Average LDOS for the Bethe lattice with connectivity $K = 2, 4$ and 8 (solid lines from bottom to top). The dashed line is the DMFT LDOS, i.e. the LDOS for $K \rightarrow \infty$. Electron-phonon coupling is turned off (pure Anderson model) and $\bar{\gamma} = 0.5$.

Chapter 3

Electron Spin Dynamics in Semiconductors [9–11]

This chapter presents a semiclassical kinetic theory for the non-equilibrium electron spin dynamics in non-magnetic semiconductors. It is based to a large extent on a preprint [9], supplemented with material from Refs. [10,11]. The approach accounts for elastic as well as inelastic scattering and treats Elliott-Yafet and motional-narrowing processes, such as D'yakonov-Perel' and variable g-factor processes, on an equal footing. Focusing on small spin polarizations and small momentum transfer scattering, we derive, starting from the full quantum kinetic equations, a Fokker-Planck equation for the electron spin polarization. The dynamics of the spin polarization is thereby visualized in terms of a “test” spin polarization which scatters off “field” particles (electrons, impurities, phonons). We then construct, using a rigorous multiple time scale approach, a Bloch equation for the macroscopic (\vec{k} -averaged) spin polarization on the long time scale, where the spin polarization decays. Spin-conserving energy relaxation and diffusion, which occur on a short time scale, after the initial spin polarization has been injected, are incorporated and shown to give rise to a weight function which defines the energy averages required for the calculation of the spin relaxation tensor of the Bloch equation. We give explicit expressions for the spin relaxation tensor, applicable to bulk and quantum wells. To illustrate our approach, we calculate for specific situations the lifetime of a photogenerated electron spin polarization in bulk GaAs and a GaAs quantum well. For the bulk GaAs, we discuss the magnetic field dependence of spin relaxation times taking electron-impurity and electron-phonon scattering into account. We focus in particular on the competition between the quenching of the D'yakonov-Perel' process and the field-induced variable g-factor process. We find an optimal magnetic field for which the spin lifetimes are maximal and point out that the sign of the slope of the field dependence of the transverse spin lifetime reveals whether the Elliott-Yafet or the D'yakonov-Perel' process dominate spin relaxation at small magnetic fields. For a GaAs quantum well, we calculate spin lifetimes at temperatures and densities where electron-electron and electron-impurity scattering dominate. We find that spin lifetimes are non-monotonic functions of temperature and density. Our results show that at electron densities and temperatures, where the cross-over from the non-degenerate to the degenerate regime occurs, spin lifetimes are particularly long.

3.1 Introductory Remarks

The spin degree of freedom of an electron provides an additional variable that potentially can be used to add new functionality to electronic, optoelectronic and magnetoelectronic devices or

to even build radically new devices entirely based on the coherence of electron spin states. This has led to the newly emerging field of spintronics. [152, 153] Of particular interest is a subclass of spintronics device concepts, which relies on the capability to inject, control, and detect electron spin polarizations in non-magnetic semiconductors. [154, 155] The spin polarization, which would enable the device operation, is here a non-equilibrium state resulting from the response to an external probe, such as absorption of circularly polarized light or electrical injection from a spin polarized contact. After the external probe is removed, the spin polarization relaxes to an unpolarized equilibrium state. The characterization of the spin polarization, e.g., in terms of lifetimes and transport coefficients, requires therefore a kinetic theory.

The main spin relaxation processes for itinerant electrons in non-magnetic semiconductors are the Elliott-Yafet (EY) process [156, 157], that leads to spin-flip scattering, the Bir-Aronov-Pikus (BAP) process [158] due to electron-hole exchange scattering, and, in materials without inversion symmetry, the D'yakonov-Perel' (DP) process [159] in which spin states precess because of spin off-diagonal Hamiltonian matrix elements resulting from a combination of spin-orbit coupling and inversion asymmetry. An external magnetic field, in many cases required to control and manipulate the electron spin, can also influence the electron spin dynamics. It quenches the DP process [160], thereby tending to extend the spin lifetimes as a function of magnetic field, and it opens a spin relaxation channel due to the \vec{k} -dependence of the electron g -factor, which forces the spin of electrons in different quantum states to precess around an external magnetic field with different rates. [11, 161] For brevity we will refer to this mechanism as a variable g -factor (VG) process.

At the microscopic level, the EY, DP, BAP, and VG spin relaxation processes are different manifestations of the spin-orbit coupling. The coupling between electron spin and orbital motion produces however not only spin decoherence but it also provides opportunities to manipulate spin polarization. For instance, spin-orbit coupling leads to optical selection rules that allow the generation and detection of a non-equilibrium spin polarization. Optical transitions across the energy gap of a semiconductor are governed by electric dipole selection rules. Absorption of circularly polarized light with a wavelength corresponding to the fundamental semiconductor gap produces in direct gap semiconductors a spin-polarized electron distribution in the conduction band. The same optical selection rules allow the dynamics of a non-equilibrium electron spin polarization to be optically probed. In fact, spin dynamics in semiconductors has been extensively studied in magneto-optics in the 1970s and 80s [162–165] using various spin-sensitive emission, transmission, and reflection spectroscopies. These spectroscopies are now readily adaptable to spatially and time resolved measurements. [166–185]

As an illustration, we show in Fig. 3.1 experimental data from Kikkawa and coworkers. [169] They employed time-resolved Faraday rotation spectroscopy to determine the spin lifetime in bulk GaAs. In a Faraday rotation experiment, one measures the pump-induced changes in the polarization of a linearly polarized, time delayed probe pulse. The pump pulse is circularly polarized and produces a non-equilibrium spin polarization. Because of the spin-dependent optical selection rules, a non-equilibrium spin polarization (imbalance of spin-up and spin-down electrons) leads to a different index of refraction for left- and right-hand polarized light propagating in the direction of the quantization axis (propagation direction of the pump pulse). The material is birefringent and thus rotates the polarization axis of linearly polarized light. The rotation angle is a direct measure of the spin polarization. Thus, its time evolution reflects the time evolution of the spin polarization. Usually a small magnetic field is applied perpendicular to the quantization axis, in which case the spin polarization precesses, giving rise to an oscillatory time dependence of the rotation angle. The envelope of the oscillations is then a direct measure of the spin lifetime.

In materials with small spin-orbit coupling, spin lifetimes are limited by the weak hyperfine

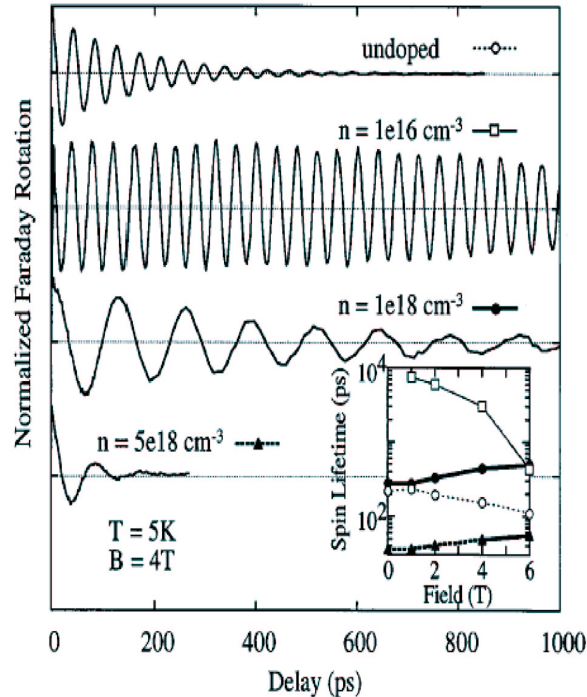


Figure 3.1: Time resolved Faraday rotation data from Kikkawa and coworkers. [169] Shown are data for undoped and n-type GaAs at $B=4\text{T}$ and $T=5\text{K}$. The authors normalized the data just after zero pump-probe delay and offset the plots for clarity, with zeros marked by dotted lines. The inset shows the transverse spin relaxation time vs. field. Electron densities are $n = 0, 10^{16}, 10^{18},$ and $5 \times 10^{18}\text{cm}^{-3}$, respectively.

interaction and therefore particularly long. On the other hand, external probes usually couple to the orbital part of the electron wavefunction. Materials with weak (or without) spin-orbit coupling provide therefore no practical means to address the spin degree of freedom and are therefore not suited for spintronics applications. A common theme of recent theoretical investigations of the spin dynamics in bulk [11, 186–189] and dimension-reduced semiconductor structures [190–203] is therefore the manipulation of the decay channels, by either external fields or heterostructure design, and the identification of conditions under which the electron spin is particularly robust.

Theoretical investigations are based on the early work [156–159] augmented by modern band structure theory for bulk and dimension-reduced semiconductors. In the simplest approach, the EY and BAP spin relaxation rates can be calculated with the Golden Rule for, respectively, direct spin flip scattering on impurities, phonons, and carriers and exchange spin-flip scattering on carriers. The calculation of the spin-flip rates due to motional-narrowing (DP and VG) processes, on the other hand, have to be based on a kinetic equation for the non-equilibrium spin polarization. Usually, a semiclassical Boltzmann-type equation, which treats only the spin quantum mechanically, is sufficient. Not always is the Boltzmann equation explicitly solved, however. Instead, a common procedure is to adapt the expression for the spin relaxation rate originally derived by D'yakonov and Perel' [159] to the scattering processes under consideration.

In this chapter we develop a systematic kinetic theory of spin relaxation, based on non-equilibrium Green function techniques, and apply it to specific physical situations in bulk and quantum wells. Because electron spin lifetimes are usually much larger than hole spin lifetimes

in semiconductors, we focus on spin relaxation of electrons. We furthermore assume that on the time scale of the experiments the optically generated valence band holes already recombined with conduction band electrons. The BAP process is then negligible. We focus therefore on the EY, DP, and VG processes.

In contrast to previous studies, we treat spin-flip (EY) and motional-narrowing (DP and VG) spin relaxation processes on an equal footing. As a result, we are able to study in detail the interplay of the various relaxation channels, in particular the competition of the DP process and the appearance of the VG process. Because of the different angle dependences, a Matthiessen-type rule holds for isotropic semiconductors. The total spin relaxation tensor is then simply the sum of the individual spin relaxation tensors. [11] Focusing on small spin polarizations and small momentum transfer scattering, we derive from the full quantum kinetic equations for the electron Green functions, a semiclassical Fokker-Planck equation for non-equilibrium spin polarization. On- and off-shell scattering processes are treated within a diffusion approximation. As a result, the time evolution of the non-equilibrium spin polarization can be visualized in terms of a “test” spin polarization scattering off “field” particles (electrons, impurities, phonons). The Fokker-Planck equation describes the time evolution on the short time scale, where spin conserving scattering occurs, and on the long time scale, where the spin decays. To separate the fast from the slow time evolution, we perform a rigorous multiple time scale analysis of the Fokker-Planck equation. Combined with an averaging procedure, the multiple time scale approach enables us to construct, on the time scale of spin relaxation, a Bloch equation for the macroscopic (\vec{k} -averaged) non-equilibrium spin polarization, which is also the quantity measured in, e.g., time-resolved Faraday and Kerr rotation experiments. [167–170, 180, 181, 183] The Bloch equation contains a spin relaxation tensor, the diagonal elements of which are the spin relaxation rates. They are either given in terms of a weighted energy average of a spin-flip rate (EY process) or a weighted energy average of a generalized relaxation time (DP and VG processes). The weight function turns out to be directly related to the quasi-stationary spin polarization, which is the terminating state of the initial, fast spin-conserving time evolution of the injected spin polarization. Thus, through a sequence of (controlled) steps, which leads us through an hierarchy of kinetic equations – quantum kinetic equation, Fokker-Planck equation, Bloch equation –, we are able to give a rather detailed picture of the time evolution of an optically injected non-equilibrium spin polarization.

3.2 Spin Dependence of Semiconductor Electronic Structure

We consider conduction band (CB) electrons in III-V semiconductors, e.g., GaAs, in the presence of an applied magnetic field. The model used here applies to both bulk and quantum well situations. A more detailed discussion of the spin dependence of the semiconductor band structure can be, e.g., found in Ref. [10]. Within an envelope function approach [204, 205], which treats the two states at the conduction band minimum explicitly and includes a large set of states perturbatively, the effective mass Hamiltonian for the CB electrons can be cast into the form

$$H_{\alpha\alpha'}(\vec{K}) = \epsilon(\vec{K})\delta_{\alpha\alpha'} + \frac{\hbar}{2}\vec{\Omega}_L \cdot \vec{\sigma}_{\alpha\alpha'} + \frac{\hbar}{2}[\vec{\Omega}_{IA}(\vec{K}) + \vec{\Omega}_g(\vec{K})] \cdot \vec{\sigma}_{\alpha\alpha'}, \quad (3.1)$$

where $\vec{K} = \vec{k} - (e/\hbar c)\vec{A}(\vec{r})$ and $\vec{A}(\vec{r})$ is the vector potential. The “spin basis” for the CB electrons used to define the model (3.1) is $\alpha = +$ and $\alpha = -$, where $\alpha = +$ ($\alpha = -$) denotes a state which is mostly spin-up (spin-down) with a small admixture of spin-down (spin-up). The small admixtures of the “wrong” spin component is a consequence of spin-orbit coupling and inversion asymmetry, which leads to an admixture of bonding p-states into the s-type conduction band wave functions. [10]

The first term denotes the dispersion of the Kramers degenerate conduction band which, depending on the sophistication of the envelope function approach, could contain nonparabolicity effects. For quantum wells \vec{k} and $\epsilon(\vec{k})$ denote the in-plane momentum and the in-plane dispersion of the conduction subband under consideration. The second term comprises the Larmor precession due to the external magnetic field, with $\hbar\vec{\Omega}_L = \mu_B g^* \vec{B}$ the Larmor energy vector. Here μ_B and g^* denote the Bohr magneton and the electron g -factor. The third term describes spin off-diagonal Hamiltonian matrix elements arising from the coupling to higher lying states. The most important of which are the splitting of the conduction band due to inversion asymmetry (IA) and the term which leads to a \vec{k} -dependent electron g -factor. For bulk semiconductors, the two contributions are given by

$$\hbar\vec{\Omega}_{IA}(\vec{K}) = 2\delta_0\vec{\kappa}_{IA}(\vec{K}) , \quad (3.2)$$

$$\hbar\vec{\Omega}_g(\vec{K}) = 2a_4K^2\vec{B} + 2a_5\{\vec{K}, \vec{B} \cdot \vec{K}\} + 2a_6\vec{\tau}(\vec{K}, \vec{B}) , \quad (3.3)$$

respectively. The definition of the vectors $\vec{\kappa}_{IA}(\vec{K})$ and $\vec{\tau}(\vec{K}, \vec{B})$ and of the parameters δ_0 and a_i can be found in Refs. [204, 205] and $\{.., ..\}$ denotes an anticommutator. The expressions for conduction subbands in a quantum well are obtained by averaging the bulk expressions (3.2) and (3.3) over the subband envelope function.

In addition to bulk inversion asymmetry, dimension-reduced semiconductors can have additional sources of asymmetry due to interfaces which share no common atom [182] or due to layer design (structural inversion asymmetry [190]). Both mechanisms can be cast into spin off-diagonal Hamiltonian matrix elements and can be therefore treated in the same way as the spin off-diagonal terms due to bulk inversion asymmetry.

For a complete description, a collision term arising from electron-impurity, electron-phonon and electron-electron scattering,

$$H_c = H_{ei} + H_{ep} + H_{ee} ,$$

is added to the effective mass Hamiltonian. The electron-impurity term reads

$$H_{ei} = \sum_{\vec{k}\vec{k}'} \sum_{\alpha\alpha'} M_{\alpha,\alpha'}(\vec{k}, \vec{k}') c_{\vec{k}\alpha}^\dagger c_{\vec{k}'\alpha'} , \quad (3.4)$$

with a scattering matrix element given by

$$M_{\alpha,\alpha'}(\vec{k}, \vec{k}') = \sum_j U(\vec{k} - \vec{k}') e^{i(\vec{k}-\vec{k}')\vec{r}_j} I_{\alpha\alpha'}(\vec{k}, \vec{k}') . \quad (3.5)$$

The Bloch states for the conduction band are not pure spin states because of spin-orbit coupling and inversion asymmetry. The scattering matrix element contains therefore an overlap factor

$$I_{\alpha\alpha'}(\vec{k}, \vec{k}') = \langle U_{\alpha,\vec{k}} | U_{\alpha',\vec{k}'} \rangle , \quad (3.6)$$

which is of order unity for $\alpha = \alpha'$ (spin conserving scattering) and is small, but not zero otherwise (spin non-conserving scattering). The electron-phonon collision term would have the same structure as Eq. (3.4) but with phonon creation and annihilation operators appearing in the matrix element $M_{\alpha\alpha'}(\vec{k}, \vec{k}')$. The electron-electron scattering contribution has the form

$$H_{ee} = \frac{1}{2} \sum_{\vec{k}_i\alpha_i} M_{\alpha_1\alpha_2\alpha_3\alpha_4}(\vec{k}_1, \vec{k}_2, \vec{k}_3, \vec{k}_4) c_{\vec{k}_1\alpha_1}^\dagger c_{\vec{k}_2\alpha_2}^\dagger c_{\vec{k}_3\alpha_3} c_{\vec{k}_4\alpha_4} , \quad (3.7)$$

where the scattering matrix element,

$$M_{\alpha_1\alpha_2\alpha_3\alpha_4}(\vec{k}_1, \vec{k}_2, \vec{k}_3, \vec{k}_4) = V(\vec{k}_1 - \vec{k}_4) I_{\alpha_1\alpha_4}(\vec{k}_1, \vec{k}_4) I_{\alpha_2\alpha_3}(\vec{k}_2, \vec{k}_3) \delta_{\vec{k}_1 + \vec{k}_2, \vec{k}_3 + \vec{k}_4}, \quad (3.8)$$

contains two overlap factors. The functions $U(\vec{k})$ and $V(\vec{k})$ denote, respectively, the potential of a single impurity (neutral or ionized) and the Coulomb potential between two conduction band electrons.

The model Hamiltonian is characterized by $\epsilon(\vec{k})$, $\vec{\Omega}_{IA}(\vec{k})$, $\vec{\Omega}_g(\vec{k})$, and $I_{\alpha,\alpha'}(\vec{k}, \vec{k}')$. These quantities need to be obtained by an electronic structure calculation. The formal structure of the kinetic theory described in the next section is independent of the particular form of these quantities.

3.3 Semiclassical Kinetic Theory

In this section we give a systematic derivation of the Fokker-Planck equation governing the electron spin relaxation in the limit of small spin polarizations. The derivation is independent of dimensionality, applying to bulk semiconductors and semiconductor heterostructures, and treats motional-narrowing (DP and VG) and spin-flip (EY) spin relaxation processes on an equal footing. To obtain a Fokker-Planck equation, we restrict ourselves to the Born approximation, but collective effects giving rise to dynamical screening of the Coulomb interaction can be approximately incorporated at the level of a quantum analog to the Lenard-Balescu equation. [206] Besides its intuitive interpretation in terms of a small “test” spin polarization scattering off a bath of “field” particles (impurities, electrons and phonons), causing dynamical friction, diffusion, and eventually relaxation for the “test” spin polarization, the Fokker-Planck equation is the starting point for a multiple time scale analysis which results in the derivation of a Bloch equation for the macroscopic (\vec{k} -averaged) spin polarization. Its decay is characterized by the diagonal elements of a spin relaxation tensor, which are quadratures of either a spin-flip rate (EY process) or a generalized relaxation time multiplied by a precession rate (DP and VG processes).¹

Since the derivation is quite lengthy and to some extent rather formal we first give a short outline of the main steps. We start from the full quantum kinetic equations for the Keldysh Green functions. [207–210] Each component of the Keldysh Green function is a 2×2 matrix in electron spin space. In the first step we derive, within the semiclassical approximation, a kinetic equation for the density matrix. This accounts to treating momentum scattering processes as instantaneous on the time scale of spin relaxation, which is usually the case. Calculating the self-energies which appear in the semiclassical kinetic equation in the Born approximation, linearizing with respect to spin polarization, and expanding the self-energies up to second order in the momentum transfer (diffusion approximation) finally yields a Fokker-Planck equation for the spin polarization, which we then analyze in terms of multiple time scale perturbation theory.

3.3.1 Kinetic Equations

For a spatially homogeneous system (we assume a constant magnetic field \vec{B}), the information about spin relaxation is contained in the electronic density matrix, which, due to the spin degree of freedom, is a 2×2 matrix in spin space,

$$N_{\alpha_1\alpha_2}(\vec{k}, t) = \langle (c_{\vec{k}\alpha_1}^\dagger c_{\vec{k}\alpha_2})(t) \rangle, \quad (3.9)$$

¹Depending on the geometry, the spin relaxation rates are usually linear combinations of the diagonal elements of the spin relaxation tensor.

but diagonal in \vec{k} -space. Here, the operators evolve in time with the full Hamiltonian, including the time-dependent perturbation, which could be, e.g., a circularly polarized light pulse applied at time $t = t_0$. To perform the averaging in Eq. (3.9) denoted by $\langle [\dots] \rangle$, we consider the system to be in thermodynamical equilibrium for $t < t_0$, take the limit $t_0 \rightarrow -\infty$ and evaluate the expectation value in Eq. (3.9) with respect to the equilibrium density matrix. [210]

To derive a kinetic equation for the density matrix it is convenient to start from Keldysh Green functions. [207, 208] For a constant magnetic field, the vector potential is a function of \vec{r} . It is therefore necessary to initially work with kinetic equations in real space. In this subsection we set $\hbar = 1$. Introducing a numerical index 1 that stands for $\vec{r}_1\alpha_1t_1$ and 2 for $\vec{r}_2\alpha_2t_2$, we write in the notation of Ref. [209]

$$i\hat{G}_{12} = i \begin{pmatrix} G_{12}^{++} & G_{12}^{+-} \\ G_{12}^{-+} & G_{12}^{--} \end{pmatrix}. \quad (3.10)$$

Note that each component of the Keldysh Green function is a 2×2 matrix in spin space. Introducing further a self-energy

$$\hat{\Sigma}_{12} = \begin{pmatrix} \Sigma_{12}^{++} & \Sigma_{12}^{+-} \\ \Sigma_{12}^{-+} & \Sigma_{12}^{--} \end{pmatrix}, \quad (3.11)$$

we set up two matrix Dyson equations, one where the time differentiation is with respect to t_1 and one where it is with respect to t_2 :

$$\partial_{t_1}\hat{G}_{12} = -i\hat{\tau}_z\delta_{12} - i(\hat{\epsilon}\hat{G})_{12} - i\hat{\tau}_z(\hat{\Sigma}\hat{G})_{12}, \quad (3.12)$$

$$\partial_{t_2}\hat{G}_{12} = i\hat{\tau}_z\delta_{12} + i(\hat{G}\hat{\epsilon})_{12} + i(\hat{G}\hat{\Sigma})_{12}\hat{\tau}_z, \quad (3.13)$$

with $\delta_{12} = \delta(t_1 - t_2)\delta(12)$ and the energy matrix $\hat{\epsilon}_{12} = \delta(t_1 - t_2)\hat{\epsilon}(12) = \delta(t_1 - t_2)\hat{\tau}_0\delta(12)\epsilon(-i\nabla_{\vec{r}_1} - (e/c)\vec{A}(\vec{r}_1))$, where we neglect nonparabolicities in the dispersion. We adopt the convention that numerical indices written as a subscript contain the time variable, whereas numerical indices written as an argument do not. Matrix multiplication with respect to the Keldysh indices is implied and internal variables are summed (integrated) over; $\hat{\tau}_z$ is a Pauli matrix and $\hat{\tau}_0$ is the unit matrix in Keldysh space.

Subtracting Eq. (3.13) from Eq. (3.12) gives

$$[\hat{L}, \hat{G}]_{12} = \hat{\tau}_z(\hat{\Sigma}\hat{G})_{12} - (\hat{G}\hat{\Sigma})_{12}\hat{\tau}_z, \quad (3.14)$$

where $[\dots, \dots]$ denotes the commutator. To compactify the notation, we introduced a differential operator

$$\hat{L}_{13} = \hat{\tau}_0\delta_{13}L(3) = \hat{\tau}_0\delta_{13}(i\partial_{t_3} - \epsilon(3)). \quad (3.15)$$

It is understood that in the second term of the commutator, the operator \hat{L}_{32} acts to the left with the temporal differential operator ∂_{t_3} replaced by its adjoint $-\partial_{t_3}$.

Equation (3.14) contains two time variables. To obtain a kinetic equation for the electronic density matrix, which depends only on a single time variable, it is necessary to perform the equal time limit. This is most conveniently done in the (mixed) Wigner representation, where the equal time limit reduces to an integration. Separating the self-energy into a singular and a regular part [209]

$$\Sigma_{12}^{pq} = \Delta^{pq}(12; t_1)\delta_{pq}\delta(t_1 - t_2) + \tilde{\Sigma}_{12}^{pq}, \quad (3.16)$$

introducing relative and center variables, $\vec{r} = \vec{r}_1 - \vec{r}_2$, $\vec{R} = (\vec{r}_1 + \vec{r}_2)/2$, $\tau = t_1 - t_2$, and $T = (t_1 + t_2)/2$, and defining a Fourier transformation with respect to the relative variables,

$$A(\vec{R}, T, \vec{k}, \omega) = \int_{-\infty}^{\infty} d\tau \int d\vec{r} e^{i\omega\tau - i\vec{k}\vec{r}} A(\vec{R}, T, \vec{r}, \tau), \quad (3.17)$$

together with a gradient operator [210]

$$\mathcal{G}^{AB} = \exp \frac{1}{2i} \left[\partial_T^A \partial_\omega^B - \partial_\omega^A \partial_T^B + \nabla_{\vec{k}}^A \cdot \nabla_{\vec{R}}^B - \nabla_{\vec{R}}^A \cdot \nabla_{\vec{k}}^B \right], \quad (3.18)$$

the equal time limit of the ++ component of Eq. (3.14) can be written as

$$D(\vec{R}, T, \vec{k}) = F(\vec{R}, T, \vec{k}) + C(\vec{R}, T, \vec{k}), \quad (3.19)$$

with a driving term on the lhs,

$$\begin{aligned} D(\vec{R}, T, \vec{k}) &= \int_{-\infty}^{\infty} \frac{d\omega}{2\pi} \left[\mathcal{G}^{LG} L(\vec{R}, T, \vec{k}, \omega) G^{++}(\vec{R}, T, \vec{k}, \omega) \right. \\ &\quad \left. - \mathcal{G}^{GL} G^{++}(\vec{R}, T, \vec{k}, \omega) L(\vec{R}, T, \vec{k}, \omega) \right], \end{aligned} \quad (3.20)$$

and a rhs, which contains a molecular field term arising from the singular part of the self-energy,

$$\begin{aligned} F(\vec{R}, T, \vec{k}) &= \int_{-\infty}^{\infty} \frac{d\omega}{2\pi} \left[\mathcal{G}^{\Delta G} \Delta^{++}(\vec{R}, T, \vec{k}) G^{++}(\vec{R}, T, \vec{k}, \omega) \right. \\ &\quad \left. - \mathcal{G}^{G\Delta} G^{++}(\vec{R}, T, \vec{k}, \omega) \Delta^{++}(\vec{R}, T, \vec{k}) \right], \end{aligned} \quad (3.21)$$

and a collision term due to the regular part

$$\begin{aligned} C(\vec{R}, T, \vec{k}) &= \int_{-\infty}^{\infty} \frac{d\omega}{2\pi} \left[\mathcal{G}^{\tilde{\Sigma}G} \tilde{\Sigma}^{++}(\vec{R}, T, \vec{k}, \omega) G^{++}(\vec{R}, T, \vec{k}, \omega) \right. \\ &\quad - \mathcal{G}^{G\tilde{\Sigma}} G^{++}(\vec{R}, T, \vec{k}, \omega) \tilde{\Sigma}^{++}(\vec{R}, T, \vec{k}, \omega) \\ &\quad + \mathcal{G}^{\tilde{\Sigma}G} \tilde{\Sigma}^{+-}(\vec{R}, T, \vec{k}, \omega) G^{-+}(\vec{R}, T, \vec{k}, \omega) \\ &\quad \left. - \mathcal{G}^{G\tilde{\Sigma}} G^{-+}(\vec{R}, T, \vec{k}, \omega) \tilde{\Sigma}^{-+}(\vec{R}, T, \vec{k}, \omega) \right]. \end{aligned} \quad (3.22)$$

The semiclassical approximation amounts to the assumption that the Green functions and self-energies vary slowly on the macroscopic scales, T and \vec{R} , respectively. It is therefore sufficient to keep in Eq. (3.19) only the leading order terms in a gradient expansion. The leading order of the rhs of Eq. (3.19) is the zeroth order, i.e., Eqs. (3.21) and (3.22) with $\mathcal{G}^{AB} \rightarrow 1$. The lhs of Eq. (3.19), however, has to be determined to first order, because the zeroth order vanishes. Using

$$L(\vec{R}, T, \omega, \vec{k}) = \omega + \epsilon(\vec{K}), \quad (3.23)$$

we explicitly obtain

$$\begin{aligned} D(\vec{R}, T, \vec{k}) &= i \int_{-\infty}^{\infty} \frac{d\omega}{2\pi} \left[\partial_T G^{++}(\vec{R}, T, \vec{k}, \omega) - \nabla_{\vec{R}} \epsilon(\vec{K}) \cdot \nabla_{\vec{k}} G^{++}(\vec{R}, T, \vec{k}, \omega) \right. \\ &\quad \left. + \nabla_{\vec{k}} \epsilon(\vec{K}) \cdot \nabla_{\vec{R}} G^{++}(\vec{R}, T, \vec{k}, \omega) \right]. \end{aligned} \quad (3.24)$$

To ensure gauge invariance of the kinetic equation we follow Ref. [211] and consider the generalized momentum $\vec{K} = \vec{k} - (e/c)\vec{A}(\vec{R})$ as an independent variable instead of the momentum \vec{k} . Using the two identities [211],

$$\begin{aligned}\nabla_{\vec{R}} a(\vec{K}) &= \nabla_{\vec{K}} a(\vec{K}) \cdot \nabla_{\vec{R}} \vec{K} + \nabla_{\vec{K}} a(\vec{K}) \times (\nabla_{\vec{R}} \times \vec{K}), \\ \vec{a} \cdot \vec{b} \times (\nabla_{\vec{R}} \times \vec{c}) &= (\vec{a} \cdot \nabla_{\vec{R}} \vec{c}) \cdot \vec{b} - (\vec{b} \cdot \nabla_{\vec{R}} \vec{c}) \cdot \vec{a},\end{aligned}$$

Eq. (3.24) becomes

$$\begin{aligned}D(\vec{R}, T, \vec{K}) &= \left(\partial_T + \frac{e}{c} \nabla_{\vec{K}} \epsilon(\vec{K}) \cdot (\vec{B} \times \nabla_{\vec{K}}) + \nabla_{\vec{K}} \epsilon(\vec{K}) \cdot \nabla_{\vec{R}} \right) \\ &\times i \int_{-\infty}^{\infty} \frac{d\omega}{2\pi} G^{++}(\vec{R}, T, \vec{K}, \omega).\end{aligned}\quad (3.25)$$

We assume weak interactions and replace the full Green functions by the noninteracting Green functions (quasi-particle ansatz),

$$G^{pq}(\vec{R}, T, \vec{K}, \omega) = G_0^{pq}(\vec{k} \rightarrow \vec{K}, \omega)|_{N_0(\vec{k}) \rightarrow N(\vec{R}, T, \vec{K})}, \quad (3.26)$$

where the noninteracting density matrix $N_0(\vec{k})$ is replaced by the full density matrix $N(\vec{R}, T, \vec{K})$. Performing the ω -integrations in Eqs. (3.21), (3.22), and (3.25) then yields the semiclassical kinetic equation for the electronic density matrix:

$$\begin{aligned}&\left(\partial_T + \frac{e}{c} \nabla_{\vec{K}} \epsilon(\vec{K}) \cdot \vec{B} \times \nabla_{\vec{K}} + \nabla_{\vec{K}} \epsilon(\vec{K}) \cdot \nabla_{\vec{R}} \right) N(\vec{R}, T, \vec{K}) = \\ &i \left[N(\vec{R}, T, \vec{K}), \Delta^{++}(\vec{R}, T, \vec{K}) + \tilde{\Sigma}^{++}(\vec{R}, T, \vec{K}, \epsilon(\vec{K})) \right] \\ &+ i N(\vec{R}, T, \vec{K}) \tilde{\Sigma}^{-+}(\vec{R}, T, \vec{K}, \epsilon(\vec{K})) + i \tilde{\Sigma}^{+-}(\vec{R}, T, \vec{K}, \epsilon(\vec{K})) [1 - N(\vec{R}, T, \vec{K})].\end{aligned}\quad (3.27)$$

To obtain a closed kinetic equation for the electronic density matrix, internal Green functions, which appear in the self-energies, have to be of course also eliminated according to Eq. (3.26). Details concerning the calculation of self-energies are given in the next section.

For a homogeneous magnetic field, the electronic density matrix does not explicitly depend on \vec{R} . The \vec{R} dependence can be therefore neglected. For a quadratic dispersion, $\epsilon(\vec{K}) = \vec{K}^2/2m^*$ ($\hbar = 1$ in this subsection), the Lorentz term moreover becomes

$$(e/c) \nabla_{\vec{K}} \epsilon(\vec{K}) \times \vec{B} \cdot \nabla_{\vec{K}} = (\vec{K} \times \vec{\Omega}_C) \cdot \nabla_{\vec{K}} = -i \vec{\Omega}_C \cdot \vec{\mathcal{L}}, \quad (3.28)$$

where $\vec{\Omega}_C = e\vec{B}/m^*c$ is the cyclotron energy vector and $\vec{\mathcal{L}}$ the angular momentum operator in \vec{K} -space, and we obtain the kinetic equation for the electronic density matrix in a more familiar form:

$$\begin{aligned}(\partial_T - i \vec{\Omega}_C \cdot \vec{\mathcal{L}}) N(T, \vec{K}) &= i \left[N(T, \vec{K}), \Delta^{++}(T, \vec{K}) + \tilde{\Sigma}^{++}(T, \vec{K}, \epsilon(\vec{K})) \right] \\ &+ i N(T, \vec{K}) \tilde{\Sigma}^{-+}(T, \vec{K}, \epsilon(\vec{K})) \\ &+ i \tilde{\Sigma}^{+-}(T, \vec{K}, \epsilon(\vec{K})) [1 - N(T, \vec{K})].\end{aligned}\quad (3.29)$$

This equation is the basis for the calculation of the spin relaxation time in spatially homogeneous systems subject to a constant magnetic field. The first term on the rhs describes the

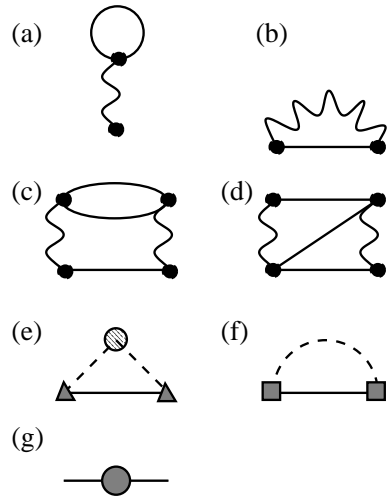


Figure 3.2: Diagrammatic representation of self-energies in the Born approximation for electron-electron (a)–(d), electron-impurity (e), and electron-phonon scattering (f). Diagram (g) denotes the self-energy due to spin off-diagonal Hamiltonian matrix elements.

coherent motion in a molecular field modified by correlation effects. If Δ^{++} , $\tilde{\Sigma}^{++}$, and N were scalar functions, as in ordinary transport theory, this term would vanish. The molecular field term is therefore a consequence of the quantum mechanical treatment of the spin degree of freedom. To the singular part of the self-energy contribute the spin off-diagonal terms in the Hamiltonian and the Hartree-Fock fields due to electron-electron scattering. Dissipation and relaxation originate from the regular part of the self-energy and give rise to the second and third term on the rhs. They are at least second order in the interaction. Formally, they correspond to the scattering-out and the scattering-in terms in a matrix-Boltzmann equation. The matrix structure is of course a consequence of the full quantum mechanical description of the spin. Only momentum scattering is treated classically.

3.3.2 Calculation of the Self-Energies

The semiclassical approach to furnish the self-energies in the matrix-Boltzmann equation (3.29), valid for magnetic fields, which do not restructure the electron dispersion, is to represent interaction processes in terms of diagrams, calculate the diagrams using standard rules [208] to obtain $\tilde{\Sigma}^{pq}(\vec{k}, t, t')$ and $\Delta^{pq}(\vec{k}, t)$, perform the zeroth order gradient expansion, and then replace all internal Green functions according to Eq. (3.26). This heuristic strategy leads to self-energies, which can be expressed in a manifestly gauge invariant form by writing the internal momentum integrations in terms of the generalized momentum \vec{K} . The formal structure of the self-energies is then the same as without magnetic field. Thus, within the semiclassical approach, the magnetic field gives only rise to the Lorentz term and the terms coming directly from the spin off-diagonal part of the Hamiltonian.

In Fig. 3.2 we depict the self-energies in the Born approximation for electron-electron (a–d), electron-impurity (e), and electron-phonon (f) scattering. Diagram (g) corresponds to the self-energy due to the spin off-diagonal term in the Hamiltonian (3.1).

The Hartree-Fock diagrams (a) and (b) contribute to the instantaneous self-energy Δ^{++} . They are second order in the spin polarization and therefore, for sufficiently small spin polarizations, negligible. There are two second order diagrams due to electron-electron scattering, the direct (c) and the exchange (d) Born diagram. Anticipating that soft scattering dominates, we neglect the

exchange diagram (d). The direct Born diagram contributes to $\tilde{\Sigma}^{++}$, $\tilde{\Sigma}^{+-}$, and $\tilde{\Sigma}^{-+}$. It can be shown, however, that $\tilde{\Sigma}^{++}$ is at least second order in the spin polarization and therefore negligible in the limit of small spin polarizations. The $\tilde{\Sigma}^{-+}$ and $\tilde{\Sigma}^{+-}$ components, contributing to the collision integral, are in contrast linear in the spin polarization and cannot be neglected. Diagrams (e) and (f), corresponding to the Born approximation for electron-impurity and electron-phonon scattering, only contribute to $\tilde{\Sigma}^{pq}$. As in the case of electron-electron scattering, the $++$ component can be again neglected, if the spin polarization is small enough, whereas the $+-$ and $-+$ components contribute in linear order in the spin polarization to the collision integral. Diagram (g), corresponding to the spin off-diagonal part of the Hamiltonian (3.1), is linear in the spin polarization and contributes to Δ^{++} . Eventually it leads to a torque force acting on the spin polarization.

Anticipating small spin polarizations, we neglect $\tilde{\Sigma}^{++}$ and the Hartree-Fock contribution to Δ^{++} . Writing in the Born approximation furthermore $I_B[N] = I_B^{ee}[N] + I_B^{ep}[N] + I_B^{ei}[N]$ for the second and third term on the rhs of Eq. (3.29), the semiclassical kinetic equation for the electronic density matrix reduces to

$$\left(\hbar\partial_t - i\hbar\vec{\Omega}_C \cdot \vec{\mathcal{L}}\right) N(\vec{k}, t) = \frac{i}{2} \left[N(\vec{k}, t), \left(\hbar\vec{\Omega}_L + \hbar\vec{\Omega}_{IA}(\vec{k}) + \hbar\vec{\Omega}_g(\vec{k}) \right) \cdot \vec{\sigma} \right] + I_B[N], \quad (3.30)$$

where we relabeled the center time $T \rightarrow t$ and adjusted to the notation of Eq. (3.9); \hbar is explicitly included and the generalized momentum is now denoted by \vec{k} .

Equation (3.30) is a matrix-Boltzmann equation similar to the semiconductor Bloch equations frequently used to describe optically pumped semiconductors. [210] Thus, numerical techniques used for the solution of the semiconductor Bloch equations can be adopted to the numerical solution of Eq. (3.30). Calculations of this kind have been successfully performed for various situations. [186, 187, 195, 201–203]

To avoid a numerical solution, we focus on small spin polarizations and linearize the Born collision integral with respect to the spin polarization. It is important to note that the equilibrium density matrix $N_{eq}(\vec{k}) = N(\vec{k}, t \rightarrow \infty)$ is not diagonal in the “spin basis”. Expanding the equilibrium density matrix in terms of Pauli matrices yields

$$N_{eq}(\vec{k}) = f(\vec{k}) + \frac{1}{2} \vec{\sigma} \cdot \vec{S}_{eq}(\vec{k}), \quad (3.31)$$

where $f(\vec{k}) = (1/2)\text{Tr}N_{eq}(\vec{k}) = (f_+(\vec{k}) + f_-(\vec{k}))/2$ is half of the sum of the equilibrium distribution functions of the spin up and spin down electrons and $\vec{S}_{eq}(\vec{k})$ is the equilibrium spin polarization (which vanishes if integrated over all momenta). Accordingly, we also write for the density matrix at arbitrary times

$$N(\vec{k}, t) = f(\vec{k}) + \delta f(\vec{k}, t) + \frac{1}{2} \vec{\sigma} \cdot [\vec{S}_{eq}(\vec{k}) + \delta \vec{S}(\vec{k}, t)], \quad (3.32)$$

with $\delta f(\vec{k}, t)$ and $\delta \vec{S}(\vec{k}, t)$ the changes induced by optical pumping or by electrical injection. We defined $N_{eq}(\vec{k})$ for $t \rightarrow \infty$, that is, it contains the electrons created by the perturbation and both $\delta \vec{S}(\vec{k}, t)$ and $\delta f(\vec{k}, t)$ have to vanish for $t \rightarrow \infty$.

Inserting the expansion (3.32) into the Boltzmann equation (3.30) yields two kinetic equations, one for the charge component $\delta f(\vec{k}, t)$ and one for the spin component $\delta \vec{S}(\vec{k}, t)$. The collision terms couple the two equations. If however only a small portion of the total number of electrons initially contributed to the spin polarization, i.e. if $\delta f(\vec{k}, t) \ll f(\vec{k})$, the coupling can be ignored and it suffices to focus on the equation for $\delta \vec{S}(\vec{k}, t)$ alone.

Since the total spin polarization $\vec{S}_{eq}(\vec{k}) + \delta\vec{S}(\vec{k}, t)$ is small, we linearize the Born collision integral with respect to both $\vec{S}_{eq}(\vec{k})$ and $\delta\vec{S}(\vec{k}, t)$. Thus,

$$I_B[N] = I_B[N_{eq}] + I_B[f + \delta f, \delta\vec{S}] . \quad (3.33)$$

If we now apply $\text{Tr}\vec{\sigma}[\dots]$ on both sides of Eq. (3.30), use $I_B[N_{eq}] = 0$ as well as $\vec{\Omega}_{IA}(\vec{k}) \times \vec{S}_{eq}(\vec{k}) = 0$, because, by construction, the equilibrium density matrix $N_{eq}(\vec{k})$ commutes with H_{IA} , and ignore furthermore δf in $I_B[f + \delta f, \delta\vec{S}]$, we get a closed kinetic equation for the non-equilibrium spin polarization

$$\left(\hbar\partial_t - i\hbar\vec{\Omega}_C \cdot \vec{\mathcal{L}} \right) \delta\vec{S}(\vec{k}, t) = \left(\hbar\vec{\Omega}_L + \hbar\vec{\Omega}_{IA}(\vec{k}) + \hbar\vec{\Omega}_g(\vec{k}) \right) \times \delta\vec{S}(\vec{k}, t) + J_B[f, \delta\vec{S}] \quad (3.34)$$

with $J_B[f, \delta\vec{S}] = \text{Tr}\vec{\sigma}I_B[f, \delta\vec{S}]$.

The collision integral can be further simplified if we split the spin-flip matrix into a leading spin conserving diagonal part and a small off-diagonal part which describes spin-flip scattering. Since nonparabolicities are small, the diagonal part is approximately equal to the unit matrix and we get $I(\vec{k}, \vec{k}') \simeq 1 + \delta I(\vec{k}, \vec{k}')$, with $\delta I(\vec{k}, \vec{k}') \ll 1$. Expanding the collision integrals up to second order in $\delta I(\vec{k}, \vec{k}')$ gives

$$J_B[f, \delta\vec{S}] = J_B[f, \delta\vec{S}]^{(0)} + J_B[f, \delta\vec{S}]^{(1)} + J_B[f, \delta\vec{S}]^{(2)} . \quad (3.35)$$

The first order term $J_B^{(1)}[f, \delta\vec{S}]$ potentially mixes EY, DP, and VG spin relaxation channels, but for semiconductors with high symmetry it does not contribute to the spin relaxation rates.

The kinetic equation for the excess spin polarization becomes therefore

$$\begin{aligned} \left(\hbar\partial_t - i\hbar\vec{\Omega}_C \cdot \vec{\mathcal{L}} \right) \delta\vec{S}(\vec{k}, t) &= \hbar\vec{\Omega}_L \times \delta\vec{S}(\vec{k}, t) + \left(\hbar\vec{\Omega}_{IA}(\vec{k}) + \hbar\vec{\Omega}_g(\vec{k}) \right) \times \delta\vec{S}(\vec{k}, t) \\ &+ J_B^{(0)}[f, \delta\vec{S}] + J_B^{(2)}[f, \delta\vec{S}] . \end{aligned} \quad (3.36)$$

This equation contains motional-narrowing (DP and VG) and spin-flip (EY) spin relaxation processes on an equal footing. The Elliott-Yafet process is simply encoded in $J_B^{(2)}[f, \delta\vec{S}]$ whereas the motional-narrowing processes result from the combined action of the torque forces given by the second term on the rhs and the spin conserving scattering processes comprising $J_B^{(0)}[f, \delta\vec{S}]$.

Independent of the scattering process, the structure of the collision integrals in Eq. (3.36) is ($\nu = \text{ei}, \text{ee}, \text{and ep}$)

$$J_\nu^{(0)}[f, \delta\vec{S}] = \sum_{\vec{q}} [W^\nu(\vec{k} + \vec{q}; \vec{q}) \delta\vec{S}(\vec{k} + \vec{q}, t) - W^\nu(\vec{k}; \vec{q}) \delta\vec{S}(\vec{k}, t)] , \quad (3.37)$$

$$J_\nu^{(2)}[f, \delta\vec{S}] = \sum_{\vec{q}} W^\nu(\vec{k} + \vec{q}; \vec{q}) \vec{g}(\vec{k}, \vec{k} + \vec{q}) \times \left[\vec{g}(\vec{k}, \vec{k} + \vec{q}) \times \delta\vec{S}(\vec{k} + \vec{q}, t) \right] , \quad (3.38)$$

where, for concise notation, we introduced a spin-flip vector

$$\vec{g}(\vec{k}, \vec{k}') = \begin{pmatrix} \text{Im}I_{+-}(\vec{k}, \vec{k}') \\ \text{Re}I_{+-}(\vec{k}, \vec{k}') \\ 0 \end{pmatrix} , \quad (3.39)$$

with $I_{+-}(\vec{k}, \vec{k}')$ the off-diagonal element of the overlap matrix (3.6). This is a result of the Born approximation and the linearization with respect to the spin polarization. In general, the structure of the collision integrals depends on the scattering process. Here, however, the scattering process

enters only through $W^\nu(\vec{k}; \vec{q})$, the probabilities for a transition between momentum state $\vec{k} - \vec{q}$ and \vec{k} . For electron-ionized-impurity scattering, for instance,

$$W^{ei}(\vec{k}; \vec{q}) = 2\pi N_i |U(q)|^2 \delta(\varepsilon(\vec{k} - \vec{q}) - \varepsilon(\vec{k})) , \quad (3.40)$$

while for electron-electron scattering,

$$\begin{aligned} W^{ee}(\vec{k}; \vec{q}) = 4\pi |V(q)|^2 \sum_{\vec{k}'} & \left\{ [1 - f(\vec{k} - \vec{q}) - f(\vec{k}' + \vec{q})] f(\vec{k}') \right. \\ & \left. + f(\vec{k} - \vec{q}) f(\vec{k}' + \vec{q}) \right\} \delta(\varepsilon(\vec{k}) + \varepsilon(\vec{k}') - \varepsilon(\vec{k} - \vec{q}) - \varepsilon(\vec{k}' + \vec{q})) , \end{aligned} \quad (3.41)$$

with $U(q)$ and $V(q)$ bare Coulomb potentials, which, however, we later screen phenomenologically. Similar expressions hold for electron-phonon scattering. For electron impurity scattering, which is elastic, $W^{ei}(\vec{k} + \vec{q}; \vec{q}) = W^{ei}(\vec{k}; \vec{q})$; moreover $W^{ei}(\vec{k}; \vec{q})$ is independent of the equilibrium distribution of the spin-up and the spin-down electrons. In general, however, the transition probabilities depend on the equilibrium distribution of the electrons, and, in the case of electron-phonon scattering, also on the equilibrium distribution of the phonons.

3.3.3 Diffusion Approximation

The simple form of the collision integrals (3.37) and (3.38) suggests to conceptualize the dynamics of the non-equilibrium spin polarization in terms of spin-polarized “test” electrons, scattering off an equilibrated bath of “field” particles (impurities, electrons, and phonons). Usually this picture can be only applied to electron-impurity and electron-phonon scattering, where the scattering partners belong to different species, and not to electron-electron scattering, where the scattering partners belong to the same species. It is only within the linearized spin dynamics, which essentially treats the electrons comprising the non-equilibrium spin polarization as a separate species, that the “test-field-particle concept” can be applied to electron-electron scattering as well. We now take full advantage of the simplicity of the collision integrals and expand the collision integrals with respect to the momentum transfer \vec{q} . As a result the integro-differential equation (3.36) becomes a differential equation.

The on-shell spin-conserving process due to elastic electron-impurity scattering yields

$$J_B^{(0),\text{on}}[f, \delta\vec{S}] = \sum_n \sum_{i_1, \dots, i_n} C_{i_1, \dots, i_n}^{\text{ei}}(\vec{k}) \frac{\partial^n}{\partial k_{i_1} \dots \partial k_{i_n}} \delta\vec{S}(\vec{k}, t) , \quad (3.42)$$

whereas the inelastic spin-conserving processes due to electron-electron or electron-phonon scattering give rise to an off-shell contribution

$$J_B^{(0),\text{off}}[f, \delta\vec{S}] = \sum_{\nu=\text{ee,ep}} \sum_n \sum_{i_1, \dots, i_n} \frac{\partial^n}{\partial k_{i_1} \dots \partial k_{i_n}} C_{i_1, \dots, i_n}^\nu(\vec{k}) \delta\vec{S}(\vec{k}, t) , \quad (3.43)$$

where, in both cases, the moments are defined by ($\nu = \text{ei}, \text{ee}, \text{ep}$)

$$C_{i_1, \dots, i_n}^\nu(\vec{k}) = \frac{1}{n!} \sum_{\vec{q}} q_{i_1} \dots q_{i_n} W^\nu(\vec{k}; \vec{q}) . \quad (3.44)$$

The transition probability $W^\nu(\vec{k}; \vec{q})$ depends on the precise modeling of the elementary scattering process and also on the dimensionality of the system. In the Appendix, we explicitly calculate, as

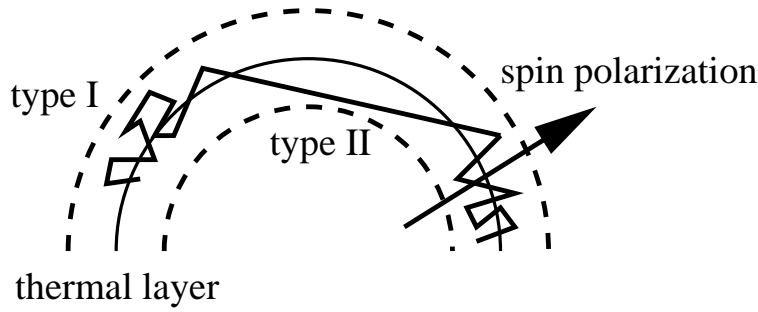


Figure 3.3: Symbolic representation of scattering processes within the thermal layer of a degenerate electron gas. The “test” spin polarization is represented by the large arrow. Type I scattering events involve small momentum transfer whereas type II scattering events involve large momentum transfer. The diffusion approximation treats type II processes approximately, which in many cases are less probable. For instance, the transition probability for Coulomb scattering diverges for small momentum transfer. Thus, type I processes occur more frequently than type II processes. Within our approximation on-shell scattering processes can be spin conserving and non-conserving whereas off-shell processes are spin-conserving.

an illustraton, the transition probabilities for electron-electron and electron-impurity scattering in a [001] quantum well. Similar calculations can be done for bulk. Note, for inelastic scattering the differential operators act on the moments $C_{i_1, \dots, i_n}^\nu(\vec{k})$ whereas for elastic scattering the moments are in front of the differential operators.

Equations (3.42) and (3.43) involve partial differential operators of arbitrary order. To obtain tractable equations, the expansion is in many cases truncated after the second order term (diffusion approximation). As a result, only scattering processes with small momentum transfer (type I processes) are treated exactly whereas scattering processes with large momentum transfer (type II processes) are treated approximately (see Fig. 3.3). Because the transition probability for the (unscreened) Coulomb potential diverges for small momentum transfer, soft Coulomb scattering events dominate, and the diffusion approximation is expected to describe Coulomb scattering reasonably well. A similar reasoning applies also to electron-LO-phonon scattering.²

Keeping therefore only the second order terms, we write

$$\begin{aligned}
 J_B^{(0)}[f, \delta\vec{S}] &= J_B^{(0), \text{on}}[f, \delta\vec{S}] + J_B^{(0), \text{off}}[f, \delta\vec{S}] \\
 &= \left[\sum_i A^{\text{ei}}(\vec{k}) \frac{\partial}{\partial k_i} + \sum_{ij} B_{ij}^{\text{ei}}(\vec{k}) \frac{\partial^2}{\partial k_i \partial k_j} \right] \delta\vec{S}(\vec{k}, t) \\
 &+ \sum_{\nu=\text{ee, ep}} \left[\sum_i \frac{\partial}{\partial k_i} A_i^\nu(\vec{k}) + \sum_{ij} \frac{\partial^2}{\partial k_i \partial k_j} B_{ij}^\nu(\vec{k}) \right] \delta\vec{S}(\vec{k}, t) \\
 &\equiv \mathcal{D}(\vec{k}) \delta\vec{S}(\vec{k}, t) , \tag{3.45}
 \end{aligned}$$

where the first two terms on the rhs come from elastic scattering processes and the last two terms encode inelastic scattering events. In Eq. (3.45) we introduced for the first and second moments ($\nu = \text{ei}, \text{ee}, \text{ep}$),

$$A_i^\nu(\vec{k}) = \sum_{\vec{q}} q_i W^\nu(\vec{k}; \vec{q}) , \tag{3.46}$$

²The singular behavior of the collision integrals is stronger in three than in two dimensions. Thus, the diffusion approximation describes perhaps scattering in bulk better than in quantum wells.

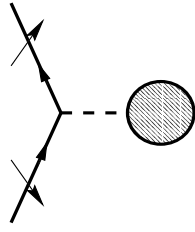


Figure 3.4: Graphical illustration of the collision terms within the diffusion approximation: A “test” spin polarization scatters off a generalized bath of equilibrated “field” particles (electrons, impurities, and/or phonons). Whereas spin-flip scattering is elastic (on-shell) within our approximation, spin-conserving scattering can be on- or off-shell, i.e. the “test” spin polarization can lose/gain energy, because the “internal degrees” of the bath can absorb/emit energy.

$$B_{ij}^\nu(\vec{k}) = \frac{1}{2} \sum_{\vec{q}} q_i q_j W^\nu(\vec{k}; \vec{q}) , \quad (3.47)$$

which have the meaning of \vec{k} -dependent dynamical friction and diffusion coefficients, respectively. Within the diffusion approximation the spin-conserving (Born) collision integrals are therefore represented by a Fokker-Planck differential operator (3.45). Each scattering process gives rise to a particular Fokker-Planck operator, with particular dynamical friction and diffusion coefficients.

In the same spirit, expanding the spin-flip collision integral $J_B^{(2)}[f, \delta\vec{S}]$ up to second order in the momentum transfer \vec{q} , and using $\vec{g}(\vec{k}, \vec{k}) = 0$, gives

$$J_B^{(2)}[f, \delta\vec{S}] = -\mathbf{R}(\vec{k})\delta\vec{S}(\vec{k}t) , \quad (3.48)$$

with a spin-flip tensor

$$\mathbf{R}(\vec{k}) = 4 \sum_{\nu=\text{ei,ee,ep}} \sum_{ij} B_{ij}^\nu(\vec{k}) \mathbf{G}_{ij}(\vec{k}) , \quad (3.49)$$

given in terms of the total diffusion coefficient and a tensor $\mathbf{G}_{ij}(\vec{k})$ which describes the rate of change of the spin-flip vector $\vec{g}(\vec{k}, \vec{k}')$:

$$\mathbf{G}_{ij}(\vec{k}) = \begin{pmatrix} O_{ij}^{yy} & -O_{ij}^{xy} & 0 \\ -O_{ij}^{yx} & O_{ij}^{xx} & 0 \\ 0 & 0 & O_{ij}^{xx} + O_{ij}^{yy} \end{pmatrix} , \quad (3.50)$$

with

$$O_{ij}^{\nu\mu} = \left[\frac{\partial}{\partial k_i} g_{\vec{k}\vec{k}'}^\nu \right]_{\vec{k}'=\vec{k}} \left[\frac{\partial}{\partial k_j} g_{\vec{k}\vec{k}'}^\mu \right]_{\vec{k}'=\vec{k}} . \quad (3.51)$$

In Fig 3.4 we illustrate the physical content of the diffusion approximation encoded in Eqs. (3.45) and (3.48): the small “test” spin polarization $\delta\vec{S}(\vec{k}, t)$ scatters off equilibrated “field” particles, which, depending on the scattering process, are either electrons, phonons, or impurities. Spin conserving scattering can be elastic and inelastic, because the “field” particles can absorb/emit energy, the bath has “internal degrees”. Spin non-conserving scattering, on the other hand, turns out to be elastic within the diffusion approximation.

We now introduce scaled atomic units and measure energy in units of a scaled atomic Rydberg $\tilde{R}_0 = R_0/s$ and length in units of a scaled atomic Bohr radius $\tilde{a}_0 = \sqrt{s}a_0$, with $\tilde{R}_0\tilde{a}_0^2 = \hbar^2/2m_0$

and $e^2 = 2\sqrt{s}\tilde{R}_0\tilde{a}_0$, where m_0 is the bare electron mass and s is a scale factor chosen to yield $\tilde{R}_0 = 1$ meV. Symmetry-adapted coordinates are then a radial coordinate $\varepsilon = k^2$ and a generalized angle variable ω , which, for bulk semiconductors comprises two angles, the polar angle θ and the azimuth angle ϕ , and for quantum wells is simply the polar angle ϕ . Before we express the Fokker-Planck equation in these symmetry adopted coordinates, we recall that the experimentally measured quantity is the macroscopic (\vec{k} -averaged) spin polarization. Normalizing the macroscopic spin polarization to N_s , the (small) number of initially spin-polarized electrons and writing the \vec{k} -integral in symmetry-adapted coordinates, we define a “macroscopic” spin polarization (per spin polarized electron) ,

$$\begin{aligned}\delta\vec{S}(t) &= \frac{1}{N_s} \sum_{\vec{k}} \delta\vec{S}(\vec{k}, t) \\ &= \frac{1}{(2\pi)^d n_s} \int_0^\infty d\varepsilon \int d\omega J(\varepsilon) \delta\vec{S}(\varepsilon, \omega, t) ,\end{aligned}\quad (3.52)$$

with d the dimension, $n_s = N_s/L^d$ the density of initially spin-polarized electrons and $J(\varepsilon)$ the energy dependent part of the Jacobian, which arises from the transformation to the symmetry-adapted coordinates. Note that due to the normalization, $\delta\vec{S}(0)$ is a unit vector in the direction of the initial spin polarization. For bulk, $d = 3$, $d\omega = d\phi d\theta \sin\theta$, and $J(\varepsilon) = \sqrt{\varepsilon}/2$, while for quantum wells $d = 2$, $d\omega = d\phi$, and $J(\varepsilon) = 1/2$. Instead of setting up the Fokker-Planck equation for $\delta\vec{S}(\varepsilon, \omega, t)$ it is more convenient to directly construct the Fokker-Planck equation for

$$\delta\vec{S}'(\varepsilon, \omega, t) = \frac{J(\varepsilon)}{(2\pi)^d n_s} \delta\vec{S}(\varepsilon, \omega, t) . \quad (3.53)$$

The differential operator describing spin conserving scattering processes in the Fokker-Planck equation for $\delta\vec{S}'$ reads in symmetry-adapted coordinates

$$\begin{aligned}\mathcal{D}(\vec{k}) &= -\frac{\partial}{\partial\varepsilon} \frac{\varepsilon}{\tau_f(\varepsilon)} + \frac{\partial^2}{\partial\varepsilon^2} \frac{\varepsilon^2}{\tau_d(\varepsilon)} - \frac{1}{4\tau_\perp(\varepsilon)} \mathcal{L}^2(\omega) \\ &= \mathcal{D}(\varepsilon) - \frac{1}{4\tau_\perp(\varepsilon)} \mathcal{L}^2(\omega) ,\end{aligned}\quad (3.54)$$

where the operator $\mathcal{L}^2(\omega)$ denotes the total angular momentum operator in momentum space. To obtain this generic form for both bulk and quantum wells it is essential to include $J(\varepsilon)$ into the definition of the spin polarization. The off-shell term $\mathcal{D}(\varepsilon)$ originates from inelastic scattering events, e.g., due to electron-electron or electron-phonon scattering. The relaxation rates $1/\tau_f(\varepsilon)$ and $1/\tau_d(\varepsilon)$ denote the rate with which the “test” spin polarization loses energy and the rate with which the “test” spin polarization diffuses in energy space, respectively. The on-shell term, describing randomization of the angle variable, is given by the last term on the rhs of Eq. (3.54). It is proportional to the total on-shell relaxation rate $1/\tau_\perp(\varepsilon)$ due to both elastic and inelastic scattering processes.

The rates characterizing the differential operator $\mathcal{D}(\vec{k})$ are obtained from a direct calculation of the coefficients $A_i^{\nu}(\vec{k})$ and $B_{ij}^{\nu}(\vec{k})$ and casting the resulting differential operator $\mathcal{D}(\vec{k})$ in the specific form given in Eq. (3.54). An explicit calculation of the symmetry-adapted form of the relaxation tensor $\mathbf{R}(\vec{k})$, which is defined in terms of the total diffusion coefficient $B_{ij}(\vec{k})$, due to both elastic and inelastic scattering processes, shows moreover that it can be expressed in terms of the same scattering rates. Thus, the three scattering rates $1/\tau_f(\varepsilon)$, $1/\tau_d(\varepsilon)$, and $1/\tau_\perp(\varepsilon)$ completely specify the two collision integrals $J_B^{(0)}[f, \delta\vec{S}]$ and $J_B^{(2)}[f, \delta\vec{S}]$. In the Appendix we

give, as an illustration, explicit expressions for the relaxation rates due to electron-electron and electron-impurity scattering in a [001] quantum well.

The dimensionless, symmetry-adapted Fokker-Planck equation for $\delta\vec{S}'$, which is the basis for the calculation of the spin relaxation rates presented in the next subsection, can be therefore written as

$$\begin{aligned} \frac{\partial}{\partial t} \delta\vec{S}'(\varepsilon, \omega, t) &= [\mathcal{D}(\varepsilon) - \frac{1}{4\tau_{\perp}(\varepsilon)} \mathcal{L}^2(\omega) + i\vec{\Omega}_C \cdot \vec{\mathcal{L}}(\omega)] \delta\vec{S}'(\varepsilon, \omega, t) \\ &+ \left[\vec{\Omega}_L + \vec{\Omega}_{IA}(\varepsilon, \omega) + \vec{\Omega}_g(\varepsilon, \omega) \right] \times \delta\vec{S}'(\varepsilon, \omega, t) \\ &- \mathbf{R}(\varepsilon, \omega) \delta\vec{S}'(\varepsilon, \omega, t) . \end{aligned} \quad (3.55)$$

It contains spin relaxation due to motional-narrowing (DP and VG processes) and spin-flip scattering (EY process). The former arises from the combined action of the off- and on-shell spin-conserving scattering events encoded in the differential operators $\mathcal{D}(\varepsilon)$ and $(1/\tau_{\perp}(\omega))\mathcal{L}^2(\omega)$, respectively, and the torque forces due to $\vec{\Omega}_{IA}(\varepsilon, \omega)$ and $\vec{\Omega}_g(\varepsilon, \omega)$, while the latter originates from the spin-flip tensor $\mathbf{R}(\varepsilon, \omega)$. Note that if more than one scattering process is considered, the relaxation rates characterizing the differential operators and the spin-flip tensor are total relaxation rates, due to whatever elastic and inelastic scattering processes are included in the model. The orbital motion of the electrons, which leads to a quenching of the motional-narrowing spin relaxation processes, is given by the term $i\vec{\Omega}_C \cdot \vec{\mathcal{L}}(\omega)$ on the rhs of Eq. (3.55). In the next subsection we develop a scheme which separates the fast spin conserving scattering processes from the slow spin decay causing processes and directly yields the time evolution of the macroscopic spin polarization.

3.3.4 Multiple Time Scale Analysis

The Fokker-Planck equation (3.55) determines the time evolution of the non-equilibrium spin polarization on the fast, spin-conserving time scale, where randomization of the angle variables (direction of the momentum) and energy relaxation and diffusion occurs, and on the long time scale, where spin non-conserving processes lead to the decay of the spin polarization. The two time scales are well separated. The fast, spin conserving stage, whose scale is given by the first term on the rhs of Eq. (3.55) and therefore by the off- and on-shell relaxation times (as well as the time it takes to complete one cyclotron orbit), terminates in a quasi-stationary state, which then evolves on the time scales set by the Elliott-Yafet term, the torque forces due to the spin off-diagonal Hamiltonian matrix elements, and the external magnetic field (Larmor precession). Experimentally relevant is usually the time evolution on the long time scale. In this subsection we employ therefore a multiple time scale approach to extract from the Fokker-Planck equation (3.55) a Bloch equation, which controls the time evolution of the macroscopic (\vec{k} -averaged) spin polarization on the long time scale. To simplify the notation, we suppress the prime. It is understood that the spin polarization $\delta\vec{S}(\varepsilon, \omega, t)$ contains the factor $J(\varepsilon)/(2\pi)^d n_s$.

As a preparatory step we first consider that part of the Fokker-Planck equation (3.55), which is spin-conserving:

$$\frac{\partial}{\partial t} \delta\vec{S}(\varepsilon, \omega, t) = [\mathcal{D}(\varepsilon) - \frac{1}{4\tau_{\perp}(\varepsilon)} \mathcal{L}^2(\omega) + i\vec{\Omega}_C \cdot \vec{\mathcal{L}}(\omega)] \delta\vec{S}(\varepsilon, \omega, t) . \quad (3.56)$$

To find the stationary solution of Eq. (3.56) we set the lhs to zero, write

$$\delta\vec{S}_{st}(\varepsilon, \omega) = p(\varepsilon) \vec{\Psi}_{st}(\varepsilon, \omega) , \quad (3.57)$$

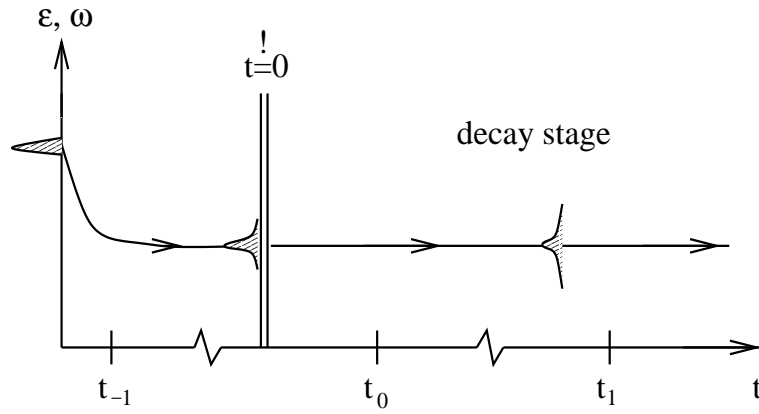


Figure 3.5: Schematic illustration of the time evolution of the non-equilibrium spin polarization as given by the Fokker-Planck equation (3.55). For simplicity we consider $\vec{B} = 0$. After injection, the spin polarization relaxes and diffuses in $\varepsilon - \omega$ space. This initial time evolution is spin-conserving and occurs on a fast time scale t_{-1} determined by τ_i ($i = f, d, \perp$). The intermediate time scale $t_0 \gg t_{-1}$ is set by the time it takes an electron spin to precess about the intrinsic magnetic field $\vec{\Omega}_{IA}$. The decay of the spin polarization occurs on an even slower time scale $t_1 \gg t_0$. It is this time scale which we eventually want to access. We are not interested in resolving the fast, spin conserving time evolution. All we need is its quasi-stationary state, which provides the initial condition for the time evolution on the slow time scale(s).

with $p(\varepsilon)$ defined by

$$\mathcal{D}(\varepsilon)p(\varepsilon) = 0, \quad (3.58)$$

and obtain for the auxiliary vector $\vec{\Psi}_{st}(\varepsilon, \omega)$ the differential equation

$$[\mathcal{D}^*(\varepsilon) - \frac{1}{4\tau_{\perp}(\varepsilon)}\mathcal{L}^2(\omega) + i\vec{\Omega}_C \cdot \vec{\mathcal{L}}(\omega)]\vec{\Psi}_{st}(\varepsilon, \omega) = 0, \quad (3.59)$$

with

$$\mathcal{D}^*(\varepsilon) = \frac{\varepsilon}{\tau_f(\varepsilon)}\frac{\partial}{\partial\varepsilon} + \frac{\varepsilon^2}{\tau_d(\varepsilon)}\frac{\partial^2}{\partial\varepsilon^2}, \quad (3.60)$$

the adjoint operator to $\mathcal{D}(\varepsilon)$. The simplest solution of (3.59) is a constant vector

$$\vec{\Psi}_{st}(\varepsilon, \omega) = \vec{e}, \quad (3.61)$$

giving rise to a stationary solution

$$\delta\vec{S}_{st}(\varepsilon, \omega) = p(\varepsilon)\vec{e}. \quad (3.62)$$

The particular form of $p(\varepsilon)$ does not matter at this point.

We now turn to the complete Fokker-Planck equation (3.55). The spin-conserving stage of the time evolution, described by the first term on the rhs, occurs on a very fast time scale and is usually experimentally not resolved. Hence, it is not necessary to explicitly keep track of it. Instead, it is sufficient to use the final state of the fast, spin-conserving time evolution, i.e. the stationary solution of the spin conserving part of the Fokker-Planck equation [cf. Eqs. (3.56)–(3.62)], as an initial state for the time evolution on the slow time scale, where spin decay occurs (see Fig. 3.5 for an illustration). We write the initial condition therefore as

$$\delta\vec{S}(\varepsilon, \omega, 0) = p(\varepsilon)\vec{e}, \quad (3.63)$$

where \vec{e} is now the direction of the initial spin polarization. This initial condition is general enough, because neither electrical nor optical spin injection produce anisotropic initial spin polarizations. Accordingly, we write for arbitrary times

$$\delta\vec{S}(\varepsilon, \omega, t) = p(\varepsilon)\vec{\Psi}(\varepsilon, \omega, t) , \quad (3.64)$$

where the time-dependent auxiliary vector $\vec{\Psi}(\varepsilon, \omega, t)$ satisfies now the time-dependent equation

$$\begin{aligned} \frac{\partial}{\partial t}\vec{\Psi}(\varepsilon, \omega, t) &= [\mathcal{D}^*(\varepsilon) - \frac{1}{4\tau_{\perp}(\varepsilon)}\mathcal{L}^2(\omega) + i\vec{\Omega}_C \cdot \vec{\mathcal{L}}(\omega)]\vec{\Psi}(\varepsilon, \omega, t) \\ &+ \left(\vec{\Omega}_L + \vec{\Omega}_{IA}(\varepsilon, \omega) + \vec{\Omega}_g(\varepsilon, \omega)\right) \times \vec{\Psi}(\varepsilon, \omega, t) \\ &- \mathbf{R}(\varepsilon, \omega)\vec{\Psi}(\varepsilon, \omega, t) , \end{aligned} \quad (3.65)$$

with an initial condition $\vec{\Psi}(\varepsilon, \omega, 0) = \vec{e}$. Note that Eq. (3.65) is the adjoint Fokker-Planck equation. The function $p(\varepsilon)$ satisfies the homogeneous differential equation (3.58) and is therefore defined only up to a normalization constant. From the initial condition for the macroscopic spin polarization, $\delta\vec{S}(0) = \vec{e}$, we conclude that $p(\varepsilon)$ has to be normalized according to $\int d\varepsilon \int d\omega p(\varepsilon) = 1$ (recall that we redefined $\delta\vec{S}$ such that it contains the factor $J(\varepsilon)/(2\pi)^d n_s$). Thus, $d\varepsilon \int d\omega p(\varepsilon)$ can be interpreted as the probability for finding a spin-polarized “test” electron in the energy interval $[\varepsilon, \varepsilon + d\varepsilon]$.

To proceed further we scale each term in Eq. (3.65) to its typical value. In the case of degenerate electrons the typical values would be the ones at the Fermi energy, whereas for non-degenerate electrons the typical values could be the ones at the average thermal energy. Denoting typical values by a caret, we introduce scaled quantities $t' = t/\hat{t}$, $\tau'_f = \tau_f/\hat{\tau}_f$, $\tau'_d = \tau_d/\hat{\tau}_d$, $\tau'_\perp = \tau_\perp/\hat{\tau}_\perp$, $\vec{\Omega}'_{IA} = \vec{\Omega}_{IA}\hat{\tau}_{IA}$, $\vec{\Omega}'_g = \vec{\Omega}_g\hat{\tau}_g$, $\vec{\Omega}'_L = \vec{\Omega}_L\hat{\tau}_L$, $\mathbf{R}' = \mathbf{R}\hat{\tau}_R$, and $\vec{\Omega}'_C = \vec{\Omega}_C\hat{\tau}_C$. The rescaled equation for $\vec{\Psi}'(\varepsilon, \omega, t')$ becomes (suppressing the arguments of the various functions)

$$\begin{aligned} \frac{\partial}{\partial t'}\vec{\Psi}' &= \left[\frac{\hat{t}}{\hat{\tau}_f} \frac{\varepsilon}{\tau'_f} \frac{\partial}{\partial \varepsilon} + \frac{\hat{t}}{\hat{\tau}_d} \frac{\varepsilon^2}{\tau'_d} \frac{\partial^2}{\partial \varepsilon^2} - \frac{\hat{t}}{\hat{\tau}_\perp} \frac{1}{4\tau'_\perp} \mathcal{L}^2 + \frac{\hat{t}}{\hat{\tau}_C} i\vec{\Omega}'_C \cdot \vec{\mathcal{L}}\right]\vec{\Psi}' \\ &+ \frac{\hat{t}}{\hat{\tau}_L} \vec{\Omega}'_L \times \vec{\Psi}' + \frac{\hat{t}}{\hat{\tau}_{IA}} \vec{\Omega}'_{IA} \times \vec{\Psi}' + \frac{\hat{t}}{\hat{\tau}_g} \vec{\Omega}'_g \times \vec{\Psi}' - \frac{\hat{t}}{\hat{\tau}_R} \mathbf{R}' \vec{\Psi}' . \end{aligned} \quad (3.66)$$

We identify three time scales. A fast time scale given by the spin conserving relaxation times $\hat{\tau}_i$ ($i = f, d, \perp$) and the time it takes to complete a cyclotron orbit $\hat{\tau}_C$, an intermediate time scale given by the time it takes to complete a precession around the intrinsic magnetic fields (due to the spin off-diagonal Hamiltonian matrix elements) $\hat{\tau}_{IA}$ and $\hat{\tau}_g$, and a long time scale, on which Larmor precession and spin-flip scattering occur, $\hat{\tau}_L$ and $\hat{\tau}_R$, respectively. For representative experimental set-ups, the typical time scale \hat{t} , on which the spin polarization has to be tracked (“observation time”), and the three typical intrinsic time scales obey the following ordering: $\frac{\hat{t}}{\hat{\tau}_f}, \frac{\hat{t}}{\hat{\tau}_d}, \frac{\hat{t}}{\hat{\tau}_\perp}, \frac{\hat{t}}{\hat{\tau}_C} = O(\eta^{-1})$, $\frac{\hat{t}}{\hat{\tau}_{IA}}, \frac{\hat{t}}{\hat{\tau}_g} = O(\eta^0)$, and $\frac{\hat{t}}{\hat{\tau}_L}, \frac{\hat{t}}{\hat{\tau}_R} = O(\eta^1)$ where we introduced a small parameter η . Accordingly, we classify each term in Eq. (3.66) by the smallness parameter η . Suppressing the primes, Eq. (3.66) is rewritten as

$$\frac{\partial}{\partial t}\vec{\Psi} = \frac{1}{\eta}[\mathcal{D}^* - \frac{1}{4\tau_{\perp}}\mathcal{L}^2 + i\vec{\Omega}_C \cdot \vec{\mathcal{L}}]\vec{\Psi} + (\vec{\Omega}_{IA} + \vec{\Omega}_g) \times \vec{\Psi} + \eta \vec{\Omega}_L \times \vec{\Psi} - \eta \mathbf{R} \vec{\Psi} . \quad (3.67)$$

Equation (3.67) is in a form where fast and slow processes can be clearly identified. The fast spin-conserving terms and the orbital motion enter in order η^{-1} , the precession around

the internal magnetic fields enters in order η^0 , whereas the Larmor precession and the spin-flip scattering terms appear in order η^1 . Naturally, taking as much advantage as possible of the existence of the small parameter η , the first thought is to expand all quantities with respect to η and apply perturbation theory. The structure of Eq. (3.67) indicates however that regular perturbation theory will lead to non-uniformity in the long-time regime, i.e. precisely in that regime, which we are interested in. To obtain the correct long-time behavior of the solution of Eq. (3.67) a multiple time scale approach is required.

In the spirit of multiple time scale perturbation theory [212], we consider therefore $\vec{\Psi}$ as a function of three time variables $t_n = \eta^n t$, $n = -1, 0, 1$, which are assumed to be independent, and substitute a second order expansion of the form

$$\vec{\Psi}(\varepsilon, \omega, t) = \vec{\Psi}^{(0)}(\varepsilon, \omega, t_{-1}, t_0, t_1) + \eta \vec{\Psi}^{(1)}(\varepsilon, \omega, t_{-1}, t_0, t_1) + \eta^2 \vec{\Psi}^{(2)}(\varepsilon, \omega, t_{-1}, t_0, t_1) \quad (3.68)$$

into Eq. (3.67), where the time derivative is extended to $\partial_t = \eta^{-1} \partial_{t_{-1}} + \partial_{t_0} + \eta \partial_{t_1}$. Equating coefficients of like powers of η yields an hierarchy of equations for the functions $\vec{\Psi}^{(n)}$. Up to $O(\eta)$ they read

$$\frac{\partial}{\partial t_{-1}} \vec{\Psi}^{(0)} = [\mathcal{D}^* - \frac{1}{4\tau_{\perp}} \mathcal{L}^2 + i\vec{\Omega}_C \cdot \vec{\mathcal{L}}] \vec{\Psi}^{(0)}, \quad (3.69)$$

$$\frac{\partial}{\partial t_{-1}} \vec{\Psi}^{(1)} + \frac{\partial}{\partial t_0} \vec{\Psi}^{(0)} = [\mathcal{D}^* - \frac{1}{4\tau_{\perp}} \mathcal{L}^2 + i\vec{\Omega}_C \cdot \vec{\mathcal{L}}] \vec{\Psi}^{(1)} + (\vec{\Omega}_{IA} + \vec{\Omega}_g) \times \vec{\Psi}^{(0)}, \quad (3.70)$$

$$\begin{aligned} \frac{\partial}{\partial t_{-1}} \vec{\Psi}^{(2)} + \frac{\partial}{\partial t_0} \vec{\Psi}^{(1)} + \frac{\partial}{\partial t_1} \vec{\Psi}^{(0)} &= [\mathcal{D}^* - \frac{1}{4\tau_{\perp}} \mathcal{L}^2 + i\vec{\Omega}_C \cdot \vec{\mathcal{L}}] \vec{\Psi}^{(2)} \\ &+ (\vec{\Omega}_{IA} + \vec{\Omega}_g) \times \vec{\Psi}^{(1)} + \vec{\Omega}_L \times \vec{\Psi}^{(0)} - \mathbf{R} \vec{\Psi}^{(0)}. \end{aligned} \quad (3.71)$$

For the analysis of this set of equations it is convenient to split $\vec{\Psi}^{(n)}$ into an angle averaged and a remaining part,

$$\vec{\Psi}^{(n)}(\varepsilon, \omega, t_{-1}, t_0, t_1) = \vec{a}^{(n)}(\varepsilon, t_{-1}, t_0, t_1) + \delta \vec{a}^{(n)}(\varepsilon, \omega, t_{-1}, t_0, t_1), \quad (3.72)$$

where $\vec{a}^{(n)} = \langle \vec{\Psi}^{(n)} \rangle_{\omega}$, with an angle average defined by

$$\langle \dots \rangle_{\omega} = \int d\omega \dots \quad (3.73)$$

and $\langle \delta \vec{a}^{(n)} \rangle_{\omega} = 0$ by definition. Since the angle variables are periodic this partitioning is always possible. From the initial condition, $\vec{\Psi}(\varepsilon, \omega, 0) = \vec{e}$, we infer the initial conditions $\vec{a}^{(n)}(\varepsilon, 0, 0, 0) = \vec{e} \delta_{n,0}$, and $\delta \vec{a}^{(n)}(\varepsilon, \omega, 0, 0, 0) = 0$. Recalling that the factor $J(\varepsilon)/(2\pi)^d n_s$ is included in the definition of $\delta \vec{S}(\varepsilon, \omega, t)$, the macroscopic non-equilibrium spin polarization defined in Eq. (3.52) can now be rewritten as

$$\delta \vec{S}(t) = \int_0^{\infty} d\varepsilon p(\varepsilon) \vec{a}(\varepsilon, t) = \langle \vec{a}(\varepsilon, t) \rangle_{\varepsilon}, \quad (3.74)$$

where we defined an energy average

$$\langle \dots \rangle_{\varepsilon} = \int_0^{\infty} d\varepsilon p(\varepsilon) \dots \quad (3.75)$$

Note that the function $p(\varepsilon)$, which determines the terminating state of the fast, spin-conserving time evolution, enters here naturally as a weight function. Formally, the weight function appears

in our theory because of the ansatz (3.64), which enabled us to switch to the adjoint Fokker-Planck equation. The expansion of $\vec{\Psi}$ implies an analogous expansion for the macroscopic (\vec{k} -averaged) spin polarization:

$$\delta\vec{S}(t) = \delta\vec{S}^{(0)}(t_{-1}, t_0, t_1) + \eta\delta\vec{S}^{(1)}(t_{-1}, t_0, t_1) + \eta^2\delta\vec{S}^{(2)}(t_{-1}, t_0, t_1) . \quad (3.76)$$

We now calculate the leading order contribution $\delta\vec{S}^{(0)}(t)$ uniformly valid for all times. As a result, we will obtain a Bloch equation which determines the long time behavior of the macroscopic spin polarization.

$O(\eta^{-1})$ equation

With the substitution (3.72), the $O(\eta^{-1})$ equation (3.69) splits into two independent equations, one for the angle averaged part and one for the angle dependent part:

$$\frac{\partial}{\partial t_{-1}} \vec{a}^{(0)} = \mathcal{D}^* \vec{a}^{(0)} , \quad (3.77)$$

$$\frac{\partial}{\partial t_{-1}} \delta\vec{a}^{(0)} = [\mathcal{D}^* - \frac{1}{4\tau_{\perp}} \mathcal{L}^2] \delta\vec{a}^{(0)} . \quad (3.78)$$

Solutions of Eqs. (3.77) and (3.78) which are compatible with the two initial conditions, $\vec{a}^{(0)}(\varepsilon, 0, 0, 0) = \vec{e}$ and $\delta\vec{a}^{(0)}(\varepsilon, 0, 0, 0) = 0$, are $\vec{a}^{(0)}(\varepsilon, t_{-1}, t_0, t_1) = \vec{a}^{(0)}(t_0, t_1)$, with $\vec{a}^{(0)}(0, 0) = \vec{e}$, and $\delta\vec{a}^{(0)}(\varepsilon, \omega, t_{-1}, t_0, t_1) = 0$. Using Eqs. (3.74) and (3.76), we find therefore

$$\delta\vec{S}^{(0)}(t_0, t_1) = \vec{a}^{(0)}(t_0, t_1) , \quad (3.79)$$

that is, due to our choice of the initial condition, the macroscopic zeroth order spin polarization is independent of the fast spin conserving time scale t_{-1} and solely evolves on the long time scales t_0 and t_1 .

$O(\eta^0)$ equation

To determine the time evolution of the macroscopic spin polarization on the long time scales t_0 and t_1 , we study the $O(\eta^0)$ equation. Substituting (3.72) into Eq. (3.70), the latter splits into two independent equations:

$$\frac{\partial}{\partial t_{-1}} \vec{a}^{(1)} = -\frac{\partial}{\partial t_0} \vec{a}^{(0)} + \mathcal{D}^* \vec{a}^{(1)} , \quad (3.80)$$

$$\frac{\partial}{\partial t_{-1}} \delta\vec{a}^{(1)} = [\mathcal{D}^* - \frac{1}{4\tau_{\perp}} \mathcal{L}^2 + i\vec{\Omega}_C \cdot \vec{\mathcal{L}}] \delta\vec{a}^{(1)} + (\vec{\Omega}_{IA} + \vec{\Omega}_g) \times \vec{a}^{(0)} , \quad (3.81)$$

where we have used $\delta\vec{a}^{(0)} = 0$, $\langle \vec{\Omega}_{IA} \rangle_{\omega} = 0$, and $\langle \vec{\Omega}_g \rangle_{\omega} = 0$. Applying the energy average $\langle \dots \rangle_{\varepsilon}$ on both sides of Eq. (3.80) yields

$$\frac{\partial}{\partial t_{-1}} \delta\vec{S}^{(1)} = -\frac{\partial}{\partial t_0} \delta\vec{S}^{(0)} - \langle \mathcal{D}^* \vec{a}^{(1)} \rangle_{\varepsilon} , \quad (3.82)$$

which, using in the second term partial integration and the definition of $p(\varepsilon)$, reduces to

$$\frac{\partial}{\partial t_{-1}} \delta\vec{S}^{(1)} = -\frac{\partial}{\partial t_0} \delta\vec{S}^{(0)} . \quad (3.83)$$

The vanishing of the second term on the rhs of Eq. (3.82) is the result of the spin conservation of the differential operator \mathcal{D} , which in turn is ensured by the identity

$$\left. \frac{d}{d\varepsilon} \frac{\varepsilon^2}{\tau_d(\varepsilon)} \right|_{\varepsilon=0} = \left. \frac{\varepsilon}{\tau_f(\varepsilon)} \right|_{\varepsilon=0} . \quad (3.84)$$

It is crucial to note that the rhs of Eq. (3.83) is independent of the fast time t_{-1} , because $\vec{a}^{(0)}$ is independent of t_{-1} . Integrating Eq. (3.83) with respect to t_{-1} , the rhs therefore gives rise to a secular term, i.e. a term which is proportional to t_{-1} . As a result, $\delta\vec{S}^{(1)}$ can be larger than $\delta\vec{S}^{(0)}$ for sufficiently large times. The expansion (3.76) would be valid only for short times, i.e. the expansion is non-uniform. Within multiple time scale perturbation theory, secular terms can be avoided by an appropriate choice of the time evolutions on the various time scales. The secular term in Eq. (3.83) can be particularly simply removed by forcing the rhs to be zero, which gives rise to the condition

$$\int_0^\infty d\varepsilon p(\varepsilon) \frac{\partial}{\partial t_0} \vec{a}^{(0)}(t_0, t_1) = 0 . \quad (3.85)$$

That is, $\vec{a}^{(0)}(t_0, t_1) = \vec{a}^{(0)}(t_1)$, which, using Eq. (3.79), leads to $\delta\vec{S}^{(0)}(t_1) = \vec{a}^{(0)}(t_1)$, i.e. the time evolution of the zeroth order macroscopic spin polarization (and therefore the spin decay) occurs solely on the long time scale t_1 . Since the rhs of Eq. (3.83) is made to vanish, we also obtain $\delta\vec{S}^{(1)}(t_{-1}, t_0, t_1) = \delta\vec{S}^{(1)}(t_0, t_1)$, i.e., $\delta\vec{S}^{(1)}$ is independent of the fast time variable t_{-1} . Using the definition of $\delta\vec{S}^{(1)}$, we furthermore conclude that $\vec{a}^{(1)}(\varepsilon, t_{-1}, t_0, t_1) = \vec{a}^{(1)}(\varepsilon, t_0, t_1)$. Both results we need in the analysis of the $O(\eta^1)$ equations, which is necessary to determine the time evolution on the remaining time scale t_1 .

$O(\eta^1)$ equations

To investigate the $O(\eta^1)$ equation (3.71), we substitute (3.72) into (3.71). Averaging over the angle and energy, we find

$$\begin{aligned} \frac{\partial}{\partial t_{-1}} \delta\vec{S}^{(2)} &= -\frac{\partial}{\partial t_0} \delta\vec{S}^{(1)} - \frac{\partial}{\partial t_1} \delta\vec{S}^{(0)} + \langle (\vec{\Omega}_{IA} + \vec{\Omega}_g) \times \delta\vec{a}^{(1)} \rangle_{\varepsilon, \omega} + \vec{\Omega}_L \times \delta\vec{S}^{(0)} \\ &\quad - \langle \mathbf{R} \rangle_{\varepsilon, \omega} \delta\vec{S}^{(0)} , \end{aligned} \quad (3.86)$$

where we used $\delta\vec{a}^{(0)} = 0$, $\langle \vec{\Omega}_{IA} \rangle_{\varepsilon, \omega} = 0$, $\langle \vec{\Omega}_g \rangle_{\varepsilon, \omega} = 0$, and $\langle \mathcal{D}^* \vec{a}^{(2)} \rangle_{\varepsilon, \omega} = 0$. The second term on the rhs of (3.86) contains $\delta\vec{a}^{(1)}$ which has to be obtained from Eq. (3.81), the angle dependent part of the $O(\eta^0)$ equation. Before we proceed with the analysis of Eq. (3.86) let us therefore turn to Eq. (3.81). Integration of Eq. (3.81) with respect to the fast time t_{-1} produces a secular term, $(\vec{\Omega}_{IA} + \vec{\Omega}_g) \times \vec{a}^{(0)} t_{-1}$, which cannot be removed, because both $\vec{\Omega}_{IA} + \vec{\Omega}_g$ and $\vec{a}^{(0)}$ are finite. A way to avoid the resulting non-uniformity is to demand

$$\frac{\partial}{\partial t_{-1}} \delta\vec{a}^{(1)} = 0 , \quad (3.87)$$

i.e., to enforce $\delta\vec{a}^{(1)}(\varepsilon, \omega, t_{-1}, t_0, t_1) = \delta\vec{a}^{(1)}(\varepsilon, \omega, t_0, t_1)$, which reduces Eq. (3.81) to

$$[\mathcal{D}^* - \frac{1}{4\tau_\perp} \mathcal{L}^2 + i\vec{\Omega}_C \cdot \vec{\mathcal{L}}] \delta\vec{a}^{(1)} + (\vec{\Omega}_{IA} + \vec{\Omega}_g) \times \delta\vec{S}^{(0)} = 0 , \quad (3.88)$$

where we used in the last term $\vec{a}^{(0)}(t_1) = \delta\vec{S}^{(0)}(t_1)$. The condition (3.87) is reminiscent of the ad-hoc quasi-stationarity assumption usually invoked in the calculation of the D'yakonov-Perel'

relaxation rates. [159] In subsection 3.4.2 we briefly describe a relaxation time approximation, which is conceptually simpler than the multiple time scale approach but requires, among others, a quasi-stationarity condition, which has to be incorporated by hand. The multiple time scale perturbation theory, in contrast, avoids this ad-hoc approach and identifies the time scale on which this assumption holds.

We now return to Eq. (3.86). Since $\delta\vec{a}^{(1)}$, $\delta\vec{S}^{(1)}$, and $\delta\vec{S}^{(0)}$ are independent of the fast time variable t_{-1} , the whole rhs of Eq. (3.86) is independent of t_{-1} . Integration with respect to t_{-1} thus gives rise to a secular term which has to be removed. We force therefore the rhs of Eq. (3.86) to vanish which can be certainly accomplished if we separately demand

$$\frac{\partial}{\partial t_0} \delta\vec{S}^{(1)} = 0, \quad (3.89)$$

$$\frac{\partial}{\partial t_1} \delta\vec{S}^{(0)} = \vec{\Omega}_L \times \delta\vec{S}^{(0)} + \langle (\vec{\Omega}_{IA} + \vec{\Omega}_g) \times \delta\vec{a}^{(1)} \rangle_{\varepsilon, \omega} - \langle \mathbf{R} \rangle_{\varepsilon, \omega} \delta\vec{S}^{(0)}. \quad (3.90)$$

From the first equation we find

$$\int_0^\infty d\varepsilon p(\varepsilon) \frac{\partial}{\partial t_0} \vec{a}^{(1)}(\varepsilon, t_0, t_1) = 0, \quad (3.91)$$

that is $\vec{a}^{(1)}$ is independent of t_0 , a result which we need below. The second equation is already a precursor of the Bloch equation for $\delta\vec{S}^{(0)}(t_1)$. It determines $\delta\vec{S}^{(0)}(t_1)$ for a given $\delta\vec{a}^{(1)}(t_0, t_1)$, is however not yet of the Bloch-type because, at this point of the calculation, $\delta\vec{a}^{(1)}$ is still a function of t_1 and t_0 .

To obtain a closed Bloch-type equation on the time scale t_1 alone, we now examine the t_0 dependence of $\delta\vec{a}^{(1)}(t_0, t_1)$. Towards that end, we consider the angle dependent part of the $O(\eta^1)$ equation (3.71), which reads

$$\begin{aligned} \frac{\partial}{\partial t_{-1}} \delta\vec{a}^{(2)} &= [\mathcal{D}^* - \frac{1}{4\tau_\perp} \mathcal{L}^2 + i\vec{\Omega}_C \cdot \vec{\mathcal{L}}] \delta\vec{a}^{(2)} \\ &+ (\vec{\Omega}_{IA} + \vec{\Omega}_g) \times \vec{a}^{(1)} + (\vec{\Omega}_{IA} + \vec{\Omega}_g) \times \delta\vec{a}^{(1)} - \langle (\vec{\Omega}_{IA} + \vec{\Omega}_g) \times \delta\vec{a}^{(1)} \rangle_\omega \\ &- \mathbf{R} \vec{a}^{(0)} + \langle \mathbf{R} \rangle_\omega \vec{a}^{(0)} - \frac{\partial}{\partial t_0} \delta\vec{a}^{(1)}. \end{aligned} \quad (3.92)$$

Except for the first term, all terms on the rhs are independent of t_{-1} , and therefore give rise to secular terms. To remove the secular terms, we set the undesired terms on the rhs to zero

$$\begin{aligned} \frac{\partial}{\partial t_0} \delta\vec{a}^{(1)} &= (\vec{\Omega}_{IA} + \vec{\Omega}_g) \times \delta\vec{a}^{(1)} - \langle (\vec{\Omega}_{IA} + \vec{\Omega}_g) \times \delta\vec{a}^{(1)} \rangle_\omega \\ &- [\mathbf{R} - \langle \mathbf{R} \rangle_\omega] \vec{a}^{(0)} + (\vec{\Omega}_{IA} + \vec{\Omega}_g) \times \vec{a}^{(1)}. \end{aligned} \quad (3.93)$$

The last two terms on the rhs of this equation are independent of t_0 and therefore again give rise to a secular term if Eq. (3.93) is integrated with respect to t_0 . In general, the last two terms are finite. Thus, to avoid non-uniformity we demand that $\delta\vec{a}^{(1)}$ is independent of t_0 , that is, we enforce $\delta\vec{a}^{(1)}(\varepsilon, \omega, t_0, t_1) = \delta\vec{a}^{(1)}(\varepsilon, \omega, t_1)$. With this constraint, Eq. (3.93) could be used to determine $\vec{a}^{(1)}(\varepsilon, t_1)$ and eventually $\delta\vec{S}^{(1)}(t_1)$. This is however beyond the required accuracy.

Because $\delta\vec{a}^{(1)}$ is independent of t_0 , Eq. (3.90) is in fact a Bloch equation on the time scale t_1 alone. The function $\delta\vec{a}^{(1)}(\varepsilon, \omega, t_1)$ satisfies Eq. (3.88), which, through $\delta\vec{S}^{(0)}(t_1)$, contains t_1 only as a parameter. Therefore, the function $\delta\vec{a}^{(1)}(\varepsilon, \omega, t_1)$ instantaneously adjusts to the function $\delta\vec{S}^{(0)}(t_1)$, which, in this sense, acts like a ‘‘slave field’’ for $\delta\vec{a}^{(1)}(\varepsilon, \omega, t_1)$.

To make the equations determining the decay of the macroscopic spin polarization explicit, we recall $t_n = \eta^n t$ and go back to the original, unscaled time variable and functions. As a result Eq. (3.90) becomes a Bloch equation for the macroscopic spin polarization,

$$\frac{\partial}{\partial t} \delta \vec{S}^{(0)}(t) = \vec{\Omega}_L \times \delta \vec{S}^{(0)}(t) - [\mathbf{\Gamma}_{\text{EY}} + \mathbf{\Gamma}_{\text{MN}}] \delta \vec{S}^{(0)}(t), \quad (3.94)$$

with initial condition $\delta \vec{S}^{(0)}(0) = \vec{e}$. The Elliott-Yafet and motional-narrowing spin relaxation tensors are given by

$$\mathbf{\Gamma}_{\text{EY}} = \langle \mathbf{R} \rangle_{\varepsilon, \omega}, \quad (3.95)$$

$$\mathbf{\Gamma}_{\text{MN}} \delta \vec{S}^{(0)}(t) = -\langle (\vec{\Omega}_{IA} + \vec{\Omega}_g) \times \delta \vec{a}^{(1)} \rangle_{\varepsilon, \omega}, \quad (3.96)$$

respectively, and $\delta \vec{a}^{(1)}$ is obtained from Eq. (3.88). Equations (3.94) – (3.96) are the main result of this section. They control the time evolution of the macroscopic spin polarization on the long time scale, where spin relaxation, i.e., decay, occurs. Equation (3.96) is an implicit definition of the spin relaxation tensor $\mathbf{\Gamma}_{\text{MN}}$. The explicit form of $\mathbf{\Gamma}_{\text{MN}}$ can be obtained by inserting the solution of Eq. (3.88), which is always linear in $\delta \vec{S}^{(0)}(t)$, and performing the angle and energy averages.

We now present the details of this calculation. To derive an explicit expression for $\mathbf{\Gamma}_{\text{NM}}$ we have to solve Eq. (3.88), which is a system of three differential equations for the three components of the fluctuation vector $\delta \vec{a}^{(1)}$. It can be decoupled by expanding the angle dependent part of $\delta \vec{a}^{(1)}$ in terms of a complete set of functions Y_λ , which are the solution of the following eigenvalue problem,

$$\left[-\frac{1}{4\tau_\perp(\varepsilon)} \mathcal{L}^2 + i\vec{\Omega}_C \cdot \vec{\mathcal{L}} \right] Y_\lambda(\omega) + \frac{1}{\tau_\lambda(\varepsilon)} Y_\lambda(\omega) = 0, \quad (3.97)$$

where $1/\tau_\lambda(\varepsilon)$ is the eigenvalue. Notice that the energy ε enters the eigenvalue problem only as a parameter through the on-shell relaxation time $\tau_\perp(\varepsilon)$. For bulk semiconductors, the functions Y_λ are the spherical harmonics ($\lambda = l, m$), whereas for a quantum well the functions Y_λ are the trigonometric functions ($\lambda = m$). The crucial point is that both $\vec{\Omega}_{IA}$ and $\vec{\Omega}_g$ can be expanded in terms of Y_λ . As a result, in each λ channel we can introduce a function $r_\lambda(\varepsilon)$ which relates the λ component of $\delta \vec{a}^{(1)}$ to the λ component of the vector $(\vec{\Omega}_{IA} + \vec{\Omega}_g) \times \delta \vec{S}^{(0)}(t)$. The function $r_\lambda(\varepsilon)$ satisfy then a scalar differential equations.

Let us be more specific. Separating the energy and angle dependences of the vectors $\vec{\Omega}_{IA}$ and $\vec{\Omega}_g$, we first write

$$\vec{\Omega}_{IA}(\varepsilon, \omega) = \frac{1}{\tau_{IA}(\varepsilon)} \vec{\kappa}_{IA}(\omega), \quad (3.98)$$

$$\vec{\Omega}_g(\varepsilon, \omega) = \frac{1}{\tau_g(\varepsilon)} \vec{\kappa}_g(\omega), \quad (3.99)$$

where we defined energy dependent precession rates $1/\tau_{IA}(\varepsilon)$ and $1/\tau_g(\varepsilon)$ which depend on the dimension and are specified below.

We then expand the angle dependent parts in terms of $Y_\lambda(\omega)$, $\kappa_{IA}^i(\omega) = \sum_\lambda C_\lambda^i Y_\lambda(\omega)$ and $\kappa_g^i(\omega) = \sum_\lambda D_\lambda^i Y_\lambda(\omega)$, with $i = x, y, z$, and rewrite the torque force terms in terms of matrices:

$$\begin{aligned} \vec{\Omega}_{IA}(\varepsilon, \omega) \times \delta \vec{S}^{(0)}(t) &= \frac{1}{\tau_{IA}(\varepsilon)} \sum_\lambda \begin{pmatrix} 0 & -C_\lambda^z & C_\lambda^y \\ C_\lambda^z & 0 & -C_\lambda^x \\ -C_\lambda^y & C_\lambda^x & 0 \end{pmatrix} \delta \vec{S}^{(0)}(t) Y_\lambda(\omega) \\ &\equiv \frac{1}{\tau_{IA}(\varepsilon)} \sum_\lambda \mathbf{C}_\lambda \delta \vec{S}^{(0)}(t) Y_\lambda(\omega), \end{aligned} \quad (3.100)$$

and

$$\begin{aligned}\vec{\Omega}_g(\varepsilon, \omega) \times \delta\vec{S}^{(0)}(t) &= \frac{1}{\tau_g(\varepsilon)} \sum_{\lambda} \begin{pmatrix} 0 & -D_{\lambda}^z & D_{\lambda}^y \\ D_{\lambda}^z & 0 & -D_{\lambda}^x \\ -D_{\lambda}^y & D_{\lambda}^x & 0 \end{pmatrix} \delta\vec{S}^{(0)}(t) Y_{\lambda}(\omega) \\ &\equiv \frac{1}{\tau_g(\varepsilon)} \sum_{\lambda} \mathbf{D}_{\lambda} \delta\vec{S}^{(0)}(t) Y_{\lambda}(\omega),\end{aligned}\quad (3.101)$$

where we defined the matrices \mathbf{C}_{λ} and \mathbf{D}_{λ} , containing the expansion coefficients C_{λ}^i and D_{λ}^i , respectively. In the following we assume for simplicity that the matrices \mathbf{C}_{λ} and \mathbf{D}_{λ} are orthogonal, that is, for a given λ either \mathbf{C}_{λ} or \mathbf{D}_{λ} is finite. This is, e.g., the case for isotropic III-V bulk semiconductors, where an explicit calculation gives \mathbf{C}_{lm} nonzero only for $l = 3$, whereas \mathbf{D}_{lm} contributes only for $l = 0, 2$.

With the above definitions, the solution of Eq. (3.88) can be written as

$$\delta\vec{a}^{(1)}(\varepsilon, \omega, t) = \Sigma_{\lambda} r_{\lambda}(\varepsilon) [\mathbf{C}_{\lambda} + \mathbf{D}_{\lambda}] \delta\vec{S}^{(0)}(t) Y_{\lambda}(\omega), \quad (3.102)$$

with $r_{\lambda}(\varepsilon)$ satisfying an inhomogeneous differential equation

$$[\mathcal{D}^*(\varepsilon) - \frac{1}{\tau_{\lambda}(\varepsilon)}] r_{\lambda}(\varepsilon) + h_{\lambda}(\varepsilon) = 0, \quad (3.103)$$

where the inhomogeneity $h_{\lambda}(\varepsilon) = (1/\tau_{IA}(\varepsilon))\delta_{\lambda \in \Lambda_{IA}} + (1/\tau_g(\varepsilon))\delta_{\lambda \in \Lambda_g}$. Here, we introduced a generalized Kronecker delta, $\delta_{\lambda \in \Lambda}$, which is 1 for $\lambda \in \Lambda$ and zero otherwise. The sets Λ_{IA} and Λ_g contain the λ 's contributing to the expansion of $\vec{\Omega}_{IA}$ and $\vec{\Omega}_g$, respectively. An alternative differential equation,

$$[\mathcal{D}(\varepsilon) - \frac{1}{\tau_{\lambda}(\varepsilon)}] p(\varepsilon) r_{\lambda}(\varepsilon) + p(\varepsilon) h_{\lambda}(\varepsilon) = 0, \quad (3.104)$$

can be obtained by multiplying Eq. (3.103) from the left with $p(\varepsilon) r_{\lambda}(\varepsilon)$, integrating over ε , and using condition (3.84). This form we need for a comparison with the relaxation time approximation to be discussed in subsection 3.4.2.

Using (3.102) in (3.96), performing the average over ω , and taking the orthogonality of \mathbf{C}_{λ} and \mathbf{D}_{λ} into account, we finally obtain

$$\mathbf{\Gamma}_{MN} = \mathbf{\Gamma}_{DP} + \mathbf{\Gamma}_{VG}, \quad (3.105)$$

with the DP and VG spin relaxation tensors explicitly given by

$$\mathbf{\Gamma}_{DP} = \sum_{\lambda\bar{\lambda}} (-\mathbf{C}_{\lambda} \mathbf{C}_{\bar{\lambda}}) \left\langle \frac{r_{\bar{\lambda}}(\varepsilon)}{\tau_{IA}(\varepsilon)} \right\rangle_{\varepsilon} \langle Y_{\lambda} Y_{\bar{\lambda}} \rangle_{\omega} \quad (3.106)$$

and

$$\mathbf{\Gamma}_{VG} = \sum_{\lambda\bar{\lambda}} (-\mathbf{D}_{\lambda} \mathbf{D}_{\bar{\lambda}}) \left\langle \frac{r_{\bar{\lambda}}(\varepsilon)}{\tau_g(\varepsilon)} \right\rangle_{\varepsilon} \langle Y_{\lambda} Y_{\bar{\lambda}} \rangle_{\omega}, \quad (3.107)$$

respectively. To perform the angle averages it is necessary to specify the orthonormality of the functions $Y_{\lambda}(\omega)$. This depends on dimension and the particular experimental set-up (e.g., direction of the magnetic field). In the following subsection we apply therefore our approach separately to specific bulk and quantum well situations.

Equations (3.106) and (3.107) reduce the calculation of the DP and VG spin relaxation tensors to quadratures. In contrast to Eq. (3.95), which defines the EY spin relaxation tensor in terms of a quadrature with an explicitly known integrand, the integrands in Eqs. (3.106) and (3.107) are not explicitly known. They contain the function $r_\lambda(\omega)$, which is the solution of a scalar differential equation (3.103), which cannot be solved analytically. Sometimes it is however sufficient to treat all scattering processes elastically. Within the elastic approximation, the differential operator $\mathcal{D}^*(\varepsilon)$ is neglected and Eq. (3.103) reduces to an algebraic equation, which is readily solved to yield $r_\lambda(\varepsilon) = \tau_\lambda(\varepsilon)h_\lambda(\varepsilon)$. As a result, the integrand of the quadratures in Eqs. (3.106) and (3.107) is now also explicitly known. In some cases all the integrands can be even obtained analytically. The quadratures can then be performed by saddle point techniques, exploiting the peaked structure of the integrands, and analytical expressions for the EY, DP, and VG spin relaxation tensors can be derived.

The macroscopic spin relaxation tensor contains the EY process and the motional-narrowing (DP and VG) processes. Due to the different angle dependences of the two motional-narrowing spin relaxation processes, Eq. (3.105) [cf. Eq. (3.96)] splits for isotropic semiconductors into two separate terms, $\mathbf{\Gamma}_{\text{DP}}$ and $\mathbf{\Gamma}_{\text{VG}}$. Accordingly, for isotropic semiconductors, a Matthiessen-type rule holds for the total spin relaxation tensor, $\mathbf{\Gamma} = \mathbf{\Gamma}_{\text{EY}} + \mathbf{\Gamma}_{\text{DP}} + \mathbf{\Gamma}_{\text{VG}}$. [11] The quenching of the motional-narrowing processes due to the orbital motion [11,160] is contained in Eq. (3.97) through the term proportional to $\vec{\Omega}_C \cdot \vec{\mathcal{L}}$. The on- and off-shell relaxation rates appearing in Eq. (3.103) are total relaxation rates due to whatever scattering processes are included. A Matthiessen rule holds separately for the on- and off-shell rates. The energy average $\langle(\dots)\rangle_\varepsilon$ is defined in Eq. (3.75). Most importantly, it contains a weight function $p(\varepsilon)$ defined as the solution of Eq. (3.58). This function describes the energy dependence of the quasi-stationary spin polarization which appears on the short time scale because of fast, spin-conserving inelastic scattering processes, i.e. because of energy relaxation and diffusion. Once the quasi-stationary spin polarization is established, it slowly decays on the long time scale set by the spin non-conserving terms in the Fokker-Planck equation.

3.4 Applications

The semiclassical kinetic theory of electron spin relaxation, which we developed in the previous section, is tailor-made for the description of the final stages of spin relaxation, where the spin subsystems are not yet balanced, but each spin subsystem is equilibrated. This stage of the time evolution is optically accessible.

When an n-type doped semiconductor is photoexcited with a short circularly polarized optical pulse tuned to an optical frequency just above the energy gap, electrons and holes are generated. Because of the spin dependent optical selection rules, the photogenerated electrons will be preferentially spin polarized with quantization axis along the optical propagation direction. The holes will rapidly scatter and lose any information concerning their initial quasi-spin variable. Electrons and holes recombine on a time scale that is short compared to electron spin relaxation. After electron-hole recombination has been completed, there will be an electron density equal to the original electron density, prior to photoexcitation, that is preferentially spin polarized with quantization axis along the optical propagation direction. The exact degree of spin polarization depends on the energy of the optical pulse, and is difficult to calibrate precisely. Our formalism is based on a linearization procedure and therefore only applicable if the initial spin polarization is small. Spin-conserving scattering processes establish a quasi-stationary spin polarization ($\rightarrow \delta\vec{S}_{st}$) on a fast time scale ($\rightarrow \tau_i$, $i = f, d, \perp$). The spin decay on the long time scale ($\rightarrow \mathbf{\Gamma}$) can then be probed by polarization sensitive optical transmission, reflection, and emission.

3.4.1 Spin Relaxation in Quantum Well Structures [9]

We consider a quantum well at low enough temperatures, where electron-impurity and electron-electron scattering dominate. We are here particularly interested in the effects of Pauli blocking and inelasticity. For illustration, we focus therefore only on the DP process, which, for small to moderate magnetic fields, is usually the dominant spin relaxation process. Moreover, if the magnetic field is small enough, the time $\hat{\tau}_C$ it takes to complete a cyclotron orbit is much longer than any of the intrinsic scattering times $\hat{\tau}_i$ ($i = f, d, \perp$), and the quenching effect of the magnetic field can be ignored.

We consider a symmetric GaAs quantum well, grown in the [001] direction, which is also the quantization axis for the electron spin. Due to the assumed structural symmetry, there is only bulk inversion asymmetry giving rise to DP spin relaxation. [191] As in the bulk case, we treat the two states at the conduction band minimum explicitly and include a large set of states perturbatively, up to third order, to include the effect of bulk inversion asymmetry. For energies close to the band minimum, the Hamiltonian for the quantum well can be cast into the form (3.1). The spin off-diagonal term in the quantum well Hamiltonian is the bulk spin off-diagonal term averaged over the envelope function of the conduction subband. Assuming for simplicity infinite confinement and restricting the calculation to the lowest conduction subband, we find (neglecting cubic terms in \vec{k})

$$\begin{aligned} \hbar\vec{\Omega}_{IA}^{QW}(\varepsilon, \phi) &= 2\delta_0\sqrt{\varepsilon}\left(\frac{\pi}{L}\right)^2 \begin{pmatrix} -\cos\phi \\ \sin\phi \\ 0 \end{pmatrix} \\ &= \frac{1}{\tau_{IA}(\varepsilon)}\vec{\kappa}_{IA}(\phi), \end{aligned} \quad (3.108)$$

where we have defined a precession rate $1/\tau_{IA}(\varepsilon) = C_{IA}^{QW}\sqrt{\varepsilon}$ with $C_{IA}^{QW} = 2\delta_0(\pi/L)^2$.

Since we are only interested in the DP spin relaxation tensor, we neglect the torque force due to $\vec{\Omega}_g$. Because we furthermore assume small magnetic fields, we also ignore the orbital motion of the electrons. In this particular case, where only one spin relaxation channel is considered, it is not necessary to formally expand $\delta\vec{a}^{(1)}(\varepsilon, \phi, t)$ in terms of the eigenfunctions of Eq. (3.97), specialized to a quantum well. Instead, a simple separation ansatz,

$$\delta\vec{a}^{(1)}(\varepsilon, \phi, t) = r(\varepsilon)\vec{\kappa}_{IA}(\phi) \times \vec{S}^{(0)}(t), \quad (3.109)$$

suffices to decouple Eq. (3.88) and reduce it to the scalar differential equation,

$$[\mathcal{D}^* - \frac{1}{4\tau_{\perp}(\varepsilon)}]r(\varepsilon) + \frac{1}{\tau_{IA}(\varepsilon)} = 0, \quad (3.110)$$

which determines the scalar function $r(\varepsilon)$. Because the differential operator \mathcal{D}^* accounts for inelastic scattering, we have to conclude that even on the long time scale, where the spin polarization decays, inelasticity cannot be ignored. Thus, inelastic scattering processes not only determine the initial condition for the decay stage but they directly affect the time evolution (of the macroscopic spin polarization) in the decay stage. Multiplying Eq. (3.110) from the left by $p(\varepsilon)r(\varepsilon)$, integrating the resulting equation over ε , and using condition (3.84) yields an equivalent differential equation,

$$[\mathcal{D} - \frac{1}{4\tau_{\perp}(\varepsilon)}]p(\varepsilon)r(\varepsilon) + \frac{p(\varepsilon)}{\tau_{IA}(\varepsilon)} = 0, \quad (3.111)$$

which can be also used to determine $r(\varepsilon)$. In Ref. [10], we adopted a less rigorous approach, based on a relaxation time approximation, to calculate spin lifetimes in GaAs quantum wells (and bulk GaAs). Equation (3.111) is useful for a comparison of the multiple time scale approach presented here and the relaxation time approach discussed in Ref. [10]. In Sect. 3.4.2 we discuss this point in more detail.

Inserting Eq. (3.109) into (3.96), ignoring the $\vec{\Omega}_g$ term, and performing the angle and energy averages finally yields for the DP spin relaxation tensor

$$\mathbf{\Gamma}_{\text{DP}} = \frac{1}{\tau_{\text{DP}}} \begin{pmatrix} 1 & 0 & 0 \\ 0 & 1 & 0 \\ 0 & 0 & 2 \end{pmatrix}, \quad (3.112)$$

with the DP spin relaxation rate given by

$$\frac{1}{\tau_{\text{DP}}} = \pi \left\langle \frac{r}{\tau_{IA}} \right\rangle_{\varepsilon}, \quad (3.113)$$

where the energy average is defined in Eq. (3.75). To determine the function $p(\varepsilon)$, we integrate Eq. (3.58), which gives

$$\left[-v(\varepsilon) + \frac{d}{d\varepsilon} w(\varepsilon) \right] p(\varepsilon) = 0, \quad (3.114)$$

where we used again condition (3.84) and introduced the dynamical friction and diffusion coefficients in ε -space, $v(\varepsilon) = \varepsilon/\tau_f(\varepsilon)$ and $w(\varepsilon) = \varepsilon^2/\tau_d(\varepsilon)$, respectively. Integrating once more, we obtain

$$p(\varepsilon) = p(0) e^{\int_0^{\varepsilon} d\varepsilon' \frac{v(\varepsilon') - w'(\varepsilon')}{w(\varepsilon')}}}, \quad (3.115)$$

with $w'(\varepsilon) = dw(\varepsilon)/d\varepsilon$ and a normalization constant $p(0)$, which we fix according to

$$\int_0^{2\pi} d\phi \int_0^{\infty} d\varepsilon p(\varepsilon) = 1. \quad (3.116)$$

Note, because of condition (3.84), the integral in Eq. (3.115) is zero for $\varepsilon \rightarrow 0$. That is, $p(\varepsilon)$ is well-defined for $\varepsilon \rightarrow 0$.

The Bloch equation (3.94) for the macroscopic spin polarization has to be solved with the spin relaxation tensor (3.112) and taking the particular geometry of the experimental set-up into account. Here, we consider the case of Kerr or Faraday rotation experiments, where the small magnetic field, which causes the spin precession, is along the x-axis. The propagation direction of the pump and probe pulses is assumed to be perpendicular to the quantum well plane, i.e., parallel to the z-axis (growth axis). The initial spin polarization is therefore along the z-axis, i.e. $\vec{e} = (0, 0, 1)^T$, and the probe pulse monitors the decay of a spin polarization which precesses in the yz-plane. Note that the spin decay in the yz-plane plane is not isotropic ($\Gamma_{yy} \neq \Gamma_{zz}$). Assuming $\tau_{\text{DP}} \gg 1/\Omega_L$, the solution of the Bloch equation is

$$\delta\vec{S}(t) = \begin{pmatrix} 0 \\ -\sin \Omega_L t \\ \cos \Omega_L t \end{pmatrix} e^{-\Gamma t}, \quad (3.117)$$

where the decay rate of the spin polarization is given by the arithmetic mean of the decay rates in y- and in z-direction: $\Gamma = (\Gamma_{yy} + \Gamma_{zz})/2 = 3/(2\tau_{\text{DP}})$.

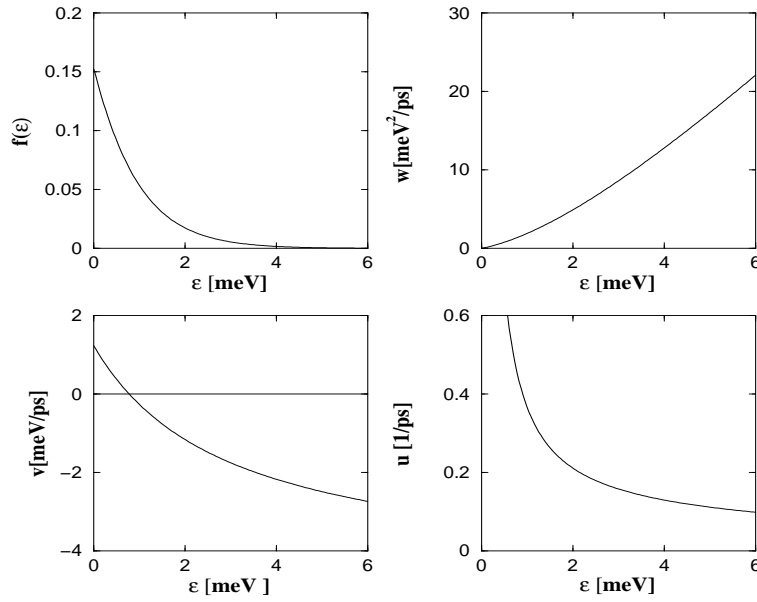


Figure 3.6: Distribution function (for the equilibrated state at $t \rightarrow \infty$), dynamical friction coefficient, dynamical diffusion coefficient, and angle randomization coefficient (anticlockwise, starting from the upper left panel) for a modulation doped quantum well at an electron density $n = 4 \times 10^9 \text{cm}^{-2}$ and $T = 10\text{K}$ (non-degenerate regime, chemical potential $\mu \approx -1.5\text{meV}$). The coefficients are calculated for electron-electron scattering only. For the purpose of the plot we switched back to physical units.

The results presented below are, if not stated otherwise, for a $L = 25\text{nm}$ GaAs quantum well. The parameter needed to specify $\hbar\vec{\Omega}_{IA}^{QW}(\vec{k})$ is $\delta_0 = 0.06\hbar^3/\sqrt{(2m^*)^3\epsilon_g}$. [164] The remaining parameters, such as the effective CB electron mass or the static dielectric constant ϵ_b (needed for the Coulomb matrix element) can be found in standard data bases. [213] Numerically, we first calculate $v(\epsilon) = \epsilon/\tau_f(\epsilon)$, $w(\epsilon) = \epsilon^2/\tau_d(\epsilon)$, which define the differential operator \mathcal{D} , and the on-shell rate $u(\epsilon) = 1/4\tau_{\perp}(\epsilon)$ taking electron-electron and electron-impurity scattering into account (see Appendix). We then determine $p(\epsilon)$ from Eqs. (3.115) and (3.116). Finally, we solve the differential equation (3.111) for $r(\epsilon)$ numerically and obtain the DP relaxation rate $1/\tau_{\text{DP}}$ by numerically integrating Eq. (3.113).

In Figs. 3.6 and 3.7 we show, for $T = 10\text{K}$, the functions $v(\epsilon) = \epsilon/\tau_f(\epsilon)$, $w(\epsilon) = \epsilon^2/\tau_d(\epsilon)$, and $u(\epsilon) = 1/4\tau_{\perp}(\epsilon)$ for a modulation doped quantum well with electron density $n = 4 \times 10^9 \text{cm}^{-2}$ (non-degenerate electrons, chemical potential $\mu \approx -1.5\text{meV}$) and $n = 4 \times 10^{11} \text{cm}^{-2}$ (degenerate electrons, chemical potential $\mu \approx 14.3\text{meV}$), respectively. We take only electron-electron scattering into account, because for a modulation doped quantum well electron-impurity scattering is negligible. The physical content of the functions $v(\epsilon)$ and $w(\epsilon)$ is that of dynamical friction and diffusion coefficients (in ϵ -space) for the “test” spin polarization resulting from the scattering between the spin-polarized “test” electrons and the equilibrated “field” electrons. The function $u(\epsilon)$ denotes the on-shell scattering rate arising from the “test” electron’s elastic scattering off “field” electrons. It randomizes the angle ϕ ; hence $u(\epsilon)$ can be interpreted as an angle randomization coefficient.

In Figs. 3.6 and 3.7 we also show the electron distribution functions which characterize the equilibrated state at $t \rightarrow \infty$. Because of our assumption that only a small portion of the total number of electrons initially contributed to the “test” spin polarization (i.e. $\delta f(\vec{k}, t) \ll f(\vec{k})$), the equilibrium distribution functions $f(\vec{k})$ are used to determine the friction, diffusion, and angle

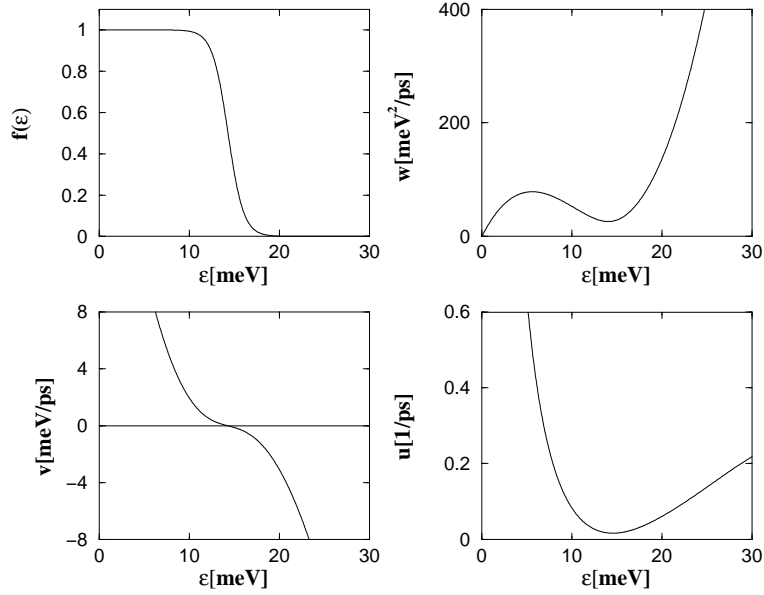


Figure 3.7: Same as in Fig. 3.6, except that the electron density is now $n = 4 \times 10^{11} \text{cm}^{-2}$ (degenerate regime, chemical potential $\mu \approx 14.3 \text{meV}$).

randomization coefficients (see Section 3.3.2 and the Appendix). In other words, we approximated at $t < \infty$ the distributions of the friction and diffusion causing spin-balanced “field” electrons by the distributions of the equilibrated electrons at $t \rightarrow \infty$, despite the fact that at $t < \infty$ of course a small number of electrons is still out of equilibrium and contributes to the finite spin polarization. Obviously, this is only permissible close enough to equilibrium.

Inelastic scattering encoded in $v(\varepsilon) = \varepsilon/\tau_f(\varepsilon)$ and $w(\varepsilon) = \varepsilon^2/\tau_d(\varepsilon)$ gives rise to spin-conserving energy relaxation and diffusion, which in turn yields a quasi-stationary spin polarization $\delta \vec{S}_{st}(\varepsilon, \phi) = p(\varepsilon)\vec{e}$, towards which any initial spin polarization relaxes very quickly without losing spins. The time scale on which this spin-conserving relaxation takes place is set by the relaxation times $\tau_i(\varepsilon)$, $i = f, d, \perp$ which, for fixed temperature and density, can be extracted from plots like the ones shown in Fig. 3.6 and 3.7. Typically, the spin conserving relaxation takes place on the sub-ps timescale. That the spin-conserving part of the Fokker-Planck equation (3.55) has the physically expected stationary solution is guaranteed by the particular form of the functions $v(\varepsilon)$ and $w(\varepsilon)$. This can be most clearly seen in the degenerate case depicted in Fig. 3.7. The dynamical friction $v(\varepsilon)$ changes sign at the chemical potential μ , that is, spin-polarized “test” electrons with an energy above (below) the chemical potential are pushed downwards (upwards) in energy, that is, the “test” electrons feel a drag towards the chemical potential. The dynamical diffusion coefficient on the other hand is always finite for $\varepsilon > 0$, as it should. Its value at the chemical potential essentially reflects the width of the quasi-stationary spin polarization.

In Figure 3.8 we show $p(\varepsilon)$ for $T = 10 \text{K}$ and three densities: $n = 4 \times 10^9 \text{cm}^{-2}$, $n = 4 \times 10^{11} \text{cm}^{-2}$, and $n = 4 \times 10^{12} \text{cm}^{-2}$. In the inset we again depict the corresponding distribution functions for the electrons which characterize the equilibrated state at $t \rightarrow \infty$. At very low densities, where the electrons are non-degenerate, $p(\varepsilon)$ is centered around $\varepsilon = 0$, while at high densities, where the electrons are degenerate, $p(\varepsilon)$ is centered around the Fermi energy for the electrons. Note, however, that $p(\varepsilon)$ describes the spin polarization at $t = 0$ while $f(\varepsilon)$ is the equilibrium distribution of the electrons at $t \rightarrow \infty$.

We now turn to the numerical results for the DP spin lifetime τ_{DP} . Figure 3.9 shows τ_{DP}

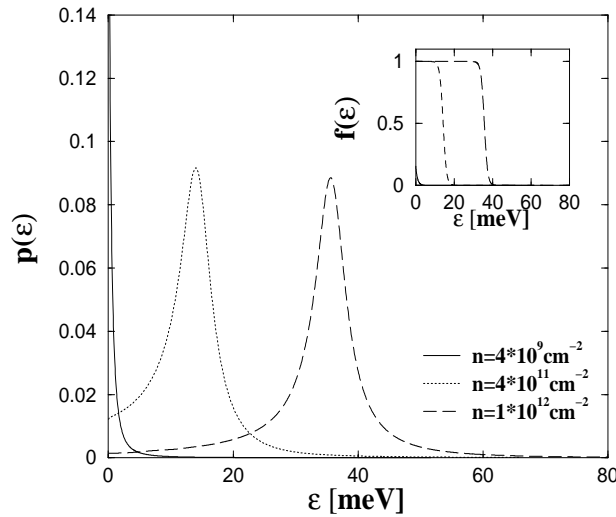


Figure 3.8: Weight function for a modulation doped quantum well at $T = 10\text{K}$ and three electron densities $n = 4 \times 10^9 \text{cm}^{-2}$ (solid line), $n = 4 \times 10^{11} \text{cm}^{-2}$ (dotted line), $n = 10^{12} \text{cm}^{-2}$ (dashed line), taking only electron-electron scattering into account. The inset shows the corresponding electron distribution functions in the equilibrated state at $t \rightarrow \infty$.

as a function of electron density for a modulation doped quantum well at three temperatures $T = 10\text{K}$, 20K , and 30K . Since in a modulation doped quantum well electron-impurity scattering is negligible, we take only electron-electron scattering into account. For fixed temperature, the spin lifetime first increases with electron density, reaches a maximum, and then decreases again. The non-monotonic density dependence of the spin lifetime follows the density dependence of the electron-electron scattering rate. At low densities, the scattering rate is small because of lack of scattering partners, while at high densities the scattering rate is suppressed because of efficient Pauli blocking. At intermediate densities, where the cross-over from non-degenerate to degenerate electrons occurs, the electron-electron scattering rate, and thus the DP spin lifetime, is maximal. The position of the maximum shifts with decreasing temperature to lower densities because the density, where the cross-over from a non-degenerate to a degenerate electron gas takes place, decreases with temperature. The relaxation time of photo-currents in optically pumped semiconductors shows a similar non-monotonic density dependence. [214]

For a fixed electron density, the DP spin lifetime decreases with temperature in the low density regime and increases with temperature in the high density regime. The latter is because of the temperature induced reduction of the Pauli blocking, giving rise to an increasing electron-electron scattering rate and therefore to an increasing DP spin lifetime. In the low density regime, on the other hand, increasing temperature broadens the electron distribution function, i.e. electrons occupy states higher up in the band. The average thermal energy increases therefore and the spin decay occurs preferentially from states higher up in the band, where the torque force induced by the bulk inversion asymmetry is larger. As a consequence, the DP spin lifetime decreases with temperature in the low density regime.

In Fig. 3.9 we also plot experimental data for $T = 10\text{K}$ from Ref. [181]. For electron densities above $n = 5 \times 10^{10} \text{cm}^{-2}$ the agreement between theory and experiment is quite good, given the fact that our calculation is based on an idealized quantum well with infinitely high confinement potential. In this density regime, we expect our results to even underestimate the spin lifetimes, because the model for the electronic structure of the quantum well most probably overestimates

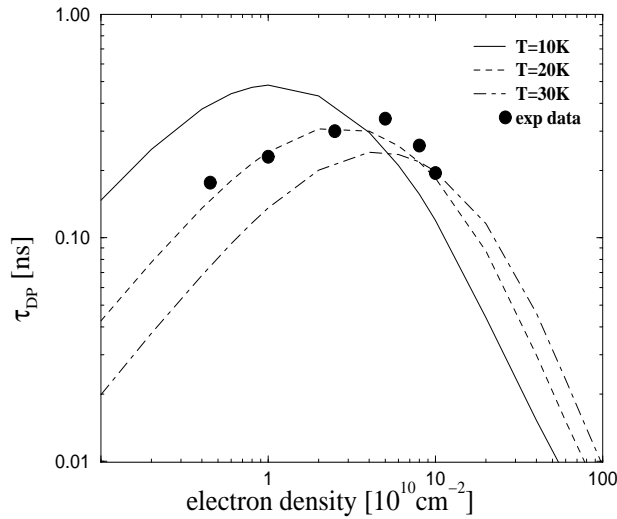


Figure 3.9: D'yakonov-Perel' spin lifetime due to electron-electron scattering for a 25nm modulation doped quantum well as a function of electron density at three temperatures $T = 10\text{K}$, $T = 20\text{K}$, and $T = 30\text{K}$. The solid dots are experimental data at $T = 10\text{K}$ from Ref. [181].

$\hbar\bar{\Omega}_{IA}^{QW}$. Indeed, the constant defining the magnitude of the splitting of the conduction subband $C_{IA}^{QW} \sim (\pi/L)^2 \sim E_1^\infty$, with E_1^∞ the confinement energy of the lowest conduction subband. For a finite confinement potential, E_1 is smaller than $E_1^\infty = \hbar^2\pi^2/2m^*L^2$, giving rise to a smaller splitting and, consequently, to a larger τ_{DP} . To obtain in this density regime better agreement between experimentally measured and theoretically calculated spin lifetimes an improved electronic structure calculation is clearly necessary. At lower densities, on the other hand, electrons are most likely localized to donors (at $T = 10\text{K}$ thermal ionization is negligibly small) and our theory, which is based on a band picture, does not apply.

In quantum wells which are not modulation doped, electron-impurity scattering due to donors and acceptors (in compensated samples) provides an additional, very efficient scattering process. The DP spin lifetime increases with scattering rate. As a result, we expect the spin lifetimes in quantum wells that are not modulation doped to be substantially longer than in modulation doped quantum wells. In compensated samples the density of ionized impurities can be larger than the density of electrons. Within the Born approximation, the transition probability for scattering on positively and negatively charged impurities is the same. Thus, calculating the Born collision integral due to electron-impurity scattering with an impurity sheet density $n_i = xn$ is a simple way to model compensated quantum wells. In Fig. 3.10 we plot the electron density dependence of the DP spin lifetime at $T = 40\text{K}$ for $x = 0$ (modulation doped), $x = 1$ (uncompensated quantum well with equal impurity and electron density), and $x = 4$ (compensated quantum well with impurity (donor and acceptor) density four times the electron density). As expected, the spin lifetimes increase with x for all electron densities. The increase is however not uniform, with the largest increase taking place at high electron densities, where Pauli blocking very effectively suppressed the DP spin lifetime in the modulation doped quantum well. The electron-impurity scattering rate is not affected by Pauli blocking and leads therefore to a substantial enhancement of the DP spin lifetime at high doping levels.

For a fixed density the character of the electron gas also changes with temperature. In particular, increasing temperature pushes the electron gas into the non-degenerate regime. For some temperature, the cross-over from a degenerate to a non-degenerate electron gas occurs,

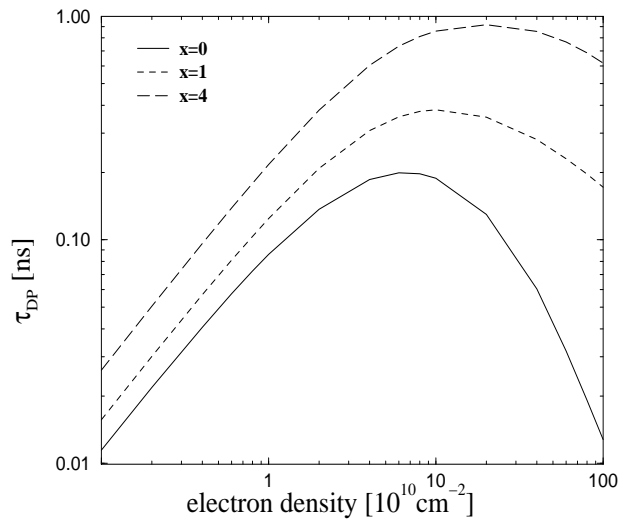


Figure 3.10: D'yakonov-Perel' spin lifetime for a 25nm quantum well at $T = 40\text{K}$ and three values of ionized (donor and acceptor) impurity concentrations: no impurities ($x = 0$), ionized impurity concentration equal to the electron density ($x = 1$), and ionized impurity concentration equal to four times the electron density ($x = 4$). For $x = 0$, only electron-electron scattering contributes to the spin lifetime, whereas for $x \neq 0$ both electron-electron and electron-impurity scattering determine the spin lifetime.

electron-electron scattering is particularly strong, and we expect spin lifetimes to be enhanced. This effect is demonstrated in Fig. 3.11, where we plot for an electron density $n = 3 \times 10^{10}\text{cm}^{-2}$ the temperature dependence of the spin lifetime for $x = 0, 1$, and 4. In the modulation doped case ($x = 0$) the enhancement of the spin lifetime in the temperature range where the cross-over from degenerate to non-degenerate takes place can be most clearly seen. For finite x , the spin lifetimes are for all temperatures longer than for $x = 0$. The enhancement is again not uniform. At high temperatures it is very small. While at low temperatures it is very large, because in that range the Pauli blocking leads to a strong suppression of the DP spin relaxation rate in modulation doped quantum wells. In fact, the spin lifetimes at low temperatures saturate by a value set by the electron-impurity scattering rate. The maximum in the spin lifetime is therefore less pronounced (or even disappears completely) in quantum wells that are not modulation doped.

In Fig. 3.12 we finally compare for a 10nm GaAs quantum well with an electron density $n = 1.86 \times 10^{11}\text{cm}^{-2}$ the theoretically obtained temperature dependence of the D'yakonov-Perel' spin lifetimes for $x = 0$ and $x = 1$ with the experimentally measured temperature dependence of the D'yakonov-Perel' spin lifetime. [183] The agreement between the experimental data points and the theoretical results for $x = 0$ is quite reasonable, suggesting that electron-electron scattering is the main source of electron spin relaxation in these samples. The remaining discrepancy between the theoretical and experimental results is most probably because of the idealistic quantum well model on which our calculation is based. The description of scattering processes within the diffusion approximation is less critical in our opinion because a calculation based on the full collision integral deviates the same order of magnitude from the experimental data. [198] We expect therefore that a more accurate description of the electronic structure of the quantum well is required to achieve better agreement between experiment and theory.

The experimental results seem to suggest that, for this particular electron density and experimental set-up, the D'yakonov-Perel' spin lifetime τ_{DP} grows monotonically with temperature, in contrast to the theoretically predicted non-monotonic behavior with a maximum at $T=100\text{K}$. The

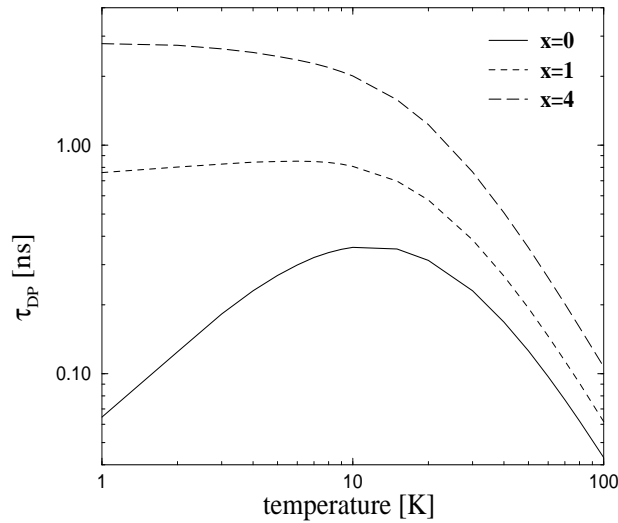


Figure 3.11: D'yakonov-Perel' spin lifetime for a 25nm quantum well as a function of temperature at an electron density $n = 3 \times 10^{10} \text{cm}^{-2}$ and three values of ionized (donor and acceptor) impurity concentrations: no impurities ($x = 0$), ionized impurity concentration equal to the electron density ($x = 1$), and ionized impurity concentration equal to four times the electron density ($x = 4$). As in Fig. 3.10, for $x = 0$, only electron-electron scattering contributes to the spin lifetime, whereas for $x \neq 0$ both electron-electron and electron-impurity scattering determine the spin lifetime.

apparent inconsistency is perhaps due to the neglect of phonons in the theoretical modeling. The maximum of τ_{DP} is a consequence of electron-electron scattering. Additional scattering processes destroy the maximum. For instance, electron-impurity scattering increases the spin lifetimes at low temperatures, resulting in a more or less monotonically decreasing spin lifetime ($x = 1$ curve in Fig. 3.12). The samples in Ref. [183] are high-quality quantum wells, where electron-impurity scattering is negligible. The electron density $n = 1.86 \times 10^{11} \text{cm}^{-2}$ is however rather high. As a result, the temperature, at which τ_{DP} is expected to be maximal, falls in a temperature range, where electron-phonon scattering cannot be ignored. In fact, we expect a calculation, which takes electron-electron and electron-phonon scattering into account, to produce a monotonically increasing τ_{DP} , as experimentally observed. At temperatures below 100K, we expect phonons to be frozen out and not much to change, that is, electron-electron scattering would dominate and τ_{DP} would be short because of the Pauli-blocking of electron-electron scattering. With increasing temperature we expect τ_{DP} to first increase because of a weakening of the Pauli-blocking. Then, at temperatures around and above 100K, that is, in the temperature range where we expect electron-electron scattering alone to produce a maximal τ_{DP} , electron-phonon scattering would gradually take over. Because the electron-phonon scattering rate would increase with temperature, we expect τ_{DP} to grow continuously. As a result, τ_{DP} would be a monotonically growing function of temperature in accordance with the experimental finding.

In this subsection we illustrated our semiclassical kinetic theory of spin relaxation by calculating the DP spin lifetime for an (idealized) quantum well, at temperatures and electron densities, where electron-electron and electron-impurity scattering dominate. Electron-electron scattering has been chosen to illustrate the effects of inelasticity and Pauli blocking. Electron spin lifetimes due to electron-electron scattering have been also calculated in Refs. [195, 197, 198, 215], using however different approaches and focusing mostly on different aspects. In particular, the non-monotonous temperature and density dependence has not been addressed until quite recently. [9, 10, 198] In modulation doped quantum wells, spin lifetimes turn out to be particularly

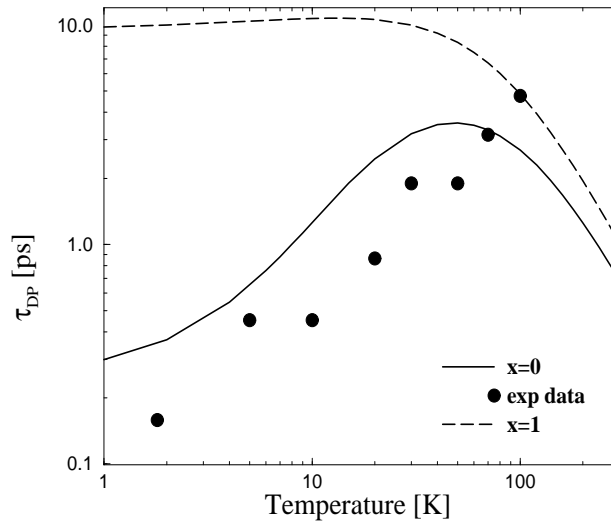


Figure 3.12: D'yakonov-Perel' spin lifetime for a 10nm GaAs quantum well as a function of temperature at an electron density $n = 1.86 \times 10^{11} \text{cm}^{-2}$. The solid and dashed lines are for $x = 0$ (no ionized impurities) and $x = 1$ (ionized impurity concentration equal to the electron density). The solid dots are experimental data form Ref. [183].

long for electron densities and temperatures, where the cross-over from the non-degenerate to degenerate regime occurs. In this regime, many-body effects beyond the Born approximation are most probably important and should be included in a more quantitative calculation of the spin relaxation times. We expect however our main conclusions to be independent of the particular modeling of the Coulomb interaction.

3.4.2 Spin Relaxation in Bulk Semiconductors [10, 11]

As a further illustration of our approach, we discuss in this subsection the magnetic field dependence of the spin relaxation rates in bulk GaAs. This was historically our first application of the Fokker-Planck equation for the non-equilibrium spin polarization in non-magnetic semiconductors. [11] To separate fast, spin-conserving from slow, spin non-conserving processes we did not yet employ the multiple time analysis. Instead, we used a relaxation time approximation, which is conceptually simpler, but requires a number of ad-hoc assumptions. Although the multiple time scale approach is more general and rigorous, the final expressions for the spin relaxation tensors are quite similar to the ones obtained from the relaxation time approximation (see below). The main difference is that the weight function $p(\varepsilon)$ defining the energy quadratures cannot be calculated within the relaxation time approximation, but has to be chosen by physical considerations. A plausible choice is to take $p(\varepsilon) \sim -N(\varepsilon)\partial_\varepsilon f(\varepsilon)$, with $N(\varepsilon)$ the density of states, and normalize it accordingly. The numerical results presented in this subsection were obtained with this particular weight function. [10, 11]

Because the numerical results are based on the relaxation time approximation, a short detour, describing the derivation of the spin relaxation tensors within the relaxation time approximation, is in order. In the spirit of Ref. [159], we employ a (regular) perturbative approach which treats all terms due to inversion asymmetry as small. We consider the torque forces due to $\vec{\Omega}_{IA}$ and $\vec{\Omega}_g$, respectively, as $O(1)$ terms, and the term involving the spin-flip tensor \mathbf{R} as an $O(2)$ term. Results are valid for $|\vec{\Omega}_{IA} + \vec{\Omega}_g|\tau_* < 1$ and $|\mathbf{R}|\tau_* < 1$, where τ_* denotes a representative value of any one of the scattering times τ_i ($i = f, d, \perp$) and $|\cdot|$ is a vector or tensor norm.

The starting point of the relaxation time approximation is a product ansatz for the non-equilibrium spin polarization,

$$\delta\vec{S}(\varepsilon, \omega, t) = p(\varepsilon)\vec{\Psi}(\varepsilon, \omega, t), \quad (3.118)$$

where the function $p(\varepsilon)$ is normalized according to $\int d\varepsilon d\omega p(\varepsilon) = 1$. At the end of the derivation we shall see that the function $p(\varepsilon)$ defines a weighted energy average as in the case of the multiple time scale approach. To construct a relaxation time approximation on the scale of the spin relaxation time τ_s , we write

$$\vec{\Psi}(\varepsilon, \omega, t) = \vec{\Psi}^{(0)}(t) + \vec{\Psi}^{(1)}(\varepsilon, \omega, t), \quad (3.119)$$

and require that, on the time scale τ_s , $\langle \vec{\psi}^{(1)} \rangle_\omega = 0$, with $\langle (\dots) \rangle_\omega = \int d\omega (\dots)$ the average over all angles, and $\partial_t \vec{\psi}^{(1)}(\varepsilon, \omega, t) \simeq 0$. From the first constraint and the normalization condition for $p(\varepsilon)$ follows that $\vec{\Psi}^{(0)}$ is equal to the macroscopic non-equilibrium spin polarization (recall that we absorbed the factor $J(\varepsilon)/(2\pi)^d n_s$ in the definition of $\delta\vec{S}$). Moreover it enforces that $p(\varepsilon)$ approximately describes the energy dependence of the angle averaged non-equilibrium spin polarization on the time scale τ_s . The second constraint imposes, again on the time scale τ_s , quasi-stationarity for the fluctuations around the total non-equilibrium spin polarization.

Although both constraints are plausible, because of physical considerations, they cannot be justified mathematically within the relaxation time approach because it is strictly speaking based on regular perturbation theory. In particular the second constraint, involving the rate of change of the function $\vec{\psi}^{(1)}(\varepsilon, \omega, t)$, is beyond regular perturbation theory. To justify the constraint requires a multiple time scale perturbation theory.

Inserting Eqs. (3.118) and (3.119) into the Fokker-Planck equation (3.55), imposing the two constraints, and collecting terms through second order, we obtain a set of two coupled equations which govern the time evolution of the total non-equilibrium spin polarization on the time scale τ_s : (we suppress the arguments of the various functions):

$$\partial_t \delta\vec{S} = \vec{\Omega}_L \times \delta\vec{S} - \langle \mathbf{R} \rangle_{\varepsilon, \omega} \delta\vec{S} + \langle (\vec{\Omega}_{IA} + \vec{\Omega}_g) \times \vec{\Psi}^{(1)} \rangle_{\varepsilon, \omega}, \quad (3.120)$$

$$\left(\mathcal{D} - \frac{1}{4\tau_\perp} \mathcal{L}^2 + i\vec{\Omega}_C \cdot \vec{\mathcal{L}} + \vec{\Omega}_L \times \right) p \vec{\Psi}^{(1)} + (\vec{\Omega}_{IA} + \vec{\Omega}_g) \times p \delta\vec{S} = 0. \quad (3.121)$$

Here we defined an weighted average $\langle (\dots) \rangle_{\varepsilon, \omega} = \int d\varepsilon d\omega p(\varepsilon) (\dots)$, in which $p(\varepsilon)$ enters as an energy weight function. Equations (3.120) and (3.121) should be contrasted with Eqs. (3.94) and (3.88), respectively, obtained within the multiple time scale approach.

Except of the Larmor term, the structure of Eq. (3.121) is the same as the structure of Eq. (3.88). Thus, it can be decoupled with the same techniques, that is, by an expansion in terms of the solutions $Y_\lambda(\omega)$ of the eigenvalue problem (3.97). The Larmor term in Eq. (3.121) is a consequence of the insufficiency of the smallness parameter “inversion asymmetry”. The torque forces due to $\vec{\Omega}_{IA}$ and $\vec{\Omega}_g$ are classified as $O(1)$ terms. The torque force due to $\vec{\Omega}_L$ on the other hand is not small with respect to “inversion asymmetry”. Hence it is classified as an $O(0)$ term and appears in Eq. (3.121). Had we classified the Larmor terms as $O(1)$, it would be absent in Eq. (3.121). For bulk GaAs it turns out that $|\vec{\Omega}_L| \tau_l \ll 1$. Thus, the Larmor term is small, but for reasons which are beyond a classification scheme based on inversion asymmetry.

Due to the Larmor term the decoupling of Eq. (3.121) is somewhat more involved than the decoupling of Eq. (3.88). We describe here the procedure for bulk in some detail. The calculation for a quantum well is analogous. In bulk, we can introduce for each momentum channel (l, m)

a diagonal matrix $\mathbf{T}_{l,m}(\varepsilon)$, which relates the (l, m) component of $\vec{\Psi}^{(1)}$ to the (l, m) component of the vector $(\vec{\Omega}_{IA} + \vec{\Omega}_g) \times \delta\vec{S}(t)$. The elements of $\mathbf{T}_{l,m}(\varepsilon)$ satisfy then decoupled differential equations. Note, without the Larmor term, $\mathbf{T}_{l,m}(\varepsilon)$ would be proportional to the unit matrix.

To decouple Eq. (3.121) we again separate the energy and angle dependences of the vectors $\vec{\Omega}_{IA}$ and $\vec{\Omega}_g$ and expand the angle dependences in terms of spherical harmonics. In addition to the cross products involving the vectors $\vec{\Omega}_{IA}$ and $\vec{\Omega}_g$, which we again express in terms of the matrices \mathbf{C}_{lm} and \mathbf{D}_{lm} containing the expansion coefficients C_{lm}^i and D_{lm}^i , respectively, we now also have to rewrite the cross product due to $\vec{\Omega}_L$ in terms of a matrix. Assuming a magnetic field along the z-axis, we find

$$\begin{aligned} \vec{\Omega}_L \times \vec{\Psi}^{(1)}(\varepsilon, \omega, t) &= \begin{pmatrix} 0 & -\Omega_L & 0 \\ \Omega_L & 0 & 0 \\ 0 & 0 & 0 \end{pmatrix} \vec{\Psi}^{(1)}(\varepsilon, \omega, t) \\ &\equiv \mathbf{\Omega}_L \vec{\Psi}^{(1)}(\varepsilon, \omega, t), \end{aligned} \quad (3.122)$$

with $\Omega_L = \mu_B g^* B / \tilde{R}_0$ the Larmor energy measured in units of \tilde{R}_0 . For this particular choice of magnetic field, the orbital motion term becomes $i\tilde{\Omega}_C \cdot \tilde{\mathcal{L}} = i\Omega_C \mathcal{L}_z$ with $\Omega_C = eB/\tilde{R}_0 m^* c$ the cyclotron energy measured in units of \tilde{R}_0 . With the above definitions, the solution of Eq. (3.121) can be expressed as

$$\vec{\Psi}^{(1)}(\varepsilon, \phi, \theta, t) = \sum_{lm} \mathbf{U}^\dagger \mathbf{T}_{l,m}(\varepsilon) \mathbf{U} [\mathbf{C}_{lm}(\phi, \theta) + \mathbf{D}_{lm}(\phi, \theta)] \delta\vec{S}(t) Y_{lm}(\phi, \theta), \quad (3.123)$$

where \mathbf{U} is the unitary matrix that diagonalizes the matrix $\mathbf{\Omega}_L$, and $\mathbf{T}_{l,m}(\varepsilon)$ is a diagonal matrix whose elements, $r_{lm}^\nu(\varepsilon)$, are the solution of the differential equation ($\nu = 1, 2$, and 3)

$$[\mathcal{D}(\varepsilon) + i(m\Omega_C + \Omega_L^\nu) - \frac{1}{\tau_l(\varepsilon)}] p(\varepsilon) r_{lm}^\nu(\varepsilon) + h_l(\varepsilon) p(\varepsilon) = 0, \quad (3.124)$$

with $1/\tau_l(\varepsilon) = l(l+1)/4\tau_\perp(\varepsilon)$, $\Omega_L^\nu = \Omega_L(\delta_{\nu 1} - \delta_{\nu 2})$, $h_l(\varepsilon) = (1/\tau_{IA}(\varepsilon))\delta_{l3} + (1/\tau_g(\varepsilon))(\delta_{l2} + \delta_{l0})$. Note, except of the Larmor term, Eq. (3.124) has the same structure as Eq. (3.104).

Using (3.123) in (3.120) and performing the average over ω and ε in the third term on the right hand side, we finally obtain a Bloch equation for the total non-equilibrium spin polarization,

$$\partial_t \delta\vec{S}(t) = \vec{\Omega}_L \times \delta\vec{S}(t) - \mathbf{\Gamma} \delta\vec{S}(t), \quad (3.125)$$

where the total spin relaxation tensor is given by $\mathbf{\Gamma} = \mathbf{\Gamma}_{EY} + \mathbf{\Gamma}_{DP} + \mathbf{\Gamma}_{VG}$, with

$$\mathbf{\Gamma}_{EY} = \langle \mathbf{R} \rangle_{\varepsilon, \omega}, \quad (3.126)$$

$$\mathbf{\Gamma}_{DP} = - \sum_{lm} \mathbf{C}_{lm} \mathbf{U}^\dagger \langle h_l(\varepsilon) \mathbf{T}_{l,-m}(\varepsilon) \rangle_\varepsilon \mathbf{U} \mathbf{C}_{l,-m}, \quad (3.127)$$

$$\mathbf{\Gamma}_{VG} = - \sum_{lm} \mathbf{D}_{lm} \mathbf{U}^\dagger \langle h_l(\varepsilon) \mathbf{T}_{l,-m}(\varepsilon) \rangle_\varepsilon \mathbf{U} \mathbf{D}_{l,-m} \quad (3.128)$$

the contributions due to the EY, the DP, and the VG processes, respectively. To perform the angle average we used the orthonormality of the spherical harmonics. Equations (3.126), (3.127), and (3.128) should be contrasted with Eqs. (3.95), (3.106), and (3.107) derived in the previous subsection within the multiple time scale approach. Obviously, the structure of the two sets of

equations is similar. The main differences are that $\mathbf{T}_{l,m}$ is a diagonal matrix and not proportional to the unit matrix and that the weight function $p(\varepsilon)$ defining the energy averages is unspecified. The relaxation time approximation does not provide an equation to determine $p(\varepsilon)$.

For bulk, the diagonal elements of the total spin relaxation tensor $\mathbf{\Gamma}$ are the longitudinal ($1/T_1 = \Gamma^{zz}$) and the transverse spin relaxation rates (magnetic field along the z -axis). From Eqs. (3.126)–(3.128) we explicitly obtain ($i = 1, 2$)

$$\frac{1}{T_i} = \frac{1}{T_i^{\text{EY}}} + \frac{1}{T_i^{\text{DP}}} + \frac{1}{T_i^{\text{VG}}}, \quad (3.129)$$

with the EY contributions

$$\frac{1}{T_1^{\text{EY}}} = \frac{2}{T_2^{\text{EY}}} = \frac{32\pi}{3} C_{sf}^2 \left\langle \frac{\varepsilon^2}{\tau_1(\varepsilon)} \right\rangle_{\varepsilon}, \quad (3.130)$$

the DP contributions

$$\frac{1}{T_1^{\text{DP}}} = 4|C_{31}^y|^2 \tilde{\tau}_{31}^3 + 4|C_{33}^y|^2 \tilde{\tau}_{33}^3, \quad (3.131)$$

$$\frac{1}{T_2^{\text{DP}}} = 2|C_{32}^z|^2 \tilde{\tau}_{32}^3 + 2|C_{31}^y|^2 \tilde{\tau}_{31}^3 + 2|C_{33}^y|^2 \tilde{\tau}_{33}^3, \quad (3.132)$$

and the VG contributions

$$\frac{1}{T_1^{\text{VG}}} = 4|D_{21}^y|^2 \tilde{\tau}_{21}^1, \quad (3.133)$$

$$\frac{1}{T_2^{\text{VG}}} = |D_{00}^z|^2 \tilde{\tau}_{00}^1 + |D_{20}^z|^2 \tilde{\tau}_{20}^1 + 2|D_{21}^y|^2 \tilde{\tau}_{21}^3, \quad (3.134)$$

where we defined

$$\tilde{\tau}_{lm}^{\nu} = \text{Re} \left\langle h_l(\varepsilon) r_{lm}^{\nu}(\varepsilon) \right\rangle_{\varepsilon}, \quad (3.135)$$

which in the elastic approximation, which neglects the differential operator $\mathcal{D}(\varepsilon)$ in Eq. (3.124) reduces to

$$\tilde{\tau}_{lm}^{\nu} = \left\langle \frac{\tau_l(\varepsilon) \left[C_{IA}^2 \varepsilon^3 \delta_{l3} + C_g^2(B) \varepsilon^2 (\delta_{l2} + \delta_{l0}) \right]}{1 + [(m\Omega_C + \Omega_L^{\nu}) \tau_l(\varepsilon)]^2} \right\rangle_{\varepsilon}. \quad (3.136)$$

Similar to the multiple time scale approach, the relaxation time approximation reduces the calculation of the spin relaxation tensor (rates) to the calculation of weighted energy averages. The weight function $p(\varepsilon)$, introduced through the product ansatz (3.118), cannot be calculated within the relaxation time approximation. This is in contrast to the multiple time scale approach, where $p(\varepsilon)$ is the solution of $\mathcal{D}(\varepsilon)p(\varepsilon) = 0$ with an appropriate normalization. The constraints imposed on the product ansatz suggest, however, that $p(\varepsilon)$ describes the energy dependence of the angle averaged non-equilibrium spin polarization in the final stages of the spin evolution, where each spin subsystem is almost equilibrated. It is therefore plausible to assume $p(\varepsilon) \sim -N(\varepsilon)\partial_{\varepsilon}f(\varepsilon)$, where $N(\varepsilon)$ is the density of states and $f(\varepsilon)$ is the distribution function of the equilibrated electrons at $t \rightarrow \infty$. Recalling $J(\varepsilon) \sim N(\varepsilon)$ and normalizing $p(\varepsilon)$, we specifically write (for bulk)

$$p(\varepsilon) = \frac{-\partial_{\varepsilon}f(\varepsilon)\sqrt{\varepsilon}}{4\pi \int d\varepsilon (-\partial_{\varepsilon}f(\varepsilon))\sqrt{\varepsilon}}. \quad (3.137)$$

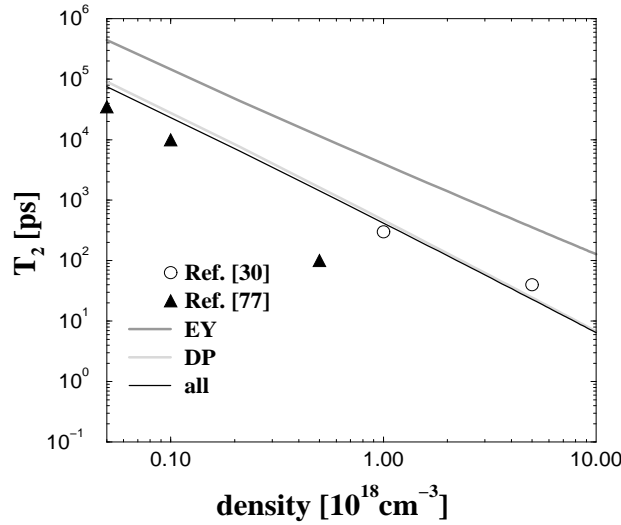


Figure 3.13: Calculated transverse spin relaxation time for electrons in GaAs at low temperatures as a function of electron density. The Elliott-Yafet, D'yakonov-Perel', and total spin relaxation times are shown. Data labeled with dots are from Ref. [169] and data labeled with triangles are from Ref. [216].

The numerical data presented below were obtained for this particular $p(\varepsilon)$.

The expressions for the spin relaxation rates one would obtain from Eq. (3.95), (3.106), and (3.107) are essentially identical to Eqs. (3.130) – (3.134). The “wrong classification” of the Larmor term within the relaxation time approximation is, at least for GaAs, irrelevant because $\Omega_L \tau_l \ll 1$. Thus, the denominator in Eq. (3.136) reduces to $1 + [m\Omega_C \tau_l(\varepsilon)]^2$ and $\tilde{\tau}_{lm}^1 = \tilde{\tau}_{lm}^2 = \tilde{\tau}_{lm}^3 = \tilde{\tau}_{lm}$. As a result, $\mathbf{T}_{l,m}$ is de facto diagonal as in the multiple time scale approach. The only difference is then that within the relaxation time approximation $p(\varepsilon)$ is given by Eq. (3.137) and not as the appropriately normalized solution of $\mathcal{D}(\varepsilon)p(\varepsilon) = 0$. Because the rigorously obtained $p(\varepsilon)$ is qualitatively very close to the ad-hoc choice (3.137), the numerical results obtained within either approach are practically identical.

For the calculation of the spin relaxation rates presented in this subsection we specifically included scattering on ionized impurities, acoustic phonons, and optical (LO) phonons. Electron-electron scattering is negligible in the considered temperature and density ranges. We are primarily interested in the magnetic field dependence of the spin relaxation rates which, at least qualitatively, does not depend on the approximation adopted to describe the scattering processes. For simplicity we adopted therefore the elastic approximation, that is, $\tilde{\tau}_{lm}^\nu$ is given by Eq. (3.136). The energy averages were calculated with saddle-point techniques, exploiting the peaked structure of the integrands at low and high temperatures. The parameters needed to specify $\vec{\Omega}_g(\vec{k})$ have been previously obtained, partly experimentally by measuring combined cyclotron resonances (a_4, a_6) and partly theoretically within a five-level Kane model (a_5): $(a_4, a_5, a_6) = (97, -8, 49) \times 10^{-24} \text{eVcm}^2 \text{Oe}^{-1}$. [205] The parameter defining $\vec{\Omega}_{IA}(\vec{k})$ is given by $\delta_0 = 0.06 \hbar^3 / \sqrt{(2m^*)^3 \epsilon_g}$. [164] The remaining parameters, such as the effective CB electron mass or the deformation potential, are available from standard data bases [213].

Figure 3.13 shows the results of a calculation of the T_2 lifetime at low temperature as a function of density for electrons in bulk GaAs. The scattering is dominated by charged impurity (donor) scattering and the density of charged donors is taken to be the same as the electron density (i.e., that the materials are uncompensated). The contribution to spin lifetime from the EY process, DP process and the total lifetimes are shown. The DP process dominates the spin

relaxation at all densities. The spin relaxation time is a strongly decreasing function of density. The spin polarization arises from electrons on the Fermi surface. As the density increases the Fermi surface rises higher in the conduction band. Both the band splitting, due to the inversion asymmetric component of the crystal potential, which is responsible for the DP spin relaxation process and the admixture of bonding p-states into the conduction band wave functions, which is responsible for the EY spin relaxation process, increase for states higher in the conduction band. Therefore both the DP and EY spin relaxation rates increase as the Fermi energy increases. Also shown on Fig. 3.13 are measured T_2 lifetimes for GaAs from Ref. [169, 216] at low temperature and degenerate electron densities. The calculated results are in reasonably good agreement with the measurements. There are no adjustable parameters in the calculation. To the low density data of Ref. [169] (not shown in Fig. 3.13) our theory, which is based on a band description of the electronic states, is not applicable because, under the conditions of the experiment, electrons are most probably bound to the donors.

A small magnetic field (< 1 Tesla) was applied to the samples in the experimental results reproduced in Fig. 3.13, in order to distinguish longitudinal and transverse relaxation times. This field is not large enough to significantly influence the spin dynamics, except, of course, for the precession of the spin polarization about the magnetic field. That is, in this range of magnetic fields the longitudinal and transverse relaxation times do not change with magnetic field. For larger magnetic fields the relaxation rates themselves become functions of the field. The Fokker-Planck equation (3.55) for the spin polarization contains terms describing the EY [term containing $\mathbf{R}(\vec{k})$] and DP [term containing $\vec{\Omega}_{IA}(\vec{k})$] spin relaxation processes and a term which describes spin precession about an applied magnetic field (term containing $\vec{\Omega}_L$). There are two additional terms that depend on magnetic field; one that describes the orbital motion of the conduction band electrons in the magnetic field (term containing $\vec{\Omega}_C$) and a term that describes the change in electron g -factor for states away from the zone center [term containing $\vec{\Omega}_g(\vec{k})$]. The EY spin relaxation process arises due to spin-flip scattering events and is not significantly influenced by a magnetic field. By contrast the DP spin relaxation process originates from an interplay of spin conserving wave vector scattering events described by the operator $\mathcal{D} - (1/4\tau_{\perp})\mathcal{L}^2$ and the torque forces due to $\vec{\Omega}_{IA}$. The cyclotron orbital motion described by $-i\Omega_C \cdot \mathcal{L}_z$ leads to a quenching of the DP process similar to that from wave vector scattering events because the axis of the torque force depends on wave vector and that axis is changed by the cyclotron orbital motion. [160] The wave vector dependence of the conduction band electron g -factor opens an additional spin relaxation process which tends to reduce the spin lifetimes in applied magnetic fields. [161] As a result of the variations in the g -factor, electrons with different wave vectors precess about a transverse magnetic field at different rates and thus lose spin coherence. We refer to this process as a variable g -factor (VG) mechanism. The VG mechanism primarily effects the T_2 lifetime. [11]

In Fig. 3.14 we show calculated longitudinal (T_1) and transverse (T_2) spin relaxation times for GaAs as a function of magnetic field at low temperature and an electron density of $n = 10^{18} \text{cm}^{-3}$. [11] We show separately the contributions to the spin relaxation times from the EY, DP and VG processes and the total spin relaxation time including all three processes. In the insets of Fig. 3.14 we give the total spin relaxation time for various electron densities at low temperature. For the temperature and density conditions in Fig. 3.14 the electrons are degenerate and electron-ionized impurity scattering dominates. The VG process makes a small contribution to T_1 which is dominated by the DP process at zero magnetic field. As the magnetic field is increased, the DP process is quenched. Thus, T_1 increases monotonically with increasing magnetic field saturating at high field at a value determined by the EY process which is not affected by the magnetic field. If the material parameters had been such that the EY process dominated the DP process for T_1

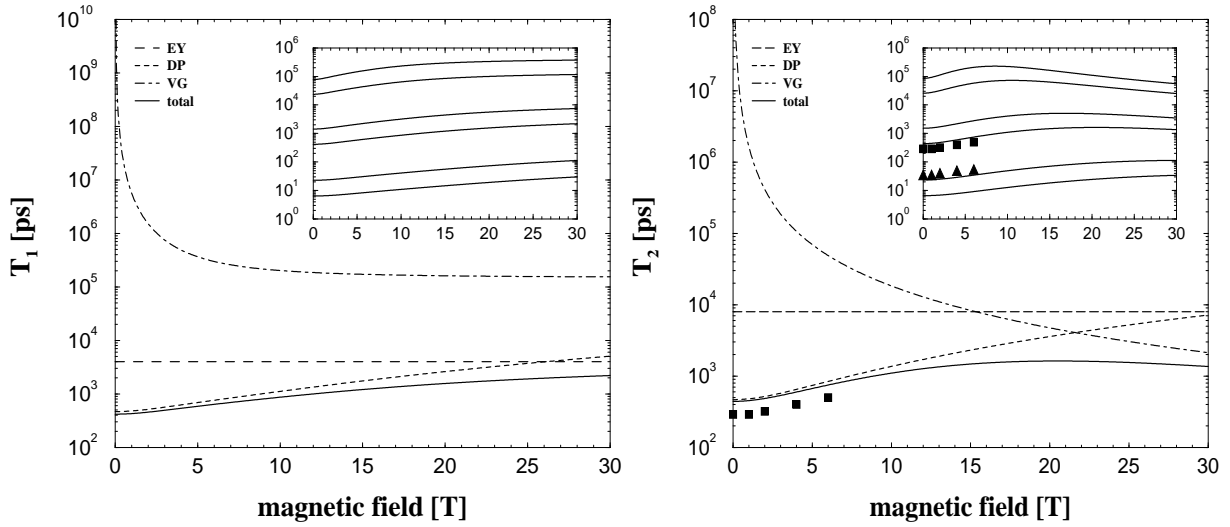


Figure 3.14: The left and right panels show, respectively, the longitudinal (T_1) and transverse (T_2) spin relaxation time in GaAs as a function of magnetic field for $T = 0$ and $n = 10^{18}\text{cm}^{-3}$. The contributions from the EY (long dash), DP (short dash) and VG (dot-dash) processes and the total relaxation time (solid) are shown in the main panels. The insets (same axis as the main panel) show the total relaxation times for $n = 5 \times 10^{16}\text{cm}^{-3}$, $1 \times 10^{17}\text{cm}^{-3}$, $5 \times 10^{17}\text{cm}^{-3}$, $1 \times 10^{18}\text{cm}^{-3}$, $5 \times 10^{18}\text{cm}^{-3}$, and $1 \times 10^{19}\text{cm}^{-3}$ (top to bottom). The squares and triangles are experimental data from Ref. [169] at the respective densities.

relaxation at zero magnetic field, T_1 relaxation would not be significantly affected by the applied field. By contrast the VG process makes a significant contribution to T_2 relaxation. At small applied magnetic fields the T_2 lifetime increases with increasing magnetic field, but as the field continues to increase the VG process begins to dominate the relaxation so that T_2 has a maximum around ~ 21 Tesla and begins to decrease for larger magnetic fields. If the material parameters had been such that the EY process dominated the DP process for T_2 relaxation at zero magnetic field, the T_2 relaxation would monotonically decrease with increasing magnetic field. The solid squares and triangles in the lower panel of Fig. 3.14 are measured T_2 spin lifetimes in GaAs at 5K from Ref. [169] at electron densities of 10^{18}cm^{-3} and $5 \times 10^{18}\text{cm}^{-3}$. There is reasonably good agreement between the calculation and measured results. There were no adjustable parameters in the calculation. The magnetic fields in Ref. [169] are not high enough to completely capture the effects due to the VG process.

The calculations in Fig. 3.14 assume uncompensated samples so that the ionized donor concentration is the same as the electron density. The scattering rate in these calculations is dominated by electron-ionized impurity scattering and this scattering rate depends on the impurity concentration. If compensated samples are considered, the density of ionized scattering centers could be increased for a fixed electron density. Within the Born approximation, the cross section for electron scattering from positively charged donors and negatively charged acceptors is the same. In Fig. 3.14, the DP process dominates the EY process at zero magnetic field. The spin relaxation rate due to the DP process decreases with increased scattering rate whereas the spin relaxation rate due to the EY process increases with increasing scattering rate. For compensated samples, the scattering rate should increase and the spin relaxation rate due to the DP process should decrease whereas the spin relaxation rate due to the EY process should increase with increasing compensation. At some level of compensation the DP and EY rates should cross. In Fig. 3.15, we show calculated transverse (T_2) spin relaxation times for GaAs as a function of magnetic field at low temperature and an electron density of $n = 10^{18}\text{cm}^{-3}$ for various compensation levels.

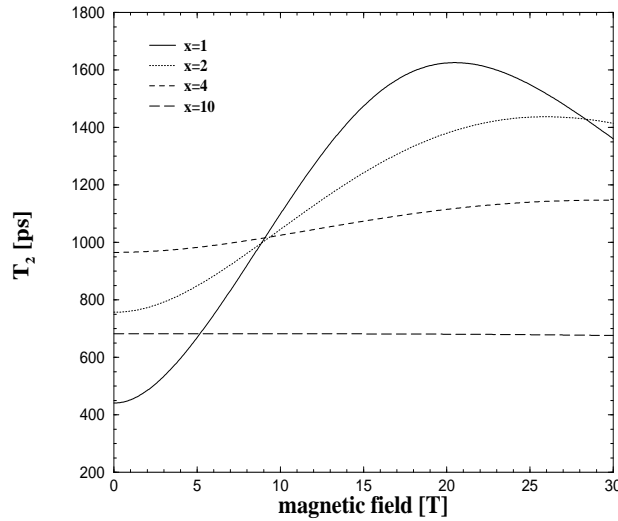


Figure 3.15: Calculated transverse spin lifetime for GaAs as a function of magnetic field for $T = 0$, $n = 10^{18} \text{cm}^{-3}$, and for various degrees of compensation. The compensation is characterized by x , the ratio of donor plus acceptor impurity concentration divided by the electron density.

The concentration of impurity scattering centers (donors plus acceptors) divided by the electron density is labelled by x . For the uncompensated case ($x = 1$), the DP process dominates at zero field and the spin relaxation time first increases with increasing magnetic field, peaks and then decreases as the VG process takes over. For more heavily compensated samples ($x > 2$), the EY process dominates at zero field and the spin relaxation time is insensitive to field.

In Fig. 3.16, we show the various contributions to the T_1 and T_2 spin relaxation for GaAs as a function of magnetic field at $T = 100\text{K}$ and an electron density of $n = 10^{17} \text{cm}^{-3}$. [11] The insets depict the total spin relaxation time as a function of magnetic field for various temperatures at $n = 10^{17} \text{cm}^{-3}$. For the temperature and density conditions in Fig. 3.16, the electrons are non-degenerate and electron-LO-phonon scattering is the dominant scattering process. As for the degenerate electron case, the VG process makes a small contribution to T_1 which is again dominated by the DP process at zero magnetic field. The DP process is quenched by the field so that T_1 increases with field at small fields and saturates at a value determined by the EY process at large fields. Similar to the degenerate electron case, the VG process makes a substantial contribution to T_2 relaxation. At small fields the T_2 lifetime increases with increasing field and at large fields the VG process begins to dominate the relaxation so that T_2 has again a maximum at some finite magnetic field. The sign of the slope in T_2 at small magnetic fields is again a clear signature of whether the EY process (T_2 decreases with increasing field) or DP process (T_2 increases with increasing field) dominates T_2 relaxation at zero magnetic field. The qualitative behavior of longitudinal and transverse spin relaxation times with increasing magnetic field is similar for degenerate and non-degenerate electrons, but the magnitude of the change is larger for non-degenerate electrons.

In this subsection, we described calculations of the longitudinal (T_1) and transverse (T_2) spin relaxation times of conduction band electrons in n-type bulk GaAs focusing on the interplay between the EY, DP, and VG spin relaxation processes as a function of the magnetic field. Scattering on ionized impurities, acoustic phonons, and optical (LO) phonons was taken into account within the elastic diffusion approximation. For all field strengths, we neglected quantization effects due to the external magnetic field. [217, 218] That is, we implicitly assumed the strong

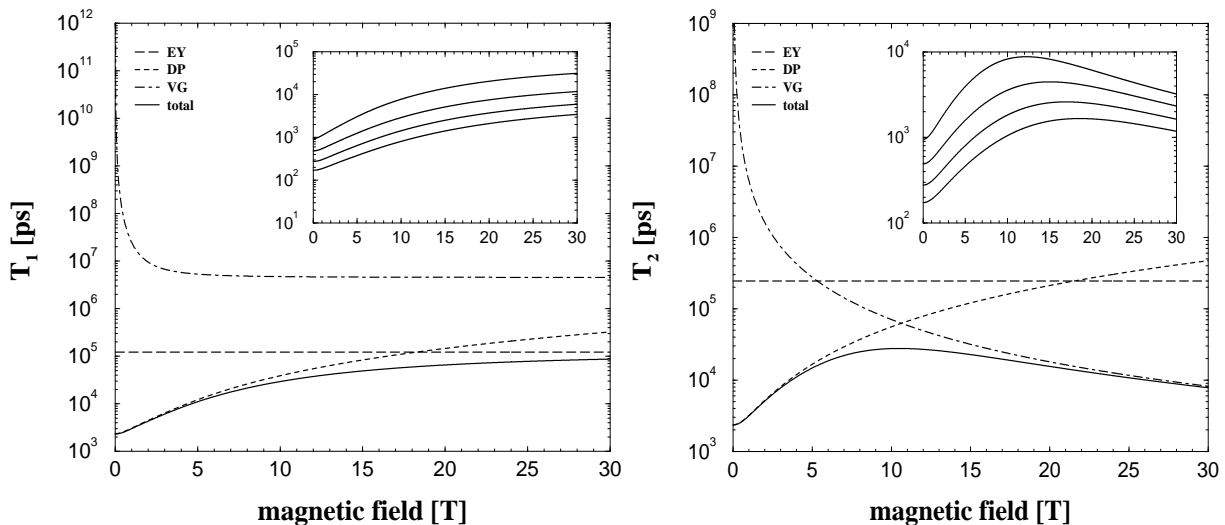


Figure 3.16: The left and right panels show, respectively, the longitudinal (T_1) and transverse (T_2) spin relaxation time in GaAs as a function of magnetic field for $T = 100\text{K}$ and $n = 10^{17}\text{cm}^{-3}$. The contributions from the EY (long dash), DP (short dash) and VG (dot-dash) processes and the total relaxation time (solid) are shown in the main panel. The insets (same axis as the main panel) show the total relaxation times for $T = 150\text{K}, 200\text{K}, 250\text{K}$, and 300K (top to bottom).

scattering limit, where Landau levels are blurred and electrons effectively reside in (restored) band states. In p-type materials, the Bir-Aronov-Pikus (BAP) process provides an additional, efficient spin relaxation channel. [158, 164, 165] The BAP process can be incorporated into the kinetic approach outlined in the previous sections by adding an additional collision integral J_B^{ehX} to the kinetic equation for the nonequilibrium spin polarization, which describes exchange scattering of electrons on equilibrium holes. The diffusion approximation cannot be applied to J_B^{ehX} , however, and the integral form of the kinetic equation (3.30) has to be used to calculate the spin relaxation rates due to the BAP process.

3.5 Concluding Remarks

Starting from the full quantum kinetic equations for the electron Green functions we derived a (semiclassical) Fokker-Planck equation for the non-equilibrium spin polarization, assuming small spin polarizations and soft scattering. The Fokker-Planck equation conceptualizes the non-equilibrium spin dynamics in terms of a “test” spin polarization, comprising a small number of spin polarized “test” electrons, which scatter off an equilibrated bath consisting of impurities, phonons, and spin-balanced “field” electrons. Because of the scattering, the bath causes for the spin polarization dynamical friction, diffusion, and relaxation (decay). We then employed a multiple time scale perturbation approach to separate the fast, spin-conserving from the slow, spin non-conserving time evolution. As a result, we extracted from the Fokker-Planck equation a Bloch equation which controls the time evolution of the macroscopic (\vec{k} -averaged) spin polarization on the long time scale, where the spin polarization decays. Our semiclassical approach accounts for elastic and inelastic scattering processes. The spin relaxation rates are given in terms of weighted energy averages of either a spin-flip rate (EY process) or a generalized relaxation time multiplied by a precession rate (DP and VG processes). The weight function for the energy averages turns out to be intimately linked to the “quasi-stationary” spin polarization, which is the terminating

state of the fast, spin-conserving time evolution taking place immediately after spin injection.

The formal development of our approach is based on a generic model for non-magnetic III-V semiconductors and treats EY and motional narrowing (DP and VG) spin relaxation processes on an equal footing. We also allowed for orbital motion of the electrons in a strong magnetic field, which potentially leads to a quenching of the motional narrowing-type spin relaxation processes. The derivation of the Fokker-Planck equation is independent of dimensionality and, as long as a soft scattering regime can be identified, also of the scattering processes, which enter the Fokker-Planck equation in the form of dynamical friction and diffusion coefficients, which have to be worked out separately for each scattering process.

As a first application of our formalism, we considered spin relaxation in a GaAs quantum well at low temperatures, where electron-electron and electron-impurity scattering dominate. We explicitly constructed the friction, diffusion and angle randomization coefficients characterizing the (symmetry-adapted) Fokker-Planck equation for that particular situation and calculated the DP spin lifetime at vanishingly small magnetic field as a function of electron density and temperature. We found that for fixed temperature (density) the density (temperature) dependence is non-monotonic. Spin lifetimes are particularly long for densities and temperatures, where the cross-over from a non-degenerate to a degenerate electron gas occurs. Spin lifetimes in compensated quantum wells are always longer than in modulation doped quantum wells with the same electron density. The enhancement of the spin lifetime is particularly strong for densities and temperatures where Pauli blocking is most efficient in suppressing the DP spin lifetime (due to electron-electron scattering) in modulation doped quantum wells.

We then discussed the magnetic field dependence of spin relaxation rates in bulk GaAs. Historically this was the first application of our semiclassical description of the non-equilibrium spin dynamics in non-magnetic semiconductors. The separation of the fast, spin conserving from the low spin non-conserving scattering processes were at that time not yet based on the multiple time scale analysis. Instead, we employed a relaxation time approximation, which is conceptually simpler but requires a number of ad-hoc assumptions. Although these assumptions can be made plausible by physical considerations, the desire to avoid them triggered the more demanding multiple time scale approach. We argued that, with an appropriate choice of the weight function $p(\varepsilon)$, which cannot be calculated within the relaxation time approximation, the numerical results for the spin relaxation rates obtained from the relaxation time approximation are practically identical to the numerical results one would obtain from the more general multiple time scale approach.

To study the magnetic field dependence we specifically applied the elastic approximation. The calculation of the spin relaxation rates reduces then to quadratures which can be done by saddle point techniques. At finite magnetic field, the VG process competes with the DP process. We find that, as a consequence of the interplay of the DP and the VG processes, T_2 can have a maximum as a function of magnetic field. In contrast, T_1 is not affected by the VG process and increases with magnetic field until it saturates at a value determined by the EY process. The sign of the change in T_2 with increasing magnetic field at small fields indicates, moreover, whether the EY process or the DP process dominates T_2 relaxation at zero magnetic field. Our calculated results are in good agreement with existing experimental data in n-type GaAs and we make additional specific predictions for the magnetic field dependence of electron spin lifetimes that are subject to experimental check.

Various extensions of our approach are conceivable and constitute research directions for the future. Semiconductor structures with structural inversion asymmetry [190] and/or native interface asymmetry [182] can be studied within our approach by augmenting the model Hamiltonian by the corresponding spin off-diagonal Hamiltonian matrix elements. In particular, the role of

the linear collision integral $J_B^{(1)}[f, \delta\vec{S}]$, which does not affect spin lifetimes in isotropic semiconductors, should be reinvestigated, e.g., for an asymmetric quantum well, where spin lifetimes can be particularly long because motional narrowing processes due to bulk and structural inversion asymmetry can be made to cancel each other. [194, 199] Since $J_B^{(1)}[f, \delta\vec{S}]$ potentially mixes spin relaxation channels, it could affect the cancellation. A Fokker-Planck equation of the form (3.55), augmented by additional driving terms, could be the starting point for a systematic calculation of spin transport coefficients (e.g., spin diffusion length) for spatially inhomogeneous systems, such as interfaces or biased heterostructures. Finally, non-linear effects due to large spin polarizations could be studied either at the level of the matrix-Boltzmann equation for the electronic density matrix [201, 202] or, if the diffusion approximation is used to simplify the collision terms, at the level of a “Fokker-Planck-Landau equation” for the spin polarization, where the differential operator, describing spin-conserving scattering events, as well as the spin-flip tensor explicitly depend on the spin polarization and the distribution of the spin polarized electrons.

Appendix

Construction of the Fokker-Planck Differential Operator

Within the diffusion approximation, the kinetic equation for the excess spin polarization is a differential equation in which spin-conserving collision processes are described by a Fokker-Planck differential operator $\mathcal{D}(\vec{k}) = \mathcal{D}(\varepsilon, \omega)$ while spin-flip scattering is encoded in a spin-flip tensor $\mathbf{R}(\vec{k}) = \mathbf{R}(\varepsilon, \omega)$. The dynamical friction and diffusion coefficients, $A_i(\vec{k})$ and $B_{ij}(\vec{k})$, which determine the differential operator and the spin-flip tensor, depend on the scattering processes and the dimensionality.

As an illustration, we now construct for a [001] quantum well the dynamical friction and diffusion coefficients due to electron-electron and electron-impurity scattering. For bulk semiconductors, the calculation is essentially the same, except of an additional angle integration. The coefficients due to electron-phonon scattering can be obtained in a similar way. From the friction and diffusion coefficients, we can then construct the symmetry-adapted differential operator $\mathcal{D}(\varepsilon, \omega)$ and the symmetry-adapted spin-flip tensor $\mathbf{R}(\varepsilon, \omega)$. Since we discuss for a quantum well only the DP process quantitatively, which originates from the interplay of the differential operator and the torque force due to inversion asymmetry, we give only explicit expressions for $\mathcal{D}(\varepsilon, \omega)$. The spin-flip tensor $\mathbf{R}(\varepsilon, \omega)$ can be obtained along the same lines.

First, we consider electron-electron scattering and calculate A_i^{ee} and B_{ij}^{ee} . To avoid the cut-off problem at large momentum transfers, which usually plagues the diffusion approximation to electron-electron scattering, we keep the full integrands in Eqs. (3.46) and (3.47), i.e., we do not expand the distribution functions and energies with respect to the momentum transfer \vec{q} . Using the identities $f(\vec{k})f(\vec{k} \pm \vec{q}) = [f(\vec{k} \pm \vec{q}) - f(\vec{k})]n(\varepsilon(\vec{k}) - \varepsilon(\vec{k} \pm \vec{q}))$, with $n(x)$ the Bose function, and $\delta(\varepsilon(\vec{k}) + \varepsilon(\vec{k}') - \varepsilon(\vec{k} - \vec{q}) - \varepsilon(\vec{k}' + \vec{q})) = \int d\omega \delta(\varepsilon(\vec{k}) - \varepsilon(\vec{k} - \vec{q}) - \omega) \cdot \delta(\varepsilon(\vec{k}') - \varepsilon(\vec{k}' + \vec{q}) + \omega)$, we rewrite the transition probability (3.41) into

$$W^{ee}(\vec{k}; \vec{q}) = 2 \int_{-\infty}^{\infty} d\omega |V(q)|^2 \text{Im}\chi(q, \omega) [n(-\omega) + f(\vec{k} - \vec{q})] \delta(\varepsilon(\vec{k}) - \varepsilon(\vec{k} - \vec{q}) - \omega), \quad (\text{A.1})$$

where we introduced the susceptibility of noninteracting electrons

$$\text{Im}\chi(q, \omega) = 2\pi \sum_{\vec{k}} [f(\vec{k} + \vec{q}) - f(\vec{k})] \delta(\varepsilon(\vec{k} + \vec{q}) - \varepsilon(\vec{k}) - \omega). \quad (\text{A.2})$$

Note, we calculate the transition probability with the distribution function $f(\vec{k})$ of the equilibrated electrons at $t \rightarrow \infty$, that is, we assume the number of “test” electrons contributing to the spin polarization to be much smaller than the number of spin-balanced “field” electrons.

The Coulomb potential $V(q)$ is taken to be statically screened with a screening length given by the Thomas-Fermi-Hückel expression, that is, $V(q) = 4\pi e^2 / \epsilon_b(q + q_s)$, with e the elementary charge, ϵ_b the background dielectric constant, and q_s the inverse Thomas-Fermi-Hückel screening length; here we assumed an ideal quantum well with infinite confinement. Had we allowed for dynamical screening, $V(q) \rightarrow V(q, \omega) = V_0(q) / \epsilon(q, \omega)$, with $V_0(q)$ the bare Coulomb potential. If $\epsilon(q, \omega)$ is approximated by the RPA expression, the resulting Fokker-Planck equation would be at the level of a quantum analog to the Lenard-Balescu equation. [206] The calculation of the relaxation rates presented below could be also performed with this more general expression for the Coulomb matrix element. For simplicity we present here however only the results for the statically screened Coulomb potential.

The dimensionless Fokker-Planck operator has the same form as in Eq. (3.45) with dynamical

friction and diffusion coefficients given by

$$A_i^{ee}(\vec{k}) = C_{ee}^m \int d\vec{q} q_i W^{ee}(\vec{k}; \vec{q}) , \quad (\text{A.3})$$

$$B_{ij}^{ee}(\vec{k}) = \frac{C_{ee}^m}{2} \int d\vec{q} q_i q_j W^{ee}(\vec{k}; \vec{q}) , \quad (\text{A.4})$$

with $C_{ee}^m = sm^*/\varepsilon_b^2 \pi m_0$ and

$$W^{ee}(\vec{k}; \vec{q}) = \int_{-\infty}^{\infty} d\omega \frac{F(k^2, \omega, q)}{(q + q_s)^2} \delta(\vec{k} \cdot \vec{q} - \frac{q^2}{2} - \frac{\omega}{2}) , \quad (\text{A.5})$$

where q_s is the Thomas-Fermi screening wave number. The function $F(k^2, \omega, q)$ originates from the statistics of the electron gas and is given by

$$F(k^2, \omega, q) = \text{Im} \tilde{\chi}(q, \omega) N(k^2, \omega) , \quad (\text{A.6})$$

$$\text{Im} \tilde{\chi}(q, \omega) = \int d\vec{k} [f(k^2 + \omega) - f(k^2)] \delta(\vec{k} \cdot \vec{q} + \frac{q^2}{2} - \frac{\omega}{2}) , \quad (\text{A.7})$$

$$N(k^2, \omega) = f(k^2 - \omega) + n(-\omega) , \quad (\text{A.8})$$

with $f(x)$ and $n(x)$ the Fermi and Bose functions, respectively. To calculate $A_i^{ee}(\vec{k})$ and $B_{ij}^{ee}(\vec{k})$ for a [001] quantum well, we first evaluate the integrals for a fixed coordinate system in which (the two-dimensional vector) $\vec{k} = k\hat{e}_x$ and then rotate to an arbitrary coordinate system. The result can be cast into the form

$$A_i^{ee}(\vec{k}) = -\frac{8}{k} G(k) k_i , \quad (\text{A.9})$$

$$B_{ij}^{ee}(\vec{k}) = \frac{2}{k} H(k) \delta_{ij} + \frac{2}{k^3} E(k) k_i k_j , \quad (\text{A.10})$$

respectively, with three functions defined by

$$G(k) = -\frac{C_{ee}^m}{4k} \int_{-\infty}^{k^2} d\omega \int_{q_{min}}^{q_{max}} dq \frac{q F(k^2, \omega, q)}{(q + q_s)^2} \frac{z}{\sqrt{1 - z^2}} , \quad (\text{A.11})$$

$$H(k) = \frac{C_{ee}^m}{2} \int_{-\infty}^{k^2} d\omega \int_{q_{min}}^{q_{max}} dq \frac{q^2 F(k^2, \omega, q)}{(q + q_s)^2} \sqrt{1 - z^2} , \quad (\text{A.12})$$

$$E(k) = -\frac{C_{ee}^m}{2} \int_{-\infty}^{k^2} d\omega \int_{q_{min}}^{q_{max}} dq \frac{q^2 F(k^2, \omega, q)}{(q + q_s)^2} \frac{1 - 2z^2}{\sqrt{1 - z^2}} . \quad (\text{A.13})$$

Note that these integrals are well defined. The range of integration originates from the ϕ -integration which also gives rise to the factor involving $z = (q^2 + \omega)/2kq$. With Eqs. (A.9) and (A.10) and a transformation to the radial variable $\varepsilon = k^2$, the spin-conserving part of the dimensionless electron-electron collision integral is given by (recall that in two dimensions $\delta\vec{S}(\varepsilon, \phi, t)$ contains the factor $J(\varepsilon)/(2\pi)^2 n_s = 1/8\pi^2 n_s$)

$$J_{ee}^{(0)}[f, \delta\vec{S}] = \mathcal{D}_{ee}(\varepsilon, \phi) \delta\vec{S}(\varepsilon, \phi, t) , \quad (\text{A.14})$$

with

$$\mathcal{D}_{ee}(\varepsilon, \phi) = -\frac{\partial}{\partial \varepsilon} v_{ee}(\varepsilon) + \frac{\partial^2}{\partial \varepsilon^2} w_{ee}(\varepsilon) - u_{ee}(\varepsilon) \mathcal{L}^2(\phi) . \quad (\text{A.15})$$

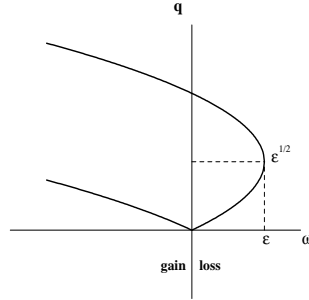


Figure 3.17: The domain bounded by the solid lines is the range of integration for the integrals (A.16), (A.17) and (A.18) defining, respectively, $v_{ee}(\varepsilon)$, $w_{ee}(\varepsilon)$, and $u_{ee}(\varepsilon)$ for a fixed ε . The “test” electrons comprising the spin polarization cannot only gain ($\omega < 0$) but also lose ($\omega > 0$) energy due to inelastically scattering off “field” electrons.

Here we have introduced the total angular momentum operator in two dimensions, $\hat{\mathcal{L}}(\phi) = -i\partial/\partial\phi$, and the friction, diffusion and angle randomization coefficients, $v_{ee}(\varepsilon)$, $w_{ee}(\varepsilon)$, and $u_{ee}(\varepsilon)$, which are linear combinations of the functions $G(k)$, $H(k)$, and $E(k)$ taken at $k = \sqrt{\varepsilon}$. Specifically, they read:

$$v_{ee}(\varepsilon) = -\frac{2C_{ee}^m}{\varepsilon^{1/2}} \int_{-\infty}^{\varepsilon} d\omega \int_{q_{min}}^{q_{max}} dq \frac{\omega F(\varepsilon, \omega, q)}{(q + q_s)^2} \frac{1}{\sqrt{1 - z^2}}, \quad (\text{A.16})$$

$$w_{ee}(\varepsilon) = 4C_{ee}^m \sqrt{\varepsilon} \int_{-\infty}^{\varepsilon} d\omega \int_{q_{min}}^{q_{max}} dq \frac{q^2 F(\varepsilon, \omega, q)}{(q + q_s)^2} \frac{z^2}{\sqrt{1 - z^2}}, \quad (\text{A.17})$$

$$u_{ee}(\varepsilon) = \frac{C_{ee}^m}{\varepsilon^{3/2}} \int_{-\infty}^{\varepsilon} d\omega \int_{q_{min}}^{q_{max}} dq \frac{q^2 F(\varepsilon, \omega, q)}{(q + q_s)^2} \sqrt{1 - z^2}. \quad (\text{A.18})$$

The range of integration, which is shown in Fig. 3.17, depends on the sign of ω , $q_{max} = q_{max}^-(\varepsilon, \omega)\Theta(-\omega) + q_{max}^+(\varepsilon, \omega)\Theta(\omega)$ and $q_{min} = q_{min}^-(\varepsilon, \omega)\Theta(-\omega) + q_{min}^+(\varepsilon, \omega)\Theta(\omega)$, with

$$q_{min}^-(\varepsilon, \omega) = -\sqrt{\varepsilon} + \sqrt{\varepsilon - \omega}, \quad \omega \leq 0, \quad (\text{A.19})$$

$$q_{max}^-(\varepsilon, \omega) = \sqrt{\varepsilon} + \sqrt{\varepsilon - \omega}, \quad \omega \leq 0, \quad (\text{A.20})$$

$$q_{min}^+(\varepsilon, \omega) = \sqrt{\varepsilon} - \sqrt{\varepsilon - \omega}, \quad 0 \leq \omega \leq \varepsilon, \quad (\text{A.21})$$

$$q_{max}^+(\varepsilon, \omega) = \sqrt{\varepsilon} + \sqrt{\varepsilon - \omega}, \quad 0 \leq \omega \leq \varepsilon. \quad (\text{A.22})$$

The functions $v_{ee}(\varepsilon)$ and $w_{ee}(\varepsilon)$ are the dynamical friction and diffusion coefficients for the spin polarization in ε -space. They originate from the scattering of the “test” electrons comprising the spin polarization with the equilibrated, spin-balanced “field” electrons. Because the scattering is inelastic, the “test” electrons gain ($\omega < 0$) or lose ($\omega > 0$) energy by scattering off “field” electrons. The on-shell function $u_{ee}(\varepsilon)$ describes randomization of the angle ϕ . The integrals defining $v_{ee}(\varepsilon)$, $w_{ee}(\varepsilon)$, and $u_{ee}(\varepsilon)$ have to be done numerically. The singularities are integrable and Gaussian integration proved to be efficient. The limiting values are $\lim_{\varepsilon \rightarrow 0} u_{ee}(\varepsilon) = u_0/\varepsilon$, $\lim_{\varepsilon \rightarrow 0} w_{ee}(\varepsilon) = 0$, and $\lim_{\varepsilon \rightarrow 0} v_{ee}(\varepsilon) = v_0$. Moreover, $w_{ee}(\varepsilon) = v_0\varepsilon$ for $\varepsilon \rightarrow 0$, i.e. $dw_{ee}(0)/d\varepsilon = v_{ee}(0)$, which is essential to guarantee spin conservation of the differential operator $\mathcal{D}_{ee}(\varepsilon, \phi)$ [see Eq. (3.84) in this respect]. The structure of the differential operator suggests to write $v_{ee} = \varepsilon/\tau_f^{ee}$, $w_{ee} = \varepsilon^2/\tau_d^{ee}$, and $u_{ee} = 1/4\tau_{\perp}^{ee}$, with $1/\tau_f^{ee}$, $1/\tau_d^{ee}$, and $1/\tau_{\perp}^{ee}$ relaxation rates describing energy relaxation, diffusion, and randomization of the angle due electron-electron scattering, respectively.

The calculation of the (on-shell) relaxation rate due to electron-impurity scattering proceeds along the same lines. The starting point is Eq. (3.37), specialized to electron-impurity scattering, that is, with $W^\nu(\vec{k}, \vec{q})$ given by Eq. (3.40). Going through the same steps as in the case of electron-electron scattering yields for the spin-conserving part of the dimensionless electron-impurity collision integral (as before $\delta\vec{S}(\varepsilon, \phi, t)$ contains the factor $1/8\pi^2 n_s$)

$$J_{ei}^{(0)}[f, \delta\vec{S}] = \mathcal{D}_{ei}(\varepsilon, \phi) \delta\vec{S}(\varepsilon, \phi, t) , \quad (\text{A.23})$$

where the differential operator is now given by

$$\mathcal{D}_{ei}(\varepsilon, \omega) = -u_{ei}(\varepsilon) \mathcal{L}^2(\phi) , \quad (\text{A.24})$$

with

$$u_{ei}(\varepsilon) = \frac{C_{ei}^m}{\varepsilon^{3/2}} \int_0^{2\sqrt{\varepsilon}} dq \frac{q^2}{(q+q_s)^2} \sqrt{1-z^2} , \quad (\text{A.25})$$

$C_{ei}^m = s(4\pi m^* n_i \tilde{a}_0^2 / \varepsilon_b^2 m_0)$ and $z = q/2\sqrt{\varepsilon}$, where n_i is the sheet density of the impurities. Because of the elasticity of electron-impurity scattering, the differential operator contains only an on-shell term. The function $u_{ei} = 1/4\tau_\perp^{ei}$ defines the relaxation time due to electron-impurity scattering. It only causes randomization of the angle ϕ . The total spin-conserving collision integral, taking electron-electron and electron-impurity scattering into account, is given by

$$\mathcal{D}(\varepsilon, \omega) = \mathcal{D}_{ee}(\varepsilon, \omega) + \mathcal{D}_{ei}(\varepsilon, \omega) . \quad (\text{A.26})$$

Similar expressions can be derived for electron-phonon scattering. For bulk semiconductors the calculation proceeds along the same lines with the obvious modifications due to the additional angle integration.

Bibliography

- [1] F. X. Bronold in *Optical Properties of 2D systems with interacting electrons*, W. J. Ossau and R. Suris, Eds., NATO Science Series Vol. **119**, 169 (2003).
- [2] F. X. Bronold, *Journal of Luminescence* **87-89**, 198 (2000).
- [3] F. X. Bronold, *Phys. Rev. B* **61**, 12620 (2000).
- [4] F. X. Bronold, A. Saxena, and A. R. Bishop, *Phys. Rev. B* **63**, 235109 (2001).
- [5] F. X. Bronold and H. Fehske, *Phys. Rev. B* **66**, 073102 (2002).
- [6] F. X. Bronold and H. Fehske, *Acta Physica Polonica* **34**, 851 (2003).
- [7] F. X. Bronold, A. Alvermann, and H. Fehske, *Phil. Mag.* **84**, 673 (2004).
- [8] A. Alvermann, F. X. Bronold, and H. Fehske, *Phys. Stat. Sol. (c)* **1**, 63 (2004).
- [9] F. X. Bronold, A. Saxena and D. L. Smith, cond-mat/0402085.
- [10] F. X. Bronold, A. Saxena and D. L. Smith, *Solid State Physics*, Vol. **58**, Eds. H. Ehrenreich and F. Spaepen, Academic Press, San Diego, 73, (2004).
- [11] F. X. Bronold, I. Martin, A. Saxena, and D. L. Smith, *Phys. Rev. B* **66**, 233206 (2002).
- [12] H. Haug and S. Schmitt-Rink, *Prog. Quant. Electr.* **9**, 3 (1984).
- [13] R. Zimmermann, *Many-Particle Theory of Highly Excited Semiconductors* (Teubner Texte für Physik, Bd. 18, Teubner Verlagsgesellschaft, Leipzig, 1988).
- [14] G. D. Mahan, *Phys. Rev.* **153**, 882 (1967); *ibid.* **163**, 612 (1967).
- [15] J. Gavoret, P. Nozières, B. Roulet, and M. Combescot, *J. de Physique (Paris)* **30**, 987 (1969).
- [16] M. Combescot and P. Nozières, *J. de Physique (Paris)* **32**, 913 (1971).
- [17] A. E. Ruckenstein and S. Schmitt-Rink, *Phys. Rev. B* **35**, 7551 (1987).
- [18] P. Nozières and C. T. De Dominicis, *Phys. Rev.* **178**, 1097 (1969).
- [19] B. Roulet, J. Gavoret, and P. Nozières, *Phys. Rev.* **178**, 1072 (1969); *ibid.* 1084 (1969).
- [20] For general references, see G. D. Mahan, *Many-Particle Physics* (Plenum Press, New York, 1990), Chapter 8.

- [21] C. Weisbuch and B. Vinter, *Quantum Semiconductor Structures: Fundamentals and Applications* (Academic Press, San Diego, 1991).
- [22] See, e.g., S. Schmitt-Rink, D.S. Chemla, and D.A.B. Miller, *Adv. Phys.* **38**, 89 (1989) and references therein.
- [23] T. Uenoyama and L. J. Sham, *Phys. Rev. Lett.* **65**, 1048 (1990).
- [24] P. Hawrylak, *Phys. Rev. B* **42**, 8986 (1990); *ibid.*, **44**, 6262 (1991); **45**, 4237 (1992).
- [25] P. Hawrylak, *Phys. Rev. B* **44**, 3821 (1991).
- [26] F. J. Rodriguez and C. Tejedor, *Phys. Rev. B* **47**, 1506 (1993); *J. Phys.: Cond. Mat.* **8**, 1713 (1996).
- [27] For a review see, e.g., J. A. Brum and P. Hawrylak, *Comments Cond. Mat. Phys.* **18**, 135 (1997).
- [28] I. V. Kukushkin, K. von Klitzing, and K. Ploog, *Phys. Rev. B* **40**, 7788 (1989).
- [29] M. S. Skolnick, D. M. Whittaker, P. E. Simmonds, T. A. Fischer, M. K. Saker, J. M. Rorison, R. S. Smith, P. B. Kirby, and C. R. H. White, *Phys. Rev. B* **43**, 7354 (1991).
- [30] W. Chen, M. Fritze, A. V. Nurmikko, D. Ackley, C. Colvard, and H. Lee, *Phys. Rev. Lett.* **64**, 2434 (1990).
- [31] W. Chen, M. Fritze, W. Walecki, A. V. Nurmikko, D. Ackley, J. M. Hong, and L. L. Chang, *Phys. Rev. B* **45**, 8464 (1992).
- [32] S. A. Brown, Jeff F. Young, J. A. Brum, P. Hawrylak, and Z. Wasilewski, *Phys. Rev. B* **54**, R11082 (1996).
- [33] H. P. van der Meulen, I. Santa-Olalla, J. Rubio, and J. M. Calleja, *Phys. Rev. B* **60**, 4897 (1999).
- [34] K. Kheng, R.T. Cox, Y. Merle d'Aubigné, Franck Bassani, K. Saminadayar, and S. Tatarenko, *Phys. Rev. Lett.* **71**, 1752 (1993).
- [35] Initially, charged excitons in semiconductor quantum wells have been theoretically discussed by B. Stébé and A. Ainane, *Superlattices Microstruct.* **5**, 545 (1989).
- [36] B. Stébé, G. Munschy, L. Stauffer, F. Dujardin, and J. Murat, *Phys. Rev. B* **56**, 12454 (1997).
- [37] B. Stébé, E. Feddi, A. Ainane, and F. Dujardin, *Phys. Rev. B* **58**, 9926 (1998).
- [38] J. Usukura, Y. Suzuki, K. Varga, *Phys. Rev. B* **59**, 5652 (1999).
- [39] W. J. Ruan, K. S. Chan, H. P. Ho, R. Q. Zhang, E. Y. P. Pun, *Phys. Rev. B* **60**, 5714 (1999).
- [40] A. Esser, E. Runge, R. Zimmermann, and W. Langbein, *W. Phys. Rev. B* **62**, 8232 (2000).
- [41] A. Esser, R. Zimmermann, and E. Runge, *phys. stat. sol. (b)* **227**, 317 (2000).

- [42] R. A. Suris, V. P. Kochereshko, G. V. Astakhov, D. R. Yakovlev, W. Ossau, J. Nürnberger, W. Faschinger, G. Landwehr, T. Wojtowicz, G. Karczewski, and J. Kossut, *phys. stat. sol. (b)* **227**, 343 (2001).
- [43] A. J. Shields, M. Pepper, D. A. Ritchie, and M. Y. Simmons, *Adv. Phys.* **44**, 47 (95).
- [44] A. Manassen, E. Cohen, Arza Ron, E. Linder, and L.N. Pfeiffer, *Phys. Rev. B* **54**, 10609 (1996).
- [45] S. Lovisa, R. T. Cox, N. Magnea, and K. Saminadayar, *Phys. Rev. B* **56**, R12787 (1997).
- [46] G. Eytan, Y. Yayon, M. Rappaport, H. Shtrikman, and I. Bar-Joseph, *Phys. Rev. Lett.* **81**, 1666 (1998).
- [47] J. Siviniant, D. Scalbert, A. V. Kavokin, D. Coquillat, J.-P. Lascaray, *Phys. Rev. B* **59**, 1602 (1999).
- [48] V. Huard, R. T. Cox, K. Saminadayar, A. Arnoult, and S. Tatarenko, *Phys. Rev. Lett.* **84**, 187 (2000).
- [49] G. Yusa, H. Shtrikman, and I. Bar-Joseph, *Phys. Rev. B* **62**, 15390 (2000).
- [50] For a recent comprehensive overview see, e.g., R. Zimmermann, Ed., *Proceedings of the Miniworkshop on Trion Physics*, *phys. stat. sol. (b)* **227** (2001).
- [51] J. Kondo, *Prog. Theoret. Phys.* **32**, 37 (1964). An introductory discussion of the Kondo effect can be found in Ref. [20], Chapter 11.
- [52] H. Haug and S. W. Koch, *Quantum Theory of the Optical and Electronic Properties of Semiconductors* (World Scientific, Singapore, 1990).
- [53] P. Schuck, *Z. Phys.* **241**, 395 (1971); P. Schuck and S. Ethofer, *Nucl. Phys. A* **212**, 269 (1973).
- [54] G. Röpke, L. Münchow, and H. Schulz, *Nucl. Phys. A* **379**, 536 (1982); G. Röpke, M. Schmidt, L. Münchow, and H. Schulz, *ibid.* **399**, 587 (1983).
- [55] J. Dukelsky, G. Röpke, and P. Schuck, *Nucl. Phys. A* **628**, 17 (1998).
- [56] M. Beyer und G. Röpke, *Phys. Rev. C* **56**, 2636 (1997).
- [57] C. Kuhrts, M. Beyer, P. Danielewicz und G. Röpke, *Phys. Rev. C.* **63**, 034605 (2001).
- [58] M. Beyer, W. Schadow, C. Kuhrts und G. Röpke, *Phys. Rev. C* **60**, 034004 (1999).
- [59] M. Beyer, S. A. Sofianos, C. Kuhrts, G. Röpke und P. Schuck, *Phys. Lett. B* **488**, 247 (2000).
- [60] H. A. Bethe and E. E. Salpeter, *Quantum Mechanics of one- and two-electron atoms* (Springer Verlag, Berlin, 1957).
- [61] J.W. Negele and H. Orland, *Quantum Many-Particle Systems* (Addison-Wesley, New York, 1988).
- [62] W. Glöckle, *The Quantum Mechanical Few-Body Problem*, Text and Monographs in Physics, (Springer-Verlag, Berlin, 1983).

- [63] P. W. Anderson, Phys. Rev. Lett. **18**, 1049 (1967).
- [64] J. J. Hopfield, Comments Solid St. Phys. **2**, 40 (1969).
- [65] A. Lande and R. A. Smith, Phys. Rev. A **45**, 913 (1992).
- [66] R. A. Smith, Phys. Rev. A **46**, 4586 (1992).
- [67] J.-P. Blaizot and G. Ripka, *Quantum Theory of Finite Systems* (MIT Press, Cambridge Massachusetts, 1986).
- [68] V. Janiš, Phys. Rev. B **60**, 11345 (1999).
- [69] W. H. Press, S. A. Teukolsky, W. T. Vetterling, and B. P. Flannery, *Numerical Recipes in Fortran 77: The Art of Scientific Computing* (Cambridge University Press, Cambridge, 1986).
- [70] Bar-Yam, Y., Egami, T., Mustre-de Leon, J., and Bishop A. R. (eds.), 1992, *Lattice Effects in High- T_c Superconductors*, (Singapore: World Scientific), pp. 377-422, and references therein.
- [71] Salje, E. K. H., Alexandrov, A. S., and Liang, W. Y., 2001, *Polarons and Bipolarons in High- T_c Superconductors and Related Materials* (Cambridge: Cambridge University Press).
- [72] S.-W. Cheong, H. Y. Hwang, C. H. Chen, B. Batlogg, L. W. Rupp Jr., and S. A. Carter, Phys. Rev. B **49**, 7088 (1994); J. Tranquada *et al.*, Nature **375**, 561 (1995).
- [73] Oyanagi, H. and Bianconi, A. (eds.), 2001, *Physics in local lattice distortions: Fundamentals and Novel Concepts*, AIP Conference Proceeding **554** (American Institute of Physics).
- [74] S. Jin, T. H. Tiefel, M. McCormack, R. A. Fastnach, R. Ramesh, and L. H. Chen, Science **264**, 413 (1994); Y. Tokura and Y. Tomioka, J. Magn. Mater. **200**, 1 (1999).
- [75] P. E. Parris, V. M. Kenkre, and D. H. Dunlap, Phys. Rev. Lett. **87**, 126601 (2001).
- [76] L. D. Landau, Z. Phys. **3**, 664 (1933).
- [77] Y. A. Firsov, *Polarons* (Nauka, Moscow, 1975).
- [78] E. I. Rashba, in *Excitons*, edited by E. I. Rashba and D. M. Sturge (North-Holland, Amsterdam 1982), p. 542; G. Wellein and H. Fehske, Phys. Rev. B **58**, 6208 (1998).
- [79] H. Löwen, Phys. Rev. B **37**, 8661 (1988).
- [80] T. Holstein, Ann. Phys. (N.Y.) **8**, 325 (1959); *ibid.* 343.
- [81] H. DeRaedt and A. Lagendijk, Phys. Rev. B **27**, 6097 (1983).
- [82] J. Ranninger and U. Thibblin, Phys. Rev. B **45**, 7730 (1992); F. Marsiglio, Phys. Lett. A **180**, 280 (1993); A. S. Alexandrov, V. V. Kabanov, and D. K. Ray, Phys. Rev. B **49**, 9915 (1994).
- [83] W. Stephan, Phys. Rev. B **54**, 8981 (1996).
- [84] M. Capone, W. Stephan, and M. Grilli, Phys. Rev. B **56**, 4484 (1997).

- [85] G. Wellein, H. Röder, and H. Fehske Phys. Rev. B **52**, 9666 (1996).
- [86] J. Bonča, S. A. Trugman, and I. Batistić, Phys. Rev. B **60**, 1633 (1999).
- [87] A. S. Alexandrov and P. E. Kornilovitch, Phys. Rev. Lett. **82**, 807 (1999); H. Fehske, J. Loos, and G. Wellein, Phys. Rev. B **61**, 8016 (2000).
- [88] P. W. Anderson, Phys. Rev. **109**, 1498 (1958).
- [89] D. J. Thouless, Phys. Rep. **13**, 93 (1974).
- [90] Besides Ref. [89], several review papers have been recently concerned with Anderson localization of noninteracting electrons. See, e.g., A. Brezini and N. Zerki, phys. stat. sol. (b) **169**, 253 (1992); and B. Kramer and A. MacKinnon, Rep. Prog. Phys. **56**, 1469 (1993).
- [91] E. Abrahams, P. W. Anderson, D. C. Licciardello, and T. V. Ramakrishnan, Phys. Rev. Lett. **42**, 673 (1979).
- [92] N. F. Mott, J. Non-Cryst. Solids **1**, 1 (1968); Phil. Mag. **22**, 7 (1968); Commun. Phys. **1**, 203 (1976); Phil. Mag. B **44**, 265 (1981).
- [93] P. W. Anderson, Nature (London) Phys. Science **235**, 163 (1972).
- [94] S. M. Girvin and M. Jonson, Phys. Rev. B **22**, 3583 (1980).
- [95] H. Mueller and P. Thomas, Phys. Rev. Lett. **51**, 702 (1983).
- [96] M. H. Cohen, E. N. Economou, and C. M. Soukoulis, Phys. Rev. Lett. **51**, 1202 (1983).
- [97] G. Kopidakis, C. M. Soukoulis, and E. N. Economou, Europhysics Lett. **33**, 459 (1996).
- [98] V. Dobrosavljević and G. Kotliar, Phys. Rev. Lett. **78**, 3943 (1997); Philos. Trans. R. Soc. Lond. , Ser. A **356**, 1 (1998).
- [99] H. Fehske, J. Loos, and G. Wellein, Z. Phys. B **104**, 619 (1997); G. Wellein and H. Fehske, Phys. Rev. B **56**, 4513 (1997).
- [100] P. Soven, Phys. Rev. **156**, 809 (1967).
- [101] B. Velický, S. Kirkpatrick, and H. Ehrenreich, Phys. Rev. **175**, 747 (1968).
- [102] B. Velický, Phys. Rev. **184**, 614 (1969).
- [103] R. J. Elliott, J. A. Krumhansl, and P. L. Leath, Rev. Mod. Phys. **46**, 465 (1974).
- [104] H. Sumi, J. Phys. Soc. Jpn. **36**, 770 (1974).
- [105] H. Miyazaki and E. Hanamura, J. Phys. Soc. Jpn. **50**, 1310 (1981).
- [106] H. Miyazaki and E. Hanamura, J. Phys. Soc. Jpn. **51**, 818 (1982); *ibid.* 828.
- [107] S. Abe, J. Phys. Soc. Jpn. **57**, 4029 (1988).
- [108] S. Abe, J. Phys. Soc. Jpn. **57**, 4036 (1988); *ibid.* **59**, 1496 (1990).
- [109] D. Paquet and P. Leroux-Hugon, Phys. Rev. B **29**, 593 (1984).

- [110] D. Vollhardt in *Correlated Electron Systems*, edited by V. J. Emery (World Scientific, Singapore).
- [111] Th. Pruschke, M. Jarrel, and J. K. Freericks, *Adv. Phys.* **44**, 187 (1995).
- [112] A. Georges, G. Kotliar, W. Krauth, and M.J. Rozenberg, *Rev. Mod. Phys.* **68**, 13 (1996).
- [113] S. Ciuchi, F. de Pasquale, S. Fratini, and D. Feinberg, *Phys. Rev. B* **56**, 4494 (1997).
- [114] E. N. Economou, M. H. Cohen, *Phys. Rev. B* **5**, 2931 (1972).
- [115] L. Schwartz and H. Ehrenreich, *Phys. Rev. B* **6**, 2923 (1972).
- [116] R. Vlaming and D. Vollhardt, *Phys. Rev. B* **45**, 4637 (1992).
- [117] L. Schwartz and E. Siggia, *Phys. Rev. B* **5**, 383 (1972).
- [118] For more details concerning how to define the various electron-phonon coupling regimes, see, e.g., D. Feinberg, S. Ciuchi and F. de Pasquale, *Int. J. Mod. Phys. B* **4**, 1317 (1990).
- [119] S. Kirkpatrick, B. Velický, and H. Ehrenreich, *Phys. Rev. B* **1**, 3250 (1970).
- [120] G. Doetsch, *Anleitung zum praktischen Gebrauch der Laplace Transformation und der Z-Transformation* (Oldenburg Verlag, München, 1989).
- [121] T. Hotta and Y. Takada, *Phys. Rev. Lett.* **76**, 3180 (1996).
- [122] A. M. Finkel'stein, *Zh. Eksp. Teor. Fiz.* **84**, 168 (1983) [*Sov. Phys. JETP* **57**, 97 (1983)]; C. Castellani, C. Di Castro, P. A. Lee, and M. Ma, *Phys. Rev. B* **30**, 527 (1984).
- [123] T. R. Kirkpatrick and D. Belitz, *J. Phys. Cond. Mat.* **2**, 5259 (1990).
- [124] Early numerical studies are described in Ref. [89]. For recent investigations see the review articles in Ref. [90].
- [125] D. Vollhardt and P. Wölfle, *Phys. Rev. B* **22**, 4666 (1980). For recent studies consult the review articles in Ref. [90] as well as D. Vollhardt and P. Wölfle in *Electronic Phase Transitions*, edited by W. Hanke and Yu. V. Kopaev (North Holland, Amsterdam, 1992).
- [126] F. J. Wegner, *Z. Phys. B* **25**, 327 (1976). For recent studies consult the review articles Ref. [90].
- [127] See, e.g., F. von Oppen, T. Wettig, and J. Müller, *Phys. Rev. Lett.* **76**, 491 (1996).
- [128] See, e.g. P. A. Lee and T. V. Ramakrishnan, *Rev. Mod. Phys.* **57**, 287 (1985).
- [129] D. Belitz and T. R. Kirkpatrick, *Rev. Mod. Phys.* **66**, 261 (1994).
- [130] A. Kamenev and A. Andreev, *Phys. Rev. B* **60**, 2218 (1999).
- [131] D. J. Thouless, *J. Phys. C* **3**, 1559 (1970).
- [132] R. Abou-Chacra, P. W. Anderson, and D. J. Thouless, *J. Phys. C* **6**, 1734 (1973).
- [133] N. Kumar, J. Heinrichs, and A. A. Kumar, *Sol. Stat. Commun.* **17**, 541 (1975); A. Brezini, *J. Phys. C* **15**, L211 (1982); A. Brezini and G. Olivier, *Phil. Mag. B* **47**, 461 (1983).

- [134] J. D. Miller and B. Derrida, *J. Stat. Phys.* **75**, 357 (1993).
- [135] J. Heinrichs, *Phys. Rev. B* **16**, 4365 (1977); L. Fleishman and D. L. Stein, *J. Phys. C* **12**, (1979); P. V. Elyutin, *Sov. Phys. Solid State* **21**, 1590 (1979); P. V. Elyutin, *J. Phys. C* **14**, 1435 (1981).
- [136] D. E. Logan and P. G. Wolynes, *Phys. Rev. B* **31**, 2437 (1985); *J. Chem. Phys.* **85**, 937 (1986); *Phys. Rev. B* **36**, 4135 (1987).
- [137] E. Miranda and V. Dobrosavljević, *J. Magn. Magn. Mat.* **226-230**, 110 (2001); E. Miranda and V. Dobrosavljević, *Phys. Rev. Lett.* **86**, 264 (2001).
- [138] M. C. O. Aguiar, E. Miranda, V. Dobrosavljević, cond-mat/0302389 (2003).
- [139] A. Mirlin and Yan. V. Fyodorov, *J. Phys. I France* **4**, 655 (1994).
- [140] A. Alvermann, Diplomarbeit (in German), Universität Bayreuth (2003).
- [141] E. W. Montroll and M. F. Shlesinger, *J. Stat. Phys.* **32**, 209 (1983).
- [142] V. S. Viswanath and G. Müller, *The Recursion Method*; M. Cini, *Phys. Rev. B* **29**, 547 (1984).
- [143] M. Capone, M. Grilli, and W. Stephan, *Eur. Phys. J. B* **11**, 551 (1999).
- [144] M. Capone and S. Ciuchi, *Phys. Rev. Lett.* **91**, 186405 (2003).
- [145] H. Zhang and M. Avignon, *Phys. Rev. B* **68**, 024301 (2003).
- [146] A. S. Alexandrov and E. A. Mazur, *Sov. Phys. JETP* **69**, 1001 (1989).
- [147] A. S. Alexandrov, *Europhys. Lett.* **56**, 92 (2001).
- [148] M. Capone, S. Ciuchi, and C. Grimaldi, *Europhys. Lett.* **42**, 523 (1998).
- [149] A. A. Abrikosov, L. P. Gorkov, and I. E. Dzyaloshinski, *Methods of Quantum Field Theory in Statistical Physics* (Dover Publications, New York, 1975).
- [150] *Handbook of Mathematical Functions*, edited by M. Abramowitz and I.A. Stegun (Dover Publications, New York, 1972).
- [151] A. Mookerjee, *J. Phys. C* **6**, L205 (1973); T. Kaplan and L.J. Gray, *Phys. Rev. B* **14**, 3462 (1976); H.W. Diehl and P.L. Leath, *Phys. Rev. B* **19**, 587 (1979).
- [152] G. Prinz, *Phys. Today* **48**, No. 4, 24 (1995).
- [153] S. A. Wolf, D.D. Awschalom, R. A. Buhrman, J.M. Daughton, S. von Molnàr, M. L. Roukes, A. Y. Chtchelkanova, and D. M. Treger, *Science* **294**, 1488 (2001).
- [154] *Semiconductor Spintronics and Quantum Computation*, eds. D.D. Awschalom, D. Loss and N. Samarth (Springer, Berlin, 2002).
- [155] *Semiconductor Science and Technology* (special issue) **17**, (no.4 April 2002, pp. 275-404), edited by H. Ohno.
- [156] R. J. Elliott, *Phys. Rev.* **96**, 266 (1954).

- [157] Y. Yafet, *Solid State Physics*, Vol. **14**, eds. F. Seitz and D. Turnbull (Academic Press, New York, 1963), p.1.
- [158] G. L. Bir, A. G. Aronov, and G. E. Pikus, *Sov. Phys.-JETP* **42**, 705 (1976) [*Zh. Eksp. Teor. Fiz.* **69**, 1382 (1975)].
- [159] M. I. D'yakonov and V. I. Perel', *Fiz. Tverd. Tela (Leningrad)* **13**, 3581 (1971) [*Sov. Phys. Solid State* **13**, 3023 (1972)].
- [160] E. L. Ivchenko, *Fiz. Tverd. Tela (Leningrad)* **15**, 1566 (1973) [*Sov. Phys. Solid State* **15**, 1048 (1973)].
- [161] A. D. Margulis and V. A. Margulis, *Fiz. Tverd. Tela (Leningrad)* **25**, 1590 (1983) [*Sov. Phys. Solid State* **25**, 918 (1983)].
- [162] J.-N. Chazalviel, *Phys. Rev. B* **11**, 1555 (1975).
- [163] G. Fishman and G. Lampel, *Phys. Rev. B* **16**, 820 (1977).
- [164] A. G. Aronov, G. E. Pikus, and A. U. Titkov, *Zh. Éksp. Teor. Fiz.* **84**, 1170 (1983) [*Sov. Phys. JETP* **57**, 680 (1983)].
- [165] *Optical Orientation, Modern Problems in Condensed Matter Science*, eds. F. Meier and B. P. Zakharchenya (North Holland, Amsterdam, 1984), Vol. 8.
- [166] L. Viña, *J. Phys.: Condens. Mater* **11**, 5929 (1999).
- [167] S.A. Crooker, J.J. Baumberg, F. Flack, N. Samarth, and D.D. Awschalom, *Phys. Rev. Lett.* **77**, 2814 (1996).
- [168] J. M. Kikkawa, D. D. Awschalom, I. P. Smorchkova, and N. Samarth, *Science* **277**, 1284 (1997).
- [169] J. M. Kikkawa and D. D. Awschalom, *Phys. Rev. Lett.* **80**, 4313 (1998).
- [170] J. M. Kikkawa and D. D. Awschalom, *Nature* **397**, 139 (1999).
- [171] W.A.J.A. van der Poel, A. L. G. J. Severens, H. W. van Kesteren, and C. T. Foxon, *Phys. Rev. B* **39**, 8552 (1989).
- [172] T.C. Damen, L. Viña, J. E. Cunningham, J. Shah, and L. J. Sham, *Phys. Rev. Lett.* **67**, 3432 (1991).
- [173] V. Srinivas, Y. J. Chen, and C. E. C. Wood, *Phys. Rev. B* **47**, 10907 (1993).
- [174] J. Wagner, H. Schneider, D. Richards, A. Fischer, and K. Ploog, *Phys. Rev. B* **47**, 4786 (1993).
- [175] R. Terauchi, Y. Ohno, T. Adachi, A. Sato, F. Matsukura, A. Tackeuchi, and H. Ohno, *Jpn. J. Appl. Phys. (Part 1)* **38**, 2549 (1999).
- [176] A. Tackeuchi, T. Kuroda, S. Muto, Y. Nishikawa, and O. Wada, *J. Appl. Phys. (Part 1)* **38**, 4680 (1999).
- [177] Y. Ohno, R. Terauchi, T. Adachi, F. Matsukura, and H. Ohno, *Phys. Rev. Lett.* **83**, 4196 (1999).

- [178] A.L.C. Triques, J. Urdanivia, F. Iikawa, M. Z. Maialle, J. A. Brum, and G. Borghs, *Phys. Rev. B* **59**, R7813 (1999).
- [179] T.F. Boggess, J.T. Olesberg, C. Yu, M.E. Flatté, and W.H. Lau, *Appl. Phys. Lett.* **77**, 1333 (2000).
- [180] A. Malinowski, R. S. Britton, T. Grevatt, R. T. Harley, D. A. Ritchie, and M. Y. Simmons, *Phys. Rev. B* **62**, 13034 (2000).
- [181] J.S. Sandhu, A. P. Heberle, J. J. Baumberg, and J. R. A. Cleaver, *Phys. Rev. Lett.* **86**, 2150 (2001).
- [182] J.T. Olesberg, W. H. Lau, M. E. Flatté, C. Yu, E. Altunkaya, E. M. Shaw, T. C. Hasenberg, and T. F. Bogess, *Phys. Rev. B* **64**, 201301 (2001).
- [183] M. A. Brand, A. Malinowski, O. Z. Karimov, P. A. Marsden, R. T. Harley, A. J. Shields, D. Sanvitto, D. A. Ritchie, and M. Y. Simmons, *Phys. Rev. Lett.* **89**, 236601 (2002).
- [184] R.I. Dzhioev, K. V. Kavolin, V. L. Korenev, M. V. Lazarev, B. Y. Meltser, M. N. Stepanova, B. P. Zakharchenya, D. Gammon, and D. S. Katzer, *Phys. Rev. B* **66**, 245204 (2002).
- [185] R.I. Dzhioev, V. L. Korenev, I. A. Merkulov, B. P. Zakharchenya, D. Gammon, A. L. Efros, and D. S. Katzer, *Phys. Rev. Lett.* **88**, 256801 (2002).
- [186] M.W. Wu and C.Z. Ning, *Eur. Phys. J. B* **18**, 373 (2000); *phys. stat. sol. (b)* **222**, 523 (2000).
- [187] M.W. Wu, *J. Phys. Soc. Jpn.* **70**, 2195 (2001).
- [188] P. H. Song and K. W. Kim, *Phys. Rev. B* **66**, 035207 (2002).
- [189] Yu.G. Semenov, *Phys. Rev. B* **67**, 115319 (2003).
- [190] Yu.A. Bychov and E. I. Rashba, *J. Phys. C* **17**, 6093 (1984).
- [191] M.I. D'yakonov and V.Yu. Kachorovskii, *Sov. Phys. Semicond.* **20**, 110 (1986).
- [192] G. Bastard and R. Ferreira, *Surf. Sci.* **267**, 335 (1992).
- [193] L.J. Sham, *J. Phys.: Condens. Mater* **5**, A51 (1993).
- [194] N.S. Averkiev and L. E. Golub, *Phys. Rev. B* **60**, 15582 (1999); N.S. Averkiev, L. E. Golub, and M. Willander, *Semiconductors (Fiz. Tekh. Polup.* **36**, 97 (2002)) **36**, no. 1, p. 91 (2002).
- [195] M.W. Wu and H. Metiu, *Phys. Rev. B* **61**, 2945 (2000).
- [196] W. H. Lau, J. T. Olesberg, and M. E. Flatté *Phys. Rev. B* **64**, 161301(R) (2001).
- [197] M.M. Glazov and E.L. Ivchenko, *JETP Lett.* **75**, 403-405 (2002).
- [198] M.M. Glazov, E.L. Ivchenko, M. A. Brandt, O. Z. Karimov, and R. T. Harley, *cond-mat/0305260*.
- [199] J. Kainz, U. Rössler, and R. Winkler, *Phys. Rev. B* **68**, 075322 (2003).

- [200] V.I. Puller, L. G. Mouroukh, N. J. M. Horing, and A. Yu. Smirnov, Phys. Rev. B **67**, 155309 (2003).
- [201] M.Q. Weng, T. Rao, M.W. Wu, and M. Ning, cond-mat/0210313.
- [202] M.Q. Weng and M.W. Wu, cond-mat/0303169.
- [203] M.Q. Weng and M.W. Wu, Phys. Rev. B **66**, 235109 (2002).
- [204] N. R. Ogg, Proc. Phys. Soc. (London) **89**, 431 (1966).
- [205] V. G. Golubev, V.I. Ivanov-Omskii, I.G. Minervin, A. V. Osutin, and D. G. Polyakov, Zh. Éksp. Teor. Fiz. **88**, 2052 (1985) [Sov. Phys. JETP **61**, 1214 (1985)].
- [206] R. Balescu, Phys. Fluids **3**, 52 (1960); A. Lenard, Ann. Phys. (New York) **10**,390 (1960).
- [207] L. V. Keldysh, Zh. Éksp. Teor. Fiz. **47**, 1515 (1964) [Sov. Phys. JETP **20**, 1018 (1965)].
- [208] E. M. Lifshitz and L. P. Pitaevskii, *Physical Kinetics* (Pergamon Press, New York, 1981).
- [209] A. V. Kutznetsov, Phys. Rev. B **44**, 8721 (1991).
- [210] H. Haug and A. P. Jauho, *Quantum Kinetics in Transport and Optics of Semiconductors* (Springer Verlag, Berlin, 1996).
- [211] D. C. Langreth, Phys. Rev. B **148**, 707 (1966).
- [212] A. H. Nayfeh, *Perturbation Methods* (Wiley-Interscience, New York, 2000).
- [213] Landoldt-Börnstein New Series: *Semiconductors*, ed. O. Madelung (Springer Verlag, Berlin, 1986).
- [214] M. Combescot and R. Combescot, Phys. Rev. B **35**, 7986 (1987).
- [215] P. Boguslawski, Solid State. Comm. **33**, 389 (1980).
- [216] Data courtesy of S. A. Crooker.
- [217] A. D. Margulis and Vl. A. Margulis, Fiz. Tverd. Tela (Leningrad) **28**, 1452 (1986) [Sov. Phys. Solid State **28**, 817 (1986)].
- [218] B.P. Zakharchenya, E.L. Ivchenko, A.Ya. Ryskin, and A.V. Varfolomeev, Fiz. Tverd. Tela (Leningrad) **18**, 230 (1976) [Sov. Phys. Solid State **18**, 132 (1976)].

Acknowledgements

It is a great pleasure to thank Holger Fehske not only for an enjoyable collaboration in “polaron matters” but also for inviting me to join him at the Ernst-Moritz-Arndt University Greifswald. This move affected not only my scientific life. I am also grateful for his thoughtful guidance and moral support during the course of this work. I am deeply obliged to Avadh Saxena for a longstanding transatlantic scientific collaboration and for friendship both within and without science. It is due to him that I could visit Los Alamos National Laboratory over the last couple of years in a rather unbureaucratic manner. Being exposed to the vibrant scientific atmosphere in Los Alamos encouraged me to continue my research. I am especially grateful to Darryl Smith. He taught me a great deal of physics and many other things – valuable not only for science but for life in general. I owe to him more than he knows. It is also a pleasure to thank John Albrecht for his patience to listen to my problems, his valuable advice in “semiconductor matters”, and his friendship. My thanks also go to my former officemate Olaf Bleibaum. From him I learned to appreciate the value of asymptotic techniques in solving physics problems. The present Habilitation is based on accepted or submitted papers. Without the pleasant and stimulating discussions with my fellow authors A. Alvermann, A. R. Bishop, H. Fehske, I. Martin, A. Saxena, and D. L. Smith they would not have existed. They all deserve my deep gratitude. I hope that many interesting projects will follow in the future. Over the years, I benefited from discussions with numerous people at the places I have been either as a visitor or as a temporary employee. I want to thank them all. In particular, however, I want to thank H. Böttger for his trust and support over the years I stayed in Magdeburg and for initiating my short-term appointment at Niigata University.

Erklärung

Hiermit erkläre ich, dass diese Arbeit bisher von mir weder der Mathematisch–Naturwissenschaftlichen Fakultät der Ernst–Moritz–Arndt–Universität Greifswald noch einer anderen wissenschaftlichen Einrichtung zum Zwecke der Habilitation vorgelegt wurde. Ferner erkläre ich, dass ich diese Arbeit selbständig verfasst und keine anderen als die angegebenen Hilfsmittel verwendet habe.

(Dr. Franz Xaver Bronold)

Curriculum Vitae

Personal data:

Name Franz Xaver Bronold
Date of Birth 01.08.1964
Place of Birth Ingolstadt
Citizenship German

School Education:

1970-1976 Primary school in Ingolstadt
1976-1980 Non-classical secondary school in Ingolstadt
1980-1983 Apprenticeship in Ingolstadt: electrician
1983-1985 Vocational secondary school in Ingolstadt

University Education:

1985-1991 Study of Physics, Universität Bayreuth
1991 Dipl. Phys. (Univ.), Universität Bayreuth
Diploma Thesis: *Nonlinear Electronic Excitations in Conjugated Polymers with Impurities* (in German)
1995 Dr. rer. nat., Universität Bayreuth,
Dissertation: *Optical Processes in Conjugated Polymers: A Coupled Exciton-Phonon Gas Approach*

Positions:

1991-1995 Graduate Research Assistant, Los Alamos National Laboratory, Los Alamos, New Mexico, USA.
1995-1996 Postdoc, Centre de Recherches sur les Très Basses Temperature, Grenoble, France.
1996-2002 Scientific Assistant, Otto-von-Guericke-Universität Magdeburg.
2002- Scientific Assistant, Ernst-Moritz-Arndt-Universität Greifswald.

Visiting positions (up-road and in Germany):

10/1999-03/2000 Assistant Professor, University Niigata, Niigata, Japan
09/2001-03/2002 Consultant, Los Alamos National Laboratory, Los Alamos, New Mexico, USA.
04/2002-09/2002 Visiting Scientist, Universität Bayreuth.
1997-2003 Various additional short term visits, Los Alamos National Laboratory, Los Alamos, New Mexico, USA.